RE-EVALUATION OF REFLECTION SEISMOLOGY FOR ARCHAEOLOGICAL INVESTIGATION

By

GUY MATTHEW CROSS
B. A. (Geophysics) The State University of New York.
M. Sc. (Geophysics) The University of British Columbia.

A THESIS SUBMITTED IN PARTIAL FULFILLMENT OF
THE REQUIREMENTS FOR THE DEGREE OF
DOCTOR OF PHILOSOPHY

in

THE FACULTY OF GRADUATE STUDIES
INTERDISCIPLINARY STUDIES
[Geophysics/Archaeology]

We accept this thesis as conforming
to the required standard

THE UNIVERSITY OF BRITISH COLUMBIA
April, 1995

In presenting this thesis in partial fulfilment of the requirements for an advanced degree at the University of British Columbia, I agree that the Library shall make it freely available for reference and study. I further agree that permission for extensive copying of this thesis for scholarly purposes may be granted by the head of my department or by his or her representatives. It is understood that copying or publication of this thesis for financial gain shall not be allowed without my written permission.

(Signature) _

Department of INTERDISCIPLINARY STUDIES

The University of British Columbia
Vancouver, Canada

Date 28 APRIL, 1995

DE-6 (2/88)

ABSTRACT

During the last decade, archaeologists have widely accepted the use of geophysical exploration techniques, including magnetic, resistivity and electromagnetic methods, for pre-excavation site assessment. Although researchers were quick to recognize the potential of seismic techniques to provide cross-sectional images of the subsurface, early feasibility studies concluded that seismic methods were inappropriate due to restricted resolving power and the relatively small-scale nature of archaeological features. Unfortunately, this self-fulfilling prophesy endures and has largely discouraged subsequent attempts to exploit seismic methods for archaeological reconnaissance. Meanwhile, however, seismic technology has been revolutionized in connection with engineering, groundwater and environmental applications. Attention to detail in developing both instrumentation and data acquisition techniques has yielded a many-fold improvement in seismic resolving power. In light of these advances, this dissertation re-examines the potential of reflection seismology for archaeological remote sensing.

It is not the objective of this dissertation to deliver an unequivocal pronouncement on the ultimate utility of reflection seismology for the investigation of archaeological sites. Rather, the goal has been to establish a sound theoretical foundation for objective evaluation of the method's potential and future development. In particular, a thorough theoretical analysis of seismic detection and resolution yields practical performance and identifies frequency response characteristics associated with optimum resolution. Findings have guided subsequent adaptation, development and integration of seismic instrumentation, resulting in a prototype system for high-resolution seismic imaging of the shallow subsurface.

Finally, to assess system performance and the suitability of optimum offset data acquisition techniques, a full-scale subsurface model has been constructed, allowing direct

comparison between experimental soundings and known subsurface structure. Results demonstrate the potential of reflection seismology to resolve near-surface features on the scale of archaeological interest. Moreover, despite conventional wisdom that the ground-penetrating radar method possesses vastly superior resolving power, acquisition of coincident radar soundings demonstrates that the two techniques provide comparable resolution.

TABLE OF CONTENTS

LIST OF FIGURES

Chapter 1
INTRODUCTION

The ground to the west of Wor Barrow was examined to ascertain if any trace of habitations could be found, but nothing of any kind could be seen upon the surface. The pick was then used to hammer on the surface, and by this means, the Angle Ditch was discovered.

Gen. A. Pitt-Rivers, 1895

Archaeological science encompasses a broad scope of interdisciplinary collaboration between archaeologists and their colleagues in the natural sciences. Techniques from physics, chemistry, biology and the geosciences have a prominent role in each phase of the archaeological process, including the reconnaissance of sites, their excavation and the subsequent analysis of recovered materials (Tite, 1972; Aitken, 1976; Butzer, 1982; Rapp and Gifford, 1985; Aitken, 1990, Tite, 1991). The present dissertation involves the branch of archaeological science devoted to use of remote sensing for archaeological site reconnaissance and, in particular, the adaptation of geophysical prospecting for detection and mapping of subsurface archaeological features (Weymouth, 1986; Scollar et al., 1990; Clark, 1990).

Archaeologists have long realized the potential of aerial photography to reveal the presence of patterned surface features that are either too large scale or too subtle to be recognized at ground level. Even where archaeological features are known to exist, an aerial perspective can expose unforeseen associations between individual features and, consequently, alter their interpretation. While relief features like earthworks and roads are archaeological remains in their own right, other features, including soil and crop marks, are more often a surface expression of buried remains. In these instances, anomalous soil moisture levels associated with subsurface structures are manifest visually as soil discolorations or related abnormalities in the maturity and vitality of overlying vegetation.

From its beginnings in First World War aviation, archaeological remote sensing has evolved from largely secondary examination of extant air photos to planned aerial reconnaissance using a variety of specialized sensors. Concurrently, with greater access to an aerial perspective, mapping of known archaeological sites has joined the search for previously undiscovered features as a primary objective of archaeological remote sensing. It

was toward this aim, that investigation of complementary ground based sensing techniques began by the early 1950s. In contrast with air photo analysis, which relies entirely on visual indication of buried remains, geophysical surveys are capable of detecting a variety of subsurface material contrasts that have little or no visible expression. Consequently, in addition to ground truthing of aerial reconnaissance, geophysical prospecting can substantially extend the base of remotely sensed information available to the archaeologist.

In view of budgetary restrictions on archaeological excavation and necessity for non-invasive, time-efficient cultural resource management, geophysical reconnaissance is valuable not only for directing the focus of limited excavation but also for extrapolating resulting information within both intrasite and intersite contexts. Geophysical methods also have obvious application where archaeological excavation is obstructed by modern pavement and buildings or prohibited by protective legislation. In light of this potential, archaeologists have largely acknowledged the value of remotely sensed information and over the past two decades geophysical sensing techniques have been widely employed for pre-excavation assessment and mapping of diverse archaeological sites. As in other applications, the complementary nature of geophysical methods has proved crucial with the most appropriate technique remaining site dependent.

Successful adaptation of resistivity and magnetic techniques by the late 1950s prompted subsequent investigation of other geophysical methods. By the mid 1970s, the full complement of geophysical exploration methods had undergone adaptation and evaluation for archaeological application. Among these, seismic techniques received early attention owing to their potential to yield cross sectional profiles of the subsurface and, consequently, to reveal the form and stratigraphic position of buried remains. However, despite the mixed findings of reported experiments (Linehan, 1956; Carson, 1962; Linington, 1963; MASCA, 1969) it was generally concluded by the early 1970s that land-based seismic methods were of limited value due to restricted resolution and the comparatively small scale nature of archaeological remains (Tite, 1972; Aitken, 1974).

It is difficult to assess the basis upon which the seminal works by Tite (1972) and

Aitken (1974) dismiss the potential of seismology. While Aitken (1974) makes no reference to the published literature, Tite (1972) refers to publications by Carson (1962) and Linington (1963). The frequently cited work by Carson (1962) describes a hammer seismic refraction survey conducted in conjunction with a resistivity survey at Harper's Ferry in West Virginia to detect and map the precise location of historic building foundation remains. Although no data are presented, departures from linear transit-time vs. distance diagrams were identified and (apparently qualitatively) attributed to either anticlinal or synclinal subsurface structures. Despite a significant correlation between predicted feature locations and subsequently excavated archaeological remains, it was noted that the average depth indicated by seismic soundings was appreciably greater than the ruins. As a result, it was concluded that transit-time anomalies were attributable to bedrock topography rather than archaeological remains within the overburden. The subsequent review of archaeological remote sensing by Linington (1963) observed, without reference, that "at present only sufficient experimental work has been done to show that a feasible method of surveying is possible". It appears that neither Carson nor Linington were aware of the earlier work of Linehan (1956) who reported a very successful programme of shallow seismic refraction measurements in connection with archaeological excavations beneath St. Peter's Basilica in Rome. Refraction surveys revealed a variety of buried architectural remains including the walls and rooms of a lower basilica, tombs and a buried circus adjacent to the present basilica of Michelangelo. Again, however, there are no representative data presented. In view of these varied findings, one must assume that the negative conclusions reached by Tite (1972) and Aitken (1974) are based to some measure on other, perhaps unpublished, field trials.

Subsequent applications of acoustic techniques in connection with marine archaeology (McGehee et al., 1969; MASCA, 1972; Meissner and Stümpel, 1979) have been decidedly successful and there have been significant attempts to adapt these higher frequency "acoustic" techniques for use on land (Hesse, 1969; Dolphin et al., 1977; Ozawa and Matsuda, 1979). Dolphin et al. (1977), for example, describe the successful application of a 4 kHz

acoustic sounder for detection and mapping of previously unknown passages and chambers within ancient Egyptian monuments at Giza and Luxor. Similarly, Ozawa and Matsuda (1979) report promising trials of a prototype seismic-acoustic apparatus comprising four microphone transducers surrounding a small weight-drop elastic source. Experiments confirmed the presence of a stone coffin within an ancient Japanese tomb. In view of the relatively complicated, special purpose instrumentation employed in the forgoing studies, it is perhaps not surprising that these experiments have not been reproduced elsewhere. In any case, despite these very promising developments, the ill-fated reputation of seismic prospection has endured (Weymouth, 1986; Scollar et al., 1990) and largely discouraged subsequent archaeological use. Meanwhile, seismic reflection technology has been revolutionized in connection with engineering and groundwater geophysics (Dobecki and Romig, 1986). Attention to detail in developing both instrumentation and data acquisition techniques has yielded a many-fold improvement in seismic resolving power that suggests renewed archaeological interest.

In light of recent advances, this dissertation reassesses the potential of seismic reflection techniques for subsurface archaeological imaging. However, in contrast with previous studies, devoted to empirical field evaluations of existing technology, this dissertation emphasizes the establishment of a sound theoretical foundation for subsequent research and development.

A thorough analysis of theoretical aspects of seismic detection and resolution is presented in Chapter 2. In particular, completely novel detection criteria are developed in connection with a treatment of isotropic scattering from a spherical archaeolological deposit embedded within a uniform host matrix. Modelling makes use of a scattering cross-section developed by Ying and Truell (1956). On establishing detectability, a subsequent analysis of vertical resolution involves a synthesis of well-known criteria and their dependence on established properties of band-limited frequency signals. In connection with this development, the author supplies demonstrations (Appendices C-L), some novel and improved, of fundamental wavelet properties. Finally analysis of spatial resolution reviews the clas-

sical optics treatment of half-period Fresnel zones on an infinite horizontal reflector and illustrates the connection between these results and a generalized seismic response for a finite horizontal reflector of developed by Trorey (1970). Two spatial resolution criteria are subsequently identified in connection with the interference of edge diffractions from a infinite-length, finite-width strip reflector. The seismic response of the strip is derived on the basis of Trorey's (1970) half-plane solution. A direct and significant connection is established between the standard Fresnel zone criterion and Rayleigh's temporal resolution limit.

The theoretical analysis of seismic detection and resolution has critical implications for the design and integration of appropriate instrumentation. Findings have guided subsequent development of a prototype system for high resolution archaeological application and Chapter 3 is devoted to description of this system and its constituent components. The seismic data acquisition system is modelled as a cascade of non-interacting, time-invariant linear systems and the general response characteristics of each system component are developed and illustrated with various degrees of original contribution. These analyses have guided design and construction of a special purpose high-frequency energy source and in-line analog pre-emphasis filter electronics. Together with a commercially available detector possessing unique high-frequency response characteristics, these components effectively compensate for the low-pass, dispersive characteristics of the subsurface to yield seismic soundings that possess a broad-band smoothly varying frequency spectrum and, consequently, enhanced resolving power.

Chapter 4 examines a simple but effective data acquisition strategy in connection with full-scale subsurface model experiments conducted to assess system performance. Acquisition of coincident ground penetrating radar profiles demonstrates that despite conventional wisdom, the reflection seismic method is capable of comparable resolution. It is emphasized that the two methods yield complementary information.

Finally, two chapter-length appendices (Appendices A and B) present detailed theoretical analyses of two previously unexplored matters of pivotal significance in connection

with small-scale, near-surface seismic exploration.

Recognizing that seismic targets of archaeological interest are commonly isolated, discontinuous inhomogeneities embedded within an otherwise homogeneous host medium, ordinary velocity analysis techniques based on the moveout characteristics of reflection events from semi-continuous geological interfaces are largely inappropriate. Consequently, in Appendix A, a novel method is developed for estimating seismic velocities from diffraction events associated with the scattering of elastic waves from subsurface discontinuities. Appendix B re-addresses the controversial subject of spatial filtering for high-resolution, near-surface seismic applications. As demonstrated in Chapters 2 and 3, a key to acquiring high-resolution seismic data is optimum exploitation of dynamic range through real-time attenuation of source-generated noise. Despite uninformed consensus that spatial array filters can be profitably employed for this purpose, standard array response analysis indicates that these techniques are not well suited for near-surface, high frequency applications like archaeology. Noting that the foregoing conclusion presupposes plane-wavefront geometry, Appendix B examines the validity and limitations of the plane-wave approximation in anticipation that the viability of spatial filtering might be misprized by neglecting wavefront curvature in near source applications like archaeology. Although the foregoing studies have considerable implications for archaeological application, they are presented in Appendices A and B as previously published for a wider audience (Cross and Knoll, 1991: Cross, 1992) and, consequently, do not possess an archaeological focus. Essential findings of these analyses have been incorporated within the main body of the dissertation.

Chapter 2

SEISMIC DETECTION AND RESOLUTION

Seismic techniques are powerful in geophysical exploration but do not lend themselves to the smaller and more detailed scale required for archaeology.

M. J. Aitken, 1974

2.1 Introduction:

Since seismic methods were deemed unsuitable for archaeological application owing to insufficient resolving power, it is fitting that re-evaluation should commence with a review of the fundamental principles of seismic detection and resolution. As an objective, we shall seek to establish whether certain types of archaeological features reside within detection and resolution limits of seismic exploration. In particular, there are two distinct classes of archaeological features amenable to remote detection and mapping by geophysical methods: localized inhomogeneities embedded within a relatively uniform host soil and semi-continuous stratigraphic horizons. The first class embraces architectural remains including foundations, pavement, walls, roads, fortifications, etc. and subsoil structures on a similar scale including earthworks, barrows, graves, storage pits, hearths, furrows and localized deposits like middens and refuse. Archaeological features of the second kind include both natural geologic interfaces and stratigraphic horizons of cultural origin.

Although the first class of features implies an approximate scale of interest, it is important to appreciate that the effective "scale" of an archaeological feature involves a significant trade-off between its gross dimensions and the degree of contrast between its material properties and those of the host medium. For example, since architectural remains are constructed from a variety of building materials, having material properties in marked contrast with those of the host soil, these features have an effective scale decidedly larger than soil features of similar dimension but having material properties only subtlely dissimilar to those of surrounding sediments. This is only a general rule of thumb, however, and in practice the relative influence of gross dimension and material contrast depend substantially upon the geophysical technique employed. For instance, while it is not uncommon

for burned soil features to yield magnetic anomalies many times larger than architectural remains comprised by relatively unweathered building stone, the latter will almost invariably produce a stronger seismic response than a corresponding subsoil structure having similar dimensions. Archaeological features of the second kind are also characterized by an enormous range of material contrasts; from subtle gradations in sediment colour, or particle size distribution, to sharp variation in soil organic matter arising from agricultural activity, to geologic unconformities between weathered bedrock and unconsolidated overburden.

More significantly, the two classes of archaeological features yield seismic responses of distinctly different character. While semi-continuous, often flat-lying, stratigraphic horizons act predominantly as reflectors of incident seismic energy, localized inhomogeneities, like architectural remains, partially reflect and partially scatter or diffract incident seismic energy. In particular, where the dimensions of the inhomogeneity are significantly less than the wavelength of incident waves, the mechanism of interaction is principally diffraction. Consequently, the character of seismic records acquired over archaeological features of the first kind can be considerably different than seismic data acquired to elucidate shallow stratigraphy or, more typically to map large scale geologic structure. In the following analysis of seismic detection and resolution, we shall find that separate criteria are associated with the two classes of archaeological features.

2.2 Detection:

In the context of remote sensing, detection is defined as the ability to recognize signal in the presence of noise. In the case of reflection seismology, the signal is elastic wave energy reflected or scattered from targets of interest. Ideally, if the fraction of incident energy reradiated from the target and received by the detector exceeds electrical and ambient seismic noise, the signal is said to be detectable. In other words the signal to noise ratio must exceed unity. Factors influencing the detectability of a given target include its dimensions, geometry, range and the contrast between its material properties and those

of the host medium. More significantly, detection depends on the wavelength of incident energy. In particular, for wavelengths significantly greater than the average target dimension, the ratio of scattered to incident wave energy and, consequently, detection are proportional to the inverse fourth power of wavelength. Scattering of this nature, termed Rayleigh scattering, typifies the seismic response of localized inhomogeneities at the limit of detectability.

A simple expression for the detection limit, appropriate for archaeological features of the first kind having dimensions significantly less than a wavelength, can be developed in the following manner. Consider a spherical wave $u_i^0(r,t) = \{u_r, u_\vartheta, u_\varphi\}$ of the form

$$\begin{aligned} u_r(r,t) &= u_r^0(t) * \delta\left(t - \frac{r - r_0}{\alpha_0}\right) \\ u_\vartheta(r,t) &= u_\vartheta^0(t) * \delta\left(t - \frac{r - r_0}{\beta_0}\right) \\ u_\varphi(r,t) &= u_\varphi^0(t) * \delta\left(t - \frac{r - r_0}{\beta_0}\right) \end{aligned} \tag{2.1a}$$

radiating from a concentrated source region surrounding the coordinate origin within a homogeneous, isotropic, linearly elastic halfspace. Here, u_r^0, u_ϑ^0 and u_φ^0 denote, respectively, radial, latitudinal and longitudinal time-dependent displacement waveforms at reference range r_0 including the source region. $r \geq r_0$ represents an arbitrary range, * the convolution operation and $\delta(t)$ denotes the Dirac delta function, having defining properties $\delta(t) = 0;\ t \neq 0$ and $\int_{-\infty}^{\infty} \delta(t)\,dt = 1$. Radial and tangential components of the wavefield are characterized by phase velocities $\alpha_0 = [(\lambda_0 + 2\mu_0)/\rho_0]^{1/2}$ and $\beta_0 = [\mu_0/\rho_0]^{1/2}$, respectively, where ρ_0 represents density and λ_0 and μ_0 are Lame's elastic constants for the host medium. For sake of simplicity, we take $u_\vartheta^0 = u_\varphi^0 = 0$ and consider a purely radial or dilatational wavefield, having sinusoidal displacement of form

$$u_r^0(t) = U_r^0\left(\frac{r_0}{r}\right) \sin(2\pi f t)\, H(t), \tag{2.1b}$$

where f is frequency and

$$H(t) = \begin{cases} 0, & t < 0; \\ 1/2, & t = 0; \\ 1, & t > 0 \end{cases}$$

is the Heaviside step function. Finally, on substituting previous expression in equation 2.1 and assuming that sufficient time has elapsed for the seismic disturbance to extend over the region of interest (i.e. $H[t-(r/\alpha_0)]=1$), we obtain the steady-state radial wavefield

$$u_i(r,t)=\left\{U_r^0\left(\frac{r_0}{r}\right)\sin\left[\frac{2\pi\alpha_0}{\lambda_{\alpha_0}}\left(t-\frac{r-r_0}{\alpha_0}\right)\right],0,0\right\}, \tag{2.1c}$$

where $\lambda_{\alpha_0}=\alpha_0/f$ is the effective wavelength. Since at any instant, the energy per unit volume possessed by a seismic disturbance having such a form is half kinetic and half potential, the corresponding energy density as a function of range is

$$\mathcal{E}_0(r,t)=\rho_0\frac{\partial u_i{}^0}{\partial t}\frac{\partial u_i{}^0}{\partial t}=4\pi^2\frac{\rho_0\alpha_0{}^2}{\lambda_{\alpha_0}{}^2}U_r{}^2\left(\frac{r_0}{r}\right)^2\cos^2\left[\frac{2\pi}{\lambda_{\alpha_0}}(r-\alpha_0 t)\right], \tag{2.2}$$

where ρ_0 is the density of the host medium. The associated intensity or mean energy per unit area transported normal to the wavefront per unit time follows as the product of phase velocity and energy density, averaged over a period. Using the result

$$\frac{1}{T}\int_{\tau}^{\tau+T}\cos^2(\phi-2\pi ft)\,dt=\frac{1}{2},$$

where $T=1/f$ denotes the period and ϕ represents an arbitrary phase angle, we obtain

$$I_0(r)=2\pi^2\frac{\rho_0\alpha_0{}^3}{\lambda_{\alpha_0}^2}U_r{}^2\left(\frac{r_0}{r}\right)^2. \tag{2.3}$$

Finally, since intensity is equivalent to average power transported per unit area, mean source power can be obtained by multiplying the intensity at arbitrary range by the surface area of the corresponding wavefront

$$P_0=4\pi r^2 I_0(r)=8\pi^3\frac{\rho_0\alpha_0{}^3 r_0{}^2}{\lambda_{\alpha_0}^2}U_r{}^2. \tag{2.4}$$

Peak source power follows as $2P_0$.

Let us now consider the interaction between this incident wavefield and a localized inhomogeneity at range r_s from the source region. Interaction is commonly quantified by computing the scattering cross-section for the inhomogeneity, defined as the ratio of mean energy scattered per unit time, to the mean energy per unit area transported per unit

time by the incident wavefront. In other words, the scattering cross-section is the ratio of scattered power to incident intensity. Consequently, for the incident wavefield considered above, the average power scattered by a localized inhomogeneity having cross-section χ_s is

$$P_1 = \chi_s I_0(r) = 2\pi^2 \frac{\rho_0 {\alpha_0}^3}{\lambda_{\alpha_0}^2} \chi_s {U_r}^2 \left(\frac{r_0}{r_s}\right)^2. \tag{2.5}$$

Although conceptually simple, evaluation of an appropriate scattering cross-section is complicated and a number of simplifying assumptions are ordinarily required. In particular, it is normally assumed that the dimensions of the inhomogeneity are small compared with range r, allowing the incident wavefront to be treated as locally planar over the region of interaction. In addition, the scattering medium is normally assumed to be homogeneous and isotropic. An exceptionally thorough treatment was presented by Ying and Truell (1956).

On prescribing the wavefield incident on a spherical inclusion, series solutions for Navier's equation in spherical coordinates are written in terms of Helmholtz potentials for both the scattered wave and the wavefield existing within the inclusion. Series coefficients are determined for an elastic inclusion by applying boundary conditions requiring continuity of net stresses and displacements across the surface of the spherical inclusion. For the case of Rayleigh scattering, where the inclusion radius ϱ is small compared with wavelength, the series solutions converge rapidly and may be truncated to give as close an approximation as desired. A general expression for the scattering cross-section follows from the scattered displacement field. For a plane dilatational wave incident on an isotropically elastic inclusion, the appropriate scattering cross-section is given by

$$\chi_s = \frac{\xi \varrho^6}{\lambda_{\alpha_0}^4} \tag{2.6}$$

with

$$\xi = \frac{64\pi^5}{9} \left\{ \left[\frac{3{\gamma_0}^2}{(3{\gamma_1}^2 - 4)M + 4} - 1 \right]^2 + \frac{1}{3}\left[1 + 2{\gamma_0}^3\right] \times \left[\frac{M}{\gamma_\beta} - 1\right]^2 \right.$$

$$\left. + 40\left[2 + 3{\gamma_0}^5\right] \times \left[\frac{M-1}{2(3{\gamma_0}^2 + 2)M + (9{\gamma_0}^2 - 4)}\right]^2 \right\},$$

referred to as the reflectivity factor, where $\gamma_0 = \lambda_{\alpha_0}/\lambda_{\beta_0} = \alpha_0/\beta_0$ and $\gamma_1 = \lambda_{\alpha_1}/\lambda_{\beta_1} = \alpha_1/\beta_1$ are ratios of dilatational to rotational velocities in the host medium and inclusion, respectively, $\gamma_\beta = \lambda_{\beta_1}/\lambda_{\beta_0} = \beta_1/\beta_0$ is the ratio of rotational wave velocities in the two media and $M = \mu_1/\mu_0 = (\rho_1/\rho_0)(\beta_1/\beta_0)^2$ is the corresponding ratio of shear moduli. Note dependence on the inverse fourth power of incident wavelength characteristic of Rayleigh scattering.

Substitution of the foregoing result in equation (2.5) yields

$$P_1 = 2\pi^2 \frac{\xi \varrho^6 \rho_0 {\alpha_0}^3}{\lambda_{\alpha_0}^6} U_r^2 \left(\frac{r_0}{r_s}\right)^2 \tag{2.7}$$

for the mean power scattered by the elastic inclusion. Further, supposing isotropic scattering, the intensity as a function of range R from the center of the inclusion is obtained by dividing the mean radiated power by the surface area of the scattered wavefront. The result is

$$I_1(R) = \frac{P_1}{4\pi R^2} = \frac{\pi}{2} \frac{\xi \varrho^6 \rho_0 \alpha_0^3}{\lambda_{\alpha_0}^6} U_r^2 \left(\frac{r_0}{r_s R}\right)^2. \tag{2.8}$$

Consequently, scattered power received by an omni-directional detector at range R_d from the scattering center and having effective capture area ζ_d is

$$\tilde{P}_1 = \zeta I_1(R) = \frac{\pi}{2} \frac{\xi \varrho^6 \rho_0 \alpha_0^3}{\lambda_{\alpha_0}^6} \zeta_d U_r^2 \left(\frac{r_0}{r_s R_d}\right)^2. \tag{2.9}$$

Recalling that detection requires a signal to noise ratio exceeding unity, a criterion defining the detection limit follows as

$$\frac{\tilde{P}_1}{P_n} = \frac{\pi}{2} \frac{\xi \varrho^6 \rho_0 \alpha_0^3}{\lambda_{\alpha_0}^6} \frac{\zeta_d U_r^2}{P_n} \left(\frac{r_0}{r_s R_d}\right)^2 > 1, \tag{2.10}$$

where P_n denotes the ambient noise power.

Having defined an ideal detection limit by the previous inequality, it must be noted that a more severe limitation may be imposed by the dynamic range of the detector and recording instrumentation. Dynamic range is defined as the ratio of maximum to minimum signal levels that are simultaneously detectable. If two signals are simultaneously incident on the detector with a power ratio exceeding the dynamic range, the more powerful signal

will effectively saturate the receiving system preventing detection of the less powerful signal. In particular, in the case of small scale archaeological applications, the primary energy source is in relatively close proximity to the detector. Assuming that the direct arrival from source to receiver constitutes the maximum signal level $P_{max} = \tilde{P}_0 = \zeta_d I_0(r)$, a more stringent detection criterion requires that the ratio of direct to scattered power received at the detector must not exceed the dynamic range of the recording system. From equations (2.3) and (2.9), we obtain the equivalent mathematical expression

$$\frac{\tilde{P}_1}{\tilde{P}_0} = \frac{1}{4\pi} \frac{\xi \varrho^6}{\lambda_{\alpha_0}^4} \left(\frac{r_d}{r_s R_d} \right)^2 > \frac{1}{\Delta}, \tag{2.11}$$

where r_d denotes the range from source to detector and $\Delta = P_{max}/P_{min} = \tilde{P}_0/P_{min}$ represents dynamic range. Here, P_{min} represents the minimum detectable signal level. Notice that, like the scattering cross-section given by equation (2.6), this detection criterion is proportional to the inverse fourth power of incident wavelength.

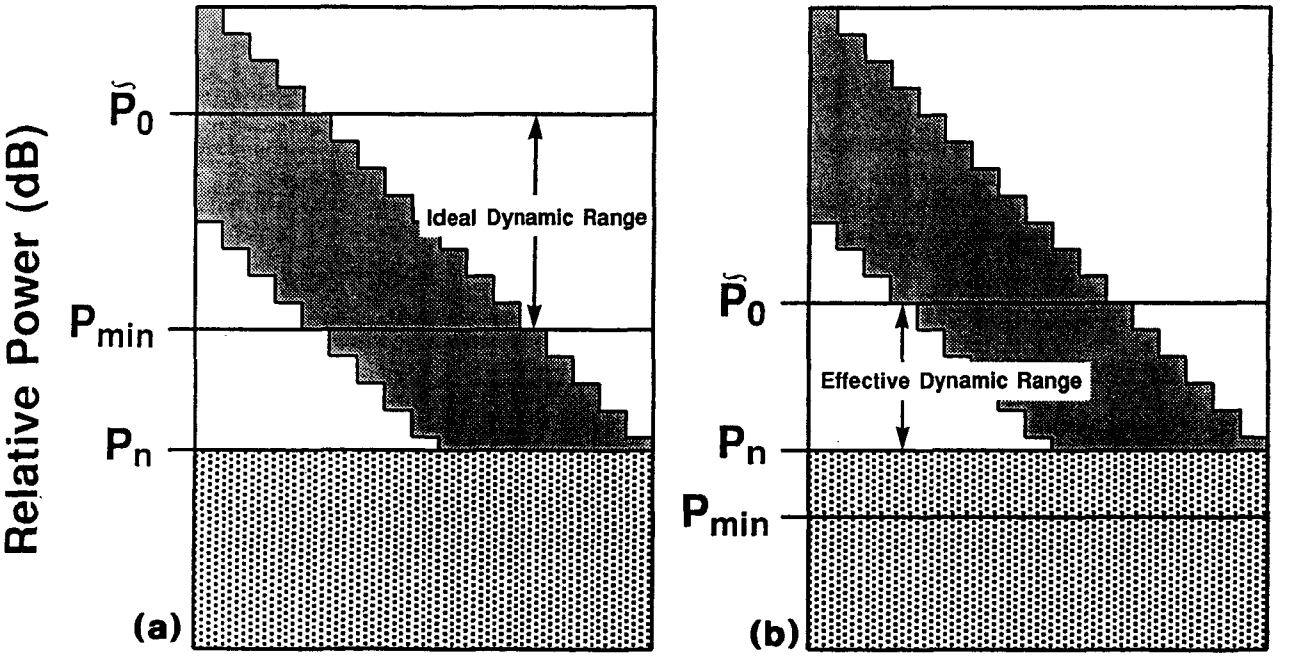

Figure 2.1. System power level diagrams comparing conditions for detection criteria given by equations (2.12) and (2.13). (a) For $P_n < P_{min}$ detection is limited by dynamic range. (b) For $P_n > P_{min}$ detection is limited by signal to noise ratio.

Equations (2.10) and (2.11) may be solved for respective limiting inclusion radii, yielding

$$\varrho_n = \left[\frac{2\lambda_{\alpha_0}^6}{\pi\xi\rho_0\alpha_0^3}\frac{P_n}{\zeta_d U_r^2}\left(\frac{r_s R_d}{r_0}\right)^2\right]^{1/6} \tag{2.12}$$

and

$$\varrho_\Delta = \left[\frac{4\pi\lambda_{\alpha_0}^4}{\xi}\frac{1}{\Delta}\left(\frac{r_s R_d}{r_d}\right)^2\right]^{1/6}. \tag{2.13}$$

Referring to Figure 2.1, if $\tilde{P}_0/P_n < \Delta$ or $P_n > P_{min}$, the minimum detectable inclusion radius is ϱ_n. If, however, $\tilde{P}_0/P_n > \Delta$ or $P_n < P_{min}$, the minimum detectable scattering radius is ϱ_Δ ($> \varrho_n$). Finally, if $P_n = P_{min}$, equation (2.12) reduces to equation (2.13), yielding a limiting radius $\varrho = \varrho_\Delta = \varrho_n$. To examine the dependence of these detection limits on controlling parameters, we adopt the following nominal velocities and associated mechanical properties for the two media as a reference model:

$$\begin{aligned}
&\alpha_0 = 350.0\ \text{ms}^{-1} && \alpha_1 = 2500.0\ \text{ms}^{-1}\\
&\beta_0 = 100.0\ \text{ms}^{-1} && \beta_1 = 1250.0\ \text{ms}^{-1}\\
&\rho_0 = 1340.9\ \text{kg m}^{-3} && \rho_1 = 2192.0\ \text{kg m}^{-3}.\\
&\gamma_0 = 3.5 && \gamma_1 = 2.0\\
&\sigma_0 = 0.456 && \sigma_1 = 0.333
\end{aligned}$$

The influence of a given parameter is appraised by varying its value over a prescribed range while holding remaining parameters constant at their respective nominal values.

Throughout the following analysis, density values are assigned on the basis of the simple empirical relation

$$\rho = 310.0\,\alpha^{1/4} \tag{2.14}$$

proposed by Gardner et al. (1974). Although this relation is not especially well suited for unconsolidated granular media, it yields densities that are not unreasonable for a broad range of earth materials and, consequently, is convenient for phenomenological modelling. Values for Poisson's ratio follow from the corresponding dilatational to rotational velocity ratio according to the well known relation

$$\sigma = \frac{1}{2}\left(\frac{\gamma^2-2}{\gamma^2-1}\right) = \frac{1}{2}\left[\frac{(\alpha/\beta)^2-2}{(\alpha/\beta)^2-1}\right] \tag{2.15}$$

or, inversely,

$$\gamma = \alpha/\beta = \left[\frac{2(1-\sigma)}{1-2\sigma}\right]^{1/2}. \tag{2.16}$$

Assuming $P_n = P_{min}$, a dynamic range of 24 decibels (8-bit analogue-to-digital conversion) and a nominal frequency of 400.0 Hz, the relationship between detection limit and source-receiver offset r_d is displayed in Figure 2.2 with total one-way transit range $R_T = r_s + R_d$ (see Figure 2.3) as a parameter.

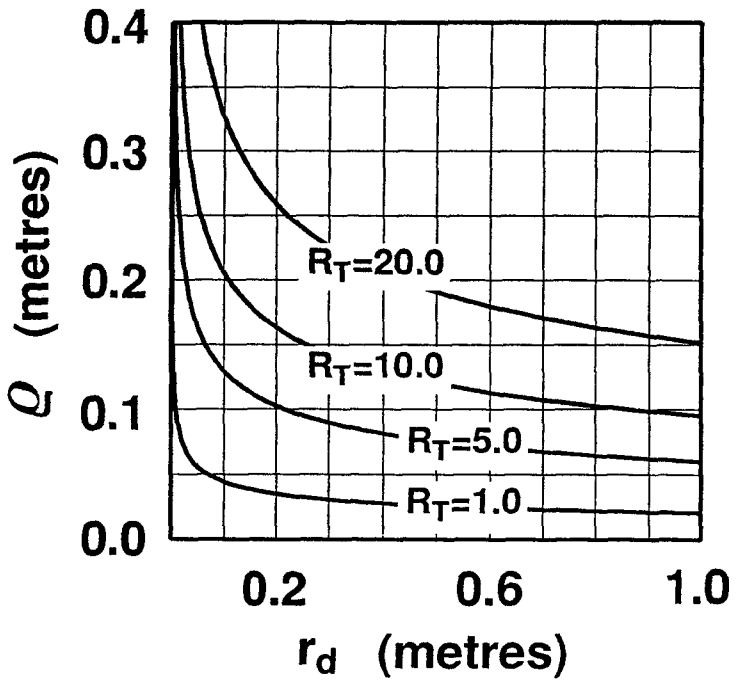

Figure 2.2. Predicted relation between detection limit $\varrho_\Delta = \varrho_n$ and source-detector offset r_d with total one-way transit range $R_T = r_s + R_d$ as a parameter.

Referring to Figure 2.3, note that for a source-detector pair deployed on a constant-z plane and separated by offset r_d, all possible inclusions for which total range from source to detector via scattering is a constant R_T lie on an ellipsoid having major axis R_T and eccentricity r_d/R_T. As predicted by equation (2.13), all curves approach infinity as the distance separating source and receiver vanishes. Practically speaking, this result illustrates that a detector deployed coincident with the source will be saturated by an instantaneous direct arrival having infinite strength so that the minimum detectable signal level and, consequently, the detection limit are also effectively infinite. Otherwise, theoretical results displayed in Figure 2.2 indicate that for r_d exceeding about 10.0 cm, the detection limit

ranges from less than 35.0 cm for $R_T = 20.0$ m to less than 5.0 cm for $R_T = 1.0$ m. Consequently, since archaeological targets are ordinarily located within a metre or two of the surface, the foregoing findings suggest that the scale of archaeological interest can reside well within the detection limit of seismic exploration. The influence of other controlling parameters, including incident wavelength and the contrast between material properties of the inclusion and host medium reinforce this conclusion.

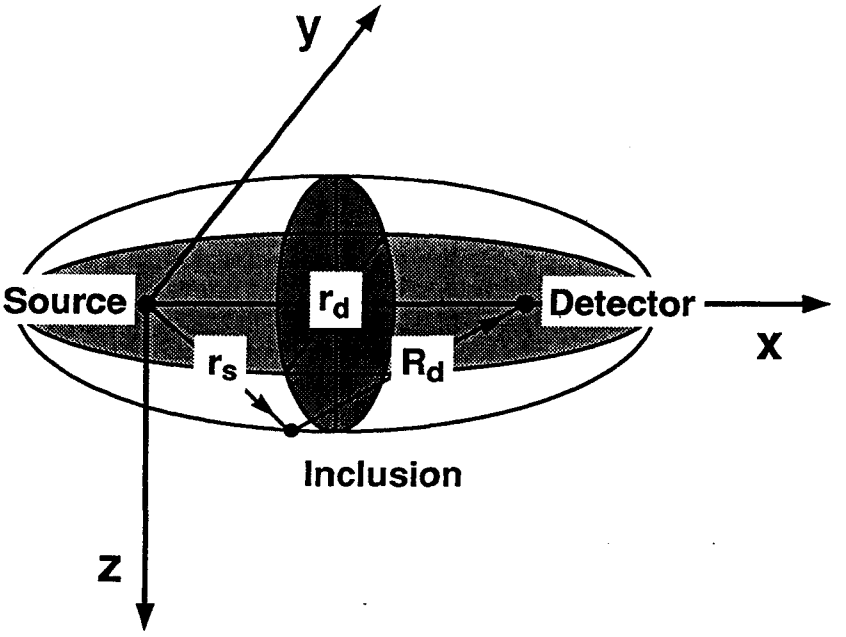

Figure 2.3. Configuration of source, detector and scatterer. All targets or scatterers for which total one-way transit range $R_T = r_s + R_d$ is constant lie on an ellipsoid having major axis R_T and eccentricity r_d/R_T.

Figure 2.4, for example, charts the relation between the detection limit and incident wavelength, assuming $r_d = 0.25$ m. As indicated by equation (2.13), minimum detectable radius increases non-linearly with increasing wavelength. Moreover, it is evident that this dependence is more pronounced as total range increases. In particular, for $\lambda_{\alpha_0} = 0.875$ m, corresponding to a nominal frequency of 400 Hz and host velocity $\alpha_0 = 350.0\,\mathrm{ms}^{-1}$, the limiting detection radius varies from approximately 2.0 to 7.0 cm. In addition, for a total one-way range of $R_T = 3.0$ m, the detection limit varies from a radius of approximately 4.0 cm for an incident wavelength of $\lambda_{\alpha_0} = 35.0$ cm at f=1 kHz, to roughly 17.5 cm for

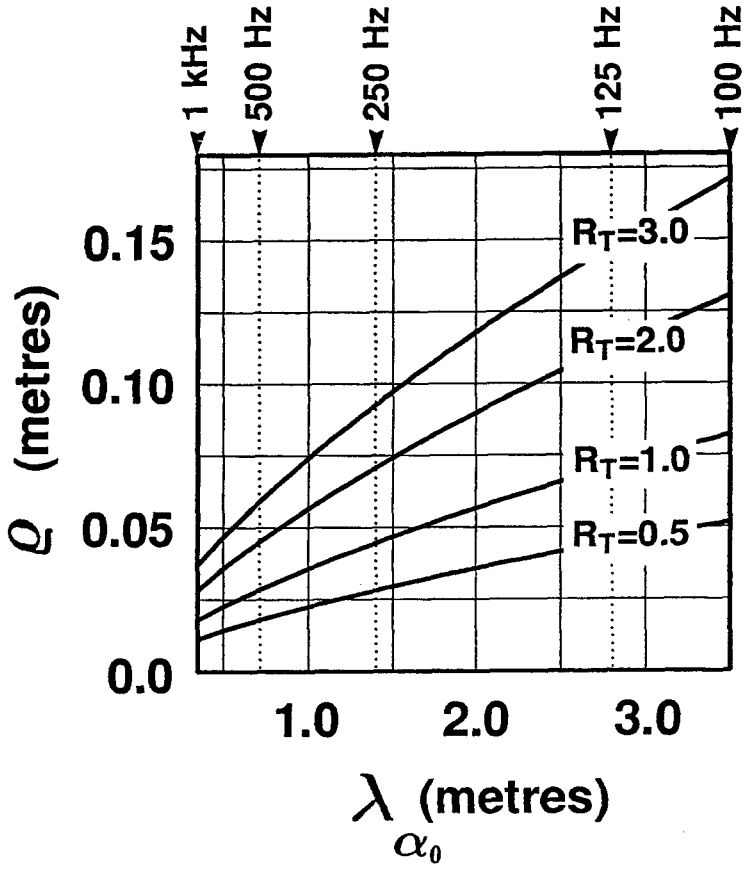

Figure 2.4. Predicted relation between detection limit $\varrho_\Delta = \varrho_n$ and incident wavelength λ with total one-way transit range $R_T = r_s + R_d$ as a parameter.

$\lambda_{\alpha_0} = 3.5$ m at f=100 Hz. In comparison, for a total transit range of $R_T = 0.5$ m, the detection limit never exceeds about 5.0 cm. These results indicate that, given a significant material contrast, seismic soundings are capable of detecting inhomogeneities having dimensions on the scale of archaeological interest; even where this scale is considerably smaller than the incident wavelength. For instance, in the case $R_T = 3.0$ m the ratio of minimum detectable radius to incident wavelength varies from approximately $\varrho/\lambda_{\alpha_0} = 0.11$ for f=1 kHz to $\varrho/\lambda_{\alpha_0} = 0.05$ for f=100 Hz. As expected, for $R_T = 0.5$ m, the corresponding values are yet smaller, ranging from $\varrho/\lambda_{\alpha_0} = 0.04$ for f=1kHz to $\varrho/\lambda_{\alpha_0} = 0.02$ for f=100 Hz.

Figures 2.5 and 2.6 display minimum detectable radius as functions of material property contrasts between the inclusion and host medium. Specifically, these curves reflect the influence of velocity contrasts between the two media as incorporated in the reflectivity factor ξ. In Figure 2.5, we fix inclusion velocities at the nominal values given above and examine the influence of variable host velocities. In Figure 2.6, on the other hand, we hold the nominal velocities of the host medium constant and analyze the effect of variable inclusion velocities. In all cases, results are depicted for the same suite of total one-way transit ranges as in Figure 2.2. Specifically, in Figure 2.5, host velocities are varied while maintaining the ratio of rotational to dilatational wave velocities constant at α_0/β_0 =3.5 (solid curve) and α_0/β_0 =4.0 (dashed curve) corresponding, respectively, to Poisson's ratios of σ_0 =0.456 and σ_0 =0.467 for unconsolidated sediments. Concurrently, as host velocity α_0 increases from 100 to 1000 ms^{-1}, the associated density ρ_0 is computed using equation (2.14). Recall that Poisson's ratio is defined as the ratio of strain parallel to an applied normal stress to the associated strain perpendicular to the applied stress and is related to Lame's elastic constants by the formula

$$\sigma = \frac{\lambda}{2(\lambda+\mu)}. \tag{2.17}$$

Assuming that Lame's constants are positive valued, Poisson's ratio ranges from σ =0.5 to σ =0.0 as the modulus of rigidity μ varies from zero to infinity. In practice, geological materials are characterized by Poisson's ratios ranging from the limiting value of $\sigma = 0.5$ for sediments in fluid suspension to approximately $\sigma = 0.2$ for extremely rigid, unweathered rocks. As depicted in Figure 2.5 for a maximum range of R_T =3.0 m and $\sigma_0 = 0.456$, the detection limit increases from a radius of approximately 2.0 cm for a dilatational velocity of 100.0 ms^{-1} to roughly 22.0 cm, corresponding to a velocity of 1000.0 ms^{-1}. Furthermore, comparison of foregoing results with those for $\sigma_0 = 0.467$ indicates that the predicted detection limit is reduced in all cases as Poisson's ratio increases; that is, as the rigidity contrast between the inclusion and host medium increases. Although enhanced detectability accompanying a decrease in host velocities is due, in large measure,

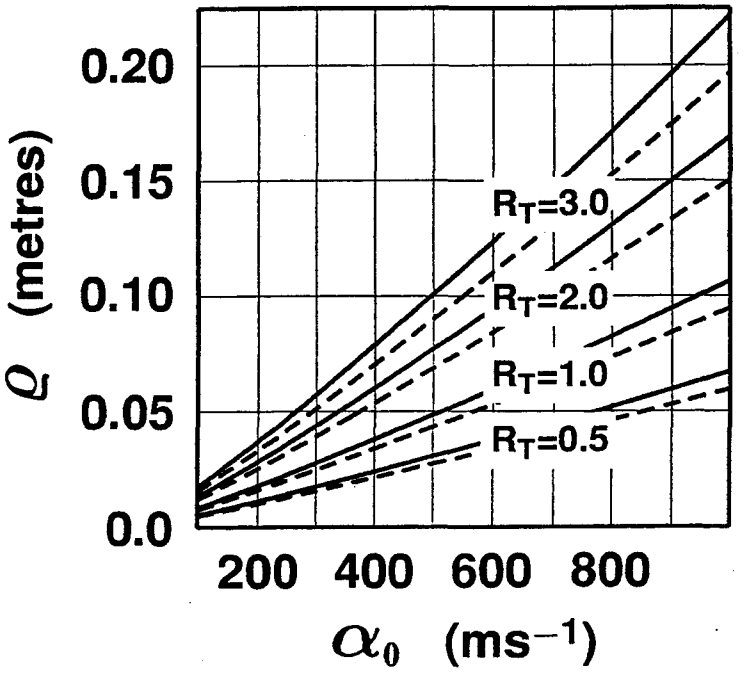

Figure 2.5. Predicted relation between detection limit $\varrho_\Delta = \varrho_n$ and the dilatational wave velocity α_0 of the host medium with total one-way transit range $R_T = r_s + R_d$ as a parameter. Results are displayed for Poisson's ratios of $\sigma_0 = .456$ (solid curve) and $\sigma_0 = .467$ (dashed curve).

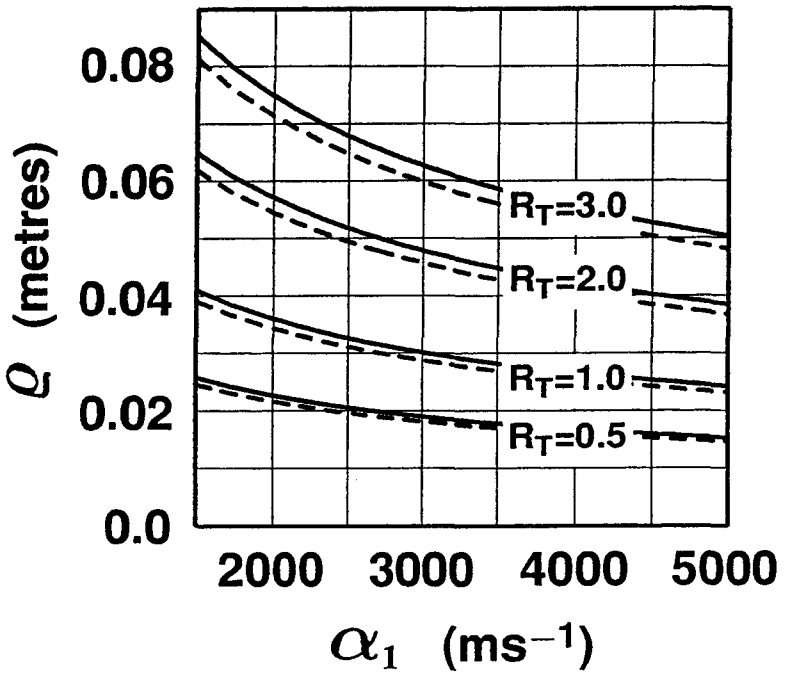

Figure 2.6. Predicted relation between detection limit $\varrho_\Delta = \varrho_n$ and the dilatational wave velocity α_1 of the inclusion with total one-way transit range $R_T = r_s + R_d$ as a parameter. Results are displayed for Poisson's ratios of $\sigma_1 = .333$ (solid curve) and $\sigma_0 = .258$ (dashed curve).

to an associated increase in the reflectivity factor, it is important to appreciate that the velocity of the host medium also controls the incident wavelength according to the relation $\lambda = \alpha_0/f$. Consequently, since the detection limit diminishes with decreasing wavelength, as illustrated in Figure 2.4, a lower host velocity yields improved detectability.

Figure 2.6 displays results for the reverse scenario. Here, on fixing velocities for the host medium, the dilatational inclusion velocity is varied from 1500.0 to 5000.0 ms^{-1} while maintaining constant velocity ratios of α_1/β_1 =2.0 and α_1/β_1 =1.75. Corresponding Poisson's ratios are, respectively, $\sigma_1 = 0.333$ for masonry or severely weathered building stone and $\sigma_1 = 0.258$ for relatively unweathered materials. For a maximum one-way transit range of 3.0 m and $\sigma_1 = 0.333$, the minimum detectable radius decreases from a maximum of approximately 8.5 cm for $\alpha_1 = 1500.0\,ms^{-1}$ to just over 5.0 cm for $\alpha_1 = 5000.0\,ms^{-1}$. As before, enhanced detectability is associated with a greater rigidity contrast and, consequently, the lesser Poisson's ratio of $\sigma_1 = 0.258$.

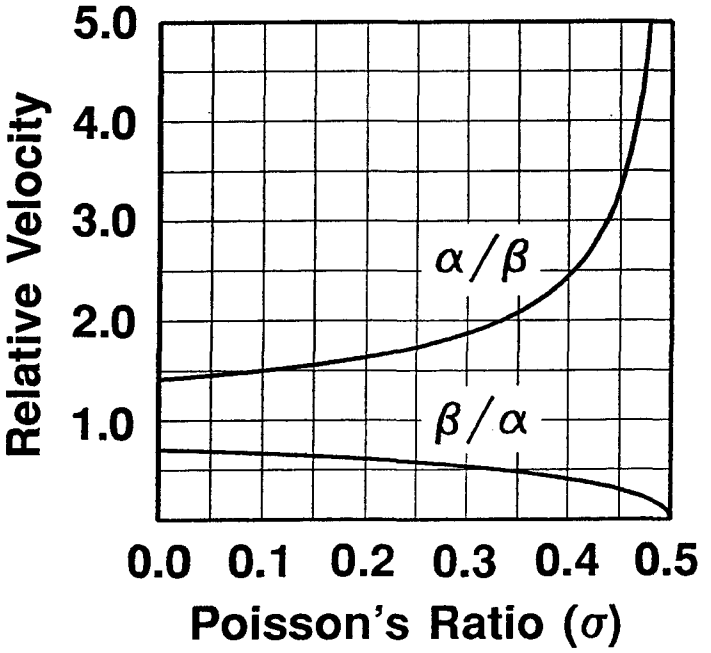

Figure 2.7. Dilatational-rotational wave velocity ratios α/β and β/α as functions of Poisson's ratio. Note that rgidity increases with decreasing Poisson's ratio.

Note that since the relation between α_0/β_0 and Poisson's ratio is nonlinear as depicted in Figure 2.7, a percent-equivalent perturbation from the nominal velocity ratio yields a

larger change in Poisson's ratio for the inclusion than for the host medium. Despite this effect, however, the corresponding influence on the predicted detection limit is comparable, suggesting that relative velocity contrast may be a more useful parameter than the corresponding contrast in Poisson's ratio.

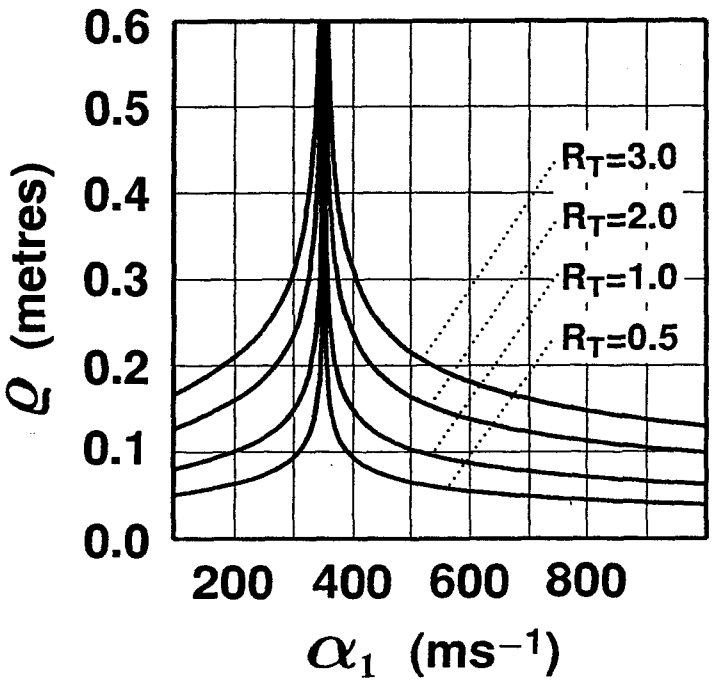

Figure 2.8. Predicted relation between detection limit $\varrho_\Delta = \varrho_n$ and inclusion velocity α_1 with total one-way transit range as a parameter. Note that the inclusion velocity spans a range including the host velocity.

Finally, in Figure 2.8, the inclusion velocity spans a range bracketing the nominal host velocity $\alpha_0 = 350.0\,\mathrm{ms}^{-1}$ and is assigned the same Poisson's ratio $\sigma_1 = \sigma_0 = .456$. With this assumption, it follows from equation (2.6) that as the inclusion velocity approaches that of the host medium, the reflectivity factor approaches zero. Consequently, as predicted by equations (2.12) and (2.13), the detection limit becomes infinite since, effectively, the inclusion no longer exists. Archaeologically, while Figures 2.5 and 2.6 model the case of a relatively dense, rigid inclusion within an unconsolidated host soil, Figure 2.8 simulates a sediment filled void, where the fill is either less or more compacted than the surrounding soil. Although the latter targets are relatively difficult to detect, results depicted in Figure

2.8 indicate that even in the case of small material contrasts, subsurface soil features of archaeological interest can be detected by seismic soundings. In particular, for dilatational velocity contrasts exceeding $\pm 200\,\mathrm{ms}^{-1}$, the predicted detection limit never exceeds 20.0 cm. For the case of an unfilled spherical cavity, the appropriate scattering cross-section takes a somewhat different form as given by Ying and Truell (1956).

In summation, the foregoing analysis of seismic detection reveals that, despite the relatively small scale nature of archaeological remains, these features are ordinarily within the detection limit of seismic exploration. In particular, archaeological features of the first kind are typically rigid, high velocity inhomogeneities buried at shallow depth within a low velocity unconsolidated soil and, fortuitously, these are optimum conditions for seismic detection. Specifically, low host velocities ($\alpha_0 = \lambda_{\alpha_0} f$) ensure that incident seismic waves are relatively short-wavelength (Figure 2.4) while sharply contrasting mechanical properties guarantee that a large proportion of incident energy will be scattered or reflected (Figures 2.5 and 2.6). As a result, seismic soundings are often capable of sensing subsurface archaeological features having dimensions significantly less than the wavelength of incident energy.

Recalling that the effective scale of an archaeological feature involves a trade-off between gross dimensions and material contrast, it is emphasized that for an inclusion of arbitrary radius, equivalent detection criteria could be formulated in terms of restrictions on the degree of material property contrast required. Moreover, as the wavelength of incident radiation becomes comparable to or less than the average target dimension, detection becomes progressively independent of wavelength and the seismic response is gradually dominated by reflection rather than scattering. This situation arises for archaeological features of the first kind having dimensions significantly larger than a wavelength and for archaeological features of the second kind in general. Since, in the latter case, the target's dimensions are effectively infinite, the detection limit is necessarily formulated as a restriction on the associated material property contrast. Assuming a dilatational wave normally incident on a plane horizontal interface, an appropriate detection criterion could

be developed by substituting a power reflection coefficient

$$\chi_r = 2\zeta_r \left(\frac{Z_0 - Z_1}{Z_0 + Z_1}\right)^2 = 2\zeta_r \left(\frac{1 - Z_1/Z_0}{1 + Z_1/Z_0}\right)^2$$

in place of the scattering cross-section χ_s in equation (2.5). Here, ζ_r represents an effective capture area for the reflector (e.g. area of first half-period Fresnel zone §2.3.2), $Z_0 = \rho_0\alpha_0$ and $Z_1 = \rho_1\alpha_1$ denote acoustic impedances for media on either side of the interface and the factor of two accounts for the fact that reflected power is restricted to the incidence side of the interface. Resulting expressions equivalent to equations (2.10) and (2.11) could, subsequently, be solved for limiting reflection coefficients necessary for detection of the interface. Further development of these criteria, however, is beyond our present scope. Instead, before turning our attention to resolving power, let's briefly consider a number of simplifying assumptions at the foundation of the foregoing treatment of seismic detection.

First, although the source and receiver are typically deployed on the surface of a heterogeneous, anisotropic and anelastic ground, our simplified model assumes that the source receiver pair are embedded within a homogeneous, isotropic, linearly elastic whole space. Practically speaking, although near surface sediments are often horizontally homogeneous, these deposits are ordinarily characterized by a significant vertical velocity gradient as a consequence of depth dependent compaction and consolidation. As a result, ray paths are curved, rather than straight, and associated wavefronts are, consequently non-spherical. In addition while weak anisotropy may, or may not, be present, unconsolidated sediments are typically associated with relatively severe frequency dependent attenuation that progressively reduces detection capacity as target range increases.

Secondly, while a point source of purely dilatational, radially isotropic waves is a reasonable assumption in the case of an explosive energy source deployed at depth, surface impact sources, like a hammer blow or weight-drop, yield a significant rotational displacement component and a distinctly directional radiation pattern. Useful theoretical treatments of this problem have been given by Miller and Pursey (1954), Mooney (1976) and Kahler and Meissner (1983). Miller and Pursey (1954) derived far-field expressions

for the displacement fields radiated by a circular disc of finite radius vibrating normal to the free surface of a semi-infinite solid.

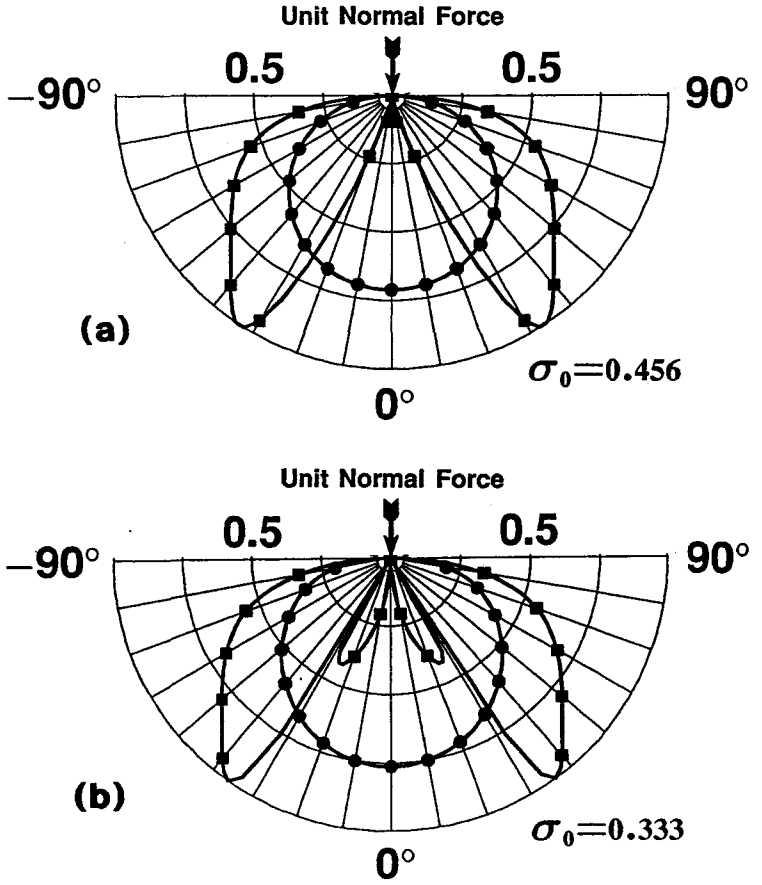

Figure 2.9. Theoretical radiation patterns arising for a circular disc of finite radius vibrating normal to the free surface of a semi-infinite solid, having Poisson's ratio (a) $\sigma_0 = .456$ and $\sigma_0 = .333$. Both radial (○) and tangential (□) displacement components are normalized with respect to maximum tangential displacement. Radial displacement components are exaggerated by (a) 7.5 and (b) 2.5 times for display.

When the radius of the disk ϱ_d is small compared to observation range r, radial and tangential displacement components as a function of azimuthal angle θ are, respectively,

$$U_r(\theta) = \frac{-\lambda_{\alpha_0}\gamma_0^2}{4\pi\rho_0\alpha_0^2}\,\frac{\varrho_d^2}{r}\,\frac{\cos\theta\left(\gamma_0^2 - 2\sin^2\theta\right)}{F_0\left(\sin\theta\right)}\,e^{i2\pi f\,(t-r/\alpha_0)} \tag{2.18}$$

and

$$U_\theta(\theta) = \frac{\lambda_{\alpha_0}\gamma_0^3}{4\pi\rho_0\beta_0^2}\,\frac{\varrho_d^2}{r}\,\frac{\sin 2\theta\left(1-\gamma_0^2\sin^2\theta\right)^{1/2}}{F_0\left(\gamma_0\sin\theta\right)}\,e^{i2\pi f\,(t-r/\beta_0)}, \tag{2.19}$$

where

$$F_0(\eta) = \left(2\eta^2-\gamma_0^2\right)^2 - 4\eta^2\left(\eta^2-1\right)^{1/2}\left(\eta^2-\gamma_0^2\right)^{1/2}.$$

Variable notation, including $\gamma_0 = \alpha_0/\beta_0$, is as previously defined. Radiation patterns for host media having Poisson's ratios of $\sigma_0 = 0.456$ ($\alpha_0/\beta_0 = 3.5$) and $\sigma_0 = 0.333$ ($\alpha_0/\beta_0 = 2.0$) are displayed in Figure 2.9. It is important to distinguish between these radiation patterns and wavefront geometry. Although the latter is approximately hemispherical for a localized source at the surface, energy density is unevenly distributed over this wavefront. Energy density transported in a given direction is proportional to the squared length of a vector from the origin to the surface of the radiation pattern in the given direction. In all cases, the radiation pattern is strongly directional. In particular, the radial or dilatational component has a nearly circular pattern, having maximum amplitude in the direction of applied force and decreasing gradually to zero parallel to the free surface. In contrast, the corresponding tangential or rotational displacement component has zero amplitude both parallel and perpendicular to the applied force, and maxima at approximately 35 degrees from vertical that can be many times greater than the corresponding radial maxima. Having said this, however, we note that the ratio of maximum radial displacement to maximum tangential displacement increases as Poisson's ratio decreases. That is, as the medium becomes more rigid. In addition, while the dilatational radiation pattern retains a similar geometry, the major lobes of the tangential radiation pattern become narrower and minor inner side lobes develop with peak amplitude at roughly 25 degrees from vertical.

Scattering is also directional. Although the simplified model employed above assumes that energy captured by the inclusion upon interaction with the incident wavefront is isotropically reradiated, in practice, the scattered wavefield can be strongly directional as demonstrated by Knopoff (1959); Aki and Richards (1980) and Wu and Aki (1985). For example, Knopoff (1959) treated the case of a plane compressional wave incident upon an infinitely dense, infinitely rigid spherical inclusion within an elastic wholespace. Assuming an inclusion radius small compared with wavelength, Knopoff obtained the following far-

field expressions for radial and tangential components of the scattered displacement field:

$$U_R(\theta) = \frac{-6\pi f \alpha_0^{-1}}{1+2\gamma_0^2} \frac{\varrho}{R} \cos\theta \, e^{i2\pi f (t - R/\alpha_0)}, \tag{2.20}$$

$$U_\theta(\theta) = \frac{6\pi f \alpha_0^{-1}}{1+2\gamma_0^2} \frac{{\alpha_0}^2}{{\beta_0}^2} \frac{\varrho}{R} \sin\theta \, e^{i2\pi f (t - R/\beta_0)}. \tag{2.21}$$

Radiation patterns are illustrated in Figure 2.10 for a Poisson's ratio of $\sigma_0 = 0.456$.

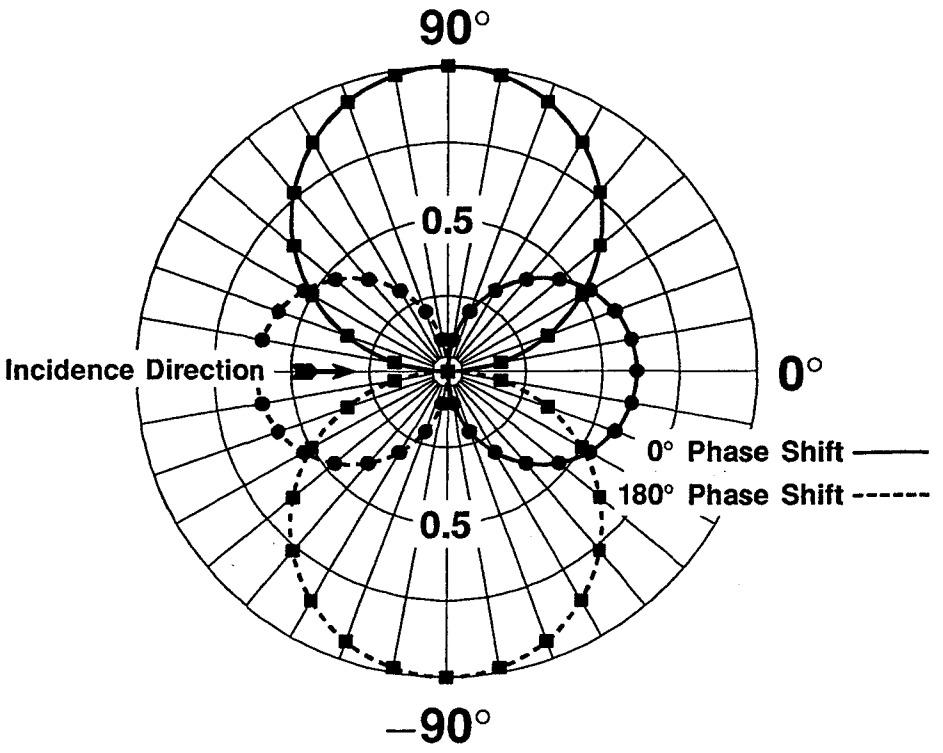

Figure 2.10. Theoretical radiation patterns (○ radial, □ tangential) arising for elastic scattering from an infinitely dense, infinitely rigid spherical inclusion embedded within a homogeneous isotropic whole space. Computation assumes inclusion radius small compared with wavelength of incident compressional plane wave. Radial displacements are exaggerated by a factor of 7.5.

Note that while both radiation patterns are doubly circular, the maximum amplitude of the tangential component is more than ten times that for the radial or compressional component. In addition, while the scattered compressional wavefield has maxima parallel and nulls broadside to the direction of incidence, the radiation pattern for the tangential component is rotated by 90 degrees. Consequently, since source and detector can be nearly coincident for small-scale archaeological applications, scattered compressional waves

received at the detector carry more energy than predicted for isotropic scattering. In general, the directional characteristics of source radiation and scattering cause the detection limit to be significantly influenced by the geometry of the sounding configuration. In the case of surface impact sources, the foregoing findings suggest that optimum detectability is achieved by a coincident source-detector positioned vertically over the target.

A third complication of our detectability model arises due to free surface and coupling effects at the detector. While our model incorporates an all-inclusive constant ζ_d, giving an effective surface area for the receiver, in practice, the detector's response is both frequency dependent and directional. Three principal factors influence the receiver's response: the geophone's intrinsic frequency response, ground coupling response characteristics and free surface effects. In particular, the effective response of a planted velocity-type detector can be adequately modeled by two damped springs in series; one representing the internal workings of the receiver and the other representing the elastic coupling of the detector to the ground. The response of each component is that of a damped harmonic oscillator characterized by a resonant frequency and corresponding damping coefficient. Consequently, in response to a periodic seismic disturbance, the detector's maximum output voltage varies considerably with the frequency of ground motion.

The detector's response is also directional. Geophones are ordinarily designed to respond only to ground motion parallel to a chosen axis of sensitivity†. Here, we are primarily concerned with vertical component detectors, having their axis of sensitivity oriented normal to the surface of deployment. In addition, because of the strong contrast between the elastic properties of the subsurface and air, the characteristics of a seismic disturbance incident on the surface can be severely altered. In effect, the vector displacement field must satisfy free surface boundary conditions, requiring displacements and associated tractions to vanish at the surface. As for the case of an internal discontinuity within the subsurface, solution of the appropriate field equations yields a set of coefficients characterizing

† Resonances due to motion non-parallel to the axis of sensitivity, referred to as parasitics, are designed to reside at frequencies outside the signal band

amplitude and phase of reflected, transmitted and converted modes relative to the incident wavefield as a function of incidence angle (Aki and Richards, 1980). For instance, on interaction with the free surface, an obliquely incident, plane dilatational wave is partly reflected and partly converted into a vertically polarized rotational wave as illustrated in Figure 2.11.

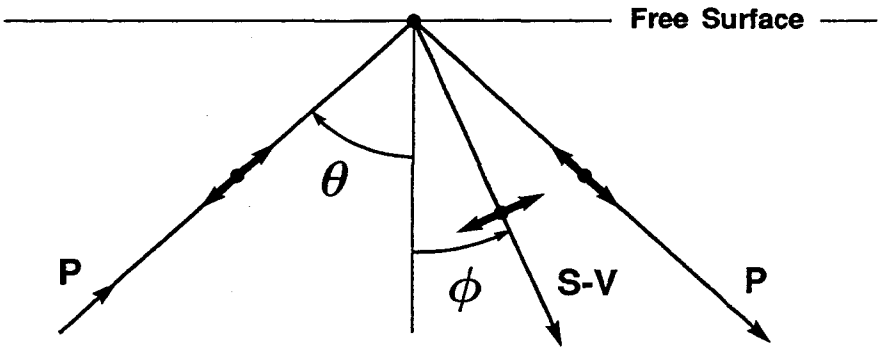

Figure 2.11. Geometry for free-surface reflection. Bold arrows indicate sense of particle displacement. ϕ denotes the angle of reflection for the converted S-V wave.

Consequently, at the instant of detection, net particle displacement is the sum of three components: the incident dilatational wave, a reflected dilatational wave and a vertically polarized rotational wave. Assuming an incident wave of unit amplitude, the net vertical displacement as sensed by a detector on the surface has peak amplitude

$$u_z(\theta) = \frac{2\cos\theta\left(2\gamma_0^{-2}\sin^2\theta - 1\right)}{\left(1 - 2\gamma_0^{-2}\sin^2\theta\right)^2 + 4\gamma_0^{-3}\sin^2\theta\cos\theta\left(1 - \gamma_0^{-2}\sin^2\theta\right)^{1/2}}, \tag{2.22}$$

where θ denotes the angle of incidence measured with respect to vertical and $\gamma_0 = \alpha_0/\beta_0$ as before. Figure 2.12 illustrates the directionality of the free surface effect for a range of Poisson's ratio. In particular, for $\sigma_0 = 0.5$ or $\gamma_0^{-1} = \beta_0/\alpha_0 = 0.0$, equation (2.22) reduces to

$$\lim_{\gamma_0 \to \infty} u_z(\theta) = -2\cos\theta, \tag{2.23}$$

where negative polarity arises on defining vertical displacement positive-downward. Consequently, for normal incidence ($\theta = 0$), maximum vertical displacement of the free-surface

is $u_z(0) = -2$. Equation (2.23) is often a reasonable approximation for unconsolidated sediments.

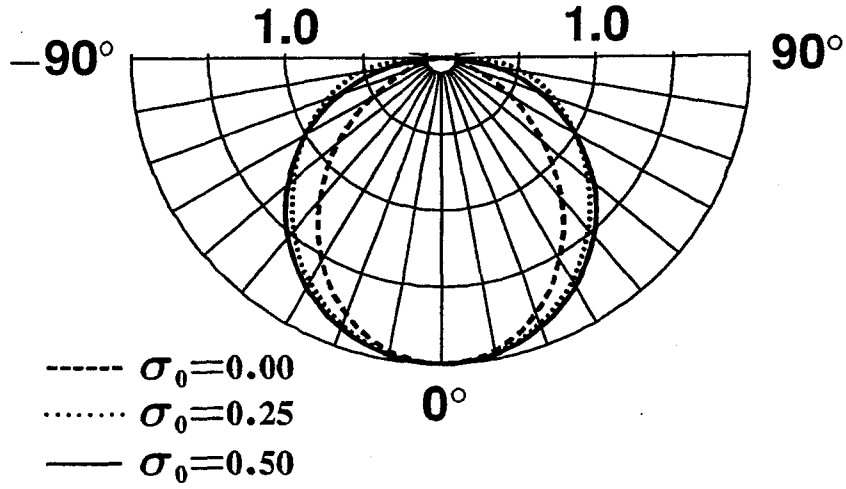

Figure 2.12. Directivity patterns for a plane dilatational wave incident at a vertical component detector deployed on a traction free surface for Poisson's ratios of $\sigma_0 = 0.5$ (solid curve), $\sigma_0 = 0.25$ (dotted curve) and $\sigma_0 = 0.0$ (dashed curve).

Finally, although our treatment of seismic detection assumes sinusoidal, monochromatic incident radiation, in practice, the typical source waveform is impulsive and consequently broadband. In other words, instead of a pure sinusoid of infinite duration, seismic sources produce a transient disturbance, like that displayed in Figure 2.13a, comprised by a spectrum of sinusoids having a range of frequencies and contributing various fractions of the total energy. If w(t) denotes the transient source pulse or wavelet, the corresponding frequency spectrum is given by

$$\begin{aligned} |W(f)| &= \left[\Re\{W(f)\}^2 + \Im\{W(f)\}^2\right]^{1/2} \\ &= \left[W(f)\,W^*(f)\right]^{1/2} \end{aligned}, \tag{2.24}$$

where

$$W(f) = \int_{-\infty}^{+\infty} w(t)\, e^{-i2\pi ft}\, dt \tag{2.25}$$

is the complex Fourier transform of the wavelet, $\Re\{W(f)\}$ and $\Im\{W(f)\}$ are, respectively, real and imaginary parts of W(f) and * denotes the corresponding complex conjugate. In particular, $|W(f)|$ is the amplitude spectrum, giving amplitude as a function of frequency

for the constituent sinusoidal components. An associated phase spectrum

$$\begin{aligned}\Theta(f) &= \tan^{-1}\left[\frac{\Im\{W(f)\}}{\Re\{W(f)\}}\right] \\ &= \tan^{-1}\left[-i\left(\frac{W(f)-W^*(f)}{W(f)+W^*(f)}\right)\right]\end{aligned} \tag{2.26}$$

characterizes relative phase shifts between components. Figures 2.13b and 2.13c depict amplitude and phase spectra corresponding to the wavelet in Figure 2.13a. Note that the amplitude spectrum displays a peak frequency of approximately $f_p = 400$ Hz and that the corresponding unwrapped phase spectrum is very nearly linear. The corresponding energy density, or power spectrum is simply the square of the amplitude spectrum

$$\mathcal{E}(f) = |W(f)|^2 = W(f)\,W^*(f). \tag{2.27}$$

It follows from foregoing analysis, that the ultimate detection limit for a broadband impulse corresponds to the spectral component having optimum balance between frequency and energy density. In practice, spectral analysis is often unnecessary and it is sufficient to estimate the wavelet's detecting power by measuring its dominant frequency characteristics. Two principal measures are illustrated in Figure 2.13a. The dominant frequency f_d is given by the reciprocal of the dominant period or the time difference between extrema of the wavelet's primary side lobes (Widess, 1973). In contrast, the wavelet's central frequency f_c is the reciprocal of twice the time separation between the main lobe's two zero crossings, dubbed by Koefoed (1981) as the central period. Either of these parameters may be used to estimate the gross detection limit of a broadband wavelet. Moreover, the reader should note that these estimates are often a better characterizations of the wavelet's overall spectral composition than the corresponding peak frequency f_p. Perhaps the most indicative measure of the wavelet's gross spectral content is its mean frequency or spectral centroid given by

$$f_m = \int_0^\infty f\,|W(f)|\,df \Big/ \int_0^\infty |W(f)|\,df, \tag{2.28}$$

which, in discrete approximation, yields an approximate value of $f_m \approx 500$ Hz for the spectrum displayed in Figure 2.13b.

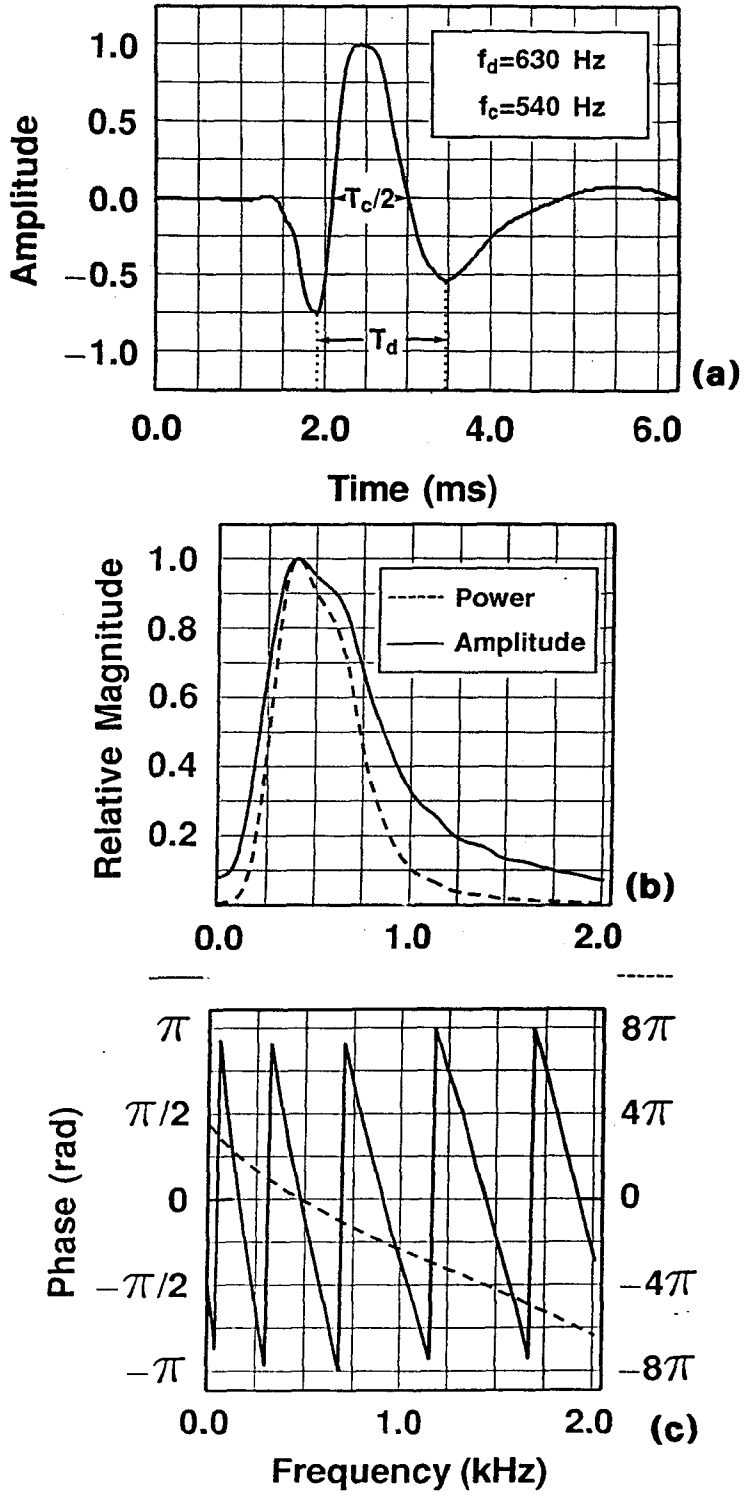

Figure 2.13. (a) Broadband seismic wavelet, characterized by dominant frequency $f_d = 1/T_d$ and central frequency $f_c = 1/T_c$, where dominant period T_d and central period T_c are measured as indicated. (b) Corresponding amplitude (solid curve) and power (dashed curve) spectra. (c) Corresponding phase spectrum before (solid curve) and after (dashed curve) unwrapping.

In conclusion, although it is important to be cognizant of complicating factors that render the detection limit directional and frequency dependent, these effects should not detract from our primary finding: that archaeological remains are ordinarily detectable by seismic exploration. In fact, it is evident that for certain plausible sounding configurations, these effects enhance detectability. Moreover, it must be appreciated that the foregoing theoretical results for source radiation, scattering and free-surface reflection are also based on simplifying assumptions and approximations. In particular, equations (2.18)-(2.23) are all founded on far-field, plane-wave approximations. In other words, these results assume that the region of interest is sufficiently remote from the source region to assume, first, that near-field contributions to the seismic disturbance are negligible and, secondly, that wavefronts have insignificant local curvature.

Aki and Richards (1980) demonstrate that in addition to so-called far-field terms, describing the spherical divergence of dilatational and rotational waves from a point source within a homogeneous, isotropic wholespace, the elastodynamic Green's function includes a third term having amplitude proportional to the inverse third power of radius and, consequently, which dominates near-field characteristics of the seismic disturbance. According to Richards (1990), the near-field term has negligible effect at a given range r from the source if, and only if, the the time between dilatational and rotational arrivals $t_{\alpha\beta} = r(1/\beta_0 - 1/\alpha_0)$ is significantly greater than the source duration. For instance, if α_0=350.0 ms^{-1}, β_0=100.0 ms^{-1} and the dominant frequency of the source wavelet is f_D=400 Hz, near-field effects are negligible only for $r >> \alpha_0\beta_0/[f_d\,(\alpha_0 - \beta_0)] = 0.35$ m. A plane-wave assumption, on the other hand, acknowledges that far from the source region, the portion of a wavefront in the vicinity of an arbitrary point becomes approximately planar. The validity of the approximation depends on the wavefront's radius of curvature and the dimensions of the region of interest. For example, since Rayleigh scattering involves wavefronts incident on inhomogeneities having radii small compared with wavelength, a plane-wave approximation is adequate at ranges comparable to or exceeding the wavelength. Although the validity of far-field, plane-wave approximations is naturally in question for shallow, small-scale archaeological applications, a complete and rigorous anal-

ysis of limitations and restrictions is beyond the scope of the present study. Consquently, we shall adopt these approximations as working assumptions unless otherwise stated. In particular, theoretical modelling of the wavefield generated by a spherically symmetric, explosive source, in Chapter 3, and a comparitive analysis of array filter responses for plane and spherical waves, in Appendix B, suggest that these assumptions are practically valid.

Now, having established the detectability of archaeological remains, let us consider the resolution of individual features.

2.3 Resolution:

Detection as treated in the foregoing section should be viewed strictly as a prerequisite for resolution. In other words, detection of a given feature does not even so much as ensure that its existence will be established, let alone its location and geometry. While detection amounts simply to data acquisition, successful and unambiguous interpretation of these data requires resolution. For instance, recall that all spherical inclusions having a particular cross-section and residing at arbitrary positions on the ellipsoidal surface in Figure 2.3 yield identical responses at the detector. More significantly, it follows that two identical inclusions at arbitrary positions on the ellipsoid yield a combined response at the detector that is indistinguishable from a single inclusion having twice the scattering cross-section. This simple example illustrates the non-uniqueness inherent in geophysical observations. Of course, the insightful reader will correctly surmise that this ambiguity can be reduced in large part by repositioning the source and receiver and redetecting the inclusions. In fact, for most configurations, repetition of this procedure could establish that two distinct inclusions exist. If, however, the two are separated by less than some critical distance, their composite response remains indistinguishable from that due to a single inclusion. This critical separation is a measure of the resolving power of the data acquisition system. Consequently, resolution is defined as the ability to discriminate between signals arising from separate but closely spaced targets and is treated in two dimensions: time and space.

2.3.1 Temporal Resolution:

Temporal resolution refers to the minimum difference between arrival times at the de-

tector for which partially overlapping signals from separate targets may be distinguished. In practice, this amounts to a limitation on the difference between associated transit ranges. This concept is illustrated in Figure 2.14, where we display synthetically modelled seismic responses arising for a wedge of uniform material having elastic impedance $Z_1 = \rho_1\alpha_1$ bounded, above and below, by media having dissimilar impedances $Z_0 = \rho_0\alpha_0$ and $Z_2 = \rho_0\alpha_0$, respectively†. Two specific cases are considered; $Z_0 << Z_1 << Z_2$ (Figure 2.14b) and $Z_0 << Z_1 >> Z_2$ (Figure 2.14c).

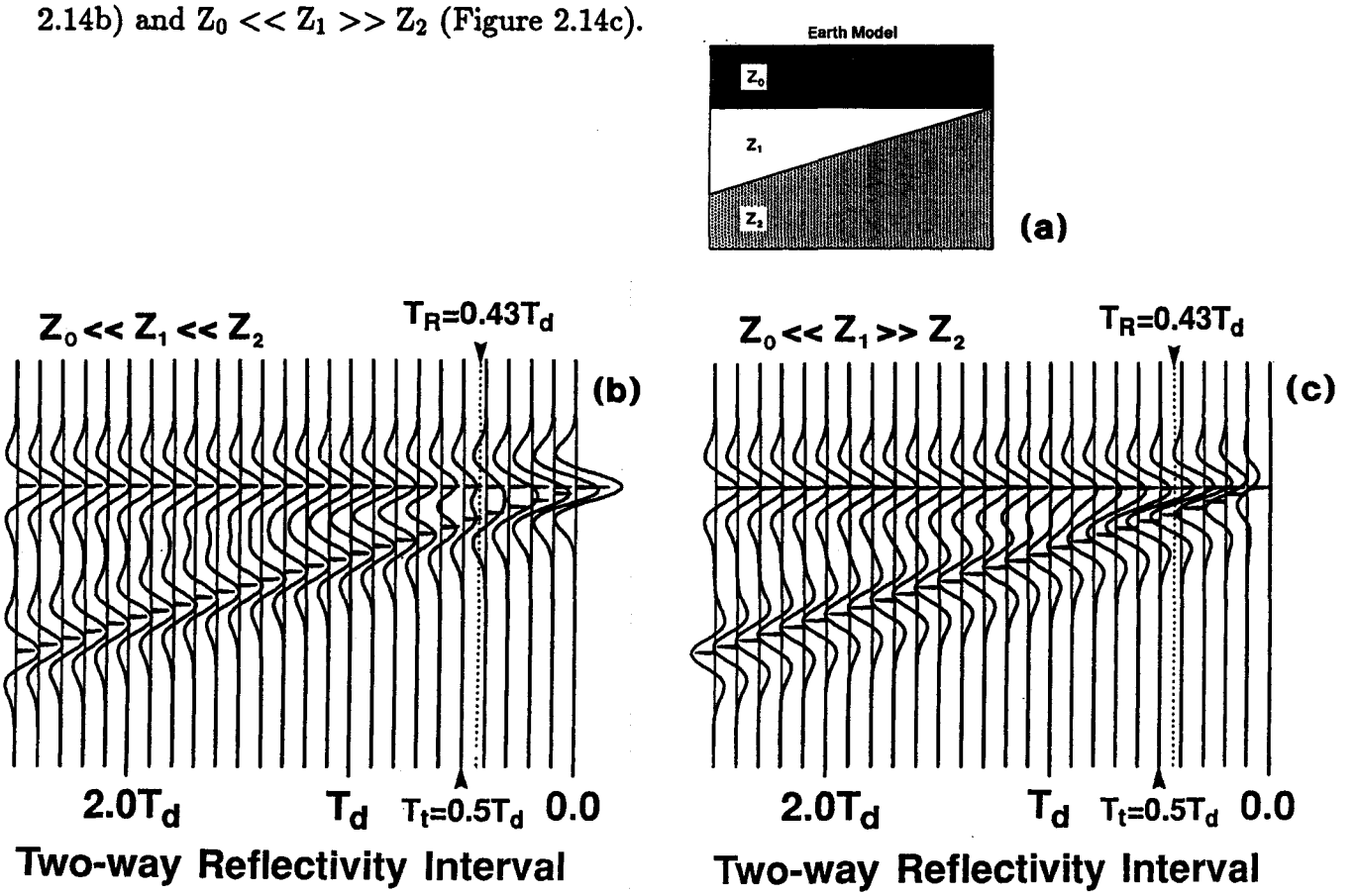

Figure 2.14. (a) Earth model for assessing temporal resolution. $Z_i = \rho_i\alpha_i$ represents the acoustic impedance of the ith layer, with ρ_i and α_i denoting density and velocity, respectively. Corresponding reflectivity series and associated synthetic seismic responses for an (b) even polarity reflectivity ($Z_0 << Z_1 << Z_2$) (c) odd polarity reflectivity ($Z_0 << Z_1 >> Z_2$) ($Z_0 = Z_2$). Responses are displayed as functions of two-way transit interval (in units of dominant period T_d) separating reflectivity impulses. Rayleigh $T_t = 0.5T_d$ and Ricker $T_R = 0.43T_d$ criteria for temporal resolution are indicated. (After Kallweit and Wood, 1982)

† Analogous with the impedance of an electrical circuit, relating applied electric potential (voltage) to induced current, elastic wave impedance is an intrinsic property of a medium relating applied mechanical potential (stress) to induced particle velocity (see Aki and Richards (1980), §5.2.2; Lipson and Lipson (1969), §2.5.2)

Synthetic seismograms are computed assuming a coincident source-detector pair deployed on the surface and incrementally shifted by some fixed interval until the model structure has been traversed. At each acquisition point, a pre-specified, discretely sampled source wavelet w_T is convolved with a time-sampled sequence of coefficients

$$r_T = \frac{Z_T - Z_{T+\Delta t}}{Z_T + Z_{T+\Delta t}} = \frac{1 - Z_{T+\Delta t}/Z_T}{1 + Z_{T+\Delta t}/Z_T} \tag{2.29}$$

giving normal-incidence reflectivity as a function of equivalent two-way transit time vertically beneath the transducer position. Here, $Z_T = \rho_T \alpha_T$ and $Z_{T+\Delta t} = \rho_{T+\Delta t}\alpha_{T+\Delta t}$ denote effective elastic impedances at discrete two-way times of T and T+Δt, respectively. The corresponding synthetic seismogram follows from the the so-called convolutional model according to the relation

$$s_T = w_T * r_T = \sum_{\tau=-\infty}^{+\infty} w_\tau \, r_{T-\tau}, \tag{2.30}$$

where * is shorthand notation for the convolution operation. In effect, convolution replaces each discrete reflectivity value r_T by an appropriately scaled version of the wavelet series w_T as illustrated in Figure 2.15.

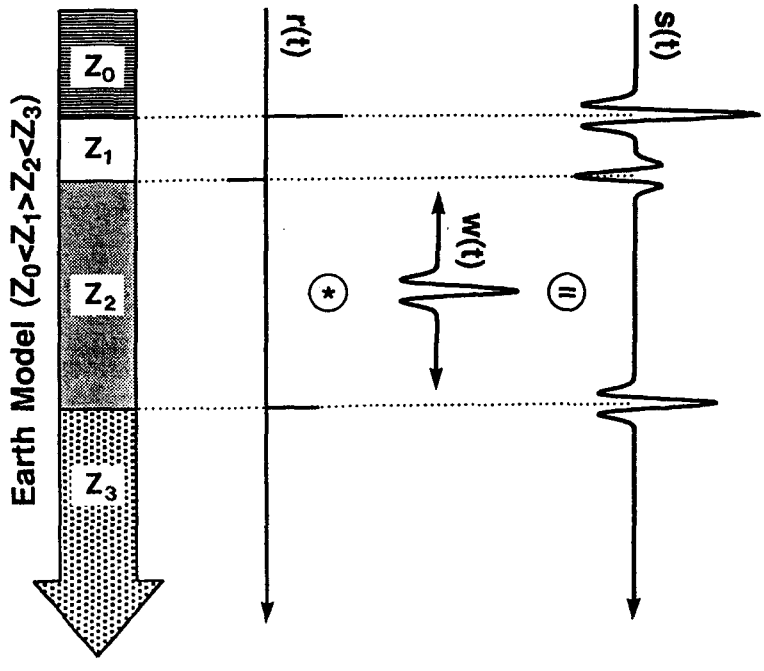

Figure 2.15. The convolutional model. A horizontally layered earth model ($Z_0 < Z_1 > Z_2 < Z_3$) gives rise to reflectivity series r(t). Subsequent convolution with wavelet series w(t) yields the synthetic seismogram s(t) = w(t) * r(t).

Synthetic seismograms in Figure 2.14 are superimposed on the corresponding reflectivity series. Since, in each case, the assumed earth model involves simple unconformities between slabs of uniform media having sharply contrasting impedances, associated reflectivities consist of a pair of isolated spikes of approximately unit amplitude which gradually converge as the wedge thins. Moreover, the reflectivity has even polarity for $Z_0 << Z_1 << Z_2$ (Figure 2.14b) and odd polarity for $Z_0 << Z_1 >> Z_2$ (Figure 2.14c).

To model the source pulse, we have adopted the Ricker wavelet (Ricker, 1953a; Hosken, 1988) given by

$$w(t) = (1 - 12f_d^2\, t^2)\, \exp\left(-6f_d^2\, t^2\right) \tag{2.31}$$

and having associated amplitude spectrum

$$|W(f)| = \left(\frac{\pi^{5/2}}{3\sqrt{6}f_d}\right)\left(\frac{f}{f_d}\right)^2 \exp\left[-\frac{\pi^2}{6}\left(\frac{f}{f_d}\right)^2\right], \tag{2.32}$$

where $f_d = 1/T_d$ is the dominant frequency as defined in the previous section and is related to corresponding central and peak frequencies by $f_d = 2\sqrt{1/3}\, f_c$ and $f_d = \pi/\sqrt{6}\, f_p$, respectively. A time shifted Ricker wavelet $w(t - \tau_0)$, together with associated amplitude and phase spectra are illustrated in Figure 2.16 for a dominant frequency of $f_d = 630$ Hz and time shift $\tau_0 = 2.5$ ms. Notice that in accordance with the shifting theorem of the Fourier transform (Bracewell, 1986), the time shift $\tau_0 = 2.5$ms is equivalent to a linear phase shift of $\Theta_0 = -2\pi f \tau_0 = -.005\pi f$ radians.

Despite theoretical shortcomings discussed by Hosken (1988), much of the existing literature on seismic resolution is founded on the pioneering work of Norman Ricker (1953a, 1953b) and utilizes his wavelet for modelling and analysis. Comparison of Figure 2.16 with Figure 2.13 indicates that, although strictly acausal, a time-shifted or, equivalently, a linearly phase-shifted Ricker wavelet closely resembles the typical source pulse acquired in connection with full-scale model experiments described in Chapter 4. Consequently, since our aim is to model the gross characteristics of recorded seismograms, Ricker's wavelet

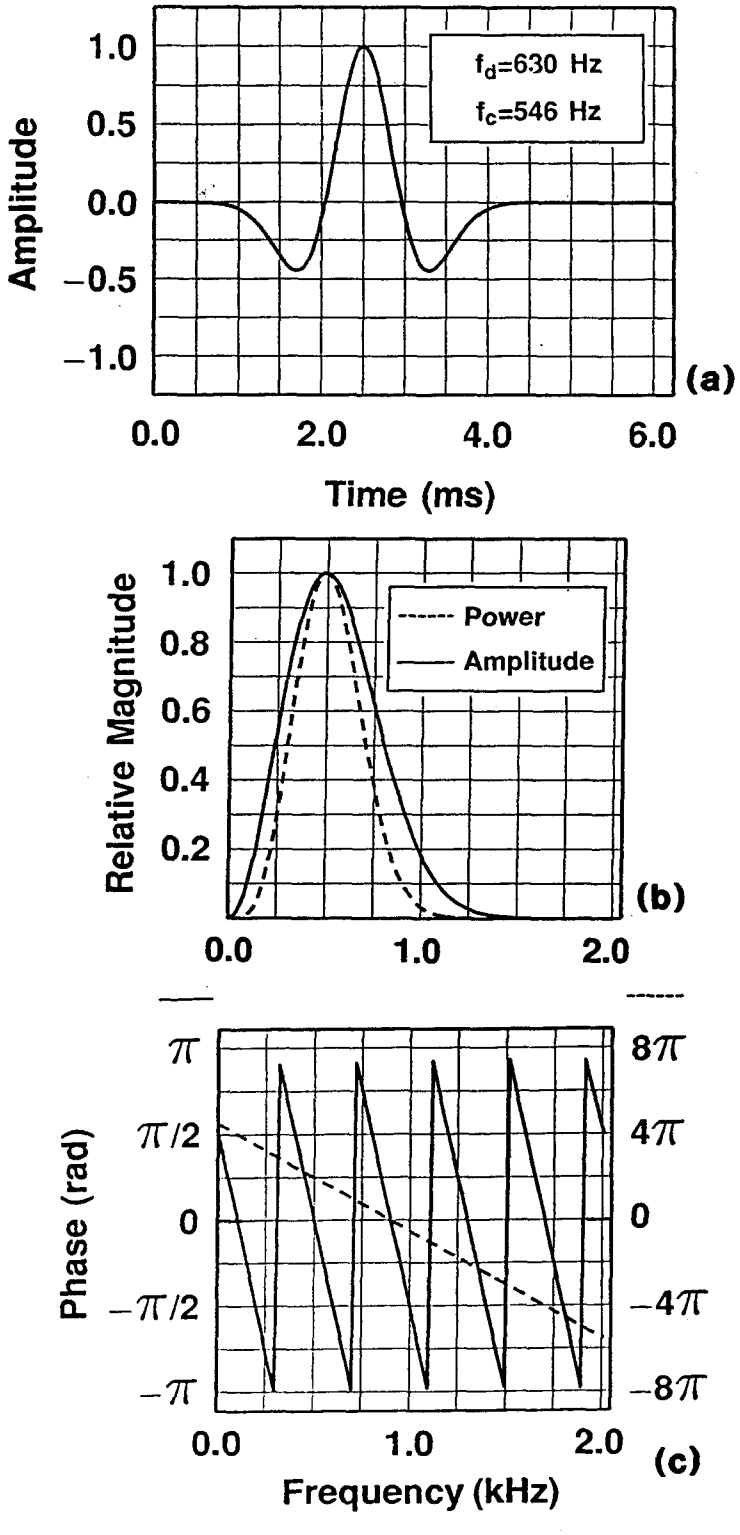

Figure 2.16. (a) Pseudo-causal Ricker wavelet $w(t - \tau_0)$, where $w(t)$ is defined by equation (2.31) and $\tau_0 = 2.5$ ms. Corresponding (b) amplitude (solid curve) and power (dashed curve) spectra (c) phase spectrum before (solid curve) and after (dashed curve) phase unwrapping.

is well suited despite its theoretical flaws. Useful alternatives are the Berlage wavelet (Aldridge, 1990) and the Rayleigh pulse (Hubral and Tygel, 1989).

Now, having described the computation of synthetic seismograms, let's consider the implications of Figure 2.14 for establishing seismic resolution criteria. Evidently, where the wedge is sufficiently thick, reflected pulses from upper and lower interfaces are detected as isolated events. As thickness decreases, however, the two wavelets merge, yielding a composite response produced by interference of the two disturbances at the detector. When the range between upper and lower interfaces reaches some critical limit, it is no longer possible to discern distinct contributions or features of the wavelet complex associated with constituent wavelets. In other words, separate arrivals and, consequently, the associated reflectors are no longer resolved. Three principal criteria have been established to quantify the corresponding resolution limit.

First, in connection with analysis of diffraction spectra and optical resolution, Lord Rayleigh arbitrarily defined the resolving limit of a rectangular aperture as the separation between two point sources of light, such that the main lobe of the diffraction pattern or image wavelet due to one source falls exactly on the first minimum of the other (Jenkins and White, 1957). Equivalently, in the context of seismic resolution, Rayleigh's criterion requires that the range separating two reflectors exceed one quarter the dominant wavelength $\lambda_d = \alpha T_d$ of the incident wavelet. This equivalence is confirmed by differentiating equation (2.20), for the Ricker wavelet, with respect to time and solving for finite non-zero roots (Appendix C). The associated temporal parameter $T_t = 0.5T_d$ is commonly referred to as the tuning thickness (Kallweit and Wood, 1982). Notice that a factor of two arises between the equivalent spatial and temporal resolution limits in connection with two-way vs. one-way transit time.

Ricker (1954) defined the resolution of his wavelet as the range separating two reflectors, having the same polarity, for which the composite waveform as depicted in Figure 2.14b is characterized by zero curvature at its central maximum. Thus, writing the wavelet

complex as

$$s(t) = w(t+\tau) + w(t-\tau), \tag{2.33}$$

Ricker's resolution criterion requires that

$$\frac{\partial^2}{\partial\tau^2} s(t) = \frac{\partial^2}{\partial\tau^2} w(t+\tau) + \frac{\partial^2}{\partial\tau^2} w(t-\tau) = 0 \tag{2.34}$$

with the corresponding temporal resolution limit following as $T_R = 2\tau$ where τ satisfies the previous relation with t=0. However, since w (t) as defined by equation (2.31) represents an even, symmetrical wavelet, we have $w(+\tau) = w(-\tau)$. Therefore,

$$\frac{\partial^2}{\partial\tau^2} w(+\tau) = \frac{\partial^2}{\partial\tau^2} w(-\tau) \tag{2.35}$$

and, consequently, equation (2.34) is satisfied by τ satisfying

$$\frac{\partial^2}{\partial\tau^2} w(\tau) = 0. \tag{2.36}$$

In other words, for even symmetrical wavelets, Ricker's temporal resolution limit T_R is equivalent to the separation between inflection points on the wavelet's central lobe (Appendix D). In particular, for the Ricker wavelet, $T_R \approx 0.43\,T_d$ or about 86 percent of the corresponding tuning thickness $T_t = 0.5\,T_d$. Consequently, according to Ricker's resolution criterion, two targets will be resolved if their ranges differ by more than about $\lambda_d/4.65$ compared with $\lambda_d/4.0$ under Rayleigh's criterion.

A third criterion for the temporal resolution limit was developed in connection with the response of a uniform, isolated layer embedded within a homogeneous halfspace as depicted in Figure 2.14c. Widess (1973) observed that as the associated time interval separating equal amplitude, opposite polarity reflectivity impulses diminishes to less than about $0.25\,T_d$, the structure of the composite waveform appears to become very nearly stable and approximates the derivative of the incident wavelet; not a surprising result, recognizing that the reflectivity sequence approaches that of a discrete differentiation filter

(ie. [...,0,0,-1,1,0,0,...]). On this basis, Widess's resolution criterion holds that an isolated layer embedded within a homogeneous halfspace is resolvable if its bounding interfaces have ranges differing by more than $\lambda_d/8.0$.

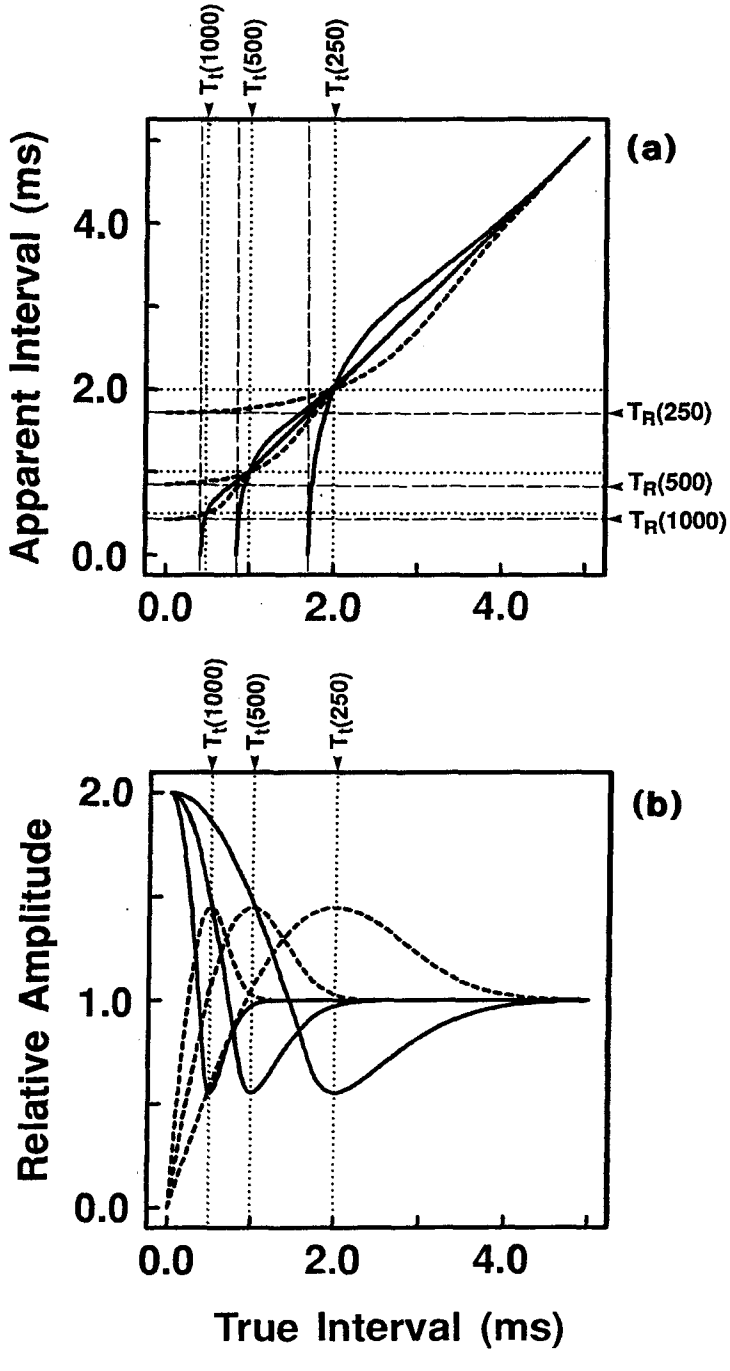

Figure 2.17. (a) Resolution curves for dominant frequencies of 250, 500 and 1000 Hz. Apparent peak-to-peak reflectivity interval for even (solid curve) and odd (dashed curve) polarities as a function of the true reflectivity interval. (b) Associated detection curves. Maximum amplitude of the wavelet complex (relative to maximum wavelet amplitude) as a function of the true reflectivity interval for equal (solid curve) and opposite (dashed curve) polarities. T_t and T_R denote Rayleigh and Ricker resolution criteria. Curves are normalized with respect to maximum wavelet amplitude. (After Kallweit and Wood, 1982)

An excellent comparative analysis of the foregoing criteria was reported by Kallweit and Wood (1982) and, although their findings confirm the significance of Rayleigh and Ricker criteria in connection with both even and odd polarity reflectivities, a physical basis for Widess's resolution limit could not be substantiated. In fact, despite its popularity and widespread application, resolution curves in Figure 2.17a suggest that there is no special significance, whatever, associated with the Widess criterion. Instead, the resolution curves indicate that apparent temporal thickness, as indicated by the associated composite waveform, yields a good approximation to true time separation between reflectivity pulses until the the Rayleigh resolution limit is reached. Here, the resolution curves intersect the diagonal associated with one-to-one correspondence between between apparent and true reflectivity intervals. Below the Rayleigh limit, apparent time separation falls off rapidly in the case of an even polarity reflectivity, reaching zero when true separation is equal to Ricker's resolution limit. For an odd polarity reflectivity, on the other hand, the apparent temporal thickness rapidly converges on Ricker's resolution limit as true separation goes to zero. Consequently, in both contexts, the effective resolution limit lies somewhere between $\lambda_d/4.0$ and $\lambda_d/4.65$ and, thus, we shall unify the two criteria referring to the range between them as the Rayleigh-Ricker resolution criterion.

Let's examine the implications of this approximate resolution criterion for archaeological applications. In general, the Rayleigh-Ricker criterion implies that resolving power is inversely related to dominant wavelength $\lambda_d = \alpha_0/f_d$ and, therefore, depends directly on the wavelet's dominant frequency f_d and inversely on host velocity α_0. Consequently, that unconsolidated sediments and soils are often characterized by dilatational velocities less than the acoustic velocity of air, suggests the near-surface nature of the archaeological features is especially well suited for achieving extended resolution. In particular, Figure 2.18 displays the Rayleigh-Ricker resolution criterion as a function of host velocity with the wavelet's dominant frequency as a parameter. It is observed that under favorable con-

ditions, archaeological features separated by less than 10 cm can be resolved by seismic exploration and that for a dominant frequency as low as 250 Hz and host velocity as high as 1000 ms^{-1} targets separated by less than a metre may still be resolved. Having drawn these conclusions, it must also be appreciated that near-surface, unconsolidated sediments are also characterized by significant attenuation of high frequencies and, consequently, that a dominant frequency of 1 kHz is currently an optimistic figure.

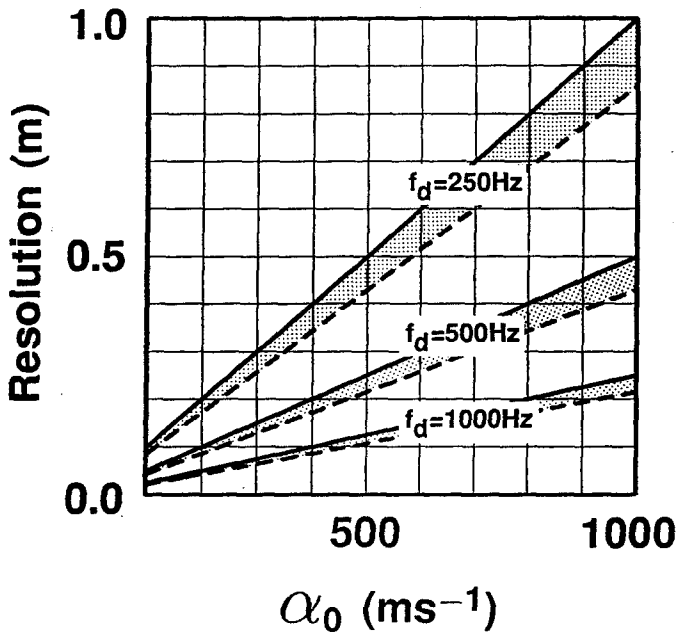

Figure 2.18. Rayleigh-Ricker resolution criterion (shaded region) for temporal seismic resolution for dominant frequencies of 250, 500 and 1000 Hz as a function of the interval velocity α_0. The Rayleigh-Ricker criterion corresponds to the range between Rayleigh $\lambda_d/4.0$ (solid curve) and Ricker $\lambda_d/4.66$ (dashed curve) criteria.

Moreover, in certain circumstances the thickness of an unresolved "thin-bed" can be ascertained by calibrated amplitude analysis of the composite waveform. In respect of such considerations, detection curves in Figure 2.17b display the variation of maximum composite amplitude as a function of the true time separation between reflectivity impulses of even and odd polarity. Here, extrema occur in connection with Rayleigh's resolution limit, further indicating its special significance. Specifically, in the context of an even polarity reflectivity, maximum composite amplitude decreases from unity at infinite separation to a minimum at Rayleigh's limit, equal to the difference between main-lobe and primary side-

lobe magnitudes and then, subsequently, increases non-linearly to twice maximum wavelet amplitude as the true temporal thickness approaches zero. Concurrently, the corresponding curve for an odd polarity reflectivity varies from unity at infinite separation to a maximum, equal to the sum of main-lobe and primary side-lobe magnitudes, at Rayleigh's limit and then, subsequently, decreases non-linearly to zero at zero temporal thickness. Although of great interest in connection with seismic stratigraphy (Widess, 1973; Meckel and Nath, 1977; Neidell and Poggiagliolmi, 1977; De Voogd and den Rooijen, 1983; Knapp, 1990), further details regarding amplitude analysis of unresolved layers is beyond the scope of our present discussion.

Instead, having established that seismic resolution, like detection, is intimately related to wavelet length or duration, let's examine the relationship between the wavelet's temporal or spatial properties and its spectral characteristics. In particular, the scaling property of the Fourier transform (Bracewell, 1986), holds that wavelet contraction in the the time domain is equivalent to spectral expansion in the frequency domain. Recalling that the Fourier spectrum $W(f)$ associated with an arbitrary wavelet $w(t)$ is defined by equation (2.25)

$$W(f) = \int_{-\infty}^{+\infty} w(t)\, e^{-i2\pi ft}\, dt,$$

consider a related wavelet $w'(t) = w(ct)$, where c represents an arbitrary positive-valued real constant. The corresponding Fourier spectrum follows as

$$\begin{aligned} W'(f) &= \int_{-\infty}^{+\infty} w'(t)\, e^{-i2\pi ft}\, dt \\ &= \int_{-\infty}^{+\infty} w(ct)\, e^{-i2\pi ft}\, dt \end{aligned} \qquad (2.37)$$

Substituting $t' = ct$ and, thus, $dt = dt'/c$ yields

$$W'(f) = \frac{1}{c} \int_{-\infty}^{+\infty} w(t')\, e^{-i2\pi (f/c)t'}\, dt' \qquad (2.38)$$

and, therefore, it follows from equation (2.25) that

$$W'(f) = \frac{1}{c} W(f/c). \qquad (3.39)$$

Consequently, if $c < 1.0$, we note that $w'(t)$ is a contracted version of $w(t)$ and the associated Fourier spectrum $W'(f)$ is a correspondingly expanded and suitably scaled version

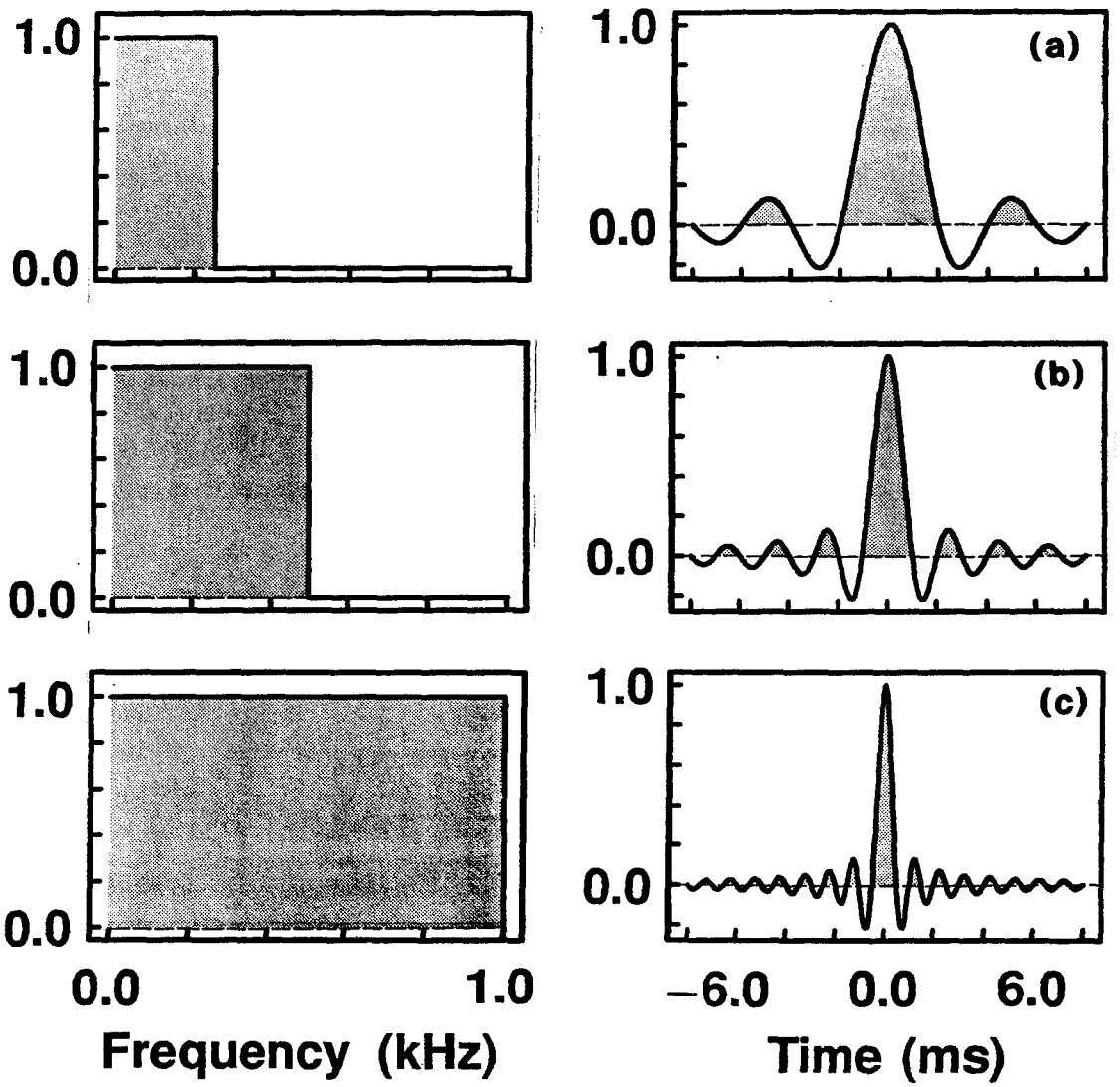

Figure 2.19. Normalized time domain sampling functions and associated low-pass frequency spectra having terminal frequencies of (a) 250 (b) 500 and (c) 1000 Hz.

of W(f). For c > 1.0, the situation is reversed. For example, consider a wavelet having a Fourier spectrum equivalent to the transfer function of an ideal low-pass filter

$$W(f) = \Pi\left(\frac{f}{2f_u}\right), \tag{2.40}$$

where

$$\Pi(\xi) = \begin{cases} 0, & |\xi| > 1/2; \\ 1, & |\xi| \le 1/2 \end{cases} \tag{2.41}$$

is a rectangular function having unit height and base and f_u denotes the terminal frequency of the pass-band. The associated wavelet is given by the following inverse Fourier transform

$$\begin{aligned} w(t) = \int_{-\infty}^{+\infty} W(f)\, e^{i2\pi ft}\, df &= \int_{-f_u}^{+f_u} e^{i2\pi ft}\, df \\ &= \frac{1}{i2\pi t}\left(e^{i2\pi f_u t} - e^{-i2\pi f_u t}\right) \\ &= \frac{1}{i2\pi t}\left[2i \sin(2\pi f_u t)\right] \\ w(t) &= \frac{\sin(2\pi f_u t)}{\pi t} = 2f_u\, Sa(2\pi f_u t) \end{aligned} \quad , \tag{2.42}$$

where $Sa(\xi) = \sin \pi\xi / \pi\xi$ is the well known sampling or sinc function. Figure 2.19 depicts normalized sinc functions arising for f_u =100, 500 and 1000 Hz. Evidently, in accordance with the scaling theorem, spectral expansion is associated with a corresponding temporal contraction of the sampling function. It follows that perfect resolution is associated with infinite spectral expansion or, stated mathematically, $\lim_{f_u \to \infty} w(t) = \delta(t)$, where $\delta(t)$ is an infinitely narrow pulse centered on t=0 and possessing unit area

$$\int_{-\infty}^{+\infty} \delta(t)\, dt = \int_{-\infty}^{+\infty} \delta(t)\, e^{-i2\pi ft}\, dt = 1.$$

In connection with seismic wavelets and resolution, it is pertinent to question whether the temporal contraction is a consequence of increased spectral breadth or, perhaps, principally due to the accompanying incorporation of higher frequencies. In this regard, it is useful to consider a more general band-limited Fourier spectrum having form

$$W(f) = \Pi\left(\frac{f}{\Delta f}\right) * [\delta(f - f_m) + \delta(f + f_m)], \tag{2.43}$$

where $\delta(\xi)$ is the Dirac delta function, $f_m = (f_l + f_u)/2$ defines the spectrum's midfrequency in terms of upper and lower terminal frequencies f_u and f_l, respectively, and $\Delta f = f_u - f_l$ is

the corresponding spectral bandwidth. Applying the convolution theorem of the Fourier transform (Appendix E), the time domain waveform associated with equation (2.43) follows as

$$w(t) = 2\frac{\sin(\pi \Delta f t)}{\pi t}\cos(2\pi f_m t), \tag{2.44}$$

or, equivalently,

$$w(t) = 2f_u \frac{\sin(2\pi f_u t)}{2\pi f_u t} - 2f_l \frac{\sin(2\pi f_l t)}{2\pi f_l t}. \tag{2.45}$$

This result is known as the sinc wavelet and is, effectively, the impulse response of an ideal band-pass filter. Recalling the double angle formula $\sin 2\xi = 2\sin\xi\cos\xi$, observe that for $f_l = 0$, equations (2.44) and (2.45) reduce to the sampling function described above. In addition, the central frequency of the sinc wavelet is $f_c = f_m$ for $f_m > \Delta f$ and $f_c = \Delta f/4$ for $f_m < \Delta f$. The associated dominant frequency f_d depends on both midfrequency f_m and bandwidth Δf and is more difficult to specify. In Figure 2.20, we illustrate the coupled influences of midfrequency and bandwidth on the character of the associated wavelet. Comparing Figures 2.20a and 2.20b reveals that shifting the spectral band to higher frequencies yields a wavelet having a substantially shorter dominant period and, consequently, on the basis of Rayleigh-Ricker resolution criterion, one that should posses significantly more resolving power. An accompanying increase in relative side-lobe energy, however, can be undesirable. Koefoed (1981) recognized that in addition to the breadth of a wavelet's central lobe, its resolving power depends on two additional factors: the side-lobe ratio, defined by Schoenberger (1974) as the ratio of principal side-lobe amplitude to main lobe amplitude, and side tail oscillation amplitude, referring to the relative amplitude of wavelet oscillations beyond the principal side lobes. Koefoed established that while higher frequencies are required to achieve a shorter dominant period, retention of low frequency content is essential for reducing the side-lobe ratio and suppressing side tail oscillations. Consequently, in addition to greater high frequency content, improved resolution requires extended bandwidth as illustrated in Figure 2.20c. Here, we attain the required contraction

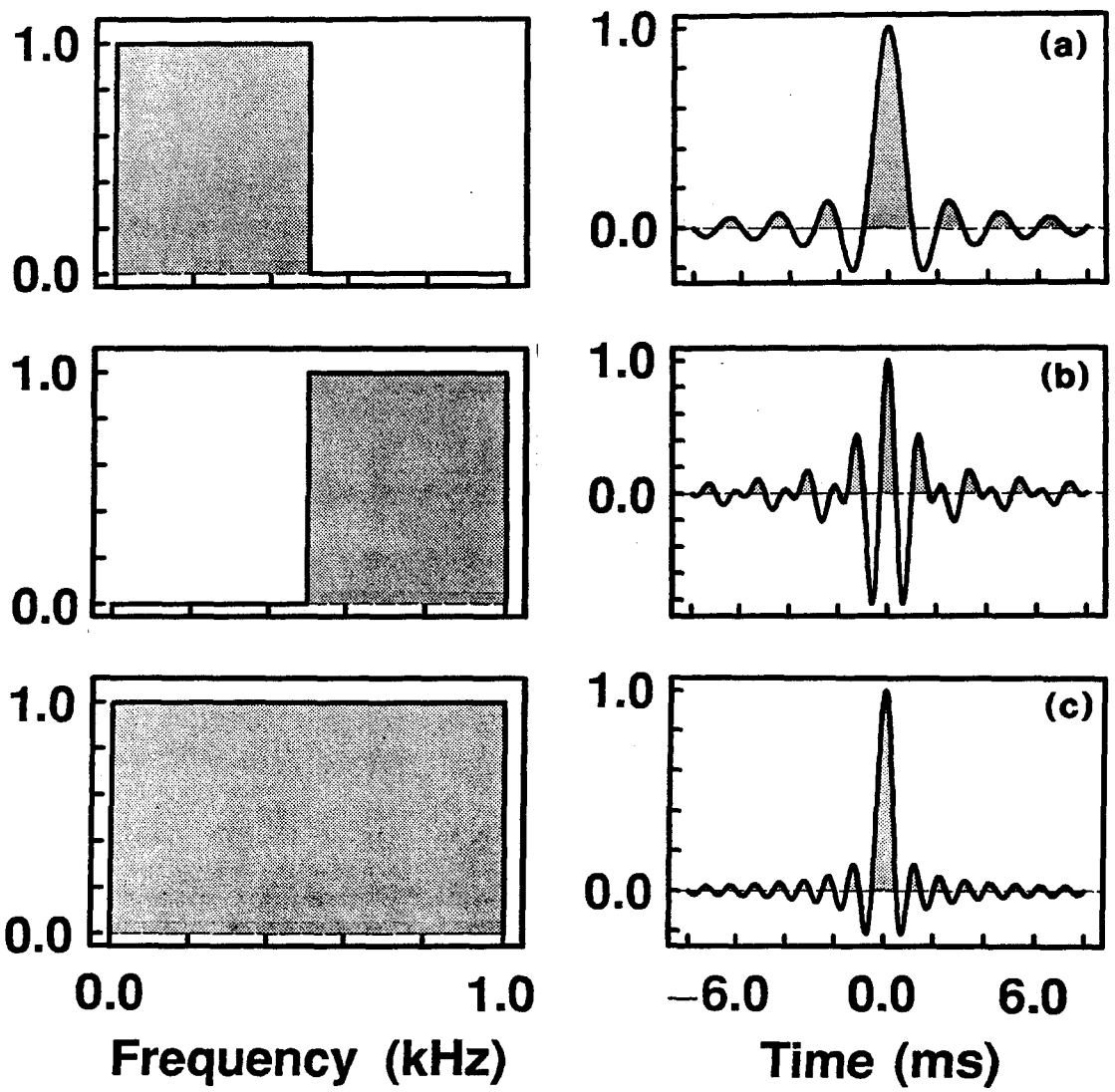

Figure 2.20. Normalized sinc wavelets and associated band-limited amplitude spectra (a) 0.1-500 Hz, (b) 500-1000 Hz and (c) 0.1-1000 Hz. Corresponding phase spectra are zero-valued.

of the wavelet while retaining its spiky character. These findings are in accordance with a generalized measure of wavelet resolving power proposed by Widess (1982) and defined for a real-valued wavelet $w(t)$ by

$$R_w = \frac{{w_{max}}^2}{E_w}, \tag{2.46}$$

where

$$E_w = \int_{-\infty}^{+\infty} w^2(t)\,dt \tag{2.47}$$

defines total wavelet energy and w_{max} denotes the maximum absolute amplitude of the wavelet. Evidently, R_w takes on a maximum value of unity for an infinitely narrow impulse of amplitude $w_{max} = \sqrt{E_w}$ and decreases as wavelet breadth and the magnitude of side lobe oscillations increase, accounting for a larger proportion of total wavelet energy.

Specific spectral characteristics leading to optimum resolving power can be assessed by introducing a related analytical measure of wavelet length or duration. Consequently, wavelet length L_w is defined as the square root of the second moment of the wavelet's energy density about an arbitrary reference time t_0, normalized by total wavelet energy. That is,

$${L_w}^2(t_0) = \frac{1}{E_w}\int_{-\infty}^{+\infty} w^2(t)\,(t-t_0)^2\,dt \tag{2.48}$$

(Lathi, 1965; Shoenberger, 1974; Berkhout, 1984). In particular, on extremalizing $L_w(t_0)$ with respect to t_0 (Appendix F), we find that "second moment length" is minimized for

$$t_0 = \tilde{t}_0 = \frac{1}{E_w}\int_{-\infty}^{+\infty} t\,w^2(t)\,dt. \tag{2.49}$$

In other words, wavelet length defined by equation (2.48) is minimized when measured relative to the wavelet's "centre" or, more precisely, the first moment of wavelet energy density about zero. This result is not surprising given prominent analogies, for instance, in connection with statistics, where an arbitrary probability density function has minimum variance measured about the mean. Although, in practice, physically realizable wavelets are strictly causal signals with definite onset time, suggesting that $t_0 \geq 0$, our present aim

is to assess the resolving power of seismic measurements using relatively simple analytical wavelet models which may or may not be causal. In particular, Ricker and sinc wavelets are symmetric about t=0, consequently acausal and, since their first moment of energy density about t=0 is zero, have minimum second moment length $L_w(0)$.

To ascertain specific spectral properties or characteristics associated with minimum wavelet length and, consequently, optimum seismic resolution, we consider the frequency domain equivalent of equation (2.48). Using the power theorem of the Fourier transform (Bracewell, 1986)

$$\int_{-\infty}^{+\infty} x(t)\, y^*(t)\, dt = \int_{-\infty}^{+\infty} X(f)\, Y^*(f)\, df, \tag{2.50}$$

where $X(f)$ and $Y(f)$ denote Fourier transforms of arbitrary functions $x(t)$ and $y(t)$, respectively, we make the particular substitution

$$x(t) = y(t) = (t - t_0)\, w(t), \tag{2.51}$$

yielding (Appendix G)

$$L_w{}^2(t_0) = \frac{1}{4\pi^2 E_w} \int_{-\infty}^{+\infty} |W(f)|^2 \left\{ \left[\frac{d}{df}\Big(\ln|W(f)|\Big) \right]^2 + \left[\frac{d}{df}\Big(\Theta(f) + 2\pi f t_0\Big) \right]^2 \right\} df. \tag{2.53}$$

where $|W(f)|$ and $\Theta(f)$ denote amplitude and phase spectra associated with an arbitrary wavelet function $w(t)$ as defined by equations (2.24) and (2.26) and where, by Parseval's theorem,

$$E_w = \int_{-\infty}^{+\infty} w^2(t)\, dt = \int_{-\infty}^{+\infty} |W(f)|^2\, df. \tag{2.54}$$

The foregoing expression reveals that wavelet length and, consequently, the wavelet's resolving power depend principally on the rate of change of its spectral characteristics. In particular, since the wavelet's amplitude spectrum must be non-vanishing and bandlimited, the first term in the integral's argument indicates that minimum length and, thus, optimum resolution is associated with a smoothly varying amplitude spectrum. Specifically, Berkhout (1984) has demonstrated that a bandlimited, zero phase wavelet possessing

some predesignated total energy has minimum second moment length $L_w(0)$ if its amplitude spectrum has the form

$$W(f) = \Pi\left(\frac{f - f_m}{\Delta f}\right) \cos\left(\frac{\pi [f - f_m]}{\Delta f}\right), \tag{2.55}$$

where, as before, $f_m = (f_l + f_u)/2$ and $\Delta f = f_u - f_l$ are, respectively, midfrequency and bandwidth and $\Pi(\xi)$ is defined by equation (2.41). Using convolution and shifting theorems of the Fourier transform (Bracewell, 1986), the corresponding optimum wavelet follows as

$$w(t) = \frac{4\Delta f}{\pi}\left[\frac{\cos(\pi \Delta f t)}{1 - (2\Delta f t)^2}\right] \cos(2\pi f_m t). \tag{2.56}$$

In Figure 2.21, we display optimum bandlimited spectra and associated wavelets for comparison with equivalent sinc wavelets in Figure 2.20. In accordance with theoretical findings, sinc wavelets, owing to their abruptly varying amplitude spectra, are evidently "longer" than corresponding optimum wavelets. Consequently, in addition to extended bandwidth, enhanced seismic resolution requires that the amplitude spectrum vary smoothly within the signal band, gradually approaching zero at the bandlimits.

The second term of equation (2.53) vanishes completely for phase spectra $\Theta_0 = \Theta(f) + 2\pi f t_0$ associated with a constant phase wavelet or its time-shifted equivalent, where the linear component $2\pi f t_0$ is associated with selection of reference time t_0 accompanying an equivalent static time-shift. Consequently, since constant and linear phase wavelets are effectively variants on a zero-phase equivalent having identical amplitude spectrum, it follows that minimum second-moment length is fundamentally associated with zero phase wavelets (Shoenberger, 1974; Berkhout, 1984). While a linear phase-shift is equivalent to static time-shift without distortion, a frequency-independent phase-shift alters wavelet character without net translation as depicted in Figure 2.22. In this regard, it is readily demonstrated (Appendix H) that the second moment length of a wavelet $w(t)$ is equivalent to the second moment length of the wavelet's envelope $|w(t)|$ and, consequently, since the wavelet envelope is unaltered by application of a frequency-independent phase-shift

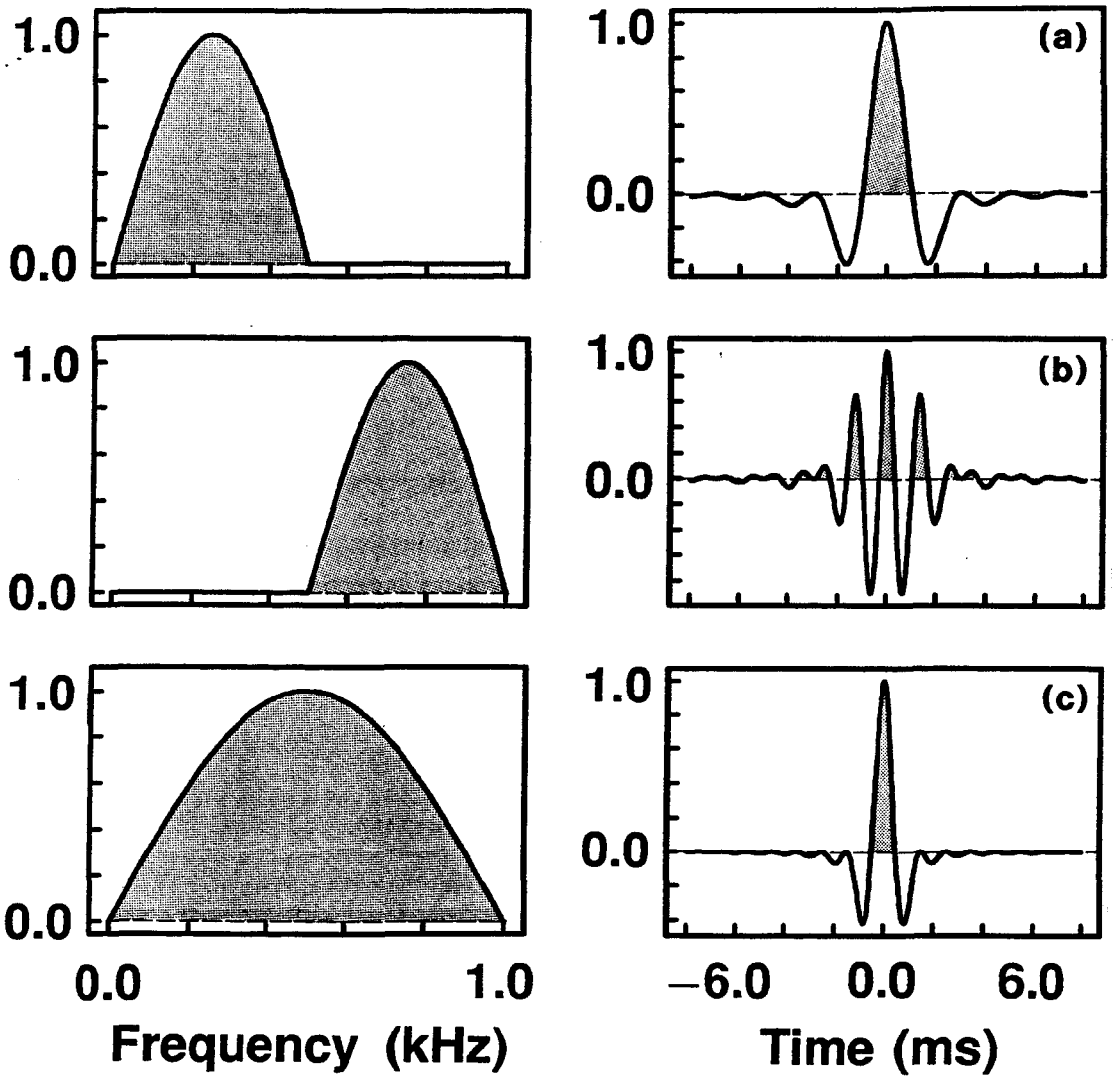

Figure 2.21. Normalized optimum wavelets and associated band-limited amplitude spectra (a) 0-500 Hz, (b) 500-1000 Hz and (c) 0-1000 Hz. Corresponding phase spectra are zero-valued.

(Appendix I), it follows that wavelet length is also invariant under constant phase-shift†. On comparing zero-phase optimum wavelets in Figure 2.21 with constant phase-shifted equivalents in Figure 2.22, it is intuitively evident that, despite length invariance, zero-phase wavelets possess superior resolving power. Consequently, although wavelet length is a useful indicator of resolving capacity and facilitates analysis of relevant spectral properties, it should not be viewed as a measure of resolving power. Rather, since the maximum amplitude w_{max} of the zero-phase wavelet exceeds that of all other wavelets possessing the same amplitude spectrum and, therefore, total energy E_w (Appendix J), its resolving power R_w as predicted by equation (2.46) is also a maximum. Having said this, however, it is important to re-emphasize that physically realizable seismic wavelets are strictly causal and, consequently, non-zero phase (Robinson and Trietel, 1980). In view of this fact, Berkhout (1973, 1984) has demonstrated that among the class of causal wavelets possessing a specified amplitude spectrum, second moment length $L_w(0)$ is minimum for the wavelet having "minimum phase" (Appendix K). In other words, the minimum length wavelet possesses maximum partial energy at any arbitrary time $0 \leq \tau \leq \infty$, where partial energy is defined for a real-valued wavelet $w(t)$ by

$$E_p(\tau) = \int_{-\infty}^{\tau} w^2(t)\,dt. \tag{2.57}$$

For this reason, the term minimum delay is often used in place of minimum phase.

In conclusion, optimum temporal resolution is associated with a wavelet possessing minimum delay phase characteristics in addition to a smoothly varying, broadband amplitude spectrum. Fortunately, common seismic sources, including explosives and impact devices, produce minimum delay disturbances by nature and, thus, a minimum phase assumption is ordinarily well founded.

† As discussed in Appendix H, an exception to wavelet length invariance under constant phase-shift arises for wavelets possessing non-zero d.c. spectral content ($|W(0)| \neq 0$). Applying a frequency-independent phase-shift to a finite length wavelet possessing non-zero area yields a wavelet having infinite second-moment length.

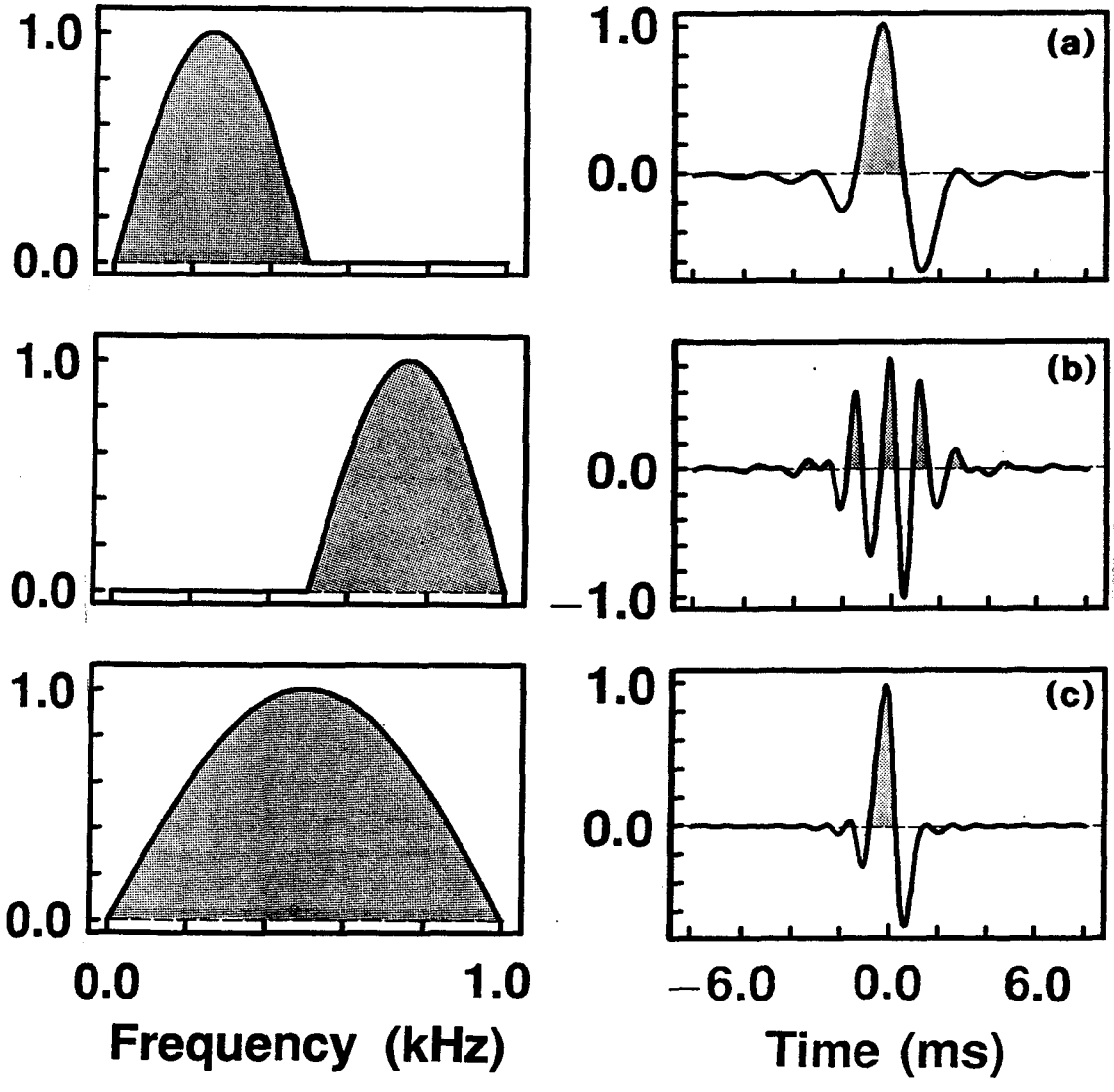

Figure 2.22. Normalized optimum wavelets after application of a frequency-independent phase shift of $\pi/4$ radians. Associated band-limited amplitude spectra (a) 0-500 Hz, (b) 500-1000 Hz and (c) 0-1000 Hz are identical to those in Figure 2.21.

Finally, for sake of physical intuition, it is useful to calibrate the analytical measure of wavelet duration $L_w(t)$ in connection with a wavelet of unambiguous length and in comparison with more practical measures, including dominant T_d and central T_c periods. Consider, for instance, a unit amplitude rectangular wavelet

$$w(t) = \Pi\left(\frac{t}{L}\right), \tag{2.58}$$

with

$$\Pi(\xi) = \begin{cases} 0, & |\xi| > 1/2; \\ 1/2, & |\xi| = 1/2; \\ 1, & |\xi| < 1/2 \end{cases},$$

centered on t=0 and having known length L. Equation (2.47) yields

$$L_w{}^2(0) = \frac{1}{E_w} \lim_{\epsilon \to 0} \left\{ 2 \int_0^{L/2-\epsilon} t^2\, dt + \int_{L/2-\epsilon}^{L/2} t^2\, dt \right\}, \tag{2.59}$$

where

$$\begin{aligned} E_w &= \lim_{\epsilon \to 0} \left\{ 2 \int_0^{L/2-\epsilon} dt + \int_{L/2-\epsilon}^{L/2} dt \right\} \\ &= \lim_{\epsilon \to 0} \{L - \epsilon\} = L. \end{aligned} \tag{2.60}$$

Consequently, we obtain

$$L_w{}^2(0) = \frac{1}{3L} \lim_{\epsilon \to 0} \left\{ 2(L/2)^3 - \epsilon \left[(L/2)^2 - 3\epsilon(L/2) + \epsilon^2 \right] \right\} \tag{2.61}$$

and, therefore,

$$L_w(0) = \frac{L}{\sqrt{12}} \approx 0.29\, L, \tag{2.62}$$

indicating that the analytical length estimate must be scaled by a factor of $1/\sqrt{12} \approx 0.29$ to yield the true length of a rectangular pulse. In comparison, we demonstrate in Appendix L that the Ricker wavelet is characterized by a second moment length $L_w(0) \approx 0.31\, T_d$ or, equivalently, $L_w(0) \approx 0.27\, T_c$, supporting the validity of the forgoing calibration. Note that the foregoing result is perfectly consistent with the analogy between second moment length and the standard deviation of a statistical distribution. Just as approximately 87 percent of the area under a Gaussian curve falls within one and one-half standard deviations of the mean, true wavelet length is very nearly three times the second moment length about the wavelet's center $\tilde{t}_0$, as given by equation (2.49).

2.3.2 Spatial Resolution:

Spatial resolution may be characterized using the concept of Fresnel zones to quantify the focus of seismic soundings. Consider a source of monochromatic spherical waves located a normal distance r_0 above a horizontal diffuse reflecting interface of infinite extent as illustrated in Figure 2.23. Accounting for two-way transit, half-period Fresnel zones are successive annular regions on the planar reflector from which reflected energy returns within half cycle intervals. Referring to Figure 2.23, we consider rings of radii R_1, R_2, ..., R_n such that corresponding ranges r_1, r_2, ..., r_k are successively longer by a quarter of a wavelength. That is,

$$r_k = r_0 + \frac{k\lambda}{4}. \tag{2.63}$$

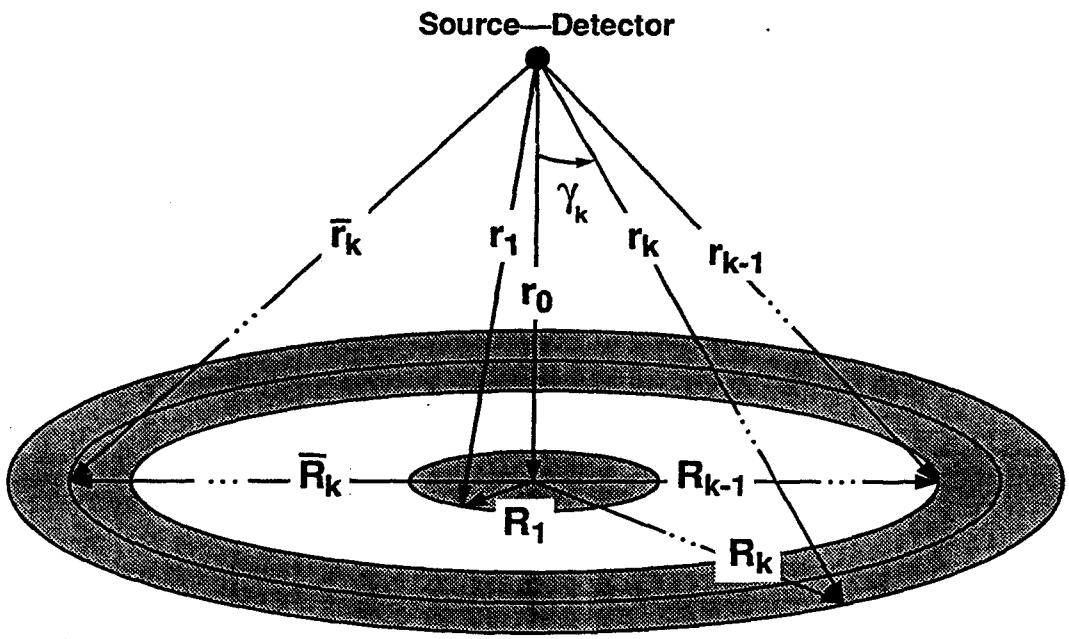

Figure 2.23. Fresnel zone geometry for a coincident source of monochromatic waves positioned a normal-incidence range r_0 above an infinite plane, horizontal reflector. r_k and R_k denote, respectively, the range to outer boundary of the kth zone and the projection of this range on the reflector. By definition, $r_k - r_{k-1} = \lambda/4$, where λ denotes the wavelength of the incident wave. $\bar{r}_k$ and $\bar{R}_k$ are, respectively, the mean range to the kth zone and its component in the plane of the reflector.

We also have that

$$R_k^2 = r_k^2 - r_0^2. \tag{2.64}$$

Now, on squaring equation (2.63) and substituting for r_k^2 in equation (2.64), we obtain

$$R_k = \left[\left(\frac{k\lambda}{4}\right)^2 + k\frac{r_0\lambda}{2}\right]^{1/2} \tag{2.65}$$

for the radius of the kth ring in terms of normal range r_0 and wavelength λ. The area of the kth Fresnel zone follows as

$$\begin{aligned} \mathcal{A}_k &= \pi\,(R_k^2 - R_{k-1}^2) \\ &= \pi\left[\frac{\lambda^2}{8}\left(k - \frac{1}{2}\right) + \frac{r_0\lambda}{2}\right]. \end{aligned} \tag{2.66}$$

Since, successive zones are, on average, $\lambda/2$ further from the coincident source-detector, the net contribution at the detector due to a given Fresnel zone is phase shifted by 180 degrees relative to contributions from adjacent zones. Since a phase shift of 180 degrees is equivalent to reversing the polarity of the arrival, the resultant amplitude detected at the receiver due to the first n Fresnel zones may be written as

$$A = A_1 - A_2 + A_3 - A_4 + \ldots + (-1)^{n-1} A_n, \tag{2.67}$$

where A_k represents the net reflection amplitude from the kth zone. Following the development of Jenkins and White (1957), we note that three controlling factors determine the magnitudes of successive terms in the foregoing series. First, equation (2.66) indicates that zonal area $\mathcal{A}_k$ increases gradually with k, yielding a larger net contribution from successive zones. Secondly, as average range $\bar{r}_k$ from source-detector to the kth zone increases with k, spherical divergence causes a reduction in the corresponding reflection amplitude. Finally, in accordance with the Huygens-Fresnel principle, the net reflection amplitude from a given zone depends on the average angle of incidence/reflection-diffraction $\bar{\xi}_k$ as embodied in a so-called inclination or obliquity factor

$$f_O(\bar{\xi}_k) = 1 + \cos\bar{\xi}_k \tag{2.68}$$

(Jenkins and White, 1957; Born and Wolf, 1975). It follows that increasing obliquity associated with successive zones tends to lessen the corresponding contribution to the resultant amplitude at the detector.

As a result, we have the following proportionality

$$A_k \propto f_O(\bar{\xi}_k)\frac{\mathcal{A}_k}{\bar{r}_k}. \tag{2.69}$$

Average range to the kth zone, or the annulus between rings having radii R_{k-1} and R_k, follows from equation (2.63) and the mean value theorem for integrals as

$$\begin{aligned}\bar{r}_k &= \left[\frac{1}{k-(k-1)}\right]\int_{k-1}^{k}\left(r_0 + m\frac{\lambda}{4}\right)dm \\ &= \left[mr_0 + m^2\frac{\lambda}{8}\right]_{k-1}^{k} \\ &= \frac{2}{\lambda}\left[\frac{\lambda^2}{8}\left(k-\frac{1}{2}\right)+\frac{r_0\lambda}{2}\right]\end{aligned} \tag{2.70}$$

Comparing the foregoing result with equation (2.66), we find that the ratio of zonal area to average zonal range is a constant

$$\frac{\mathcal{A}_k}{\bar{r}_k} = \lambda\frac{\pi}{2}, \tag{2.71}$$

independent of k. Consequently, the proportionality (2.69) becomes

$$A_k \propto \lambda\frac{\pi}{2}f_O(\bar{\xi}_k), \tag{2.72}$$

indicating that the relative amplitude contribution A_k, due to the kth Fresnel zone depends solely upon the obliquity factor equation (2.68) and, thus, on the average angle of incidence/reflection $\bar{\xi}_k$. Recognizing that the rate of change in $\bar{\xi}_k$ increases with increasing R_k, we regroup the terms in equation (2.67) as

$$A = \frac{A_1}{2} + \left(\frac{A_1}{2} - A_2 + \frac{A_3}{2}\right) + \left(\frac{A_3}{2} - A_4 + \frac{A_5}{2}\right) + \ldots + \frac{A_n}{2} \tag{2.73}$$

or

$$A = A_1 - \frac{A_2}{2} - \left(\frac{A_2}{2} - A_3 + \frac{A_4}{2}\right) - \left(\frac{A_4}{2} - A_5 + \frac{A_6}{2}\right) - \ldots - \frac{A_{n-1}}{2} + A_n. \tag{2.74}$$

Noting that each term in equation (2.67) exceeds the arithmetic mean of its neighboring terms, it follows that terms in parentheses are negative valued and, consequently, we may

form the inequality

$$\left(\frac{A_1}{2}+\frac{A_n}{2}\right) > A > \left(A_1-\frac{A_2}{2}-\frac{A_{n-1}}{2}+A_n\right). \tag{2.75}$$

Now, assuming that $r_0 >> \lambda$, A_1 is very nearly equal to A_2 and the previous inequality reduces to

$$\left(\frac{A_1}{2}+\frac{A_n}{2}\right) > A > \left[\frac{A_1}{2}+\left(A_n-\frac{A_{n-1}}{2}\right)\right]. \tag{2.76}$$

Further postulation that A_{n-1} and A_n are approximately equal yields

$$\left(\frac{A_1}{2}+\frac{A_n}{2}\right) \approx A \approx \left(\frac{A_1}{2}+\frac{A_n}{2}\right) \tag{2.77}$$

and, finally, on letting n approach infinity we have $\lim_{n\to\infty} A_n = 0$ and, thus,

$$A \approx \frac{A1}{2}. \tag{2.78}$$

In other words, resultant amplitude detected by a coincident source-receiver pair, situated above an infinite horizontal reflector, is approximately half that contributed by the first Fresnel zone. Consequently, the diameter of the first half-period Fresnel zone

$$D_1 = \left(\frac{\lambda^2}{4}+2r_0\lambda\right)^{1/2} \tag{2.79}$$

(see equation (2.65)) is routinely adopted as a measure of spatial resolution. In fact, since $r_0 >> \lambda$ is ordinarily a reasonable assumption in connection with large-scale seismic exploration, the second order term in λ is commonly neglected, yielding the approximation

$$D_1 \approx (2r_0\lambda)^{1/2} \tag{2.80}$$

(Sheriff, 1985; Lindsey, 1989). Although the condition $r_0 >> \lambda$ is often invalid for near-surface archaeological applications, the first Fresnel zone diameter given by equation (2.79) remains a useful measure of spatial resolution. Indeed, departures from approximations $A_2 \approx A_1$ and $A_{n-1} \approx A_n$ leading from equation (2.75) to equation (2.77) are offsetting so that the approximation $A \approx A_1/2$ remains valid. Fresnel zone concepts may also be

extended to complexly stratified media and arbitrary source-detector geometries by considering the Fresnel volume or "physical ray", enveloping all possible Fresnel zones along the associated ray-path (Hubral, et.al., 1993; Cerveny and Soares, 1992).

Having adopted equation (2.79) as our spatial resolution criterion, let's examine its practical significance. Despite its development in connection with an infinite reflector, the Fresnel zone criterion is principally employed to assess the capacity for resolving finite or discontinuous features. It is commonly conjectured that the Fresnel zone criterion quantifies the focus of seismic imaging by characterizing the effective cross-sectional area of seismic illumination as a function of wavelength and range from the source. It is evident from foregoing development, however, that equation (2.78) is only valid for a reflector having infinite extent and that any discontinuity of the reflector or departure from its planar nature will disturb the convergence of equation (2.67), yielding a deviation from the response predicted by equation (2.78). As we shall demonstrate, the difference is directly associated with diffraction from the discontinuity. Consequently, the seismic response measured above an arbitrary reflector of finite extent is not insensitive to portions of the reflector or, indeed, other reflectors outside the first Fresnel zone. An approximate analytical expression for this response has been developed by Trorey (1970) on the basis of the integral theorem of Kirchoff.

Kirchoff's theorem embodies the fundamental principle of the Huygens-Fresnel principle, by expressing the solution of the homogeneous wave equation

$$\nabla^2\varphi = \frac{\partial^2\varphi}{\partial \mathrm{r}^2} + \frac{2}{\mathrm{r}}\frac{\partial\varphi}{\partial \mathrm{r}} = \frac{1}{\alpha^2}\frac{\partial^2\varphi}{\partial \mathrm{t}^2} \tag{2.81}$$

at an arbitrary point p within the wavefield in terms of its solution and associated partial derivatives over an arbitrary surface $\mathcal{S}$ surrounding p. The result is

$$\varphi_p(\mathrm{t}) = \frac{1}{4\pi}\int\int_{\mathcal{S}}\left\{\frac{1}{\mathrm{r}}\left[\frac{\partial\varphi_{\mathcal{S}}}{\partial \mathrm{n}}\right] - [\varphi_{\mathcal{S}}]\frac{\partial}{\partial \mathrm{n}}\left(\frac{1}{\mathrm{r}}\right) + \frac{1}{\alpha \mathrm{r}}\frac{\partial \mathrm{r}}{\partial \mathrm{n}}\left[\frac{\partial\varphi_{\mathcal{S}}}{\partial \mathrm{t}}\right]\right\}\mathrm{d}\mathcal{S}, \tag{2.82}$$

where r denotes the distance from p to an arbitrary element of $\mathcal{S}$, n is the associated

outward normal and square brackets denote evaluation of the corresponding function on $\mathcal{S}$ at retarded time $t - r/\alpha$, where r/α is the time required for a specified disturbance originating at an arbitrary position on the surface $\mathcal{S}$ to reach p (Jeans, 1948; Born and Wolf, 1975). Consequently, in analogy with Huygens principle, each elemental area on $\mathcal{S}$ may be viewed as a point source of secondary radiation incident at p. Subsequent superposition of these secondary disturbances, in accordance with equation (2.82), yields the resultant field at p.

Prescribing an appropriate geometry for the surface $\mathcal{S}$, Trorey (1970) has formulated an approximate form of Kirchoff's solution for a finite plane reflector illuminated by a point source coincident with the detector at p. The solution is developed in the Laplace transform domain beginning with the equivalent relations

$$\nabla^2\tilde{\varphi} = \frac{\partial^2\tilde{\varphi}}{\partial r^2} + \frac{2}{r}\frac{\partial\tilde{\varphi}}{\partial r} = \left(\frac{s}{\alpha}\right)^2\tilde{\varphi} \tag{2.83}$$

and

$$\tilde{\varphi}_p(s) = \frac{1}{4\pi}\int\int_{\mathcal{S}} e^{-sr/\alpha}\left\{\frac{1}{r}\frac{\partial\tilde{\varphi}_{\mathcal{S}}}{\partial n} - \tilde{\varphi}_{\mathcal{S}}\frac{\partial}{\partial n}\left(\frac{1}{r}\right) + \frac{s}{\alpha r}\tilde{\varphi}_{\mathcal{S}}\frac{\partial r}{\partial n}\right\} d\mathcal{S}, \tag{2.84}$$

where

$$\tilde{\varphi}(s) = \mathcal{L}[\varphi(t)] = \int_{-\infty}^{+\infty}\varphi(t)\,e^{-st}\,dt \tag{2.85}$$

defines the Laplace transform of $\varphi(t)$. In addition, we have made use of the shift theorem of the Laplace transform (Kaplan, 1981)

$$\mathcal{L}\left[\varphi\left(t - \frac{r}{\alpha}\right)\right] = e^{-sr/\alpha}\,\mathcal{L}[\varphi(t)] = e^{-sr/\alpha}\,\tilde{\varphi}(s) \tag{2.86}$$

and the particular transform

$$\mathcal{L}\left[\frac{\partial}{\partial t}\varphi(t)\right] = s\,\tilde{\varphi}(s) - \varphi_0, \tag{2.84}$$

with initial condition $\varphi_0 = 0$. Assuming a homogeneous, isotropic acoustic medium having velocity α, the wavefield $\tilde{\varphi}_{\mathcal{S}}$ on a finite horizontal surface $\mathcal{S}$ due to a point source at p',

the image of p with respect to $\mathcal{S}$, and satisfying equation (2.83) is

$$\tilde{\varphi}_{\mathcal{S}}(s) = \mathcal{R}\,\tilde{w}(s)\frac{e^{-sr/\alpha}}{r}, \tag{2.88}$$

where $\mathcal{R}$ denotes the associated reflection coefficient and $\tilde{w}(s) = \mathcal{L}[w(t)]$ represents the Laplace transform of the source wavelet. Substituting the foregoing result in equation (2.84) yields

$$\tilde{\varphi}_p(s) = \frac{r_0\mathcal{R}}{2\pi}\,\tilde{w}(s)\int_{\mathcal{S}} e^{-sr/\alpha}\left(\frac{1}{r^4} + \frac{s}{\alpha r^3}\right) d\mathcal{S}, \tag{2.89}$$

where r_0 denotes the normal distance from the coincident source-detector to the underlying reflector. Finally, reducing equation (2.89) to an integral about the boundary of $\mathcal{S}$, as depicted in Figure 2.24, Trorey obtained the following solution for the seismic response measured by coincident source-detector positioned above a finite plane reflector bounded by an arbitrary curve

$$\tilde{\varphi}(s) = \frac{\mathcal{R}}{2r_0}\,\tilde{w}(s)\,e^{-2sr_0/\alpha} - \frac{r_0\mathcal{R}}{4\pi}\,\tilde{w}(s)\int_{\theta}\frac{e^{-2sr(\theta)/\alpha}}{r^2(\theta)}\,d\theta, \tag{2.90}$$

where $r(\theta)$ represents range to the boundary of $\mathcal{S}$ and integration is performed such that a point q traverses the boundary of $\mathcal{S}$ in clockwise sense. Notice that we have dropped the subscript p to simplify notation. In what follows, $\tilde{\varphi}(s)$ denotes the Laplace transform of the resultant seismic response.

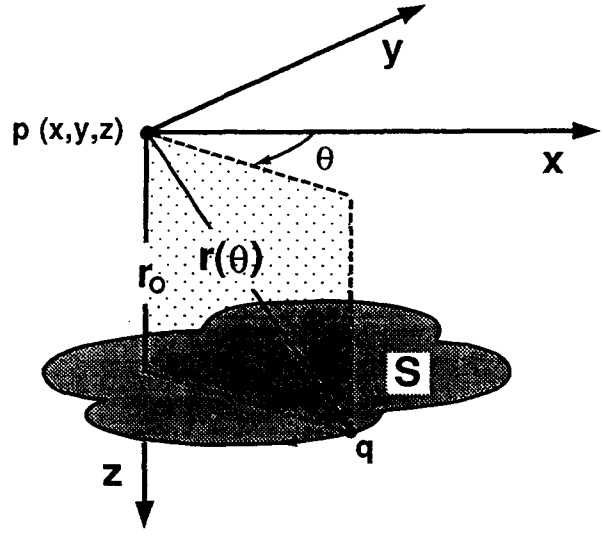

Figure 2.24. Geometry for evaluation of equations (2.89) and (2.90) for the total seismic response of an arbitrarily shaped plane reflecting interface $\mathcal{S}$ as detected by a coincident source-detector pair at the origin (adapted from Trorey (1970)).

As Trorey (1970) recognized, the first term of the foregoing solution gives the simple reflection response for an infinite plane reflector at depth r_0. More interestingly, the second term may be viewed as a correction term accounting for diffraction from the reflector's boundary. In particular, note that if the reflector is actually infinite in extent, $r(\theta)$ also becomes infinite, causing the diffraction term to vanish. Alternatively, if source-detector are not positioned over the reflector, the reflection term vanishes and the diffraction term is phase-shifted by 180 degrees. Let's examine the connection between these findings and the earlier discussion of Fresnel zones.

First it must be emphasized that while the concept of Fresnel zones applies to a monochromatic incident wavefield, the forgoing development based on Kirchoff's theorem, admits a generalized source wavelet $w(t)$. Consequently, in exploring the connection between the two models, it is assumed that $\tilde{w}(s)$ represents the Laplace transform of a monochromatic waveform. Having said this, consider the total response predicted by equation (2.90) for a plane circular reflector centered a vertical distance r_0 beneath a coincident source-detector pair and having radius R_k as depicted in Figure 2.25. Since the bounding curve is circular and, consequently, at constant range $r(\theta) = r_k = \sqrt{r_0^2 + R_k^2}$, equation (2.90) reduces as follows

$$\begin{aligned}
\tilde{\varphi}(s) &= \frac{\mathcal{R}}{2r_0}\,\tilde{w}(s)\,e^{-2sr_0/\alpha} - \frac{r_0\mathcal{R}}{4\pi}\,\tilde{w}(s)\,\frac{e^{-2sr_k/\alpha}}{r_k^2}\int_0^{2\pi} d\theta \\
&= \frac{\mathcal{R}}{2r_0}\,\tilde{w}(s)\,e^{-2sr_0/\alpha} - \frac{r_0\mathcal{R}}{2r_k^2}\,\tilde{w}(s)\,e^{-2sr_k/\alpha} \\
&= \frac{\mathcal{R}}{2r_0}\,\tilde{w}(s)\,e^{-2sr_0/\alpha}\left[1 - \left(\frac{r_0}{r_k}\right)^2 e^{-2s(r_k - r_0)/\alpha}\right]
\end{aligned} \tag{2.91}$$

It is easily observed from this result that $\lim_{r_k \to r_0} \tilde{\varphi}_p(s) = 0$. In other words, as the reflector shrinks to a point, its response vanishes (i.e. a "point diffractor" is a purely theoretical convenience). More interestingly, the response of the kth Fresnel zone follows as

$$\tilde{\varphi}_k(s) = \frac{\mathcal{R}}{2r_0}\,\tilde{w}(s)\,e^{-2sr_0/\alpha}\left[\left(\frac{r_0}{r_{k-1}}\right)^2 e^{-2s(r_{k-1} - r_0)/\alpha} - \left(\frac{r_0}{r_k}\right)^2 e^{-2s(r_k - r_0)/\alpha}\right]. \tag{2.92}$$

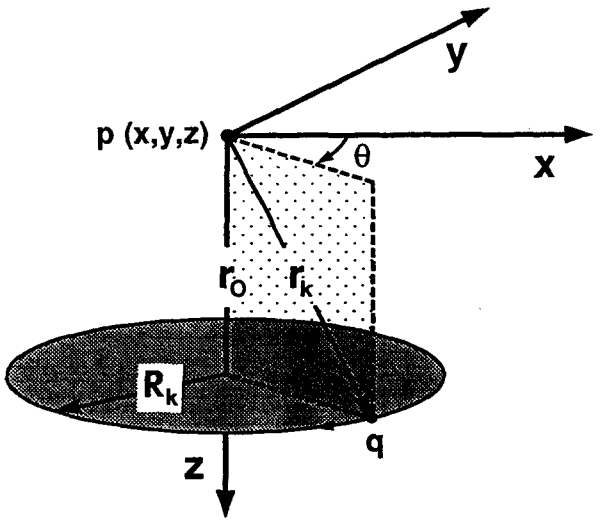

Figure 2.25. Specialized geometry (particular case of Figure 2.24) for evaluation of equations (2.89) and (2.90) in connection with a plane circular reflector, having radius R_k, centered a vertical range r_0 beneath the coincident source-detector.

In particular, letting k = 1, we obtain

$$\tilde{\varphi}_1(s) = \frac{\mathcal{R}}{2r_0}\,\tilde{w}(s)\,e^{-2sr_0/\alpha}\left[1 - \left(\frac{r_0}{r_1}\right)^2 e^{-2s(r_1-r_0)/\alpha}\right] \tag{2.93}$$

or, on recalling from equation (2.68) that $r_1 = r_0 + \lambda/4$,

$$\tilde{\varphi}_1(s) = \frac{\mathcal{R}}{2r_0}\,\tilde{w}(s)\,e^{-2sr_0/\alpha}\left[1 - \left(\frac{r_0}{r_0+\lambda/4}\right)^2 e^{-s\lambda/2\alpha}\right]. \tag{2.94}$$

Now, recalling the shift theorem of the Laplace transform defined by equation (2.86), we recognize that the factor $\exp(-s\lambda/2\alpha)$ represents a half-period time lag between diffracted and reflected waveforms or, equivalently, a 180 degree phase shift and, thus, a change of sign. Consequently, the previous result may be rewritten as

$$\tilde{\varphi}_1(s) = \frac{\mathcal{R}}{2r_0}\,\tilde{w}(s)\,e^{-2sr_0/\alpha}\left[1 + \left(\frac{r_0}{r_0+\lambda/4}\right)^2\right] \tag{2.95}$$

and on assuming $r_0 >> \lambda$ in accordance with the earlier treatment of Fresnel zones, the

term in brackets gives 2, yielding

$$\tilde{\varphi}_1(s) \approx \frac{\mathcal{R}}{r_0}\,\tilde{w}(s)\,e^{-2sr_0/\alpha} \tag{2.96}$$

or, referring to equation (2.90), approximately twice the response of an infinite plane reflector, in agreement with equation (2.78). In contrast, however, the foregoing treatment provides a more general characterization of the seismic response and, in particular, reveals the very significant contribution of diffracted energy. Specifically, for a plane, circular reflector having diameter equivalent to that of the first half-period Fresnel zone, the foregoing analysis demonstrates that the diffraction term accounts for approximately half the total response. As the reflector's radius increases to that of the second Fresnel zone, the diffraction term changes sign and roughly cancels the reflection term, yielding the comparatively negligible response

$$\tilde{\varphi}_2(s) = \frac{\mathcal{R}}{2r_0}\,\tilde{w}(s)\,e^{-2sr_0/\alpha}\left[\left(\frac{r_0}{r_0+\lambda/2}\right)^2 - \left(\frac{r_0}{r_0+\lambda/4}\right)^2\right], \tag{2.97}$$

as predicted by equation (2.92). Further increase in the reflector's radius is accompanied by a growing resultant response, reaching a maximum that is only slightly less than that given by equation (2.96) at a radius equal to that of the third half-period Fresnel zone. Subsequently, as the radius of the circular reflector approaches the fourth Fresnel zone radius, the resultant response is again diminished reaching a minimum that is marginally larger than that given by equation (2.97). For reflectors having larger radii, the progression continues converging, as anticipated, to

$$\tilde{\varphi}_\infty(s) = \frac{\mathcal{R}}{2r_0}\,\tilde{w}(s)\,e^{-2sr_0/\alpha} \tag{2.98}$$

for an infinite reflector. Note that while this convergence is perfectly consistent with equation (2.67), the present analysis emphasizes the modulating influence of the diffraction response. To facilitate a complete characterization of the seismic response, we transform equation (2.91) to the time domain.

Application of the shift theorem, given by equation (2.86), together with convolution theorem

$$\mathcal{L}[w(t) * r(t)] = \int_{-\infty}^{+\infty} e^{-st} \left[\int_{-\infty}^{+\infty} w(\tau)\, r(t-\tau)\, d\tau \right] dt = \mathcal{L}[w(t)]\, \mathcal{L}[r(t)], \qquad (2.99)$$

for the Laplace transform (Kaplan, 1981) yields

$$\varphi(t) = w(t) * \left\{ \frac{\mathcal{R}}{2r_0} \left[\delta\left(t - \frac{2r_0}{\alpha}\right) - \left(\frac{r_0}{r_k}\right)^2 \delta\left(t - \frac{2r_k}{\alpha}\right) \right] \right\}, \qquad (2.100)$$

illustrating that the resulting seismic response involves convolution of the wavelet with two time-shifted delta functions. Consequently, although foregoing analysis predicts that the response due to the first Fresnel zone is approximately twice that for an infinite reflector, this finding must be qualified by noting that it is valid only for $t \geq 2r_1/\alpha$. In other words, on writing the monochromatic waveform as

$$w(t, r) = H\left[t - \frac{r}{\alpha}\right] \frac{w_0}{r} \sin\left[\frac{2\pi}{\lambda}(r - \alpha t)\right], \qquad (2.101)$$

with w_0 denoting waveform amplitude at unit distance from the source and

$$H[\tau] = \begin{cases} 0, & \tau < 0; \\ 1/2, & \tau = 0; \\ 1, & \tau > 0 \end{cases}$$

the Heaviside step function, it is evident that if the source is activated at $t = 0$, no response is detected until onset of the reflected arrival after two-way transit time $t = 2r_0/\alpha$. Moreover, the reflected wave alone constitutes the resultant seismic response for a subsequent interval $\delta t_r = 2(r_1 - r_0)/\alpha$ prior to arrival of the diffracted wave, at $t = r_1/\alpha$. For $t \geq r_1/\alpha$, reflected and diffracted wavelets interfere constructively to yield a resultant response nearly twice that due to reflection alone. Consequently, in a strict sense, the resultant response predicted by equation (2.91) should be viewed as a steady-state response established only for $t \geq r_k/\alpha$.

Unlike the observation of optical phenomenon, where steady-state responses are measured, the time lag $\delta t_r = 2(r_k - r_0)/\alpha$ is critical in connection with seismic imaging, especially in view of the transient nature of broadband seismic wavelets (Knapp, 1991).

Obviously, if the time lag exceeds wavelet duration, or length, there will be no interference whatever between reflected and diffracted wavelets. For time lags comparable to wavelet length, on the other hand, the resultant seismic response is a wavelet complex as examined previously in connection with temporal resolution. Consequently, spatial seismic resolution depends on the nature of interference between reflected and diffracted wavelets at the detector and, thus, on wavelet length as well as the reflector's dimensions and geometry. In particular, as the range from a coincident source-detector to the boundary of a plane circular reflector approaches that corresponding to the wavelet's first half-dominant-period Fresnel zone, the time lag between reflected and diffracted arrivals approaches Rayleigh's limit $T_t = 0.5\,T_d$. Thus, a connection is established between the Fresnel zone criterion for spatial resolution and the Rayleigh-Ricker criterion for temporal resolution. While wavelet complexes associated with reflectors having larger radii are resolved, reflectors having lesser radii yield reflection responses that are indistinguishable from the associated diffraction event. In particular, as the reflector's radius shrinks to zero, the time lag separating reflected and diffracted arrivals decreases until the reflected wavelet is exactly canceled by a polarity reversed equivalent due to diffraction from the reflector's vanishing circular boundary. It should also be appreciated that as the coincident source-detector is offset from the center of a circular reflector of finite radius, the diffraction response is no longer impulsive since the range $r(\theta)$ in equation (2.90) is no longer a constant.

The foregoing findings are illustrated in connection with the response derived by Trorey (1970) for an infinite half-plane as depicted in Figure 2.26. Observing that

$$r(\theta) = \left[\Delta x^2 \tan^2\theta + \left(\Delta x^2 + r_0^2\right)\right]^{1/2}, \tag{2.102}$$

the corresponding response follows from equation (2.90) and (2.99) as

$$\varphi(x,t) = w(t) * \Omega(x,t) = \int_{-\infty}^{\infty} w(\tau)\,\Omega(x, t-\tau)\,d\tau, \tag{2.103}$$

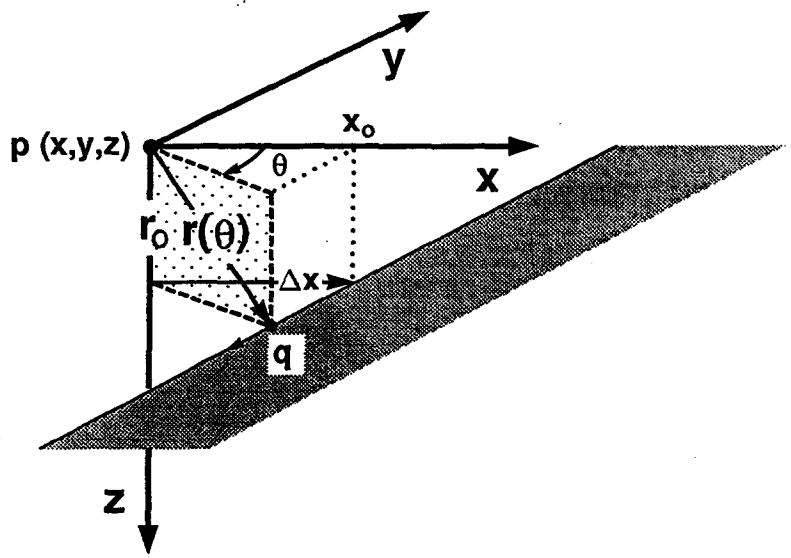

Figure 2.26. Geometry for evaluation of equation (2.90) for the total seismic response of an infinite half-plane as detected by a coincident source-detector pair at the origin (adapted from Trorey (1970)). Note that $r_0 = \Delta z$ is assumed constant.

where

$$\Omega(x,t) = \left\{ \frac{\mathcal{R}}{2r_0} \left[H[x - x_0]\, \delta\left(t - \frac{2r_0}{\alpha}\right) - \frac{4r_0^2 \tau_x}{\pi\alpha^2} \frac{H[t-\tau]}{t\,(t^2 + \tau_x^2 - \tau^2)\,(t^2 - \tau^2)^{1/2}} \right] \right\}, \quad (2.104)$$

with

$$H[\tau] = \begin{cases} 0, & \tau < 0; \\ 1, & \tau \geq 0 \end{cases}$$

and

$$\tau_x = \frac{2\Delta x}{\alpha}, \quad (2.105)$$

$$\tau = \frac{2\left(\Delta x^2 + r_0^2\right)^{1/2}}{\alpha}, \quad (2.106)$$

$$\Delta x = x - x_0. \quad (2.107)$$

Note that while the delta function in the first term is impulsive for $t = t_0 = 2r_0/\alpha$, corresponding to arrival of the reflected wavelet, the diffraction term is characterized by an inverse-root singularity for $t = \tau$ which too becomes impulsive as τ approaches t_0. For modelling purposes, equation (2.103) is evaluated numerically as a discrete convolution

and, since a practical sampling interval may not provide adequate characterization of the continuous diffraction operator

$$D(t) = \frac{1}{t\,(t^2 + \tau_x^2 - \tau^2)\,(t^2 - \tau^2)^{1/2}}, \tag{2.108}$$

especially for $t \approx \tau$, we require an accurate yet discrete representation. Using a technique described by Dalton and Yedlin (1990), we define the discrete diffraction operator via the midpoint rule as

$$d(T) = d_T = \frac{1}{\Delta t}\int_{T-\Delta t/2}^{T+\Delta t/2} D(t)\,dt, \tag{2.109}$$

where Δt denotes the temporal sampling interval. Integration yields

$$\begin{aligned} d_T = \frac{-1}{2\Delta t\tau\,|\tau_x|\,(\tau_x^2 - \tau^2)} \Bigg\{ & 2|\tau_x| \sin^{-1}\left[\frac{\tau}{\Delta t/2 + T}\right] - \tau \sin^{-1}\left[\frac{\tau^2 + c(T + \Delta t/2)}{\tau(\Delta t/2 + T + c)}\right] \\ & -\tau \sin^{-1}\left[\frac{\tau^2 - c(T + \Delta t/2)}{\tau(\Delta t/2 + T - c)}\right] + 2|\tau_x| \sin^{-1}\left[\frac{\tau}{\Delta t/2 - T}\right] \\ & -\tau \sin^{-1}\left[\frac{\tau^2 - c(\Delta t/2 - T)}{\tau(\Delta t/2 - T - c)}\right] - \tau \sin^{-1}\left[\frac{\tau^2 + c(\Delta t/2 - T)}{\tau(\Delta t/2 - T + c)}\right]\Bigg\}, \end{aligned} \tag{2.110}$$

where

$$c = (\tau + \tau_x)^{1/2}\,(\tau - \tau_x)^{1/2}.$$

Now, writing

$$\delta_T = \frac{1}{\Delta t}\int_{T-\Delta t/2}^{T+\Delta t/2} \delta(t - t_0)\,dt = \frac{1}{\Delta t}\,\Pi\left(\frac{T - t_0}{\Delta t}\right), \tag{2.111}$$

with

$$\Pi(\xi) = \begin{cases} 0, & |\xi| > 1/2; \\ 1, & |\xi| \le 1/2 \end{cases},$$

as the discrete representation of the time-shifted Dirac delta function, we obtain the following discrete form of equation (2.103)

$$\varphi_{X,T} = w_T * \Omega_{X,T} = \sum_{\tau=-\infty}^{\infty} w_\tau\,\Omega_{X,T-\tau}, \tag{2.112}$$

where

$$\Omega_{X,T} = \left\{ \frac{\Delta t \mathcal{R}}{2r_0} \left[H[X - x_0]\, \delta_T - \frac{4r_0^2 \tau_x}{\pi \alpha^2} H[T - \tau]\, d_T \right] \right\}. \tag{2.113}$$

Multiplication by Δt invokes normalization for an arbitrary sampling interval. While evaluation of the reflection term is straight forward, the diffraction operator defined by equation (2.110) is valid only for $T \geq \tau + \Delta t/2$ due to the step discontinuity at $T = \tau$. For $\tau < T < \tau + \Delta t/2$, we substitute $\tilde{\Delta} t/2 = (T - \tau) + \epsilon$ for $\Delta t/2$ in equation (2.110), where ϵ represents a vanishingly small positive constant. The corresponding result is subsequently scaled by $\Delta t/\tilde{\Delta} t$.

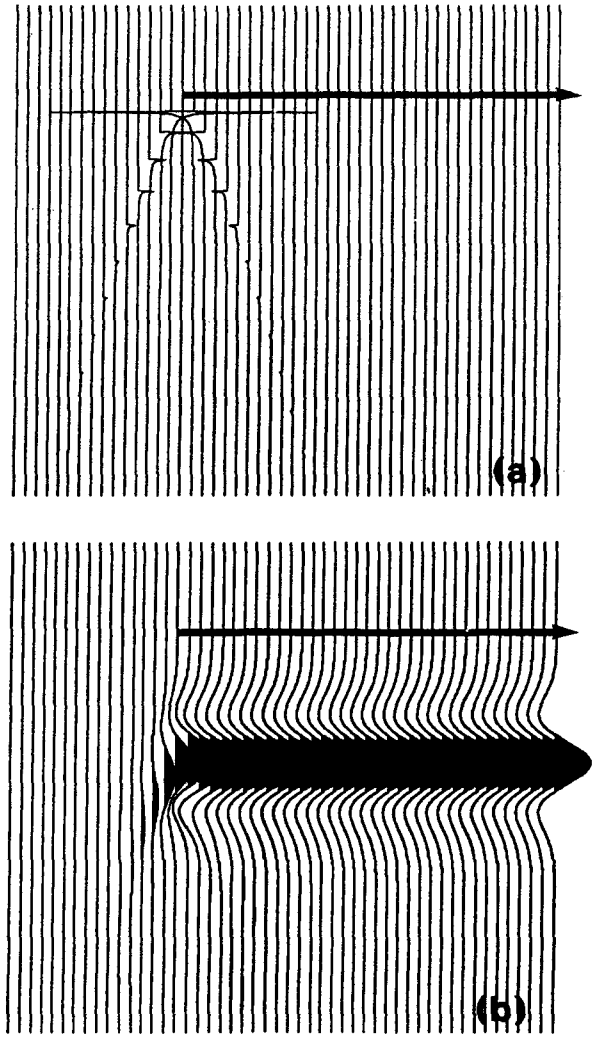

Figure 2.27. Seismic (reflection-diffraction) response for an infinite half-plane. (a) Reflector's cross-section, indicated by bold line, together with associated diffraction operators antisymmetric about the reflector's edge. (b) After convolution with a pseudo-causal Ricker wavelet.

The combined response predicted by equation (2.112) is illustrated in Figure 2.27 before and after convolution with a discretely sampled Ricker wavelet $w(t - 1.25\,T_d)$, defined by equation (2.31). Note, in particular, that for $T = \tau$ equation (2.109) reduces to

$$d(T) = d_T = \frac{1}{\Delta t}\int_T^{T+\Delta t/2} D(t)\,dt, \tag{2.114}$$

yielding

$$\begin{aligned} d_T = \frac{-1}{2\Delta t\tau\,|\tau_x|\,(\tau^2-\tau_x^2)}\Bigg\{ & 2|\tau_x|\sin^{-1}\left[\frac{\tau}{\Delta t/2+T}\right] - \tau\sin^{-1}\left[\frac{\tau^2+c(T+\Delta t/2)}{\tau\,(\Delta t/2+T+c)}\right] \\ & -\tau\sin^{-1}\left[\frac{\tau^2-c(T+\Delta t/2)}{\tau\,(\Delta t/2+T-c)}\right] - 2\,|\tau_x|\sin^{-1}\left[\frac{\tau}{T}\right] \\ & +\tau\sin^{-1}\left[\frac{\tau^2+cT}{\tau\,(T+c)}\right] + \tau\sin^{-1}\left[\frac{\tau^2-cT}{\tau\,(T-c)}\right]\Bigg\}. \end{aligned} \tag{2.115}$$

where, as before,

$$c = (\tau+\tau_x)^{1/2}(\tau-\tau_x)^{1/2}.$$

Now, letting $\Delta t \to 0$, we have $\tau_x \to 0$, $c \to \tau$, $\tau = t_0$ and, consequently,

$$\lim_{\Delta t\to 0} d_T = \frac{1}{2\Delta t\tau^3\tau_x}(\pi\tau) = \frac{\pi}{2\Delta t\,t_0^2\tau_x}. \tag{2.116}$$

On substituting the foregoing result in equation (2.112) and recognizing that $4r_0^2/\alpha^2 = t_0^2$, we obtain

$$\begin{aligned} \varphi_{X,T} &= w_T * \left\{\frac{\Delta t\mathcal{R}}{2r_0}\left[\frac{1}{\Delta t} - \frac{4r_0^2\tau_x}{\pi\alpha^2}\left(\frac{\pi}{2\Delta t\,t_0^2\tau_x}\right)\right]\right\} \\ &= w_T * \left\{\frac{\Delta t\mathcal{R}}{2r_0}\left[\frac{1}{\Delta t} - \frac{1}{2\Delta t}\right]\right\}, \end{aligned} \tag{2.117}$$

thus, revealing that the diffraction response measured by a source-detector pair positioned directly above the edge of an infinite half-plane is an impulse of opposite polarity and half the amplitude of the associated reflection response. As we shall demonstrate, the polarity reversal or 180 degree phase shift is constant from one side of the discontinuity to the other. In other words, our Kirchhoff-based diffraction model predicts that the diffraction response of an infinite half-plane is perfectly anti-symmetric about the edge. While this is an adequate approximation for present purposes, exact solutions (Dalton and Yedlin,

1989) reveal a slight asymmetry with stronger amplitudes detected over the reflector. It should also be emphasized that while the foregoing development assumes a coincident source-detector, a study by Trorey (1977) concluded that the influence of nonzero offset is practically negligible, suggesting that the response depends principally on the source-detector midpoint.

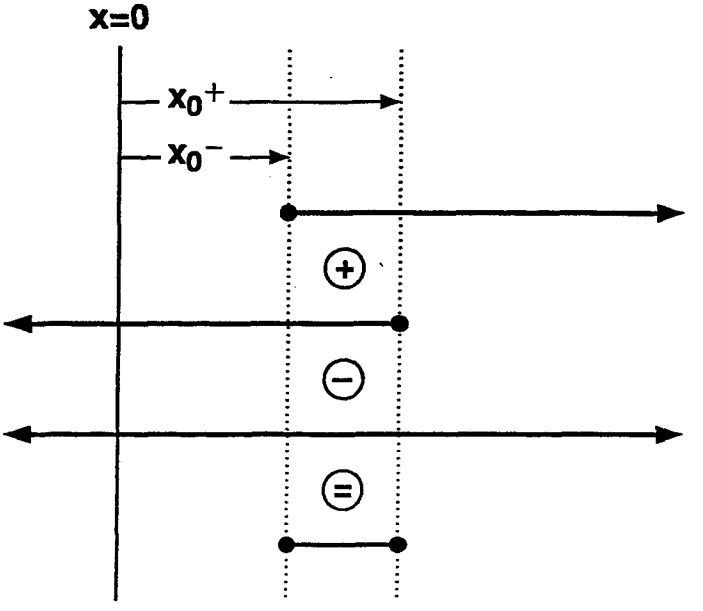

Figure 2.28. Derivation of infinite strip reflector as the sum of two infinite half-planes less an infinite plane reflector. The two infinite half-planes have edges at $x = x_0^+$ and $x = x_0^-$ and extend in positive and negative directions, respectively.

We are now prepared to illustrate the Fresnel zone criterion for spatial resolution in connection with the response of an infinite reflecting strip having finite width and strike normal to the line of survey. As illustrated in Figure 2.28, the associated response follows from foregoing development as the net response of two infinite half-planes less that of an infinite plane reflector. The combined response of two overlapping half-planes extending in opposite directions and having edges at x_0^- and x_0^+ follows from equations (2.112) and (2.113) as

$$\varphi_{X,T} = w_T * \left\{ \Omega^-_{X,T} + \Omega^+_{X,T} \right\}, \tag{2.118}$$

where superscripts - and + indicate that $\Omega_{X,T}$ is evaluated for parameter values $x_0 = x_0^-$ and $x_0 = x_0^+$, respectively. Consequently, recalling the response of an infinite plane reflector

given by equation (2.98) and using equation (2.110), we obtain

$$\begin{aligned}\varphi_{X,T} &= w_T * \left\{ \Omega^-_{X,T} + \Omega^+_{X,T} - \frac{\Delta t \mathcal{R}}{2r_0}\,\delta_T \right\} \\ &= w_T * \left\{ \frac{\Delta t \mathcal{R}}{2r_0} \left[\left(H\left[X - x_0^-\right] + H\left[x_0^+ - X\right] - 1 \right) \delta_T \right.\right. \\ &\qquad \left.\left. - \frac{4r_0^2}{\pi\alpha^2} \left(\tau_x^- H\left[T - \tau^-\right]\, d_T^- - \tau_x^+ H\left[T - \tau^+\right]\, d_T^+ \right) \right] \right\}\end{aligned} \quad , \qquad (2.119)$$

where, as above, superscripts - and + indicate evaluation of the associated function for respective parameter values $x_0 = x_0^-$ and $x_0 = x_0^+$. The result is illustrated in Figure 2.29.

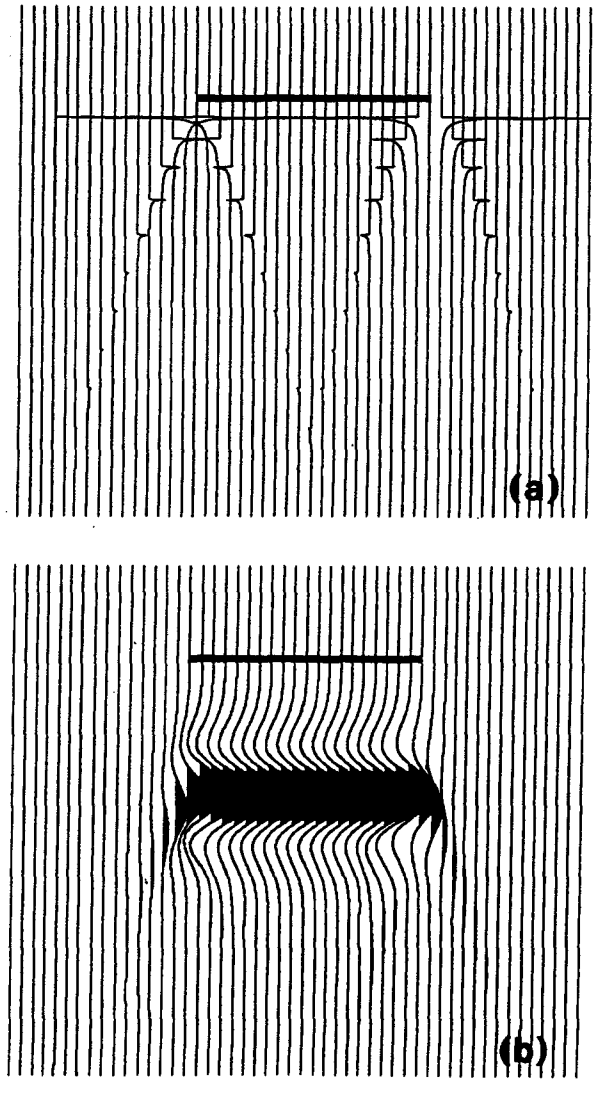

Figure 2.29. Seismic (reflection-diffraction) response for an infinite strip reflector striking in and out of the page. (a) Reflector's cross-section, indicated by bold line, together with associated diffraction operators anti-symmetric about the strip's edges. (b) After convolution with a pseudo-causal Ricker wavelet.

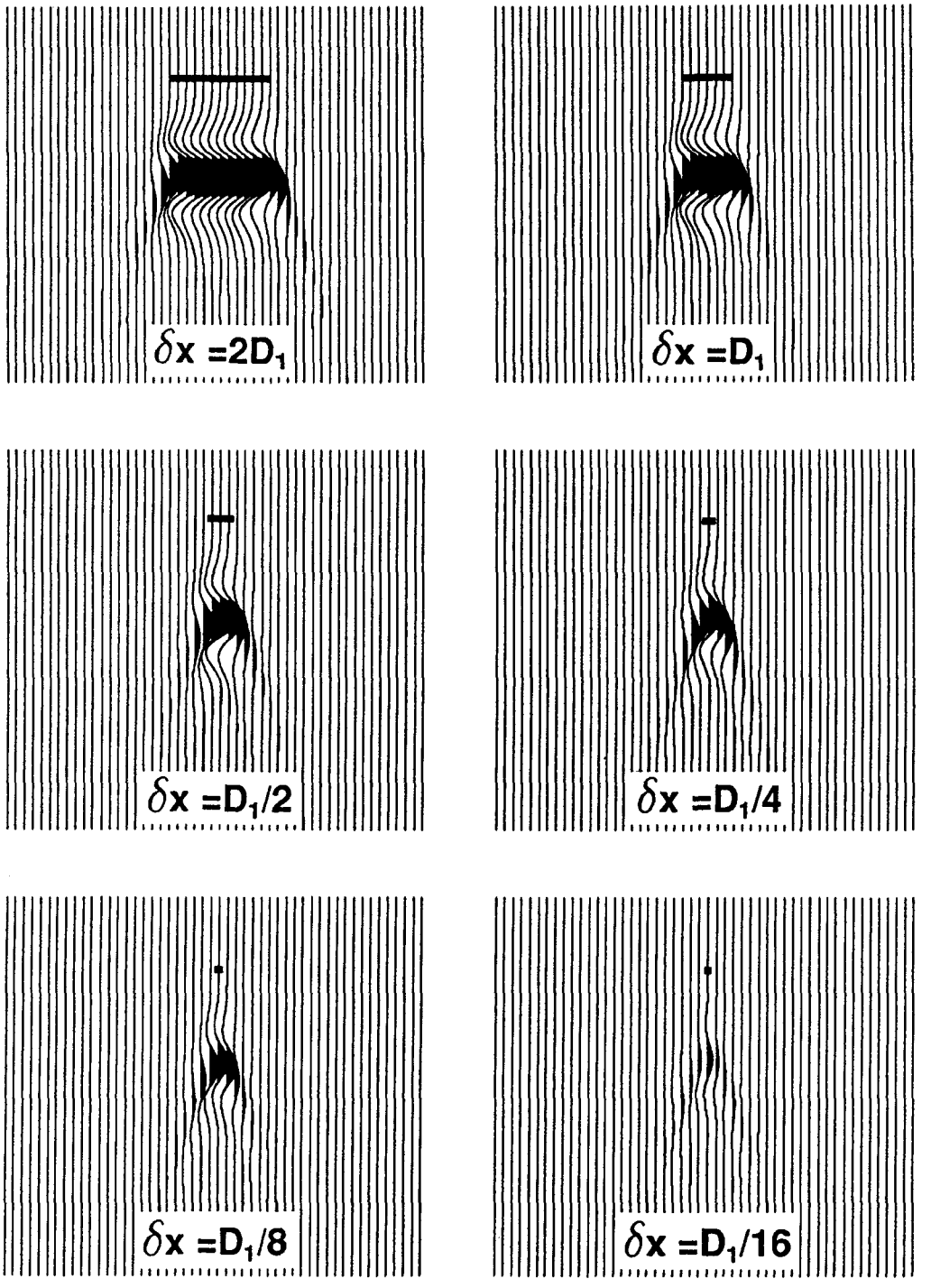

Figure 2.30. Seismic (reflection-diffraction) response for infinite strip reflector's having widths $\delta x = 2D_1$, D_1, $D_1/2$, $D_1/4$, $D_1/8$ and $D_1/16$, where D_1 denotes diameter of the first half-dominant-period Fresnel zone. For the case illustrated, $D_1 = 1.1\lambda_d$.

Responses predicted by the previous expression for infinite strip reflectors having widths $\delta x = 2D_1$, D_1, $D_1/2$, $D_1/4$, $D_1/8$ and $D_1/16$ are displayed in Figure 2.30, where D_1 is the diameter of the corresponding first half-dominant-period Fresnel zone. The nature of these synthetic responses is consistent with the foregoing analysis of circular reflectors. Reflecting strips having widths comparable to or exceeding the diameter of the first Fresnel zone yield responses that are approximate images of the reflector's cross-section. Despite smearing due to the superposition of edge diffractions associated with terminations of the reflection response, the relector's flat-lying geometry and approximate width are easily inferred from the resulting image. In other words, the reflector is resolved. In contrast, as the reflector's width becomes less than the Fresnel zone diameter, the two mirror-image edge diffractions coalesce to produce a composite diffraction event that eventually cancels the associated reflection response. As illustrated by Figure 2.30, seismic images of reflectors having widths less than about half the Fresnel zone diameter no longer reveal the reflector's geometry. The associated event is indistinguishable from a so-called point diffraction and remains unaltered with further reduction of the reflector's width. Continued reduction of the reflector's width only reduces the event's amplitude until it is no longer detectable and, finally, vanishes as the reflector's width approaches zero. Consequently, while Fresnel zone diameter may be viewed as a conservative estimate of spatial resolution, a limiting criterion is established by examining the interference of edge diffractions beyond the margins of the reflector. As illustrated in Figure 2.31, a coincident source-detector pair at arbitrary position x registers the onset of edge diffractions from $x = x_0^-$ and $x = x_0^+$ at times

$$\tau^-(x) = \frac{2}{\alpha}\left[(x - x_0^-)^2 + r_0^2\right]^{1/2} \tag{2.120}$$

and

$$\tau^+(x) = \frac{2}{\alpha}\left[(x - x_0^+)^2 + r_0^2\right]^{1/2}, \tag{2.121}$$

respectively. In particular, we consider the the time lag $\delta t_d(x) = |\tau^-(x) - \tau^+(x)|$ for offsets $|x - x_0^-|$ and $|x - x_0^+|$ large compared with reflector depth r_0.

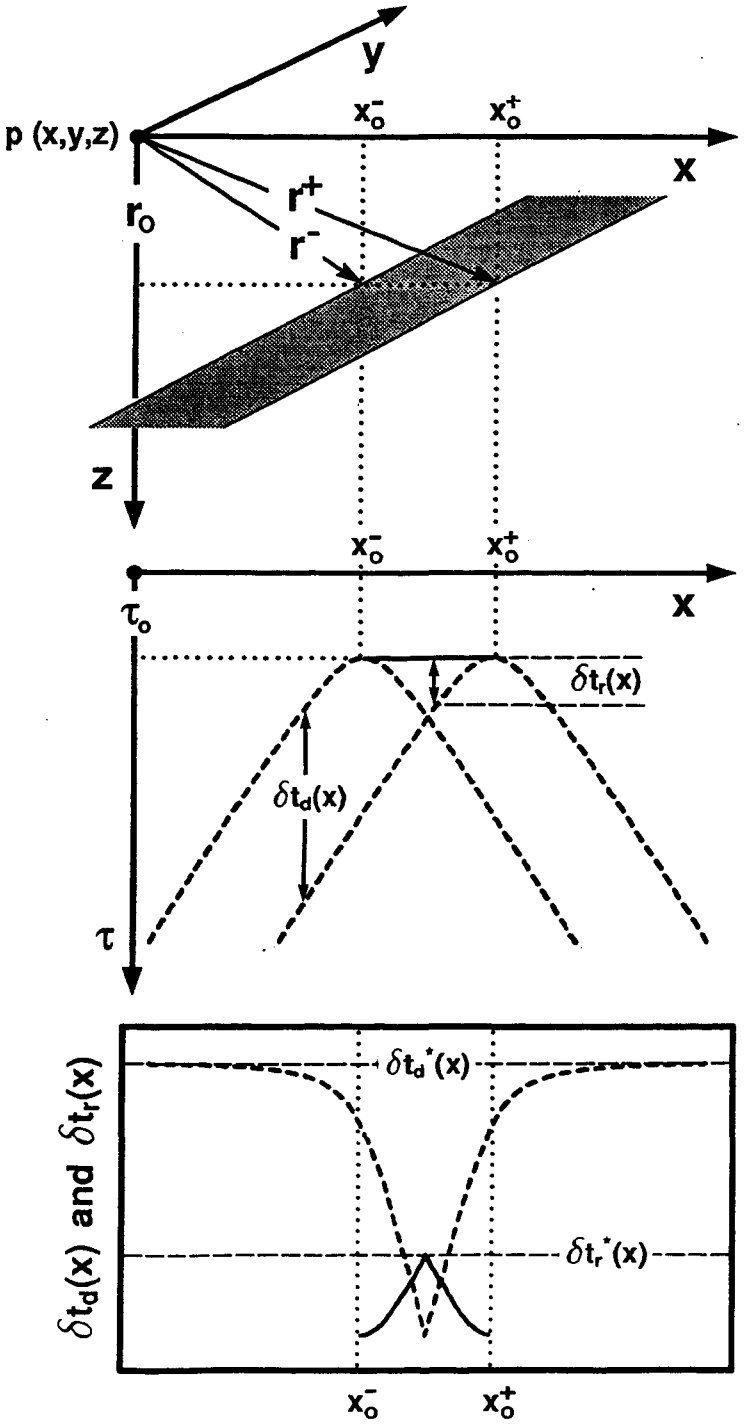

Figure 2.31. Diagrammatic illustration of Fresnel zone $\delta t_r^* \geq T_t$ and limiting $\delta t_d^* \geq T_t$ criteria for spatial resolution. Both criteria are extensions of Rayleigh's temporal resolution criterion, requiring that the time lag separating two identical wavelets must exceed the tuning thickness $T_t = T_d/2 = \lambda_d/2\alpha$. The Fresnel zone criterion considers the time lag $\delta t_r(x)$ between reflected and diffracted arrivals. The limiting criterion examines the time lag $\delta t_d(x)$ separating diffracted arrivals from the reflector's two edges.

Under the foregoing condition, we have

$$\tau^{-}(x) \approx \frac{2}{\alpha}\left|x - x_0^{-}\right|,$$

$$\tau^{+}(x) \approx \frac{2}{\alpha}\left|x - x_0^{+}\right|$$

and, consequently, the critical time lag

$$\begin{aligned}\delta t_d^{*} &= \frac{2}{\alpha}\left[\left|x - x_0^{-}\right| - \left|x - x_0^{+}\right|\right] \\ &= \frac{2}{\alpha}\left(x_0^{+} - x_0^{-}\right) \\ &= \frac{2}{\alpha}\delta x\end{aligned}, \tag{2.122}$$

where $\delta x = (x_0^{+} - x_0^{-})$ represents the reflector's width. As illustrated in Figure 2.31, this asymptotic time lag is a maximum and thus, according to Rayleigh's criterion $\delta t_d^{*} \geq T_t$, separate edge diffractions are resolved for $\delta x \geq \lambda_d/4$.

The Fresnel zone criterion is also illustrated in Figure 2.31. Recall that according to the latter, the reflector is resolved if, and only if, the time lag separating reflected and diffracted arrivals registered by a coincident source-detector situated above the reflector's midpoint is equal to or exceeds Rayleigh's criterion $T_t = T_d/2 = \lambda_d/2\alpha$. In other words, for a coincident source-detector positioned above the reflector, we consider the time lags

$$\begin{aligned}\delta t_r^{-}(x) &= \tau^{-}(x) - \tau_0 \\ &= \frac{2}{\alpha}\left[\left(x - x_0^{-}\right)^2 + r_0^2\right]^{1/2} - \tau_0\end{aligned} \tag{2.123}$$

and

$$\begin{aligned}\delta t_r^{+}(x) &= \tau^{+}(x) - \tau_0 \\ &= \frac{2}{\alpha}\left[\left(x - x_0^{+}\right)^2 + r_0^2\right]^{1/2} - \tau_0\end{aligned}, \tag{2.124}$$

where $\tau_0 = 2r_0/\alpha$. As illustrated in Figure 2.31, $\delta t_r^{-}(x)$ and $\delta t_r^{+}(x)$ form an envelope function

$$\delta t_r(x) = \begin{cases} \delta t_r^{-}(x), & x_0^{-} \leq x < x_m; \\ \delta t_r^{*}, & x = x_m; \\ \delta t_r^{+}(x), & x_m < x \leq x_0^{+} \end{cases},$$

where $x_m = (x_0^- + x_0^+)/2$ represents the reflector's midpoint and, thus,

$$\delta t_r^* = \delta t_r^-(x_m) = \delta t_r^+(x_m) = \frac{2}{\alpha}\left\{\left[\left(\frac{\delta x}{2}\right)^2 + r_0^2\right]^{1/2} - r_0\right\}. \tag{2.125}$$

denotes the critical time lag associated with the Fresnel zone criterion. Specifically, Rayleigh's criterion $\delta t_r^* \geq T_t$ leads to the associated restriction

$$\begin{aligned}\left[\left(\frac{\delta x}{2}\right)^2 + r_0^2\right]^{1/2} - r_0 &\geq \frac{\lambda_d}{4} \\ \left(\frac{\delta x}{2}\right)^2 + r_0^2 &\geq \left(\frac{\lambda_d}{4} + r_0\right)^2 \\ \delta x^2 &\geq \left(\frac{\lambda_d}{2}\right)^2 + 2r_0\lambda_d = D_1^2\end{aligned} \tag{2.126}$$

and, consequently, reflected and diffracted arrivals are resolved for $\delta x \geq D_1$.

Practically speaking, the limiting criterion $\delta x \geq \lambda_d/4$ represents an upper limit on spatial resolution and is often an overestimate, especially for deeper targets in higher velocity media at lower frequencies. True spatial resolution lies somewhere between $\delta x^* = \lambda_d/4$ and the Fresnel zone diameter $\delta x^* = D_1 = \sqrt{(\lambda_d/2)^2 + 2r_0\lambda_d}$ and depends on the nature of the target. In particular, for a finite width reflecting strip as illustrated in Figure 2.30, the transition from detection to resolution is perhaps most easily identified by observing the convergence of the observed response toward a point diffraction pattern, suggesting resolution approaching the limiting criterion $\delta x^* = \lambda_d/4$. Figure 2.32, on the other hand, portrays the converse scenario where two infinite half-planes are separated by an interval corresponding to the respective reflector width in the previous Figure. Here, spatial resolution is effectively a question of reflector continuity, suggesting that the Fresnel criterion $\delta x^* = D_1$ is more natural estimate of the resolution limit.

Consequently, as in the case of temporal resolution, we shall adopt a hybrid resolution criterion stipulating that the spatial resolution limit resides within the range bounded by the Fresnel zone diameter $D_1 = \sqrt{(\lambda_d/2)^2 + 2r_0\lambda_d}$ and the limiting criterion $\lambda_d/4$. Figure 2.33 summarizes the foregoing criterion for spatial resolution of archaeological targets.

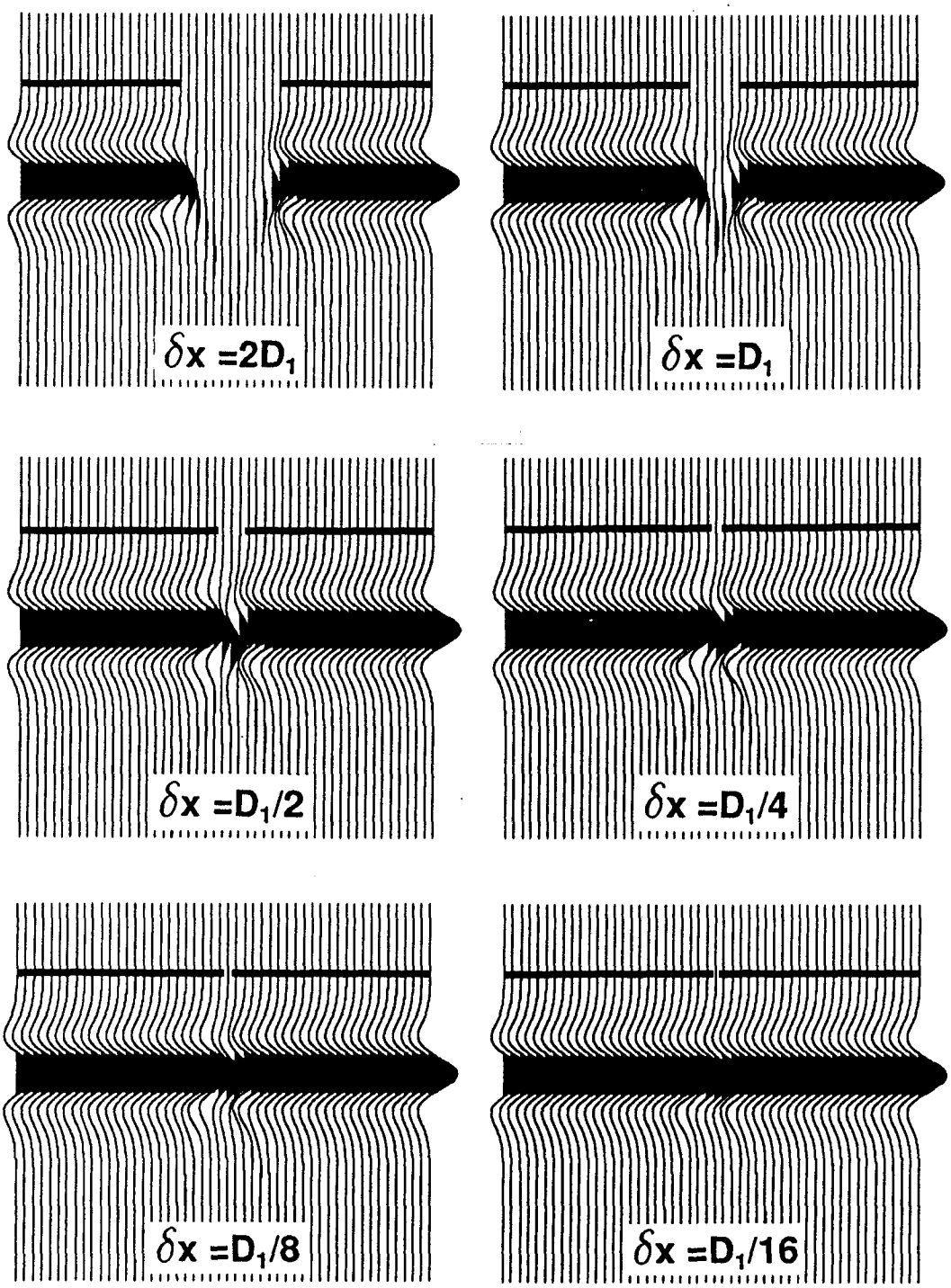

Figure 2.32. Seismic (reflection-diffraction) response for two infinite half-planes separated by $\delta x = 2D_1$, D_1, $D_1/2$, $D_1/4$, $D_1/8$ and $D_1/16$, where D_1 denotes diameter of the first half-dominant-period Fresnel zone. For the case illustrated, $D_1 = 1.1\lambda_d$.

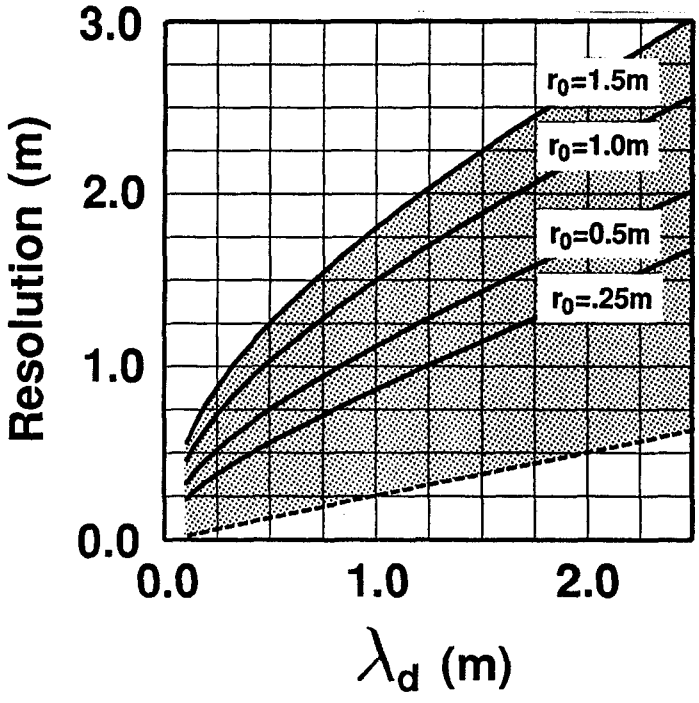

Figure 2.33. Hybrid spatial resolution criterion as a function of dominant wavelength $\lambda_d = \alpha_0/f_d$ with normal-incidence range as a parameter. For a given range r_0, the resolution limit lies between the associated Fresnel zone diameter $\delta x^* = D_1$ (solid curve) and the limiting criterion $\delta x^* = \lambda_d/4$ (dashed curve).

Fresnel zone diameter is displayed as a function of dominant wavelength with target range r_0 as a parameter. The limiting criterion $\delta x^* = \lambda_d/4$ is, of course, independent of reflector range. The minimum dominant wavelength considered $\lambda_d = \alpha_0/f_d = 10.0$ cm corresponds to end-member values $f_d = 1000$ Hz and $\alpha_0 = 100\,\mathrm{ms}^{-1}$ examined in Figure 2.17. The Fresnel zone criterion has a corresponding minimum value of approximately 25 cm at a target range of 25.0 cm, increasing to roughly 50 cm at a range of 1.5 m. The lower limit of spatial resolution degrades rapidly as dominant wavelength increases, reaching 1.0 m at just under $\lambda_d = 30$ cm for $r_0 = 1.5$ m and approximately $\lambda_d = 1.25$ m for $r_0 = 25.0$ cm. Although comparison of Figures 2.17 and 2.33 reveals that spatial resolution is significantly more restrictive than temporal resolution, the near-surface nature of archaeological targets is also favorable for achieving high spatial resolution. In addition to a relatively short dominant wavelength due to reasons discussed in connection with Figure 2.17, the shallow

nature of archaeological features ensures a relatively "focused" Fresnel zone. As a result, we conclude that the seismic methods are indeed capable of resolution, both temporal and spatial, on the scale of archaeological interest.

2.4 Concluding Remarks:

Beyond intrinsic detection and resolution limits associated with data acquisition and recording, a variety of computer-based procedures have been devised for post-acquisition resolution enhancement. In particular, deconvolution (Yilmaz, 1987; Ziolkowski, 1984) seeks to improve temporal resolution by inverting the convolution operation represented by equation (2.30) to yield the corresponding reflectivity series with perfect resolution. In practice, this goal is approximately attained by modifying characteristics of the source wavelet. Specifically, in accordance with foregoing findings, deconvolution enhances temporal resolution by balancing or whitening the wavelet's amplitude spectrum and zeroing its phase. In view of the unifying connection between spatial and temporal resolution criteria, it is clear that deconvolution also provides for concomitant enhancement of spatial resolution. In addition, a second category of data processing techniques, known collectively as migration methods (Yilmaz, 1987; Claerbout, 1985), correct seismic images for distortions caused by structural complexities and discontinuities. In particular, migration collapses diffraction events like those illustrated in Figures 2.27 and 2.28, associated with edges of the reflecting strip. By redistributing diffracted energy at its source, migration alleviates the blurring or smearing influence of diffraction to yield a sharper image of subsurface structure. In terms of the Fresnel zone criterion for spatial resolution, migration may be viewed as a de-propagation or reverse extrapolation of the wavefield sampled by detectors at the surface to an arbitrary reference plane beneath the surface. As a result, migration reduces the effective sounding range to a given reflector and, consequently, the effective Fresnel zone diameter.

While it is important to recognize the potential for post-acquisition enhancement, it

must be emphasized that once a seismic sounding has been recorded, its ultimate resolving power is restricted. Although resolution can be improved to some extent by post-acquisition computer processing methods, their advantage remains limited by the bandwidth of the original signal. Consequently, the present study is restricted to assessing the intrinsic detection and resolving capacity of the acquisition system and procedures. In particular, the foregoing theoretical analysis has guided design and subsequent development of a prototype system for detection and imaging of subsurface archaeological remains. The following two chapters describe, respectively, the system and a full-scale model experiment conducted to assess its performance.

Chapter 3

INSTRUMENTATION AND SYSTEM DESIGN

In spite of their importance in geological exploration, seismic techniques, ... , have proved to be of limited value for the location of the small-scale features of interest in archaeology and are therefore not considered further.

M. S. Tite, 1972

3.1 Introduction:

As specifications of an integral system are ultimately restricted by the weakest component, generating a broad-band source pulse is only a first step toward acquiring high-resolution seismic data. Wavelet characteristics are subsequently modified during transmission, detection and recording. While effects of transmission through the subsurface are beyond our control, the influence of detection and recording instrumentation can be tailored to suit our needs. In practice, a fundamental obstacle to preserving bandwidth is the dynamic range of the recording device. Dynamic range refers to the ratio of largest to smallest signals that can be registered simultaneously and is related in practice to the number of bits comprising the seismograph's digital output. Since the relative contributions of individual frequencies comprising a seismic disturbance can differ dramatically, insufficient dynamic range may result in the loss of discrete frequency components carrying significant information but comprising a relatively small fraction of incident energy. For example, if a narrow band of frequency components are stronger than any other component by a relative amount exceeding the dynamic range, the recorded waveform will be composed entirely of frequencies within that band. Consequently, in addition to degrading resolution by restricting the effective bandwidth, the resulting seismogram is unlikely to be a faithful representation of the actual disturbance. To avoid these effects, the spectral composition of the signal must be balanced prior to recording.

While coupling of source energy to the subsurface yields a wavelet that is invariably deficient of high frequencies, further spectral imbalances arise from two principal sources. First, for practical purposes, the frequency response of the subsurface is effectively that of a low-pass filter. A combination of frequency selective absorption mechanisms attenuate high

frequency energy and together with associated dispersion cause a progressive broadening of the wavelet with increasing propagation distance. Secondly, in addition to the primary compressional wave, the source generates other modes including Rayleigh surface waves that are predominantly lower frequency and higher amplitude. Although this energy, commonly known as ground-roll, propagates at only a fraction of compressional wave speed, its direct path from source to receiver is shorter than the corresponding reflection ray-path leading to interference and corruption of the reflected wavelet at the detector.

To counteract the foregoing effects, the acquisition system must discriminate against low frequencies that are dominated by interfering ground-roll and reinforce high frequencies attenuated by the subsurface. While these aims are furthered to some extent by employing a source that yields a relatively large proportion of high frequency energy and a detector having a high-pass frequency response, spectral balancing is achieved primarily by utilizing special purpose analog filters to selectively attenuate and enhance appropriate portions of the frequency spectrum. Since the ultimate resolving power of seismic signals is limited by the bandwidth of original recordings, so called pre-emphasis filtering is performed in "real time", prior to recording, in order to take maximum advantage of available dynamic range.

Previous studies have addressed the foregoing considerations but have resulted largely in "one of a kind" systems that are either too costly or require too much technical expertise to be used widely (Dolphin et al., 1977; Ozawa and Matsuda, 1979). Our goal has been to remain relatively less complicated and use commercially available components wherever possible so that the resulting technology is accessible, cost-effective and easy to use.

3.2 System Description:

The foregoing design philosophy has guided development of a simple but effective system for acquiring high-resolution seismic images of near-surface structure. A block diagram of the resulting system is depicted in Figure 3.1.

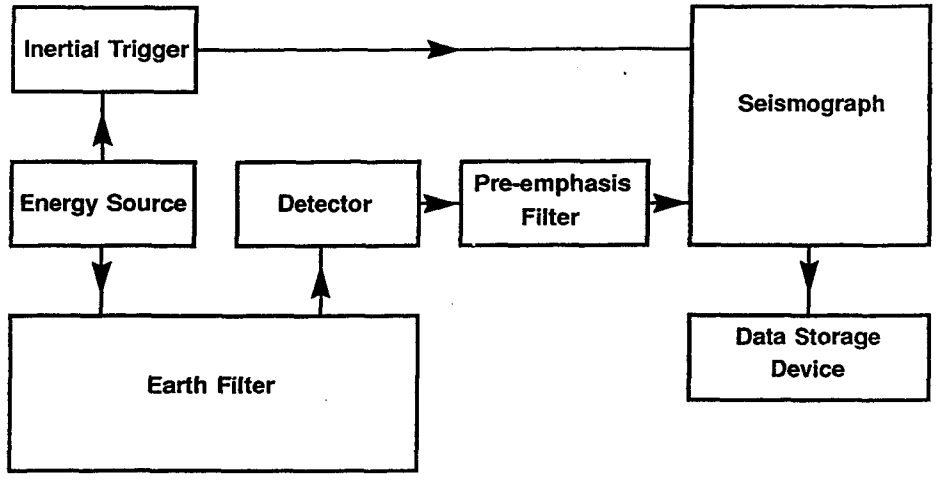

Figure 3.1. Seismic system block diagram, identifying and illustrating the configuration of sub-system components.

In general, a system may be defined as a functionally related set of distinct sub-systems interconnected in specific configuration (Lathi, 1965; Oppenheim and Willsky, 1983). At any instant a given input to the system yields a certain output determined by the characteristic response of individual sub-systems and their mutual interaction. For practical purposes, we shall treat constituent sub-systems identified in Figure 3.1 as causal, non-interacting, time-invariant linear systems.

Causality embodies the physical notion that a system cannot anticipate future inputs and, consequently, the instantaneous output of a causal system depends only on current and past inputs.

The assumption of non-interaction recognizes the practical potential of one system to significantly influence the response of another interconnected system, and holds that this interaction is negligible.

Time-invariance requires that for a given input, the system's output is invariable, independent of time. Using the notation

$$x(t) \rightarrow y(t) \tag{3.1}$$

to denote system transformation of input signal $x(t)$ to output signal $y(t)$, time-invariance implies

$$x(t-\tau) \rightarrow y(t-\tau), \tag{3.2}$$

where τ represents an arbitrary constant time shift.

Finally, linearity implies that if a weighted sum of several distinct signals comprises the system input, its output is simply the superposition of outputs arising in response to constituent inputs separately. For instance, if $x_1(t)$ and $x_2(t)$ denote two separate system inputs yielding output signals $y_1(t)$ and $y_2(t)$, that is

$$x_1(t) \rightarrow y_1(t)$$

$$x_2(t) \rightarrow y_2(t), \tag{3.3}$$

linearity requires

$$[w_1 x_1(t) + w_2 x_2(t)] \rightarrow [w_1 y_1(t) + w_2 y_2(t)], \tag{3.4}$$

where w_1 and w_2 represent arbitrary weighting constants. In effect, linearity embodies two separate properties characterizing linear systems: the scaling property

$$w_1 x_1(t) \rightarrow w_1 y_1(t)$$

$$w_2 x_2(t) \rightarrow w_2 y_2(t), \tag{3.5}$$

and the additive property

$$[x_1(t) + x_2(t)] \rightarrow [y_1(t) + y_2(t)]. \tag{3.6}$$

In principle, the behaviour of a linear time-invariant system may be described by a ordinary linear differential equation having constant coefficients. Specifically, consider the nth order linear differential equation

$$c_n \frac{d^n}{dt^n} y(t) + c_{n-1} \frac{d^{n-1}}{dt^{n-1}} y(t) + \ldots + c_1 \frac{d}{dt} y(t) + c_0 y(t) = x(t) \tag{3.7}$$

with constant coefficients $c_0, c_1, \ldots, c_{n-1}, c_n$. Utilizing the derivative property of the Fourier transform (Bracewell, 1986), we obtain the corresponding frequency domain relation

$$\left[\left(i2\pi f\right)^n c_n + \left(i2\pi f\right)^{n-1} c_{n-1} + \ldots + i2\pi f\, c_1 + c_0 \right] Y(f) = X(f), \tag{3.8}$$

where $X(f)$ and $Y(f)$ represent Fourier spectra associated system input $x(t)$ and output $y(t)$ signals, respectively.

Equivalently, we may write

$$Y(f) = S(f)X(f), \tag{3.9}$$

where the complex polynomial

$$S(f) = \left[c_0 + i2\pi f\, c_1 + \ldots + \left(i2\pi f\right)^{n-1} c_{n-1} + \left(i2\pi f\right)^{n} c_n\right]^{-1} \tag{3.10}$$

is referred to as the system transfer function. Consequently, the Fourier spectrum of the system output $Y(f)$ is given by the product of the input spectrum $X(f)$ and the system transfer function $S(f)$ or, on adopting polar notation,

$$Y(f) = |Y(f)|\, e^{i\,\Theta_y(f)} = |S(f)|\,|X(f)|\, e^{i\,[\Theta_s(f)+\Theta_x(f)]}; \tag{3.11}$$

the product of corresponding amplitude spectra and the sum of associated phase spectra. Finally on applying the convolution theorem of the Fourier transform to equation 3.9, we obtain the equivalent time domain relation

$$y(t) = s(t) * x(t), \tag{3.12}$$

where

$$s(t) = \int_{-\infty}^{+\infty} S(f)\, e^{i2\pi f t}\, df, \tag{3.13}$$

referred to as the system impulse response, is the output generated by the system in response to an impulsive input $x(t) = \delta(t)$. Here $\delta(t)$ denotes the Dirac delta function, having defining properties

$$\delta(t) = 0; \qquad t \neq 0$$

and

$$\int_{-\infty}^{\infty} \delta(t)\, dt = 1.$$

It follows from foregoing analysis that if two sub-systems are cascaded in series so that the output of the first system $[s_1(t) * x(t)]$ serves as input to the second system, the net system output will be $y(t) = s_2(t) * [s_1(t) * x(t)]$ or, in general, for n sub-systems in series configuration

$$y(t) = [s_n(t) * s_{n-1}(t) * \ldots * s_2(t) * s_1(t)] * x(t). \tag{3.14}$$

Here, we have appealed to the associative property of convolution $a * (b * c) = (a * b) * c$. The equivalent frequency domain relation is

$$Y(f) = \left[S_n(f)\, S_{n-1}(f) \ldots S_2(f)\, S_1(f)\right] X(f) \tag{3.15}$$

or

$$Y(f) = \Sigma(f)\, X(f), \tag{3.16}$$

where

$$\Sigma(f) = S_n(f)\, S_{n-1}(f) \ldots S_2(f)\, S_1(f) \tag{3.17}$$

represents the net system transfer function or "frequency response".

Similarly, using the distributive property of convolution $(b * a)+(c * a)=(b + c) * a$, the net output for n sub-systems in parallel configuration is

$$y(t) = [s_n(t) + s_{n-1}(t) + \ldots + s_2(t) + s_1(t)] * x(t) \tag{3.18}$$

or, equivalently,

$$Y(f) = \left[S_n(f) + S_{n-1}(f) + \ldots + S_2(f) + S_1(f)\right] X(f), \tag{3.19}$$

implying the net system transfer function

$$\Sigma(f) = S_n(f) + S_{n-1}(f) + \ldots + S_2(f) + S_1(f) \tag{3.20}$$

Neglecting inertial trigger and data storage components, the system depicted in Figure 3 comprises five linear time-invariant sub-systems cascaded in series configuration and, consequently, a net system response given by

$$\begin{aligned} \Sigma(f) &= S_s(f)\, S_e(f)\, S_d(f)\, S_f(f)\, S_r(f) \\ &= \left[|S_s(f)|\, |S_e(f)|\, |S_d(f)|\, |S_f(f)|\, |S_r(f)|\right] e^{i\left[\Theta_s(f)+\Theta_e(f)+\Theta_d(f)+\Theta_f(f)+\Theta_r(f)\right]}, \end{aligned} \tag{3.21}$$

where subscripts s, e, d, f and r signify source, earth filter, detector, pre-emphasis filter and recorder sub-systems, respectively. In accordance with the foregoing expression, we have sought to achieve optimum resolving power by selecting instrumentation having complementary frequency characteristics which, in connection with the low-pass earth filter

response, yield a smoothly varying, broad-band, minimum phase wavelet. The following sections describe sub-system components and give a general characterization of associated amplitude and phase spectra.

3.2.1 Energy Source

Until recently, seismic exploration of the shallow subsurface relied entirely upon surface impact sources; in particular, the venerable sledge hammer. Although adequate for acquiring first break refraction data, impact sources are not well suited for reflection sounding, where the emphasis is on discrimination and resolution of interfering arrivals. Elastic wave energy radiated by a surface impact source is partitioned between body and surface waves in accordance with coupling characteristics and the mechanical properties of the subsurface. Miller and Pursey (1955) examined the radiation field of a circular disk vibrating normally to the free-surface of a homogeneous, isotropic, linearly elastic half-space. For a Poissson's ratio $\sigma = 0.25$ ($\alpha/\beta = \sqrt{3}$), theory predicts the following distribution: 7% dilatational; 26% rotational; 67% surface. Despite a modest increase and subsequent reduction in the fraction of energy imparted to dilatational waves as Poisson's ratio increases to σ=0.333 and beyond (Mooney, 1976), the majority of energy continues to be propagated by surface waves, regardless of the medium's rigidity. Consequently, since ground-roll interference constitutes a principal obstacle to achieving a balanced spectrum, surface impact sources generate an intolerably high proportion of surface wave energy for high-resolution reflection applications. Rather, we require an energy source that produces as large a proportion of dilatational energy as possible. Toward this end, we turn our attention to explosive energy sources that, ideally, generate a purely dilatational wavefield, propagating radially outward from the source region.

Experimental observations (O'Brien, 1969) suggest that the seismic disturbance generated by an explosive source is consistent with a so-called "equivalent radiator" model (Sharpe, 1942; Blake, 1952). Ignoring nonlinear processes occurring in the immediate vicinity of the explosion, the source region is treated as a spherical cavity having radius

equivalent to the range at which tensile stresses associated with the explosive disturbance become less than the tensile strength of the host medium. In other words, the radius of the equivalent radiator R is defined such that the theory of linear elasticity is valid for $r \geq R$. An explosive disturbance is modelled by specifying a time-dependent cavity pressure $p(t)$ and seeking the corresponding solution of the elastodynamic wave equation which satisfies the boundary condition that stress within the host medium reduces to applied cavity pressure on the radiator's surface. Assuming an infinite medium, resulting particle motion is everywhere radial and irrotational.

In particular, on specifying a purely impulsive forcing

$$p(t) = \delta(t), \tag{3.22}$$

where $\delta(t)$ denotes the Dirac delta function, and invoking the radiation condition, the resulting particle displacement has the form

$$s_i(r,t) = \frac{H(t-\tau)}{\rho\alpha\sqrt{1-\gamma^2}} \left(\frac{R}{r}\right) \left\{\cos\left[\omega_0(t-\tau)+\phi_0\right] + \frac{R}{2\gamma r}\sin\left[\omega_0(t-\tau)\right]\right\} e^{-\alpha_0(t-\tau)} \tag{3.23}$$

where $H(t)$ is the Heaviside step function, $\tau = (r-R)/\alpha$ is a parameter (transit time to observation range r), $\gamma = \beta/\alpha$, $\alpha_0 = (2\beta/R)\gamma$, $\omega_0 = (2\beta/R)\sqrt{1-\gamma^2}$ and $\phi_0 = \tan^{-1}(\alpha_0/\omega_0)$ is a constant phase shift (Gurvich, 1965; Aldridge, 1993). Note that in immediate proximity to the source cavity ($r << R/2\gamma$), the second term in brackets is dominant and a so-called "near-field" approximation to the true particle displacement is obtained by ignoring the contribution of the first term. Conversely, at large distances from the source region ($r >> R/2\gamma$), the second term is practically insignificant and may be ignored, leading to a "far-field" approximation. For present purposes, it is appropriate to retain the general expression.

The corresponding spectrum or transfer function is

$$S_i(r,f) = \frac{1}{i\,2\pi}\left(\frac{1}{\rho\alpha}\right)\left(\frac{R}{r}\right)\left[\frac{f-Z_1}{(f-P_1)(f-P_2)}\right] e^{-i\,2\pi f r}, \tag{3.24}$$

where

$$Z_1 = \frac{-\alpha}{i2\pi r}$$

and

$$P_1 = \frac{\beta}{\pi R}\left[\sqrt{1-\gamma^2}+i\gamma\right], \qquad P_2 = \frac{\beta}{\pi R}\left[-\sqrt{1-\gamma^2}+i\gamma\right].$$

Normalized radiator impulse responses and associated amplitude and phase spectra have been computed and are displayed in Figures 3.2 and 3.3 for a fixed cavity radius of R=0.1 m, velocity ratio γ=.417 (σ=0.395) and observation ranges r=R=0.1 m and r=0.5 m (the latter value being representative of acquisition geometries employed for model studies described in the following chapter). Near-field and Far-field responses are also displayed for comparison. Results indicate that for R/r = 0.1/0.5 = 0.2, the radiator's impulse response is effectively "far-field". Even at the equivalent cavity radius R/r = 0.1/0.1 = 1.0, the response shows substantial contributions from both near-field and far-field components. Compared with the near-field response in Figure 3.3, the far-field response is characterized by a relative reduction in spectral content below the peak frequency and an attendant enhancement of higher frequencies. Peak frequency and bandwidth are not strongly influenced by the ratio of cavity radius to observation range (R/r).

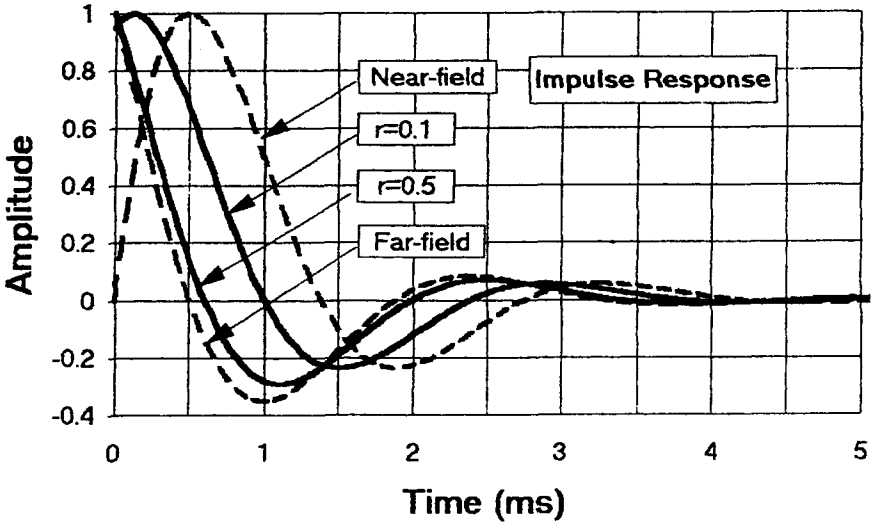

Figure 3.2. Spherical radiator impulse responses with observation range r as parameter. Dashed curves represent limiting near-field and far-field responses. Equivalent cavity radius R=0.1 m is constant.

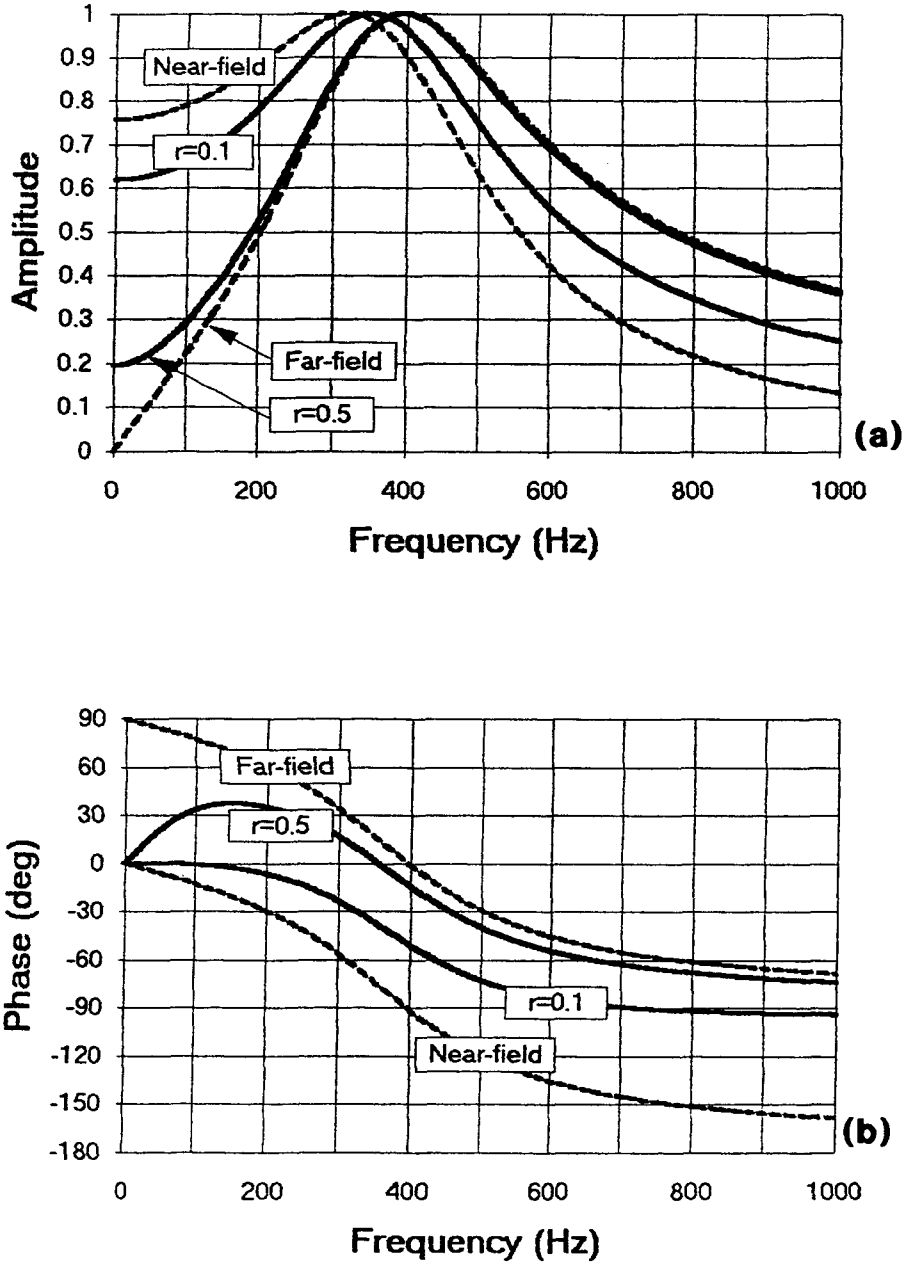

Figure 3.3. Influence of observation range on spherical radiator frequency response: (a) amplitude spectra, (b) phase spectra with observation range r as parameter. Dashed curves rep[resent limiting near-field and far-field responses. Equivalent cavity radius R=0.1 m is constant.

Equivalent cavity radius is a more critical factor as illustrated in Figure 3.4. Here, normalized spectra are displayed for cavity radii of R=0.05, 0.1, 0.2 and 0.5 m with the ratio of cavity radius to observation range fixed at R/r=0.2 and $\gamma = 0.417$ (σ=0.395). It is evident that spectral centroid decreases with increasing cavity radius and, consequently, since effective cavity radius increases in proportion to the cube root of charge weight (O'Brien, 1957; Gurvich, 1965), smaller charges produce source disturbances that are relatively rich in high frequencies. Moreover, as the velocity ratio $\gamma = \beta/\alpha$ decreases (increasing Poisson's ratio - decreasing rigidity), corresponding amplitude spectra become narrower and peak at lower frequency. This behaviour is illustrated in Figure 3.5 for $\gamma = \beta/\alpha$=0.333, 0.417, 0.500 and 0.587 (σ=0.438, 0.395, 0.333 and 0.242). Thus, broad-band, high frequency source wavelets are generally associated with smaller charges in relatively rigid media.

To model the particle displacement field radiated by an explosive source, we must further specify a time-dependent forcing function p(r=R,t), describing the outward normal pressure applied to the interior surface of the spherical cavity. The resulting particle displacement field is obtained by convolving this forcing function with the radiator's impulse response or, alternatively, by multiplying the radiator's transfer function $S_i(r,f)$ in equation 3.24 by the Fourier transform of the forcing function

$$P(f) = \int_{-\infty}^{+\infty} p(t)\, e^{-i2\pi ft}\, dt,$$

to yield

$$S_s(f) = P(f) * S_i(f). \tag{3.25}$$

For example, consider the simple forcing function

$$p(t) = p_0\, H(t)\, e^{-\kappa t}, \tag{3.26}$$

having Fourier spectrum

$$\begin{aligned} P(f) &= \frac{p_0}{\kappa + i2\pi f} \\ &= p_0 \left[\left(\frac{\kappa}{\kappa^2 + 4\pi^2 f^2} \right) - i \left(\frac{2\pi}{\kappa^2 + 4\pi^2 f^2} \right) \right]. \end{aligned} \tag{3.27}$$

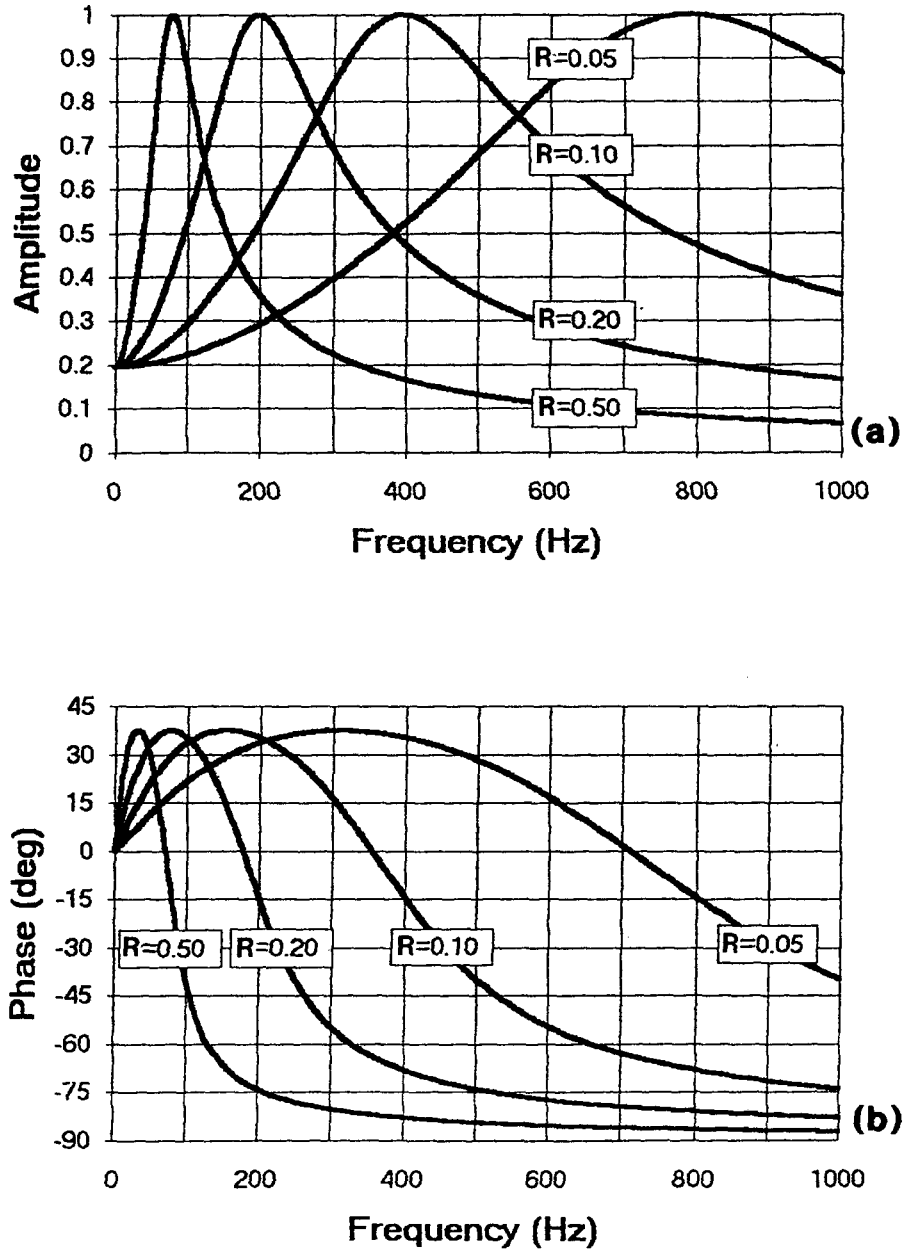

Figure 3.4. Influence of equivalent cavity radius on spherical radiator frequency response: (a) amplitude spectra, (b) phase spectra with equivalent cavity radius R as parameter. The ratio of cavity radius to observation range R/r=0.2 and the velocity ratio γ=0.417 are constant. Peak amplitude increases with increasing cavity radius.

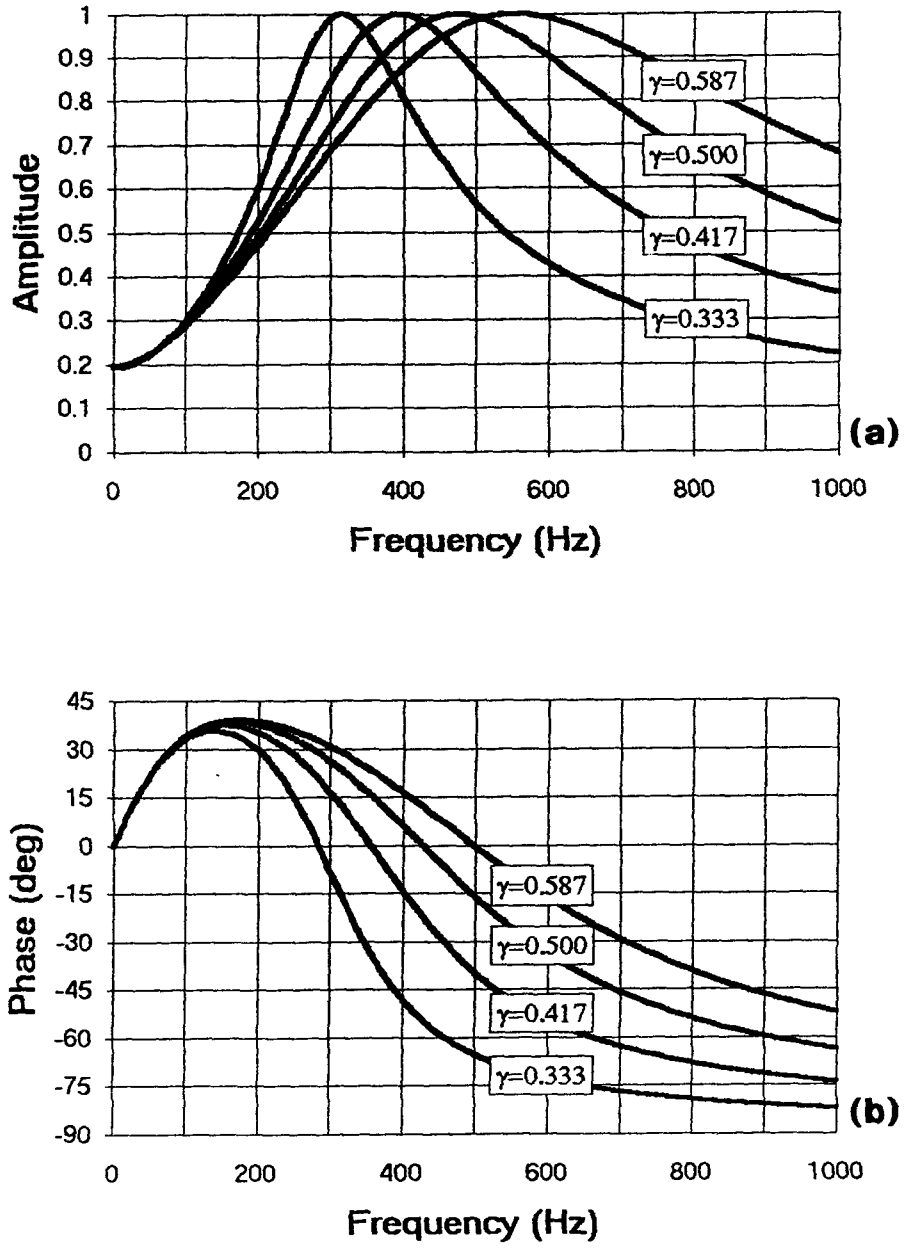

Figure 3.5. Influence of material rigidity on spherical radiator frequency response: (a) amplitude spectra, (b) phase spectra with ratio of shear to compressional wavespeed γ as parameter. The ratio of cavity radius to observation range R/r=0.2 is constant. Peak amplitude increases with decreasing rigidity (increasing γ).

Figure 3.6 displays applied pressure functions of this form, corresponding particle displacement waveforms

$$\begin{aligned} s_s(t) &= p(t) * s_i(t) \\ &= \int_{-\infty}^{+\infty} P(f)\, S(f)\, e^{i2\pi ft}\, df \end{aligned} \tag{3.28}$$

and associated velocity waveforms for $p_0 = 1$ and a range of decay constants: κ=500.0, 1000.0 and 2500.0. An obvious shortcoming of this forcing function is its instantaneous onset which leads to a discontinuous and, consequently, "non-physical" particle velocity waveform.

Sharp(1942) suggested the more realistic forcing function

$$p(t) = p_0 \left(e^{-\kappa t} - e^{-\eta t}\right), \tag{3.29}$$

having both finite rise-time and duration. The associated Fourier spectrum is given by

$$\begin{aligned} P(f) &= p_0 \left(\frac{1}{\kappa + i2\pi f} - \frac{1}{\eta + i2\pi f}\right) \\ &= p_0 \left[\left(\frac{\kappa}{\kappa^2 + 4\pi^2 f^2} - \frac{\eta}{\kappa^2 + 4\pi^2 f^2}\right) - i2\pi f \left(\frac{1}{\kappa^2 + 4\pi^2 f^2} + \frac{1}{\eta^2 + 4\pi^2 f^2}\right)\right]. \end{aligned} \tag{3.30}$$

Figure 3.7 displays forcing functions of this type for $p_0 = 1$ and the same decay constants κ=500.0, 1000.0 and 2500.0 used in Figure 3.6. Corresponding rise-time constants are $\eta = 3\kappa$= 1500.0, 3000.0 and 7500.0. Note that, in this case, associated particle velocity waveforms are well-behaved, continuous functions.

Moreover, on interpreting Z_1 as a zero, and P_1 and P_2 as poles of equation (3.24) for a complex valued frequency, and observing that all three are located in the upper half of the complex frequency plane, it follows that the spherical radiator impulse response is causal and minimum phase. Consequently, since prescribed cavity pressure functions given by equations (3.27) and (3.29) are also minimum delay (O'Brien, 1963), resulting particle displacement waveforms are also minimum phase and, thus, possess optimum resolution properties as discussed in Chapter 2 (Appendix 2.9).

Finally, recalling that the foregoing development assumes an explosive source within a uniform whole-space, it is important to consider the influence of a stress-free surface boundary. The presence of a free surface leads to generation of Rayleigh surface waves or

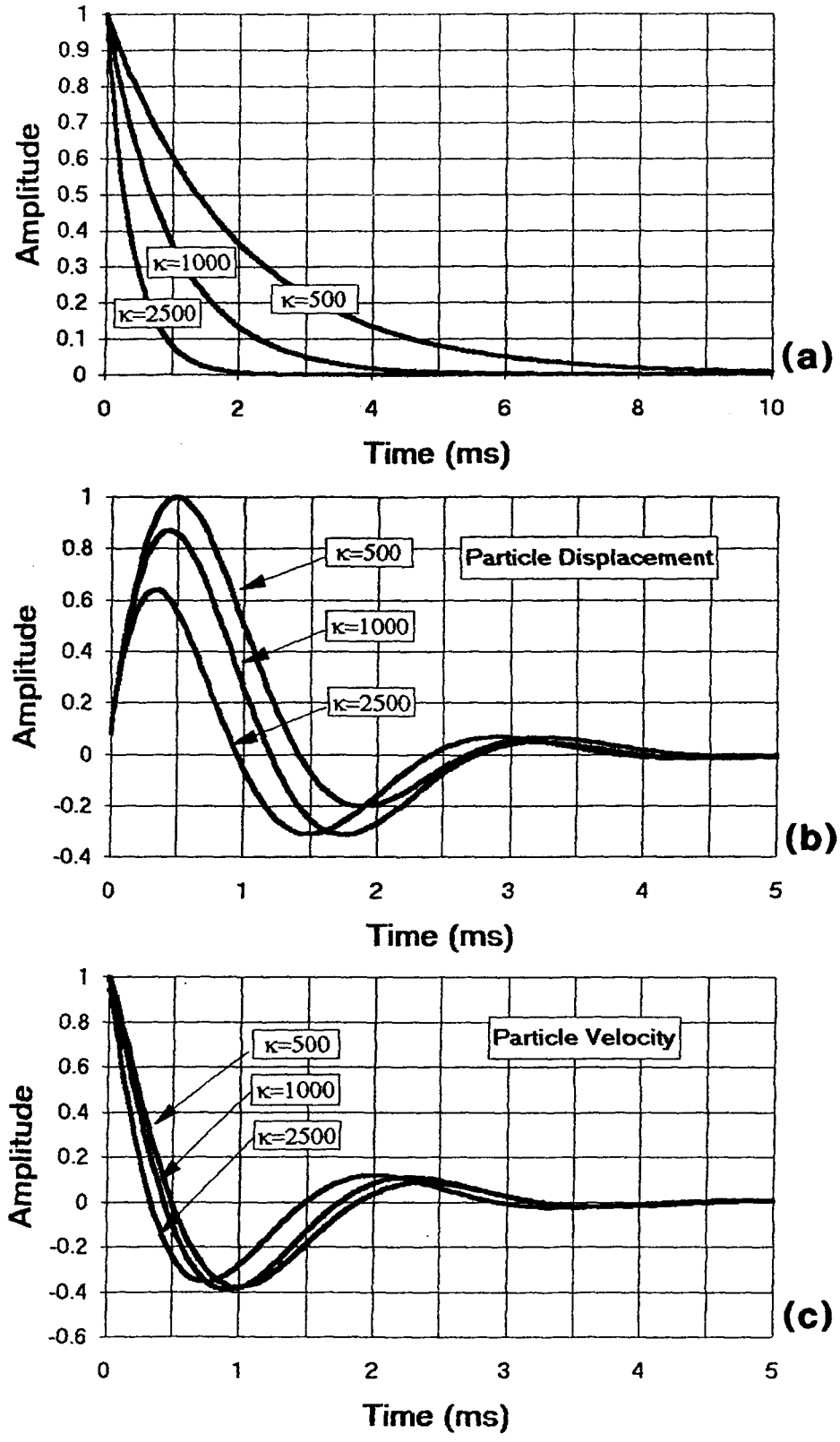

Figure 3.6. (a) Time-dependent cavity pressure functions of form $p(t) = p_0 e^{-\kappa t}$ and resulting (b) particle displacement and (c) particle velocity waveforms with decay constant κ as parameter.

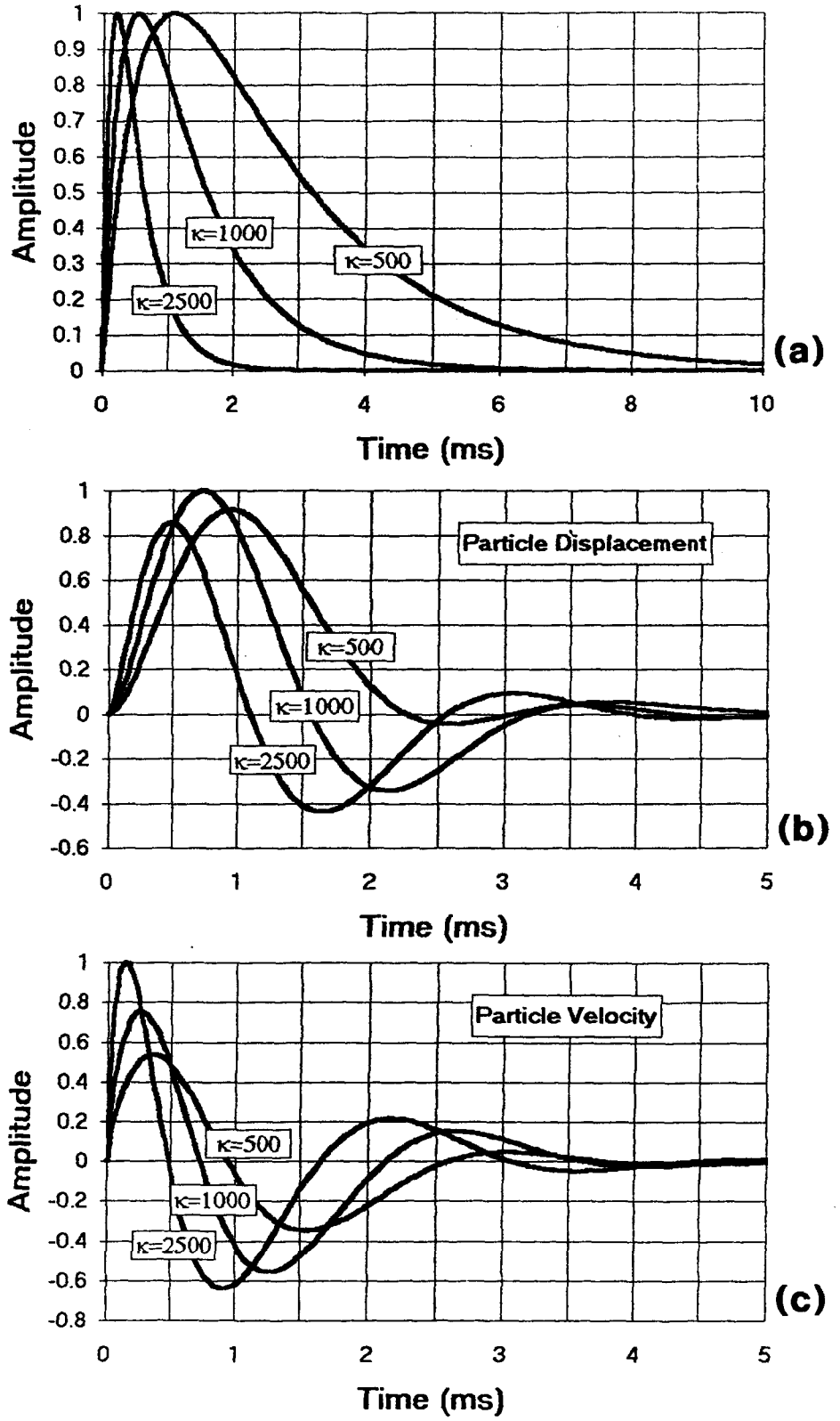

Figure 3.7. (a) Time-dependent cavity pressure functions of form $p(t) = p_0(e^{-\kappa t} - e^{-\eta t})$ and resulting (b) particle displacement and (c) particle velocity waveforms with decay constant κ as parameter. Rise-time constant $\eta = 3\kappa$.

"ground-roll" which, as previously discussed, constitute a major source of low-frequency, large amplitude interference. Empirical observation reported by Dobrin (1951) suggest that the amplitude of Rayleigh waves generated by an explosive source within near-surface, unconsolidated media varies with shot depth according to the relation

$$R(f) = \begin{cases} c_1 e^{k_1 z}, & z \leq z^*; \\ c_2 e^{-k_2 z}, & z > z^* \end{cases}, \tag{3.31}$$

where constants c_1, k_1, c_2, k_2 and z^* are site dependent. Dobrin (1951) attributed this behaviour to more efficient transmission of energy into the subsurface with increasing consolidation within a critical depth z^*. Beyond z^* the degree of consolidation ceases to be depth dependent and amplitude falls off exponentially with increasing depth as predicted by theory for a homogeneous elastic medium. Assuming that effective consolidation and, consequently, the critical depth z^* scale inversely with charge weight, this conclusion appears to be consistent with Sharp's (1944) observation that increased charge weight may produce a higher ratio of reflected energy to ground-roll interference. Moreover, Mooney (1977) reported similar findings for Rayleigh waves generated by a surface impact, concluding that Rayleigh wave amplitude decreases as the inverse square-root of Poisson's ratio.

A wide variety of source devices have been developed for high resolution seismology (Miller et al., 1986; 1992). Each device has advantages and drawbacks. For reasons discussed above, we require a subsurface explosive source, having moderate energy yield to ensure a high-frequency compressional disturbance accounting for as large a proportion of total wave energy as possible. Taking account of additional factors including cost, repeatability, energy focus and destructive potential, we have modelled our source after a design introduced by Pullan and MacAulay (1987). This simple apparatus, assembled from standard pipe and fittings at modest cost, allows detonation of a standard firearm cartridge at a set depth beneath the surface. The original design, intended for shallow geological mapping, has been scaled down to utilize a .22 calibre cartridge in place of a 12 gauge load. The resulting source device is illustrated in Figure 3.8. A cartridge is

loaded into the approximately 10 cm long barrel assembly and subsequently attached to the extension tube and handle via a Swagelok Quick-Connector® to facilitate rapid reloading. The cartridge is detonated by inserting a specially machined firing rod at the breech of the extension tube and dropping from several centimeters onto the cartridge, seated within the barrel assembly. Nearly instantaneous recoil closes a built-in inertial switch to activate the recorder.

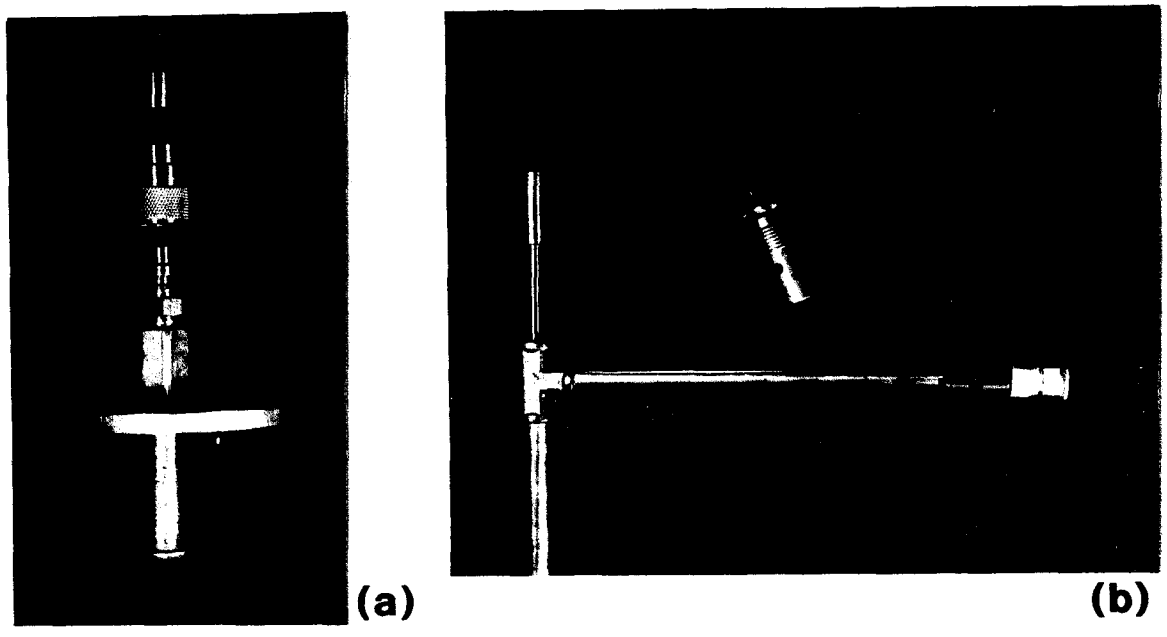

Figure 3.8. Special purpose .22 cal. energy source constructed from standard pipe and fittings. (a) Barrel assembly with Quick-Connector® attachment to extension tube. (b) Extension tube and handle assembly, showing firing rod in place at breech.

Although intuition suggests that projectile impact should enhance the coupling of explosive energy into the subsurface, experimentation with a variety of .22 calibre loads, including slugs and shot, indicates that there is no practical advantage. In fact, there is some evidence that the delay between detonation and impact may cause a minor degradation of high-frequency signal content. Consequently, To minimize soil disturbance and for sake of safety, we use blank loads manufactured for powder actuated tools. These loads are commercially available in a range of energy levels extending well beyond that of ordinary firearm cartridges and are subject to less restrictive transportation safety guidelines.

In comparison with the sledge hammer and striking plate, commonly used to generate elastic wave energy, the .22 calibre source is highly repeatable, better focussed and

yields a predominantly higher frequency disturbance as illustrated by comparing representative wavelets in Figure 3.9. The wavelets depicted in Figure 3.9 are typical direct-arrival wavelets recorded at an optimum offest of 0.3 m in connection with full-scale model experiments as described in the following chapter.

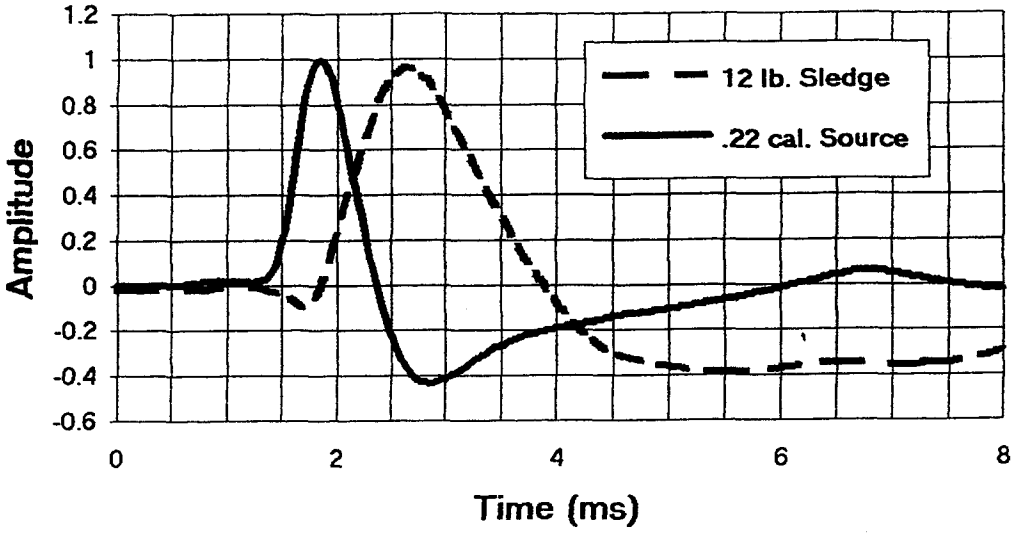

Figure 3.9. Representative source wavelets as generated by a 12 lb. sledge hammer impact at the surface and the .22 cal. source discharged at approximately 0.1 m below surface.

Associated amplitude and phase spectra are displayed in Figure 3.10. In addition to a significantly higher dominant frequency, the .22 cal. source wavelet possesses a substantially broader bandwidth. The slower rise-time and longer dominant period of the hammer generated wavelet results in a relative phase shift of approximately 180 degrees between the two wavelets as confirmed by corresponding phase spectra in Figure 3.10. Phase spectra are approximately linear at higher frequencies with a slope of roughly $2\pi\tau=3.5\pi$ rad/ms, corresponding to an arrival time of approximately $\tau=1.75$ ms.

Finally, while Figures 3.8 and 3.9 facilitate a useful comparison of source characteristics, it must be appreciated that these results necessarily incorporate subsurface transmission effects, and the response characteristics of detection and recording instrumentation as described in subsequent sections.

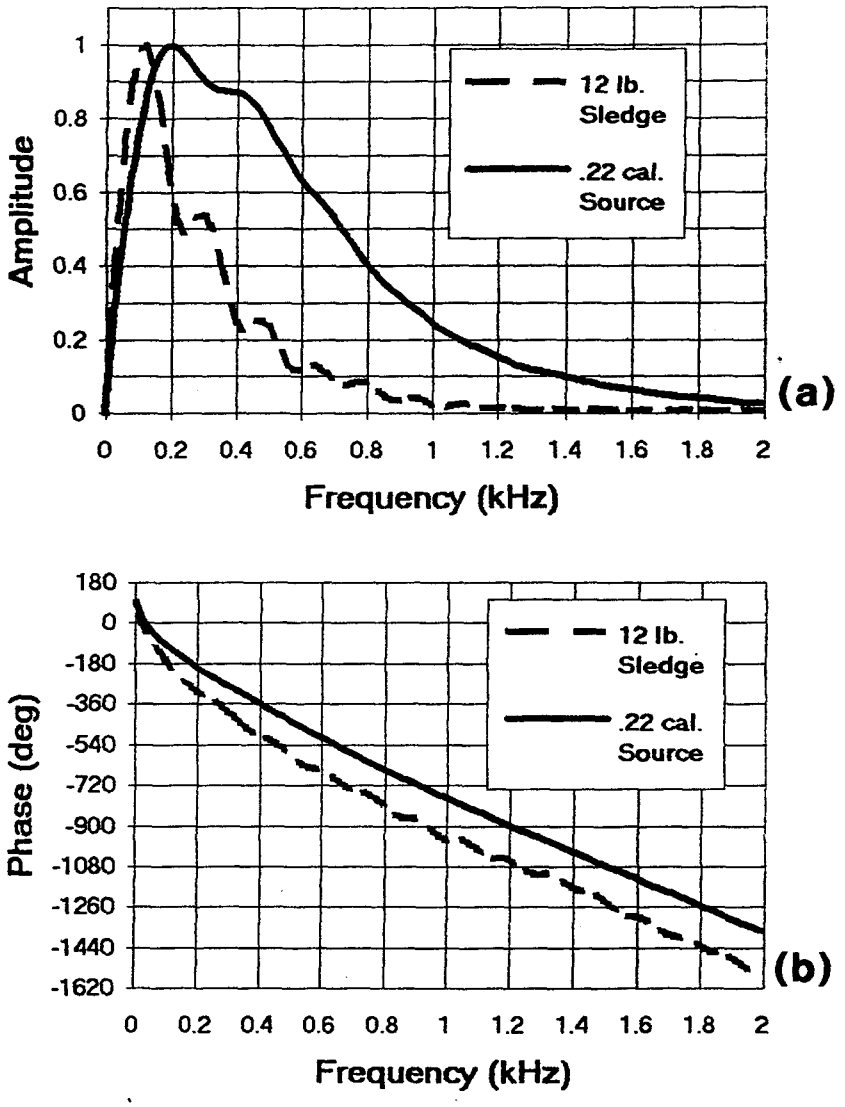

Figure 3.10. Representative (a) amplitude and (b) phase spectra associated with corresponding wavelets in Figure 3.9.

3.2.2 Earth Filter

We have already noted that on propagating through the subsurface, high-frequency components of a broad-band seismic pulse are preferentially attenuated, yielding a progressively broader wavelet having proportionately lower resolving power. Although we are unable to control the filter characteristics of the subsurface, it is useful to develop a general characterization of its frequency response so that the response of remaining system components may be tailored to compensate and, consequently, ensure that the recorded

wavelet possesses a balanced spectrum and, thus, optimum resolving power.

Consider a broad-band seismic disturbance propagating radially outward from a spherical source region, having radius r_0, within a homogeneous isotropic medium. Beyond the source region $r \geq r_0$, such a disturbance may be described mathematically as

$$u(r,t) = \left(\frac{r_0}{r}\right) u_0(r,t), \tag{3.31}$$

where the factor (r_0/r) accounts for spherical divergence and

$$u_0(r,t) = \int_{-\infty}^{+\infty} U(r,f)\, e^{i2\pi ft}\, df$$

describes the wavelet at arbitrary range and time as a superposition of monochromatic waves weighted by the Fourier spectrum

$$U(r,f) = U_0(r_0,f)\, S_e(r,f). \tag{3.32}$$

Here,

$$U_0(r_0,f) = \int_{-\infty}^{+\infty} u(r_0,t)\, e^{-i2\pi ft}\, dt \tag{3.33}$$

denotes the Fourier spectrum of the initial seismic disturbance as measured at reference range $r = r_0$ and $S_e(r,f)$ represents the range and frequency dependent transfer function of the earth propagation filter. Recalling the shifting theorem of the Fourier transform,

$$g(x) \rightarrow G(k)$$

$$g(x-\chi) \rightarrow G(k)\, e^{-i2\pi k\chi},$$

it follows that

$$S_e(r,f) = e^{-i2\pi k(r-r_0)}, \tag{3.34}$$

and, consequently, equation (3.32) becomes

$$U(r,f) = U_0(r_0,f)\, e^{-i2\pi k(r-r_0)}. \tag{3.35}$$

Moreover, the propagation "constant" k is, in general, a complex frequency-dependent quantity

$$k(f) = k'(f) - i\,k''(f) \tag{3.36}$$

and, thus, equation (3.34) has the general form

$$\begin{aligned} S_e(r,f) &= e^{-i2\pi[k'(f)-i\,k''(f)](r-r_0)} \\ &= e^{-2\pi k''(f)(r-r_0)}\, e^{-i2\pi\, k'(f)(r-r_0)}. \end{aligned} \tag{3.37}$$

Substituting the foregoing result in equation (3.35) yields

$$\begin{aligned} U(r,f) &= |U_0(r_0,f)|\, e^{i\Theta(r_0,f)}\, S_e(r,f) \\ &= |U_0(r_0,f)|\, e^{-2\pi k''(f)(r-r_0)}\, e^{i\left[\Theta(r_0,f)-2\pi\, k'(f)(r-r_0)\right]}, \end{aligned} \tag{3.38}$$

where $|U_0(r_0,f)|$ and $e^{i\Theta(r_0,f)}$ are, respectively, the amplitude and phase spectra of the wavelet at $r = r_0$. Equation (3.38) reveals that the factor $e^{-2\pi k''(f)(r-r_0)}$, incorporating the imaginary part of the complex propagation constant, produces a frequency dependent attenuation while the factor $e^{-i2\pi k'(f)(r-r_0)}$, incorporating the real-valued component of the propagation constant introduces a frequency dependent phase-shift or distortion of the wavelet. Defining a corresponding attenuation function

$$\alpha(f) = 2\pi k''(f) \tag{3.39}$$

and writing the associated phase-shift in terms of a frequency dependent phase velocity $v(f) = f/k'(f)$, we obtain

$$|U_0(r_0,f)|\, e^{-\alpha(f)(r-r_0)}\, e^{i\left[\Theta(r_0,f)-2\pi f(r-r_0)/v(f)\right]}. \tag{3.40}$$

Finally, it follows that the transfer function of the earth filter may be written in polar form as

$$S_e(r,f) = |S_e(r,f)|\, e^{i\,\Theta_e(r,f)}, \tag{3.41}$$

where corresponding amplitude and phase spectra are, respectively,

$$|S_e(r,f)| = e^{-\alpha(f)(r-r_0)} \tag{3.42}$$

and

$$\Theta_e(r,f) = -2\pi f \frac{(r-r_0)}{v(f)}. \tag{3.43}$$

In the case of a linearly elastic medium, the propagation constant is, in fact, a real-valued frequency independent quantity so that $k(f) = k'$, $\alpha(f) = 0$, $|S_e(r,f)| = 1$, $v(f) = v_0$ and $\Theta_e(r,f) = -2\pi f(r - r_0)/v_0$. That is, the earth filter is an all-pass linear phase-shift filter and, consequently, propagates the wavelet without attenuation or distortion. This conclusion is reinforced by examining the corresponding time-domain impulse response given by the inverse Fourier transform

$$s_e(r,t) = \int_{-\infty}^{+\infty} |S_e(r,f)|\, e^{i\,\Theta_e(r,f)} e^{i2\pi ft}\, df \tag{3.44}$$

In particular,

$$\begin{aligned} s_e(r,t) &= \int_{-\infty}^{+\infty} e^{-i2\pi f(r-r_0)/v_0} e^{i2\pi ft}\, df \\ &= \delta\left[t - (r - r_0)/v_0\right]. \end{aligned}$$

The result is a Dirac delta function time-shifted by the transit time $\tau = (r - r_0)/v_0$. In accordance with the convolution theorem of the Fourier transform (Bracewell, 1985), equation (3.32) may be cast as the equivalent time-domain convolution

$$u_0(r,t) = u_0(r_0,t) * s_e(r,t) \tag{3.45}$$

and, consequently, from equation (3.31)

$$u(r,t) = \left(\frac{r_0}{r}\right)\left[u_0(r_0,t) * s_e(r,t)\right]. \tag{3.46}$$

Thus, since $s_e(r,t) = \delta(\tau)$ for a linear elastic medium, $u(r,t)$ is simply the original wavelet $u_0(r_0,t)$ shifted by the appropriate transit time $\tau = (r - r_0)/v_0$.

Although linear elasticity is a common assumption for modelling seismic wave propagation, all geological materials are anelastic to some degree. In particular, soils and unconsolidated sediments are often characterized by non-linear stress-strain relations and exhibit pronounced hysteresis (Ivanova, et al., 1970; Mitchell, 1993). Empirical findings of both field and laboratory studies of seismic attenuation indicate that the attenuation rate $\alpha(f)$ is approximately proportional to frequency for a wide range of geological media, including unconsolidated sediments (Parkhomenko, 1967; Hamilton, 1972; Hatherly, 1986;

Badri and Mooney 1987). Thus, within the seismic frequency band, we have approximately

$$\alpha(f) = \alpha_0 f = \frac{\pi f}{Q_0 v_0}, \tag{3.47}$$

where $\alpha_0 = \pi/(Q_0 v_0)$ is the linear attenuation coefficient and

$$Q(f) = \frac{\pi f}{\alpha(f) v(f)} = \frac{\pi}{\alpha_0 v_0} = Q_0$$

is a dimensionless intrinsic parameter termed the quality factor. Consequently, assuming "constant-Q" $Q(f) = Q_0$, the earth propagation filter $S_e(r,f) = |S_e(r,f)|\, e^{i\Theta_e(r,f)}$ has amplitude and phase spectra

$$|S_e(r,f)| = e^{-\alpha_0 f (r-r_0)} \tag{3.48}$$

and

$$\Theta_e(r,f) = -2\pi f \frac{(r-r_0)}{v_0}, \tag{3.49}$$

respectively.

Let's begin our analysis of the foregoing result by considering a number of special cases. First, for $Q = \infty$, we have $\alpha(f) = 0$ and the transfer function $S_e(r,f)$ reduces to that for a perfectly elastic medium. As previously described, the corresponding impulse response or propagation operator is a delta function, shifted by transit time $\tau = (r - r_0)/v_0$. As expected, the propagation operator is also a delta function $\delta(0)$ for $r = r_0$, independent of the the quality factor Q. This follows from our definition of the reference range r_0. Finally, when the seismic disturbance has propagated an infinite distance from the source region $r - r_0 = \infty$, $|S_e(\infty,f)| = 0$, meaning the wavelet has been completely attenuated. In this regard, it follows from equation (3.48) that the pulse is attenuated to 1/e of its initial amplitude at $r = r_0$ when $r = r_s = 1/(\alpha_0 f) + r_0$. The parameter r_s is the so-called skin depth which, from equation (3.41) has the general, frequency dependent form

$$r_s(f) = \frac{1}{\alpha(f)} + r_0. \tag{3.50}$$

Returning to the case of constant-Q, Figure 3.11 displays amplitude and phase spectra computed in accordance with equations (3.48) and (3.49) for Q_0=10, 25 and 50, v_0=500 m/s and $r - r_0$=1.0 m. Corresponding impulse responses obtained by FFT implementation of equation (3.44) are depicted in Figure 3.12.

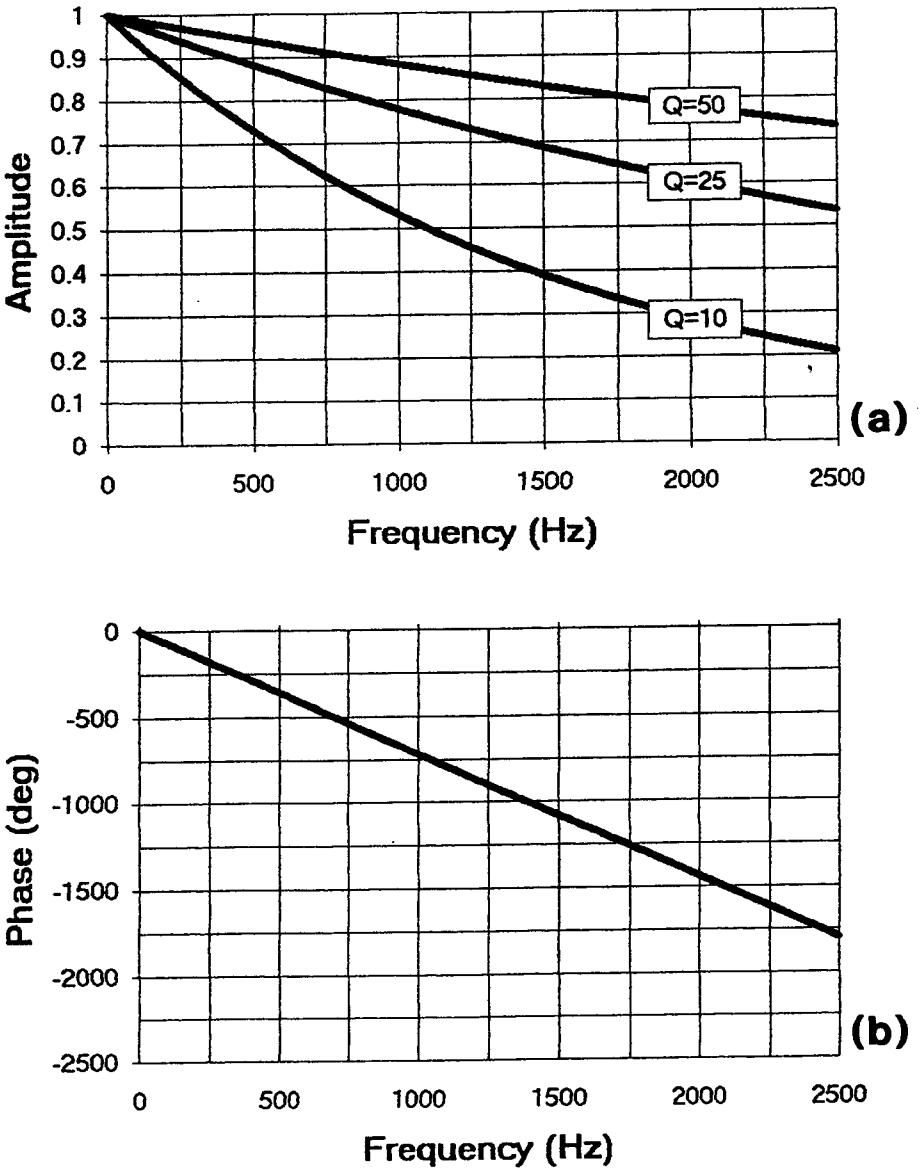

Figure 3.11. (a) Amplitude spectra for constant-Q earth filter for Q_0=10, 25 and 50, $r - r_0$=1.0 and v_0=500 m/s. (b) Corresponding phase spectrum is independent of Q.

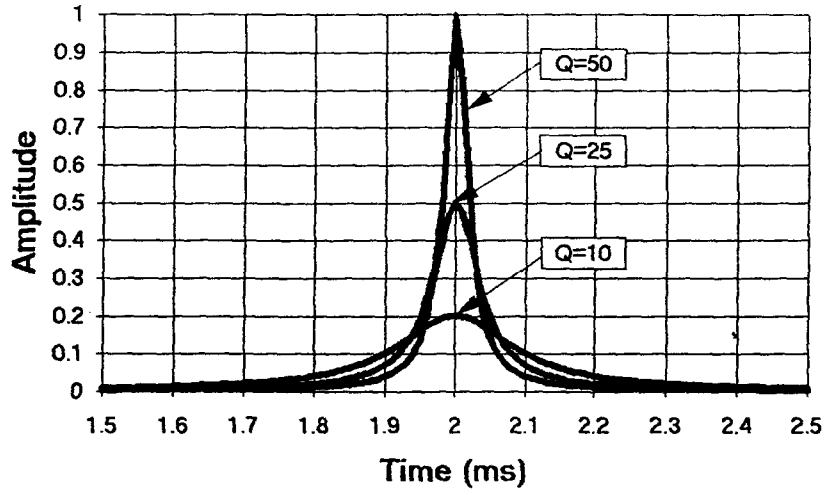

Figure 3.12. Constant-Q propagation operators, obtained via FFT implementation of equation (3.44) for Q_0=10, 25 and 50, $r - r_0$=1.0 m and v_0=500 m/s.

As expected, the propagation operators are progressively lower-frequency, lesser amplitude approximations to the corresponding time-shifted delta function obtained for a linearly elastic ($Q_0=\infty$) medium. It follows from equation (3.48) that increasing propagation range $r - r_0$ has the same effect as decreasing the quality factor Q_0.

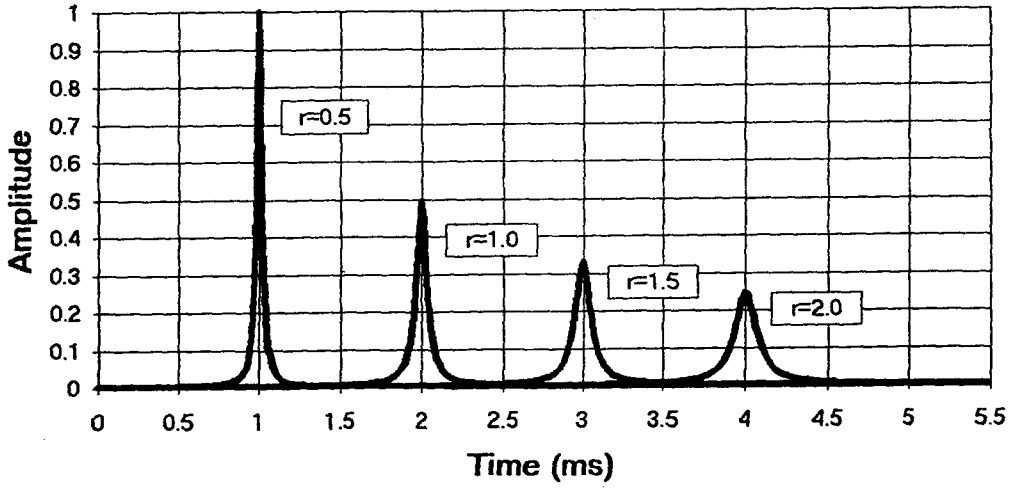

Figure 3.13. Constant-Q propagation operators, obtained via FFT implementation of equation (3.44) for $r - r_0$=0.5, 1.0, 1.5 and 2.0 m, Q_0=25 and v_0=500 m/s.

This is illustrated in Figure 3.13, where we display impulse responses for r=0.5, 1.0, 1.5 and 2.0 m (r_0=0) with Q_0=25 and v_0=500 m/s. An unacceptable feature of the propagation operators in Figures 3.12 and 3.13 is the presence, in all cases, of non-zero amplitudes at times preceding the transit time $\tau = (r - r_0)/v_0$. In other words, these impulse responses are acausal and, consequently, non-physical.

Elaborating on the work of Kalinin, et al. (1967) and Azimi, et al. (1968), Aki and Richards (1980) demonstrate that the requirement of causality implies that attenuation must be accompanied by attendant velocity dispersion. In other words, an attenuating medium, having attenuation rate $\alpha(f)$, must also be characterized by a frequency dependent phase velocity, satisfying the relation

$$v(f) = \left[\frac{1}{v_\infty} + \frac{\mathcal{H}\{\alpha(f)\}}{2\pi f}\right]^{-1}, \tag{3.51}$$

where $v_\infty = \lim_{f\to\infty} v(f)$ and

$$\mathcal{H}\{\alpha(f)\} = \int_{-\infty}^{+\infty} \alpha(f)\,[i\ \mathrm{sgn}(f)]\, e^{i2\pi ft}\, df \tag{3.52}$$

is the Hilbert transform of the attenuation rate, with

$$\mathrm{sgn}(f) = \begin{cases} -1, & f < 0; \\ 0, & f = 0;. \\ 1, & f > 0 \end{cases}$$

Moreover, since the amplitude and phase spectra of a causal minimum delay function

$$g(t) = \int_{-\infty}^{+\infty} |G(f)|\, e^{i\Gamma(f)}\, e^{i2\pi ft}\, df$$

are related by the equation

$$\Gamma(f) = \mathcal{H}\left\{\ln|G(f)|\right\},$$

it follows from equation (3.51) that the propagation operator p(r,t) given by equation (3.44) is minimum delay relative to arrival time $\tau = (r - r_0)/v_\infty$.

Returning to our development of a constant-Q earth filter, it follows from foregoing causality considerations that we must replace equation (3.49) by the more general, nonlinear phase spectrum given by equation (3.43), incorporating a frequency dependent phase

velocity v(f) and which, together with the amplitude spectrum in equation (3.48), satisfies the causality condition given by equation (3.51). Unfortunately, an exact dispersion relation fulfilling this requirement does not exist. Consequently, given convincing evidence for constant-Q attenuation and the necessity for attendant velocity dispersion, in accordance with the causality condition, one of two approaches may be taken. First, we may insist upon constant-Q attenuation and deduce an associated dispersion relation which approximately satisfies equation (3.51) (e.g. Strick, 1970; Kjartansson, 1979) or, alternatively, we may relax the constant-Q assumption, seeking an approximately linear attenuation rate $\alpha(f)$ and corresponding dispersion relation v(f) which exactly satisfy the causality condition. Here we shall take the latter approach, adopting the quasi-linear attenuation law

$$\alpha(f) = \frac{\alpha_0 f}{1 + \alpha_1 f} \tag{3.53}$$

proposed by Azimi et al. (1968), where the parameter α_1 is adjusted so that the attenuation rate is effectively linear within the frequency band of seismic investigation. That is, $\alpha_1 f << 1$ for f=0-1 kHz. The corresponding Hilbert transform is

$$\mathcal{H}\{\alpha(f)\} = \frac{2\alpha_0 f}{\pi(1 - \alpha_1^2 f^2)} \ln\left(\frac{1}{\alpha_1 f}\right) \tag{3.54}$$

and, consequently, from equation (3.51) we obtain the corresponding dispersion relation

$$v(f) = \left[\frac{1}{v_\infty} + \frac{\alpha_0}{\pi^2(1 - \alpha_1^2 f^2)} \ln\left(\frac{1}{\alpha_1 f}\right)\right]^{-1}. \tag{3.55}$$

The frequency dependent attenuation rate $\alpha(f)$ and corresponding phase velocity v(f) are displayed in Figure 3.14 for Q=10, 25 and 50, v_∞=500 m/s, $\alpha_1 = 0.4\pi \times 10^{-6}$ and $r - r_0$=1.0 m. The corresponding earth filter $S_e(r,f) = |S_e(r,f)| e^{i\Theta_e(r,f)}$ has amplitude and phase spectra

$$\begin{aligned} |S_e(f)| &= e^{-\alpha(f)(r-r_0)} \\ &= e^{-\alpha_0 f/(1+\alpha_1 f)} \end{aligned} \tag{3.56}$$

and

$$\begin{aligned} \Theta_e(r,f) &= 2\pi f \frac{(r - r_0)}{v(f)} \\ &= 2\pi f (r - r_0)\left[\frac{1}{v_\infty} + \frac{\alpha_0}{\pi^2(1 - \alpha_1^2 f^2)} \ln\left(\frac{1}{\alpha_1 f}\right)\right] \end{aligned} \tag{3.57}$$

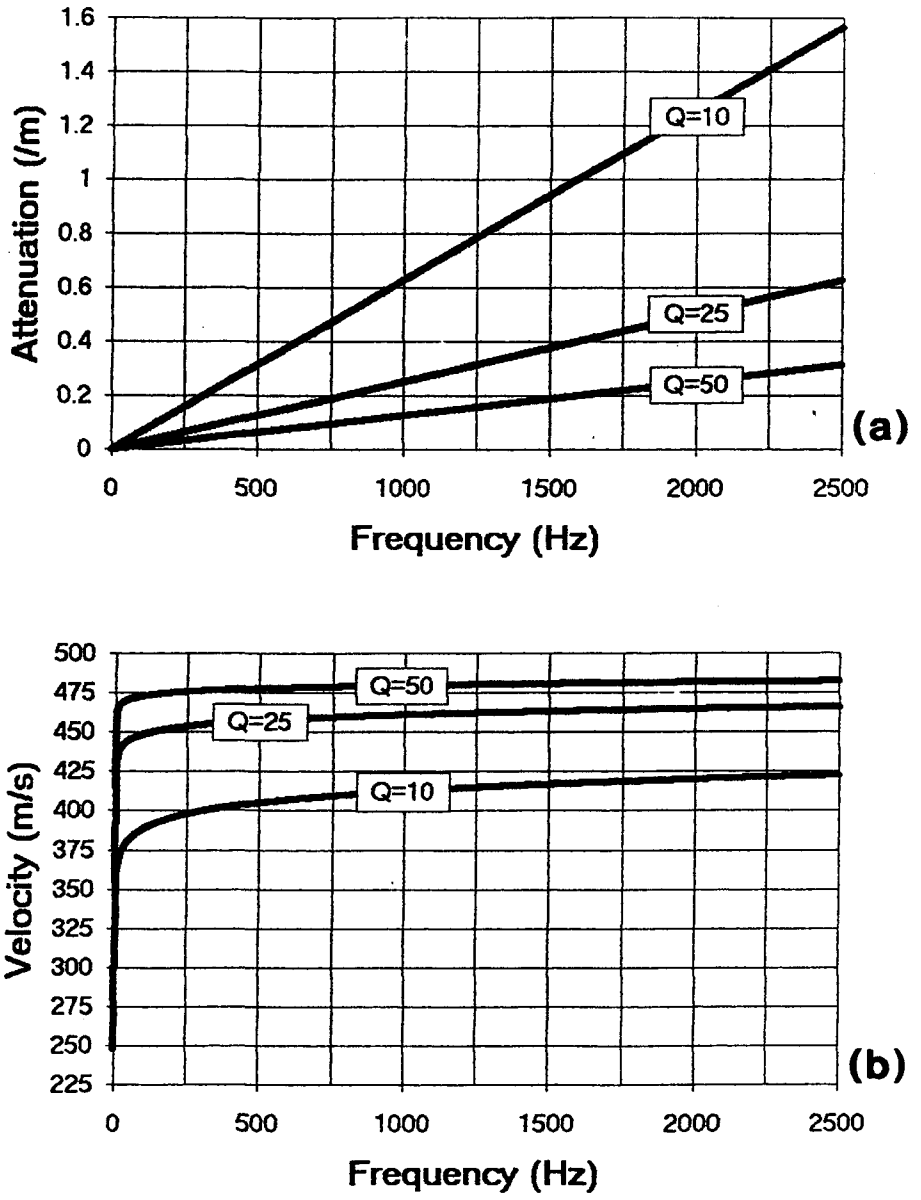

Figure 3.14. (a) Quasi-linear attenuation rate given by equation (3.53) for Q_0=10, 25 and 50, $r - r_0$=1.0 m and v_∞=500 m/s. (b) Associated frequency dependent phase velocity given by equation (3.55).

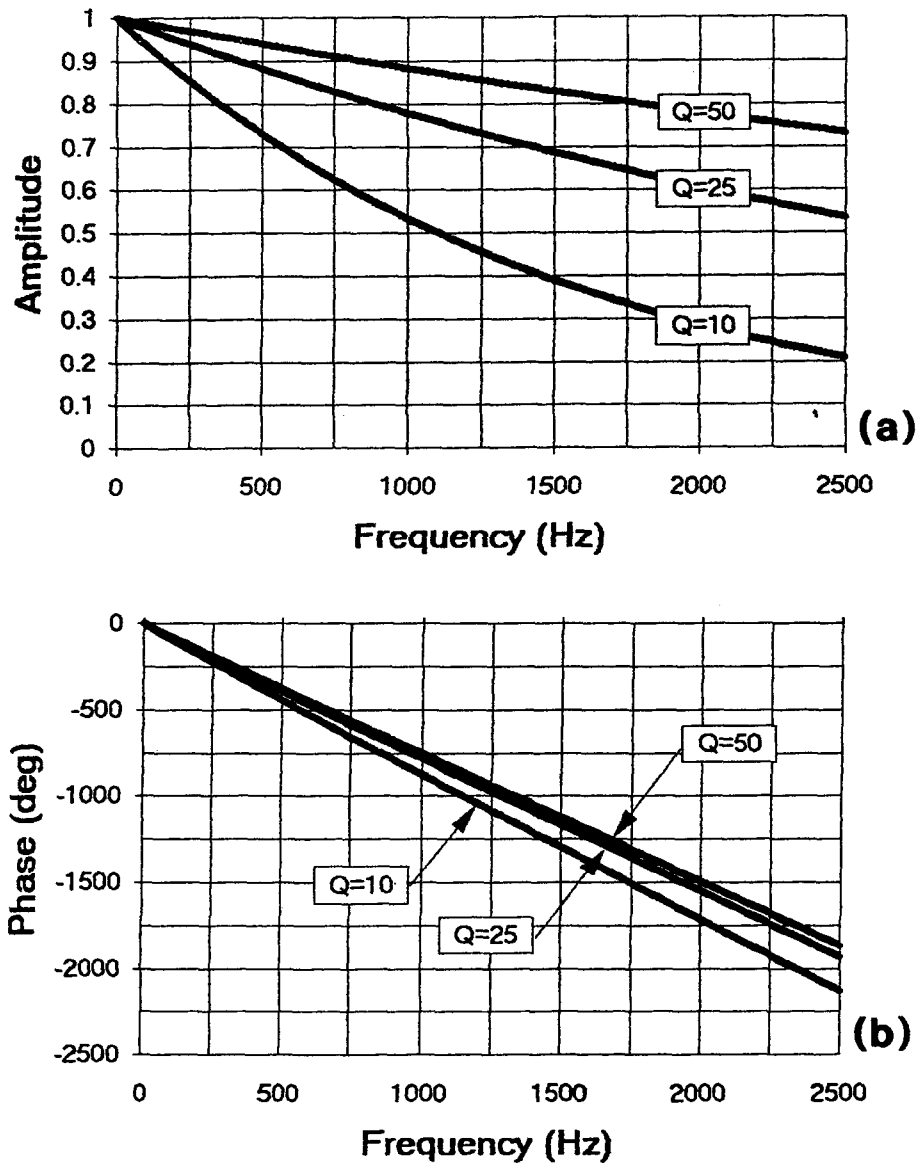

Figure 3.15. (a) Amplitude and (b) phase spectra for quasi-constant-Q earth filter, having frequency dependent attenuation rate and phase velocity depicted in Figure 3.14.

as displayed in Figure 3.15. Comparison of these spectra with Figure 3.11 confirms that the amplitude spectra are effectively identical within the seismic frequency band and reveals only minor non-linearity in phase spectra. Corresponding propagation operators are depicted in Figure 3.16.

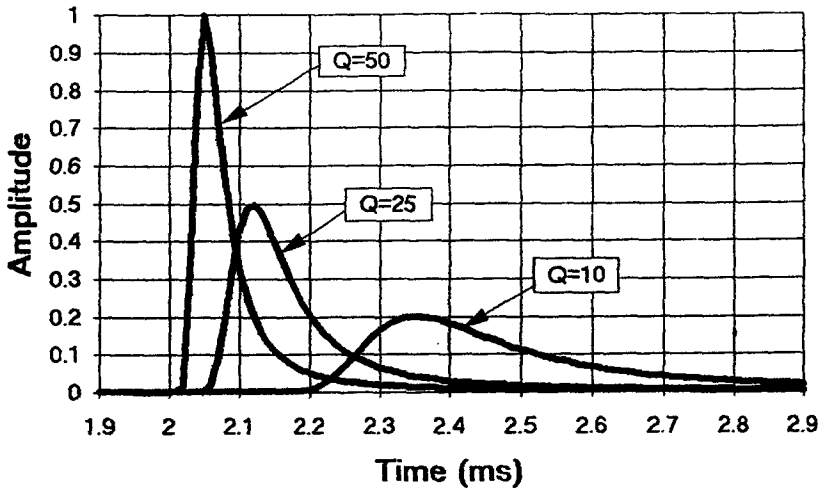

Figure 3.16. Quasi-constant-Q propagation operators, obtained via FFT implementation of equation (3.44) for Q_0=10, 25 and 50, $r - r_0$=1.0 m and v_∞=500 m/s.

As in Figure 3.12, resulting impulse responses possess a progressively lower dominant frequency and lesser amplitude as Q increases. However, in contrast with the impulse responses computed for a non-dispersive medium, those in Figure 3.16 are causal.

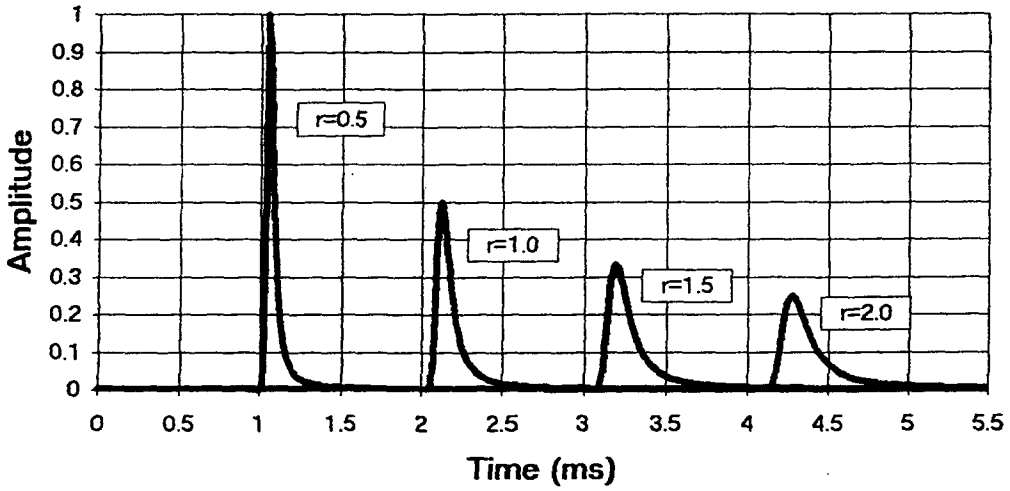

Figure 3.17. Constant-Q propagation operators, obtained via FFT implementation of equation (3.44) for $r - r_0$=0.5, 1.0, 1.5 and 2.0 m, Q_0=25 and v_∞=500 m/s.

Similar results are obtained on increasing the propagation range as illustrated in Figure 3.17 for $r - r_0$=0.5, 1.0, 1.5 and 2.0 m ($r_0 = 0$) for Q_0=25 and v_∞=500 m/s. Finally, an increasingly significant time delay is observed between the transit time $t = (r - r_0)/v_\infty$ and the onset of the propagation operator. Although this delay is apparently consistent with increased velocity dispersion at lower Q values and greater range, implications for a minimum delay wavelet are uncertain. The time lag appears to be related to selection of the parameter α_1.

The foregoing analysis quantifies the well known low-pass, nonlinear phase frequency response of the earth filter. We have already observed that seismic sources generate wavelets that are relatively deficient of high-frequencies and it is evident that propagation through the subsurface only accentuates this spectral imbalance. Although the frequency response of the earth filter is beyond control, knowledge of its characteristics are important in the design of detectors, real-time filters and post-acquisition data enhancement techniques to compensate for the attenuation of high frequencies and concomitant pulse distortion, resulting from velocity dispersion.

3.2.3 Detector

In addition to converting ground motion into a representative electrical signal, the detector can have a significant role in shaping the frequency characteristics the resulting waveform. A wide range of detectors are commercially available and a useful guide is that by Lepper (1981). For most applications, seismic detectors are velocity sensitive devices known as geophones. In particular, modern geophones are typically of the moving-coil electromagnetic variety as depicted in Figure 3.18. The schematic diagram gives a simplified, cross-sectional view of principal component parts of a vertical-component detector. The geophone housing incorporates a permanent magnet in the form of a vertical cylinder. A central south magnetic pole is separated from an annular north magnetic pole by a cylindrical slot. A sensing coil, consisting of n turns of low-resistivity wire around a cylindrical former, is suspended within the slot by means of light leaf springs.

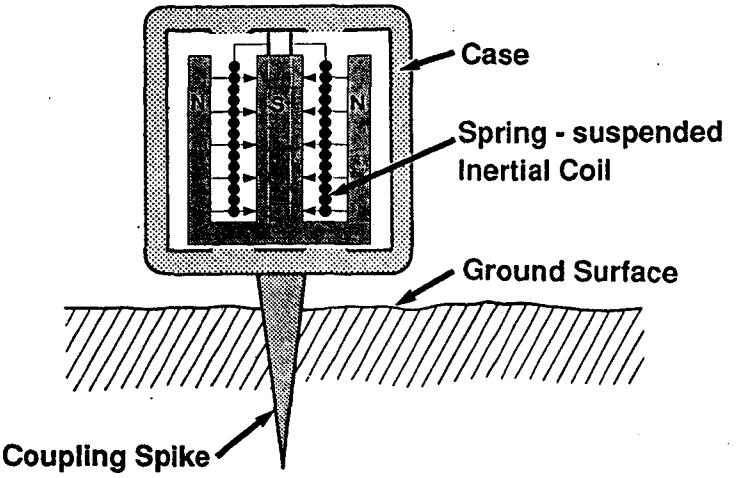

Figure 3.18. Schematic diagram of moving-coil electromagnetic geophone.

The geophone is normally coupled to the subsurface via a spike to ensure firm connection. As a result, while the geophone case and enclosed magnet move in unison ground motion caused by an incident seismic disturbance, the the suspended sensing coil remains effectively in place in accordance with Newton's laws of motion. Consequently, relative motion between the coil and the static magnetic field produces an output voltage between the terminals of the coil in accordance with Faraday's induction law. Coil suspension is designed to eliminate relative motion between the inertial element and magnet in response to horizontal ground motion, thereby ensuring that the vertical-component detector is effectively insensitive to motion perpendicular to its axis of sensitivity.

As developed by Dennison (1953) and Pieuchot (1984), the frequency response of an ideal (self-inductance $L_C \approx 0$) moving-coil geophone is

$$S_d(f) = \frac{S_G f^2}{f^2 - i2hf_0 f - f_0^2}, \tag{3.58}$$

where f_0 denotes the natural frequency, h represents the effective damping factor and $S_G = D_{em}/(1 + R_C/R_L)$ is the geophone's intrinsic sensitivity, with D_{em} denoting the transduction coefficient, R_C the coil resistance and R_L the external load resistance. In effect, the frequency response is that of a damped harmonic oscillator. Figure 3.19 displays theoret-

ical amplitude and phase spectra as functions of frequency, normalized by the geophone's natural frequency

$$f_0 = \frac{1}{2\pi}\sqrt{\frac{k_C}{M_C}}, \tag{3.59}$$

where k_C is an effective elastic constant for the coil suspension mechanism and M_C is the mass of the coil. In particular, Figure 3.19a charts relative geophone output for constant velocity excitation. Note that the high frequency response of a moving-coil electromagnetic geophone is approximately flat and, consequently, proportional to ground velocity. In practice, effective bandwidth is limited by the presence of parasitic resonances, generated by horizontal ground motion, at approximately ten times the geophone's natural frequency. These effects are nicely illustrated in frequency response curves measured by Lepper (1981) for a selection of commercially available geophones.

Returning to the ideal geophone response, spectra in Figure 3.19 are parameterized by the effective damping factor

$$h = \frac{1}{4\pi f_0 M_C}\left(D_m + \frac{D_{em}^2}{R}\right), \tag{3.60}$$

as a fraction of critical damping, where $R = R_C + R_L$ denotes total circuit resistance, including sensing coil resistance R_C and external load resistance R_L, D_m represents the mechanical or open-circuit damping coefficient and $D_{em} = 2\pi Bnr$ is the electromagnetic damping or transduction coefficient, with B representing the magnetic flux density and n the number of turns of radius r on the coil. In practice, effective damping is controlled by placing a shunt resistance R_S across the geophone terminals and, thus, in parallel with the external load resistance R_L. The effective load resistance becomes

$$\begin{aligned} R'_L &= \left[\frac{1}{R_L} + \frac{1}{R_S}\right]^{-1} \\ &= \left[\frac{1}{(R_T + R_A)} + \frac{1}{R_S}\right]^{-1}, \\ &= \frac{R_S\,(R_T + R_A)}{R_S + (R_T + R_A)} \end{aligned} \tag{3.61}$$

where R_T and R_A denote transmission line and amplifier resistances, respectively. As illustrated in Figure 3.19, an effective damping factor of h=0.6-0.7 provides an optimally

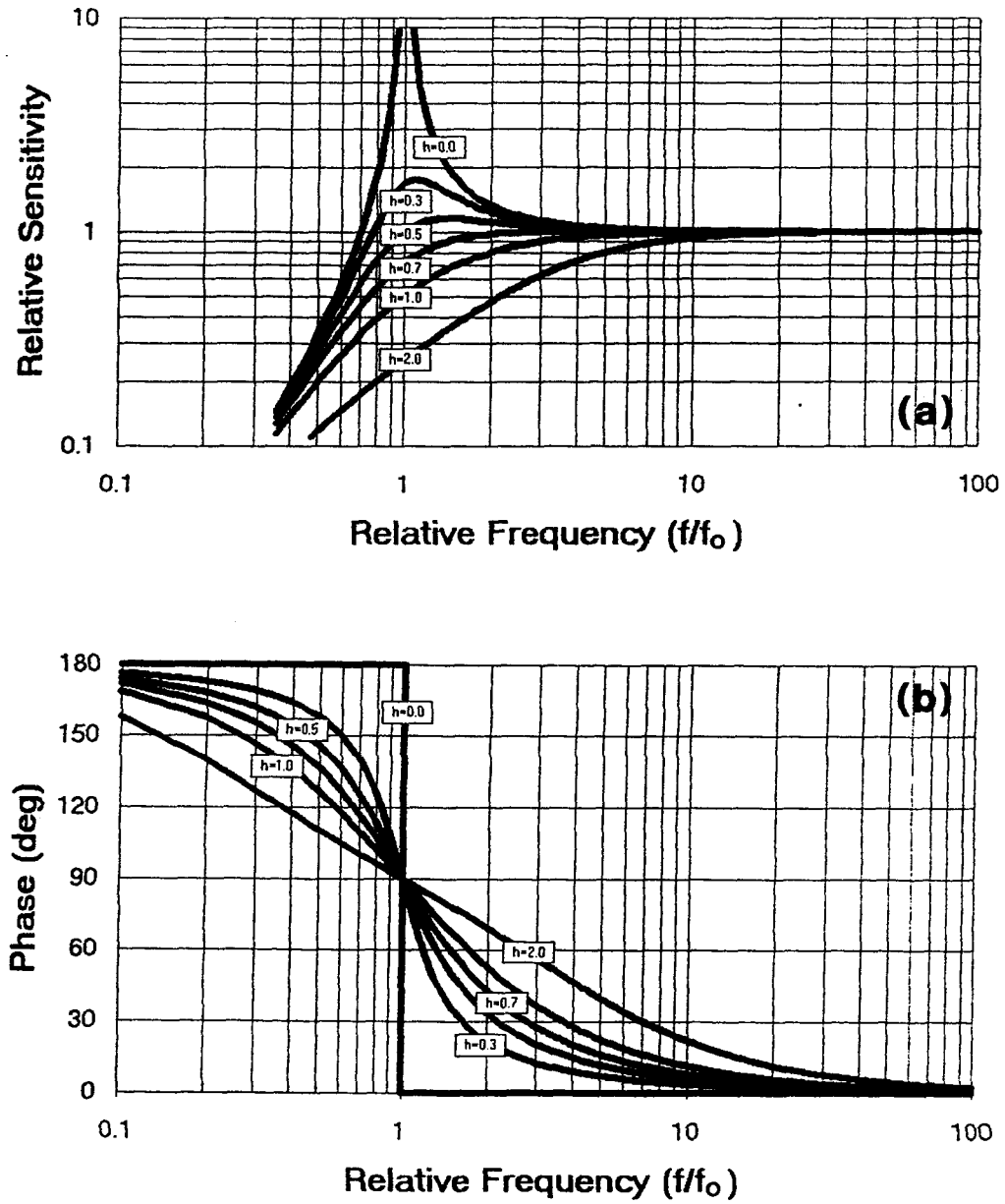

Figure 3.19. Frequency response of moving-coil geophone. (a) Amplitude spectra normalized by geophone sensitivity S_G and (b) relative phase spectra between output current and particle velocity as functions normalized frequency (f/f_0) with effective damping factor h as a parameter.

flat response and a relatively fast roll-off of approximately 12 dB/octave below the natural frequency. Consequently, the geophone may be employed, effectively, as a high-pass filter to attenuate large amplitude, low frequency ground-roll and enhance higher frequencies which, as we have seen, are deficient in the source spectrum and further attenuated by the earth filter. Moving-coil geophones having natural frequencies as high as 100 Hz are commercially available. Finally, the non-linearity of phase spectra depicted in Figure 3.19b suggests that the conversion of ground motion into an electrical signal is accompanied by significant distortion of the seismic wavelet. Despite a more nearly linear phase with increased damping, corresponding impulse responses (Dennison, 1953) indicate that 70% critical damping yields a favourable tradeoff between bandwidth and pulse distortion.

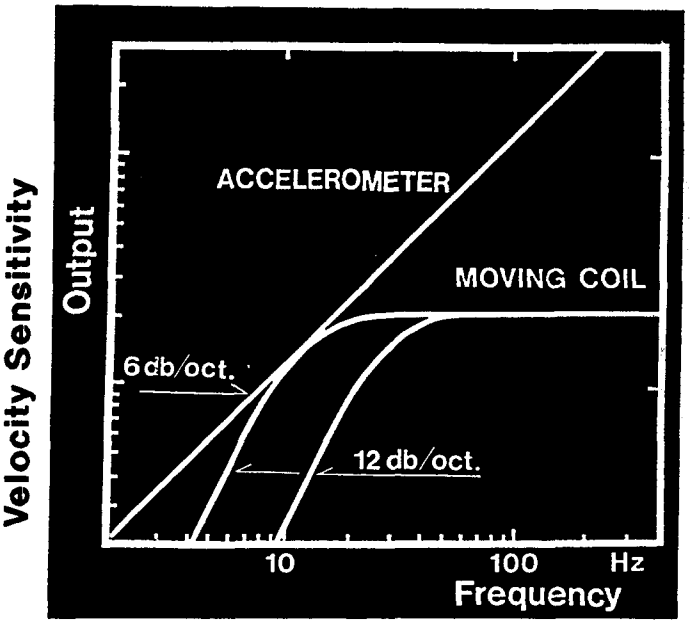

Figure 3.20. Frequency response curve of accelerometer compared with moving-coil geophone responses (f_0=10 and 28 Hz, h=0.7). (After Hall and Kanemori, 1986)

An alternative receiver for high resolution applications is the accelerometer, which is typically comprised by an internal mass resting on a sensing element of piezoelectric ceramic. In response to ground acceleration caused by an incident seismic disturbance, the internal mass exerts a modulated pressure (force per unit area) on the active element, deforming the piezoelectric ceramic which, as a result, produces a measurable electrical

potential. The amplitude of the resulting output voltage is in direct proportion to applied pressure and, consequently, to ground acceleration. The accelerometer's frequency response, to constant velocity excitation, is compared with that of a moving-coil electromagnetic geophone in Figure 3.20. It is observed that the accelerometer exhibits a gain of approximately 6 dB/octave in sensitivity as frequency increases toward a natural frequency of typically 2-5 kHz. Consequently, although accelerometers do not attenuate lower frequencies as effectively as the velocity geophone, they do provide a significant relative enhancement of higher frequencies that are critical to achieving improved resolution. A drawback is that accelerometers are typically low output, high impedance devices and require additional instrumentation to amplify the output and match the recorders input impedance.

Our prototype system employs an OYO Eddy-Seis® detector, having response characteristics between those of a velocity geophone and an accelerometer. As illustrated in Figure 3.22, the Eddy-Seis detector is constructed in much the same fashion as moving-coil electromagnetic geophone. The moving coil, however, is replaced by an electrically conductive sleeve and the sensing coil is fixed, along with the magnet, to the geophone case.

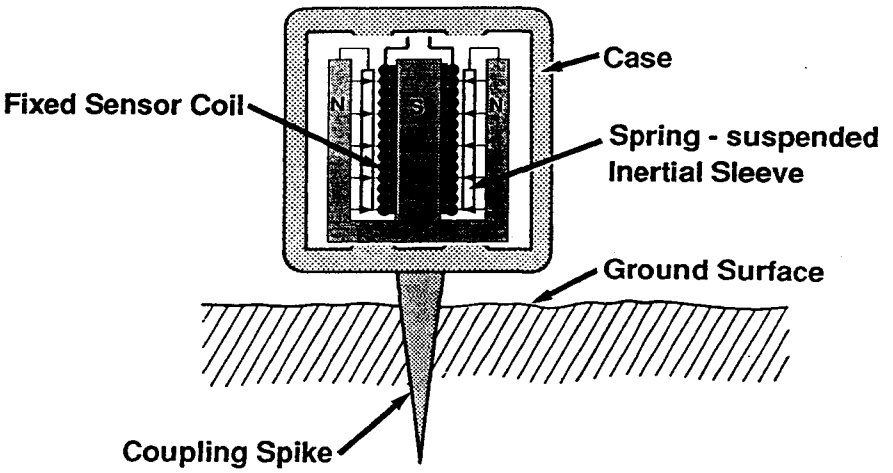

Figure 3.21. Schematic diagram of the OYO Eddy-Seis detector.

Consequently, ground motion caused by an incident seismic disturbance results in relative

motion between the conductive sleeve and the static magnetic field, producing eddy currents within the conductive sleeve. These eddy currents generate a secondary magnetic field that, in turn, induces current flow within the sensing coil. Hall and Kanemori (1986) demonstrate that this unique design results in a constant-velocity frequency response having form

$$S_d(f) = \left[\frac{-S_E f^2}{f^2 + i2h(f) f_0 f - f_0^2}\right]\left[\frac{i2\pi f}{1 + i(f/f_\alpha)}\right], \tag{3.62}$$

where

$$f_0 = \frac{1}{2\pi}\sqrt{\frac{k_S}{M_S}} \tag{3.63}$$

denotes the detector's natural frequency, with k_S representing an effective elastic constant for the sleeve suspension mechanism, M_S the mass of the conductive sleeve and

$$f_\alpha = \frac{1}{2\pi}\left(\frac{R_S}{L_S}\right) \tag{3.64}$$

defines a transition frequency, with R_S and L_S denoting, respectively, the effective resistance and inductance of the conductive sleeve. Modelling the conductive sleeve as an n-turn coil of radius r, the detector's intrinsic sensitivity is $S_E = L_m D_{em}/R_S$, with $D_{em} = 2\pi Bnr$ denoting the effective electromagnetic damping or transduction coefficient and L_m the mutual inductance between the sleeve and the sensor coil. Finally,

$$h(f) = \frac{1}{4\pi f_0 M_S}\left(D_m + \frac{D_{em}^2}{R_S}\left[\frac{1}{1 + i(f/f_\alpha)}\right]\right) \tag{3.65}$$

defines a frequency dependent complex-valued damping factor, where D_m and D_{em} denote mechanical and electromagnetic damping coefficients, respectively. In practice, the frequency dependence is weak and to good approximation

$$h(f) = h = \frac{1}{4\pi f_0 M_S}\left(D_m + \frac{D_{em}^2}{R_S}\right). \tag{3.66}$$

In view of this approximation, Hall and Kanemori (1986) observed that the first term of equation (3.62) is, apart from the sensitivity constant, the frequency response of a moving coil geophone (equation (3.58)). The second term is identified as the frequency response of a high-pass filter, having corner frequency (-3dB) f_α. The resulting Eddy-Seis frequency response is illustrated in Figure 3.22 as a function of relative frequency with approximate

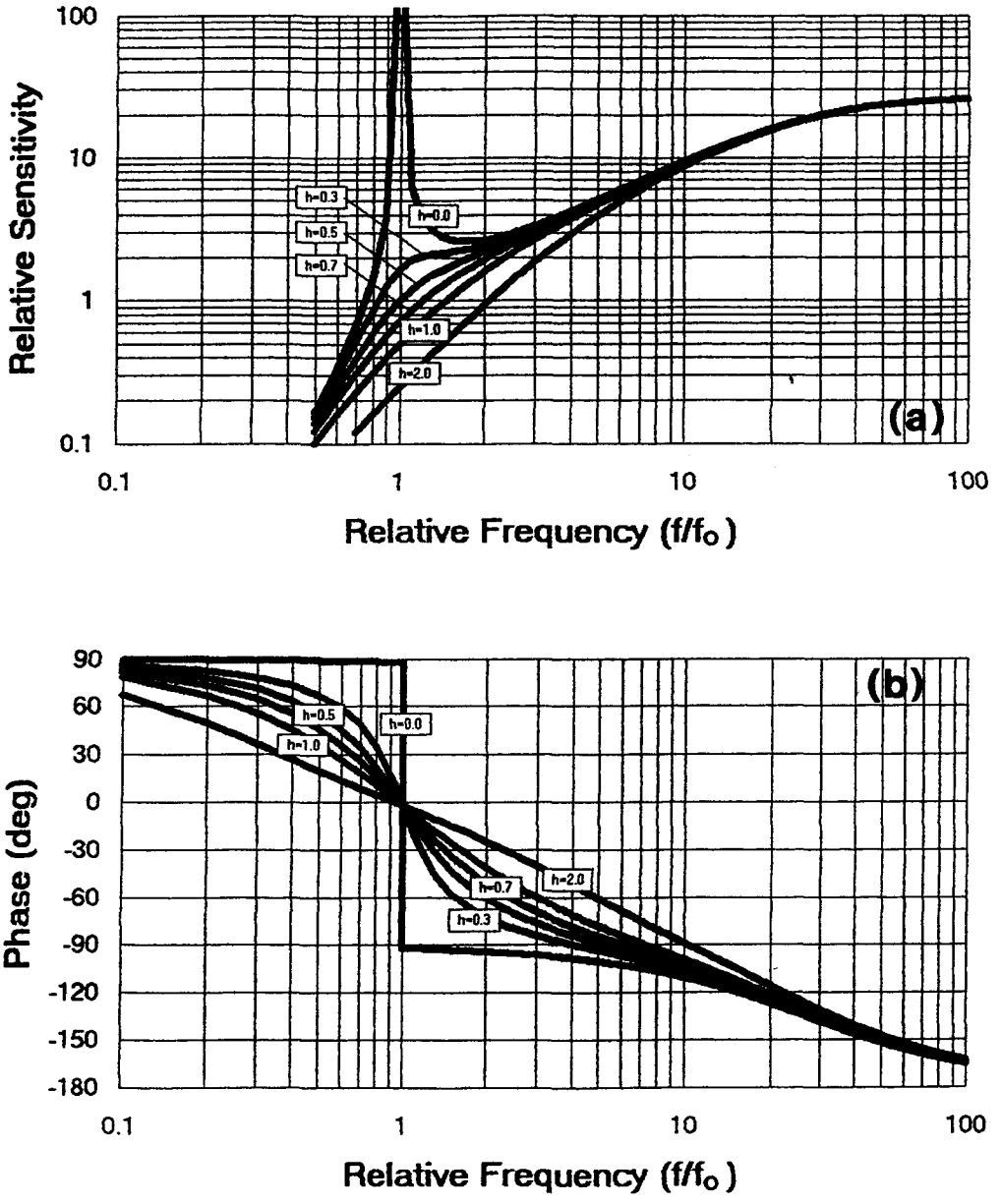

Figure 3.22. Frequency response of Eddy-Seis detector. (a) Amplitude spectra normalized by geophone sensitivity S_E and (b) relative phase spectra between output current and particle velocity as functions normalized frequency (f/f_0) with approximate damping factor h as a parameter.

damping factor h as a parameter. Comparison with moving coil geophone responses in Figure 3.19 reveals that in addition to faster roll-off characteristics below the natural frequency, the Eddy-Seis detector is substantially more responsive to high-frequency ground motion.

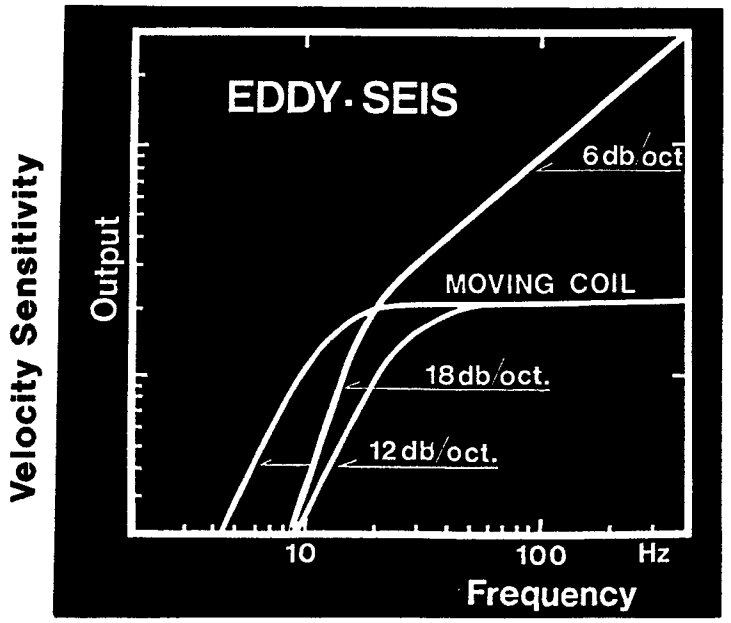

Figure 3.23. Frequency response of Eddy-Seis compared with moving-coil geophone responses (f_0=10 and 28 Hz, h=0.7). (After Hall and Kanemori, 1986)

Specifically, as illustrated in Figure 3.23 for a fixed† damping factor of h=0.7, the Eddy-Seis delivers an accelerometer like gain of 6 dB/octave from a natural frequency of $f_0 = 17$ Hz to a transition frequency of $f_\alpha = 450$ Hz, beyond which the response is flat to at least 2 kHz (OYO Corporation, personal communication). Concurrently, the Eddy-Seis provides enhanced attenuation of 18 dB/octave below the natural frequency. Finally, although the Eddy-Seis sensitivity is significantly lower ($S_E \approx (0.01 - 0.1)\, S_G$) than a typical moving-coil geophone, it does not pose the impedance matching problem associated with a true accelerometer. In fact, given the close proximity of source and receiver for small scale applications, a moderately lower output voltage can be advantageous.

† In contrast with the moving-coil geophone, the effective damping factor for the Eddy-Seis detector is insensitive to the external load resistance (i.e. equations (3.60) and (3.65)) and, consequently, cannot be adjusted after assembly.

3.2.4 Filter and Switching Unit

Although the high-pass response of the seismic detector serves as a first line of defense against low-frequency source-generated noise, technical limitations restrict their natural frequency and roll-off characteristics. Enhanced flexibility is achieved by incorporating a high-pass filter section between the detector and seismic recorder. As the objective of in-line filtering is to further enhance or emphasize high-frequency signal content prior to recording, the process is commonly referred to as pre-emphasis filtering. All modern engineering seismographs provide some facility for pre-emphasis filtering and flexibility is in direct relation to cost. To remain cost effective, the prototype system described here employs a relatively modest seismograph having only a 40 Hz, fixed frequency pre-emphasis filter. To provide enhanced flexibility, a special purpose filter unit has been designed and constructed locally.

The core of the unit is a high-pass Bessel filter, having selectable corner frequencies from 50-500 Hz and passband roll-off of 10-13 dB/octave. The Bessel filter is realized via the general purpose voltage-controlled voltage-source (VCVS) active filter network depicted in Figure 3.24.

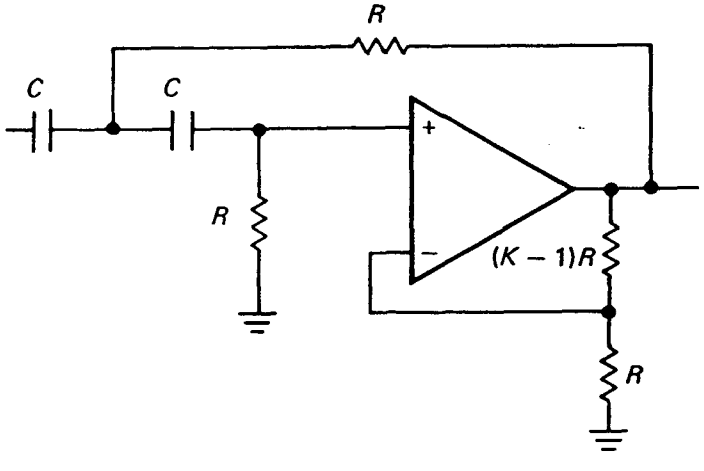

Figure 3.24. VCVS high-pass active filter network.

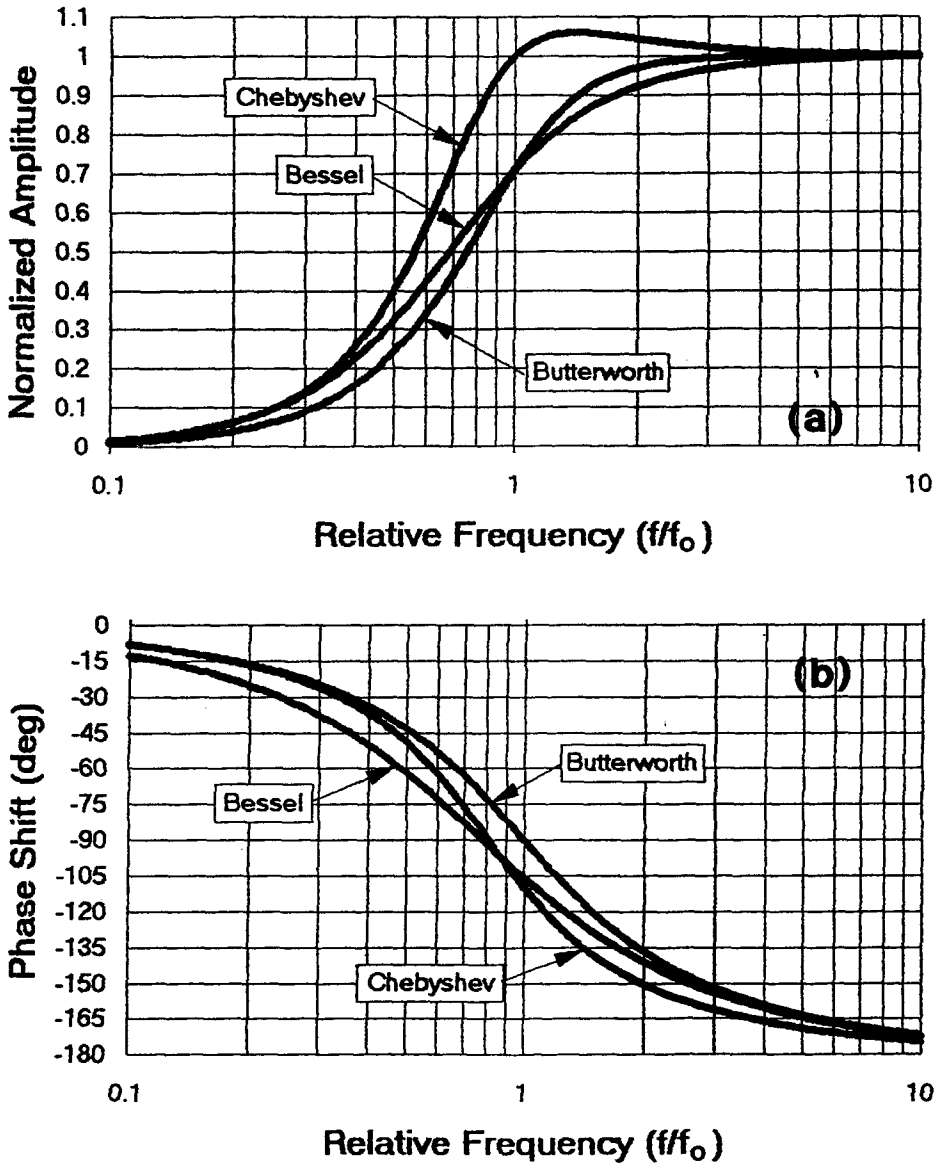

Figure 3.25. 2-pole VCVS High-pass active filter responses. (a) Amplitude and (b) phase spectra for second-order Chebyshev, Butterworth and Bessel filters. The ideal high-pass amplitude response is indicated by a dashed curve.

The frequency response of this circuit is (Hilburn and Johnson, 1980)

$$S_f(f) = \frac{2\pi K f^2}{2\pi f^2 - i2af - b}, \tag{3.67}$$

where

$$K = 1 + \frac{R_2}{R_1},$$

$$a = \frac{(3-K)}{RC}$$

and

$$b = \left(\frac{1}{RC}\right)^2.$$

Consequently, the filter's response characteristics are controlled by selecting the gain K and time constant $\tau = RC$. The range of realizable response characteristics is represented by three principal filter types; Chebyshev, Butterworth and Bessel.

As illustrated in Figure 2.25, the Chebyshev filter most closely approximates the amplitude response of an ideal high-pass filter. Unfortunately, the corresponding phase characteristics and, consequently, time-domain performance are relatively poor. While the ideal low-pass filter is zero-phase, the Chebyshev filter possesses a non-zero and, moreover, strongly non-linear phase spectrum. As a result, individual frequency components comprising a signal entirely within the Chebyshev's pass-band experience variable time-delays, resulting in distortion of the time-domain wavelet. In contrast, the Bessel filter possesses an optimally linear phase spectrum at the expense of a more gradual transition from pass-band to reject-band. In other-words, the Bessel filter most closely approximates a constant phase-shift or constant time-delay filter and, thus, provides optimum time-domain performance. Finally, the Butterworth filter offers a tradeoff between time-domain and frequency-domain performance. In particular, the Butterworth filter possesses an optimally flat pass-band and phase characteristics between those of the Chebyshev and Bessel filters.

For present application, time-domain characteristics are of paramount importance and, consequently, the Bessel filter was selected to avoid potential timing errors associated with

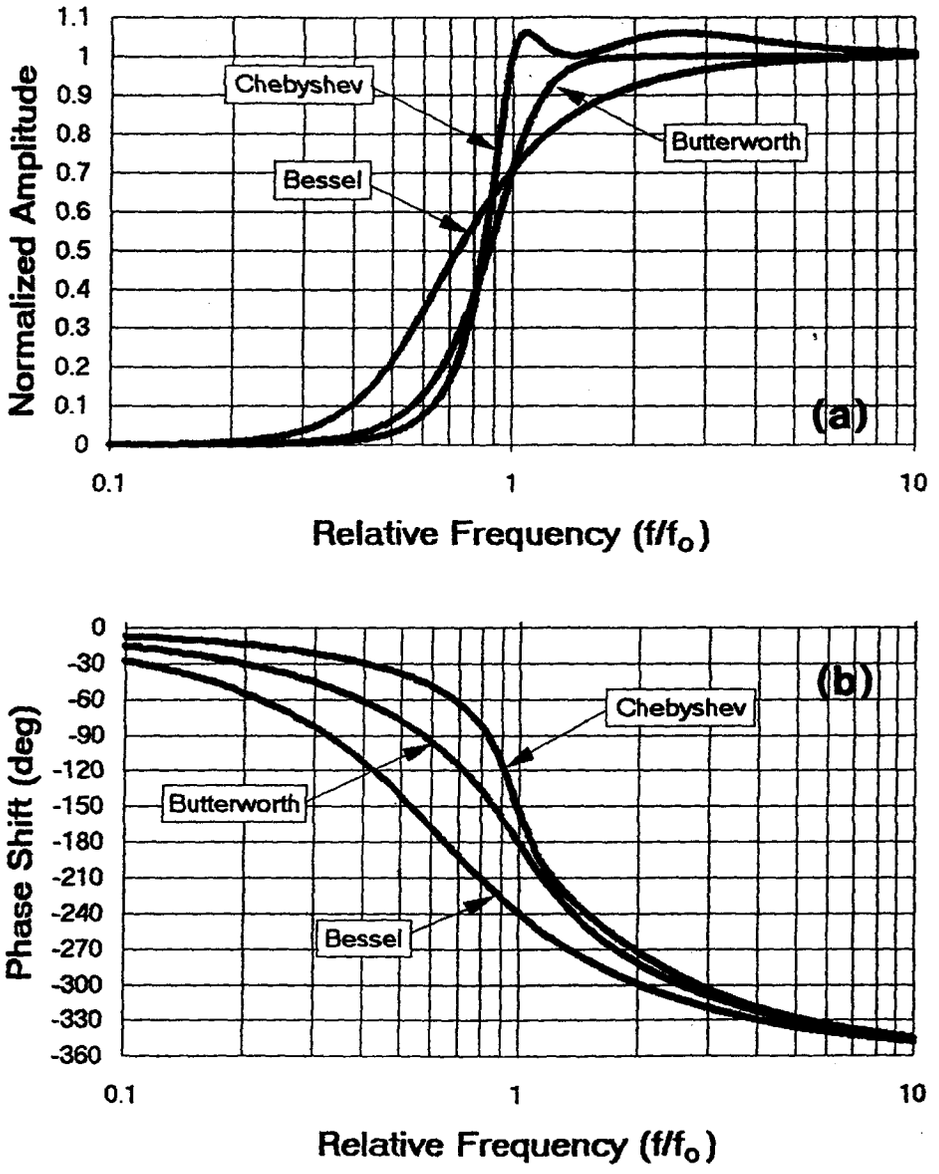

Figure 3.26. 4-pole VCVS High-pass active filter responses. (a) Amplitude and (b) phase spectra for fourth-order Chebyshev, Butterworth and Bessel filters. The ideal high-pass amplitude response is indicated by a dashed curve.

wavelet distortion. Steeper transition from passband to stopband is achieved by cascading an additional 2-pole VCVS network with the principal filter. The theoretical frequency response of the resulting fourth-order Bessel filter is compared with corresponding Chebyshev and Butterworth response characteristics in Figure 2.26. The roll-off rate for the Bessel filter increases from about 10 dB/octave for a 2-pole filter to approximately 13 dB/octave for the 4-pole filter. Figure 3.27 displays actual calibration curves for 2-pole Bessel filters with corner frequencies (-3 dB) of 175, 225 and 250 Hz. As calibration measurements were made after passage through the analog input stage of the seismic recorder, the amplitude response curves are band-limited by the recorder's high-frequency roll-off characteristics. The recorder's frequency response is also depicted with the filter section out.

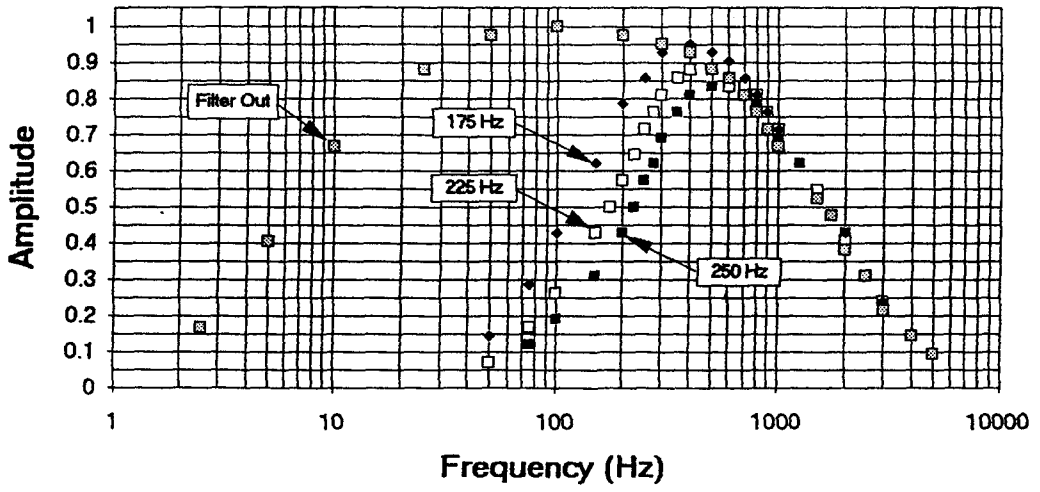

Figure 3.27. Calibrated amplitude response curves for 2-pole active Bessel filter after passage through ES-1225 analog input section. Response curves are depicted for corner frequencies 175, 225 and 250 Hz. The amplitude response of the ES-1225 is depicted with filter section out.

The effect of pre-emphasis filtering is illustrated in Figures 2.28 and 2.29. Here we compare the unfiltered .22 cal. source wavelet and associated spectra from Figures 3.9 and 3.10 with the corresponding wavelet and spectra after pre-emphasis filtering at 250 Hz (2-pole Bessel). Note that pre-emphasis filtering has resulted in a significantly higher dominant frequency and, consequently, improved resolving power. The filtered source

wavelet in Figure 2.28 is representative of wavelets recorded in connection with the full-scale model experiment described in the following chapter.

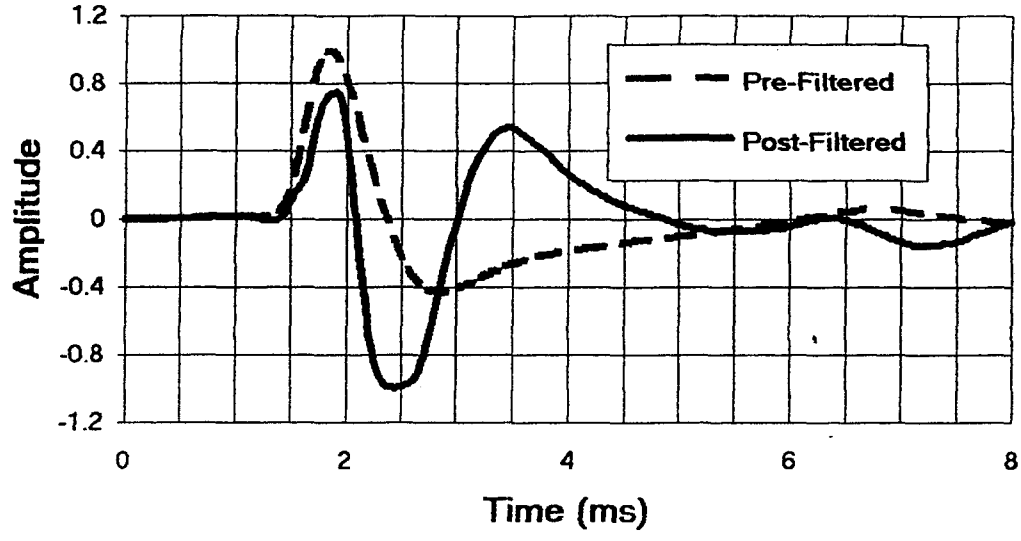

Figure 3.28. Effect of pre-emphasis filtering on recorded source wavelet generated by the .22 cal. source device. Representative wavelets before and after application of a 250 Hz, 2-pole, high-pass Bessel filter.

Finally, the filter unit also comprises a 12-pole rotary switch allowing the filtered signal to be diverted to a preselected recorder channel. By recording data from successive traverse positions on consecutive channels, we assemble 12-trace segments in the recorder's memory that are later joined by computer to produce a seismic profile of the subsurface.

3.2.5 Seismic Recorder

On selecting a seismic recorder for high resolution applications, the most critical specifications are frequency response, sampling frequency and dynamic range. The current system is assembled around a Geometrics ES-1225 12-channel digital seismograph having flexible gain control, interactive CRT display and signal enhancement capability. The effective frequency response $S_r(f)$ is displayed in Figure 3.27. Although a bandwidth of roughly 5 Hz - 1 kHz and sampling frequency to 40 kHz are more than sufficient, the available dynamic range is only adequate.

Dynamic range is dictated by the number of bits comprising the binary output of

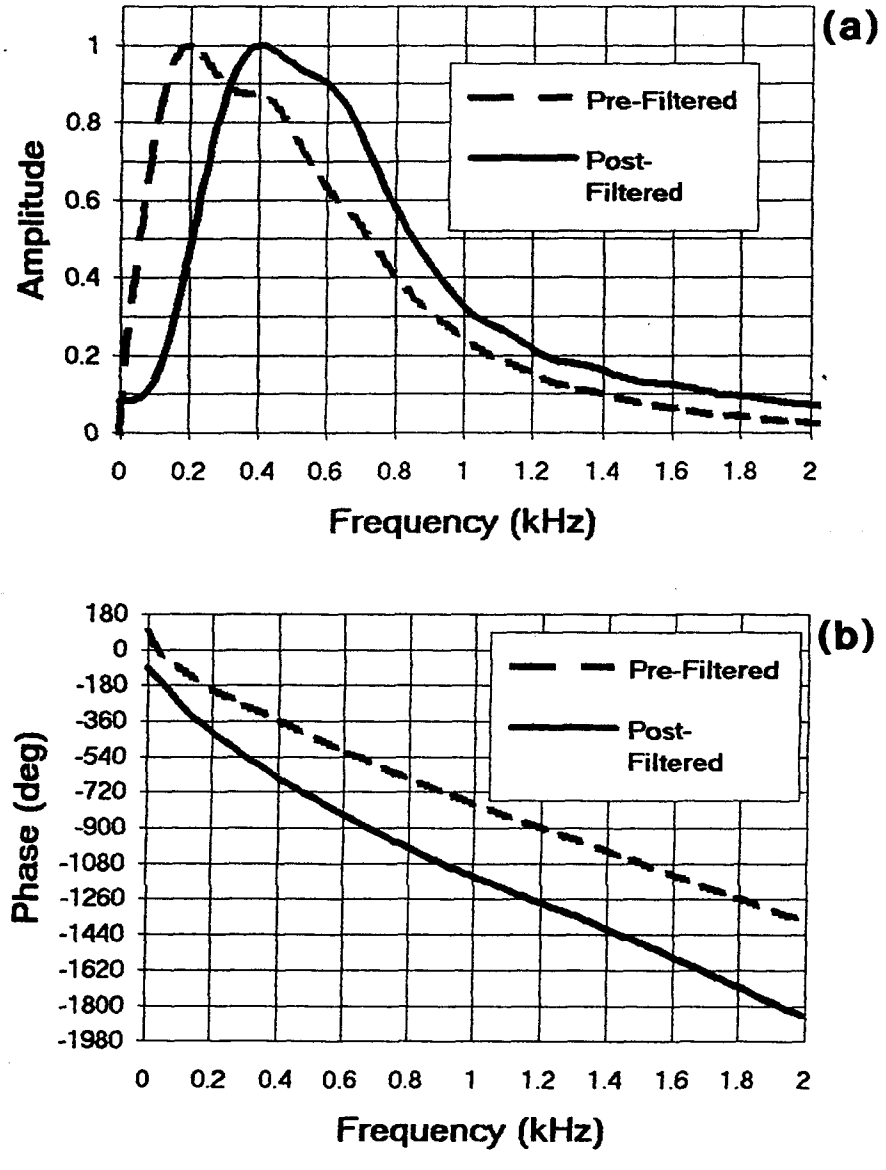

Figure 3.29. Effect of pre-emphasis filtering on (a) amplitude and (b) phase spectra associated with corresponding source wavelets in Figure 3.28.

the analog to digital (A/D) converter and is simply the ratio of largest to smallest digital numbers that can be represented. Since the ES-1225 uses an 8-bit A/D converter, dynamic range cannot exceed 48 dB. A new generation of engineering seismographs typically offers dynamic range from 72-96 dB and we expect substitution of such an instrument to yield a ready improvement in overall system performance. Currently, however, our aim is to demonstrate that sufficient resolving power can be achieved with only a modest seismograph.

3.3 Summary and Conclusion:

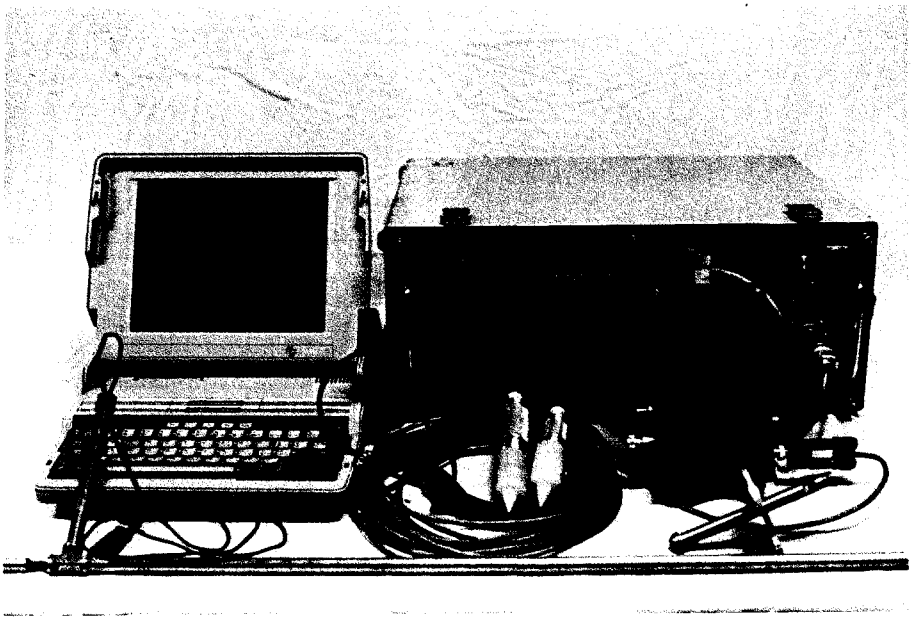

Figure 3.30. Prototype data acquisition system.

The resulting prototype system is depicted in Figure 3.30. Its net frequency response or transfer function is given by equation 3.21

$$\Sigma(f) = S_s(f)\, S_e(f)\, S_d(f)\, S_f(f)\, S_r(f),$$

where approximate or generalized transfer functions for individual system components $S_s(f)$, $S_e(f)$, $S_d(f)$ and $S_f(f)$ are given by equations (3.25), (3.56-7), (3.62) and (3.67) and illustrated in Figures 3.3, 3.15, 3.22 and 3.25, respectively. In addition, the effective transfer function of the seismic recorder $S_r(f)$ is depicted in Figure 3.27. As their interpretation

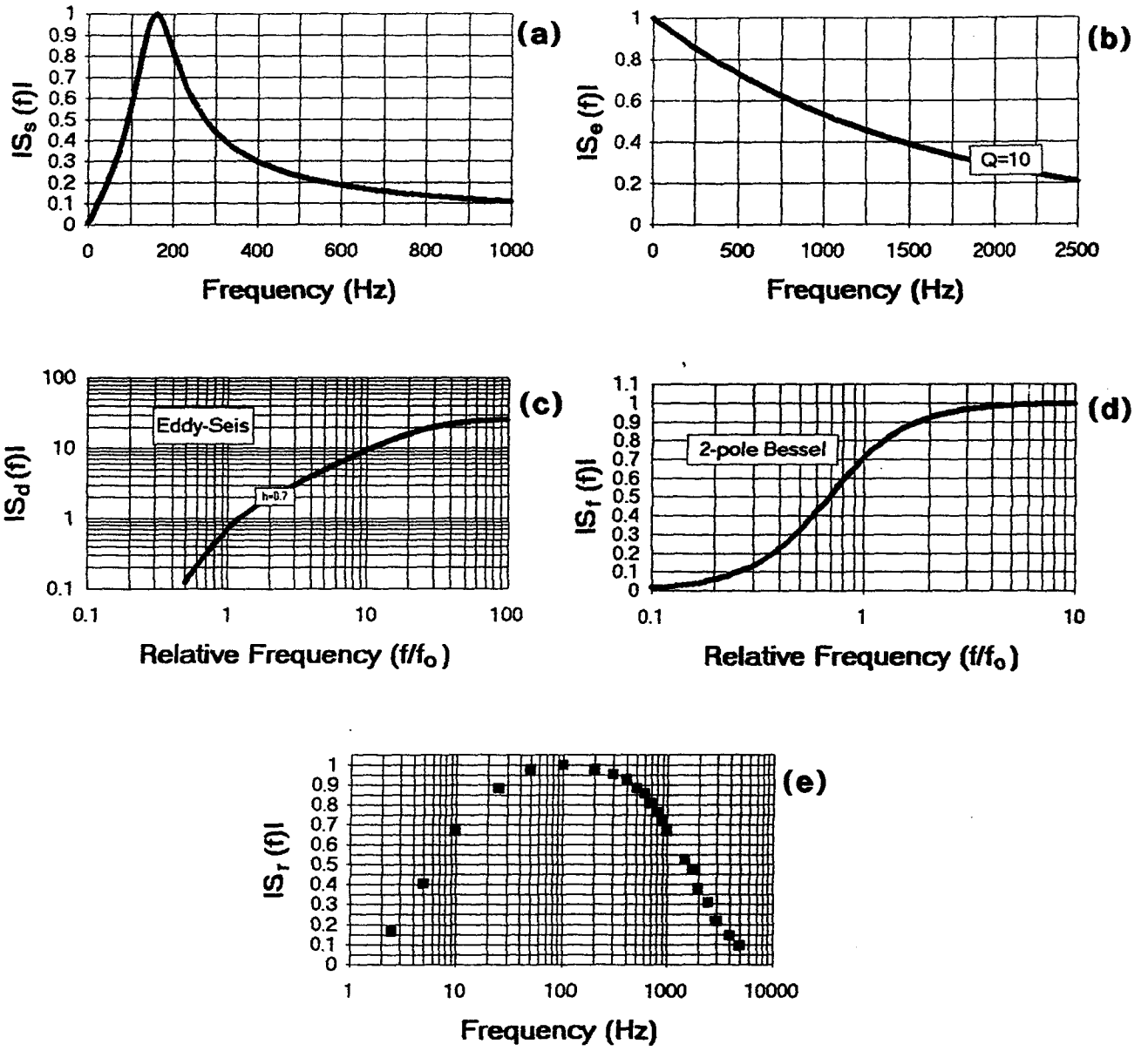

Figure 3.31. Summary of component amplitude responses: (a) source $|S_s(f)|$ with R=R/r=0.2, γ=0.417; (b) earth filter $|S_e(f)|$ with Q_0=10; (c) Eddy-Seis detector $|S_d(f)|$ with f_0=17 Hz; (d) Bessel pre-emphasis filter $|S_f(f)|$ with f_0=250 Hz; (e) ES-1225 recorder $|S_r(f)|$ empirical.

is more intuitive, corresponding amplitude responses are summarized in Figure 3.31. In short, despite frequency characteristics that are vastly superior to those of surface-impact devices, the .22 cal source spectrum (Figure 3.31a) remains deficient of high-frequency content. Subsequent transmission through near-surface soils and sediments results in further attenuation of high-frequencies (Figure 3.31b) and associated dispersion, producing an ever broader wavelet possessing proportionately lower resolving power. In contrast, the frequency response of the detector (Figure 3.31c) is inherently high-pass and, consequently, counteracts the earth filter by attenuating frequencies below its natural frequency and enhancing higher frequencies. Introduction of a high-pass pre-emphasis filter (Figure 3.31d) reinforces low-frequency attenuation by the detector and provides significantly more flexibility to yield a balanced wavelet spectrum and, consequently extended bandwidth. Of course, bandwidth is ultimately limited by the recorder's dynamic range. To the extent that the wavelet possesses frequency characteristics matching those of the recorder (Figure 3.31e), we have achieved our objective.

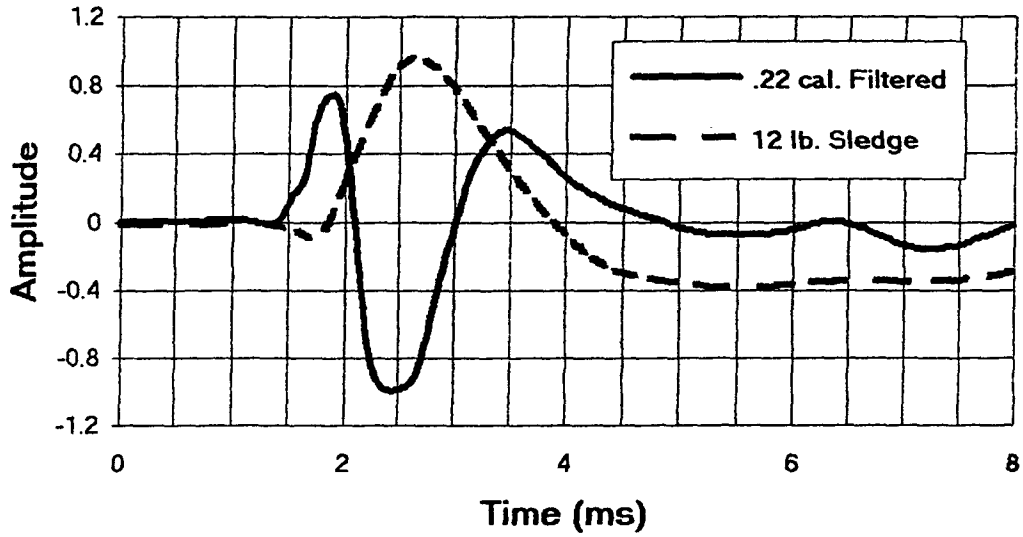

Figure 3.32. Improved resolving power. Comparison between unfiltered wavelet generated by 12 lb. sledge hammer and .22 cal. wavelet with 250 Hz pre-emphasis filtering.

Figures 3.32 and 3.33 provide a practical indication of our success in achieving extended resolving power. Here we compare the wavelet generated by a 12 pound sledge

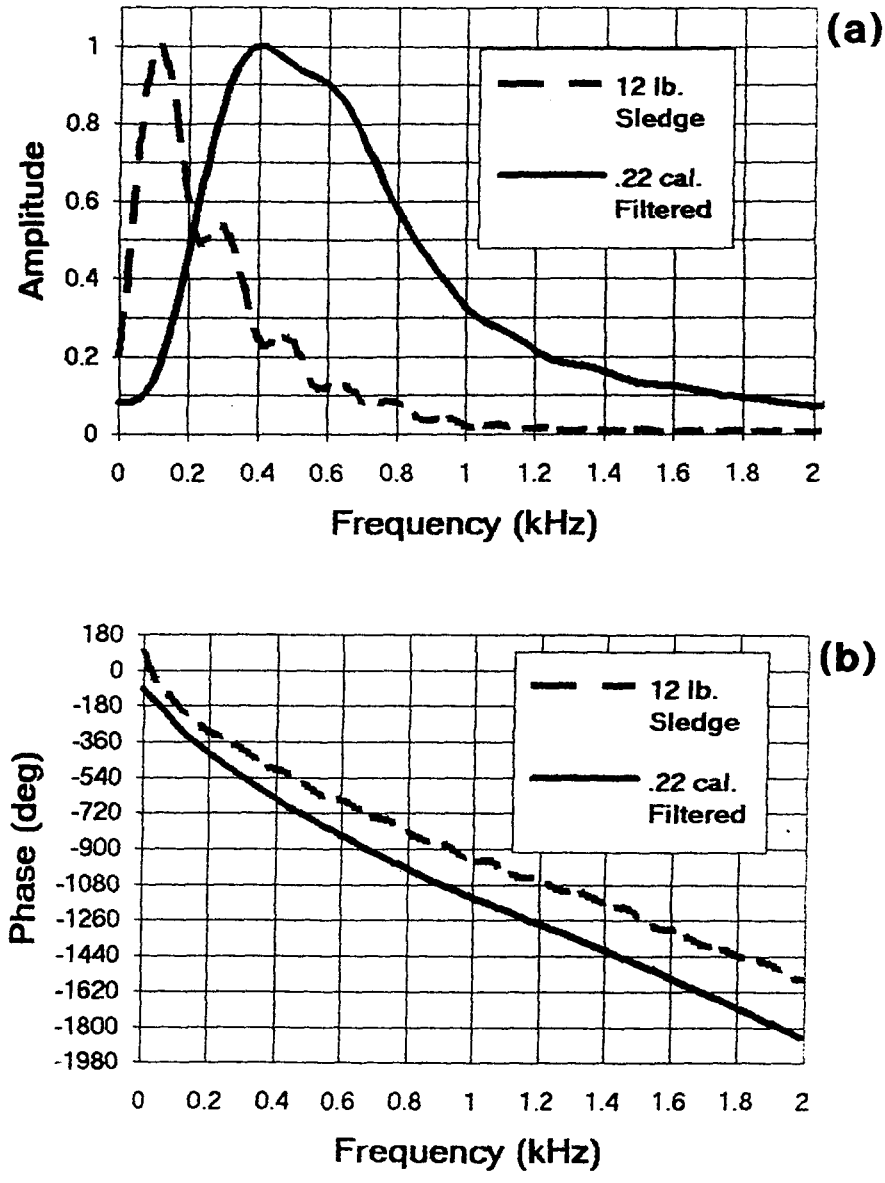

Figure 3.33. Improved resolving power. (a) Amplitude and (b) phase spectra associated with corresponding wavelets in Figure 3.32.

hammer with that obtained using the special purpose source device described in section 3.2.1 with 250 Hz pre-emphasis filtering. The wavelets possess dominant frequencies of approximately 250 Hz and 550 Hz, respectively with a corresponding three-fold increase in bandwidth. In a qualitative sense, this comparison illustrates the potential for improved resolution of archaeological features. Having said this, it must be emphasized that extended resolving power is not a matter of instrumentation alone. Judicious design and selection of acquisition parameters is crucial for realization of potential resolving power. In the following chapter data acquisition techniques are discussed in connection with a full-scale model experiment conducted to assess the practical utility of the prototype system.

Chapter 4

DATA ACQUISITION AND MODEL EXPERIMENTS

For summaries of most geophysical methods (for surveying of archaeological sites) see Aitken (1974) or Tite (1972).

J. W. Weymouth, 1985

4.1 Introduction:

To assess the practical limitations of the prototype system described above, a full-scale subsurface model has been constructed. By comparing experimental seismic profiles with the known model geometry, we obtain a practical appraisal of system performance and useful insight into the seismic expression of a certain class of archaeological remains. A photograph and plan diagram of the model are presented in Figure 6.

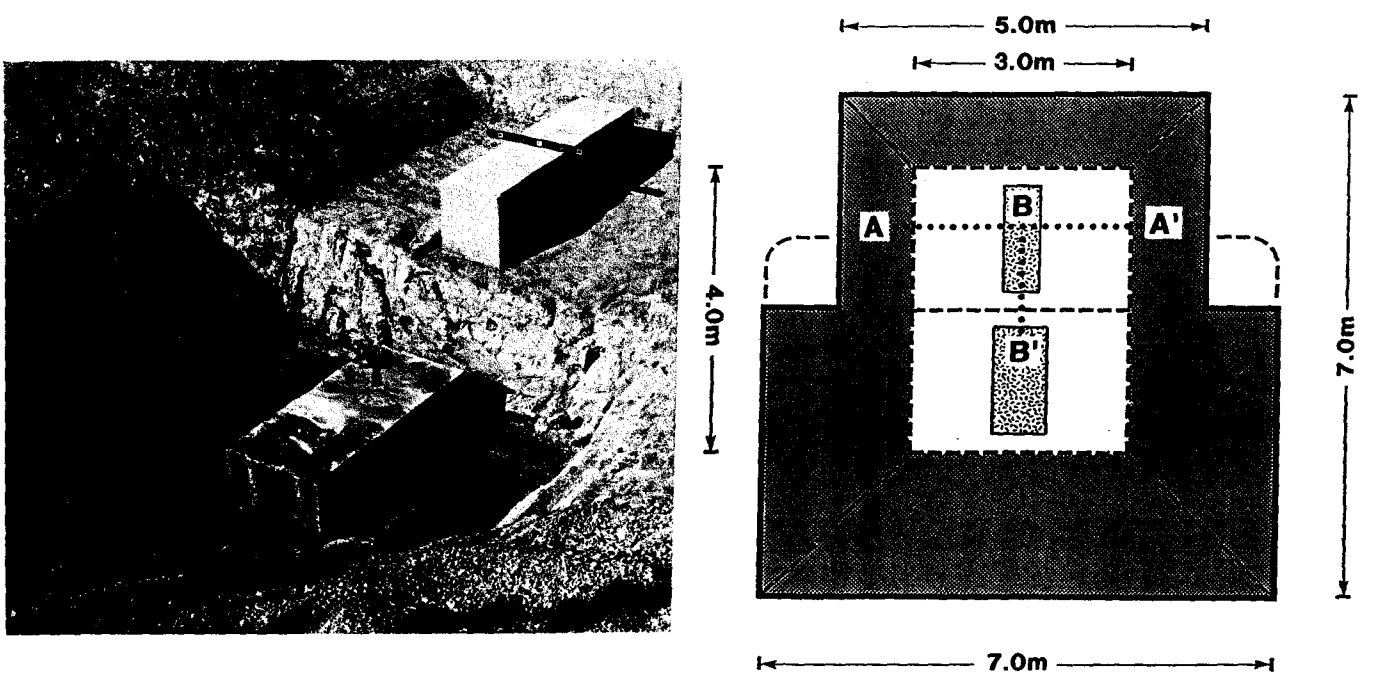

Figure 4.1. (a) Photograph of full-scale subsurface model. (b) Plan diagram indicating dimensions of the model facility. Shallow (1 m base) and deep (2 m base) model blocks are, respectively, 0.4 m and 0.6 m wide.

A stepped trench, roughly 3.0 m wide, was excavated to depths of approximately 1.0 and 2.0 m below the ground surface. Each level extends roughly 2.0 m along the axis of the the trench. In order to reduce any effect of the trench itself on subsequent experiments, the walls slope upward from the base of each level at approximately 45°, resulting in

overall dimensions of about $7 \times 7m^2$ at the surface. After preparing the void, forms were constructed and concrete poured to produce the simple model pictured in Figure 4.1a.

The dimensions of the model were chosen to approximate those of common architectural remains such as walls and foundations. Upper and lower blocks are both approximately 2.0 m long and 1.0 m high and have width of 0.4 m and 0.6 m respectively. After precise mapping in reference to a permanent datum, the void was back-filled with homogeneous sand.

4.2 Optimum Offset Data Acquisition:

There are two principal approaches to the acquisition of high-resolution near-surface seismic reflection data; small-scale, multichannel common-depth-point (CDP) techniques (Knapp and Steeples, 1986; Steeples and Miller, 1988) and the single channel optimum offset technique (Hunter et al., 1984; Hunter and Pullan, 1989). Both methods rely on preliminary walk-away noise tests to identify a range of source-receiver offsets over which the reflection from a given target interface is received with minimum interference from source generated noise.

The walk-away test may be conducted in either multi-channel or single channel mode. In single channel mode, the source device is activated repeatedly at some fixed position and the source-detector offset is extended by an incremental distance with each shot. Resulting data are displayed as a two dimensional function of time and offset as illustrated in Figure 4.2a for simple case of a layer over a half-space. In connection with multi-channel data acquisition, this result is ordinarily referred to as a common shot gather. Associated first-order ray-paths are depicted in Figure 4.2b. Corresponding transit-time distance relations are (e.g. Telford, et al., 1990)

1. Direct Ground Wave:

$$t_1(x) = \frac{x}{\alpha_0} \tag{4.1}$$

2. Reflected Wave:

$$t_2(x) = \left[\left(\frac{x}{\alpha_0}\right)^2 + \left(\frac{2z}{\alpha_0}\right)^2\right]^{1/2} \tag{4.2}$$

or

$$t_2^2(x) = \frac{x^2}{\alpha_0^2} + t_0^2,$$

where $t_0 = 2z/\alpha_1$ denotes the normal incidence transit time.

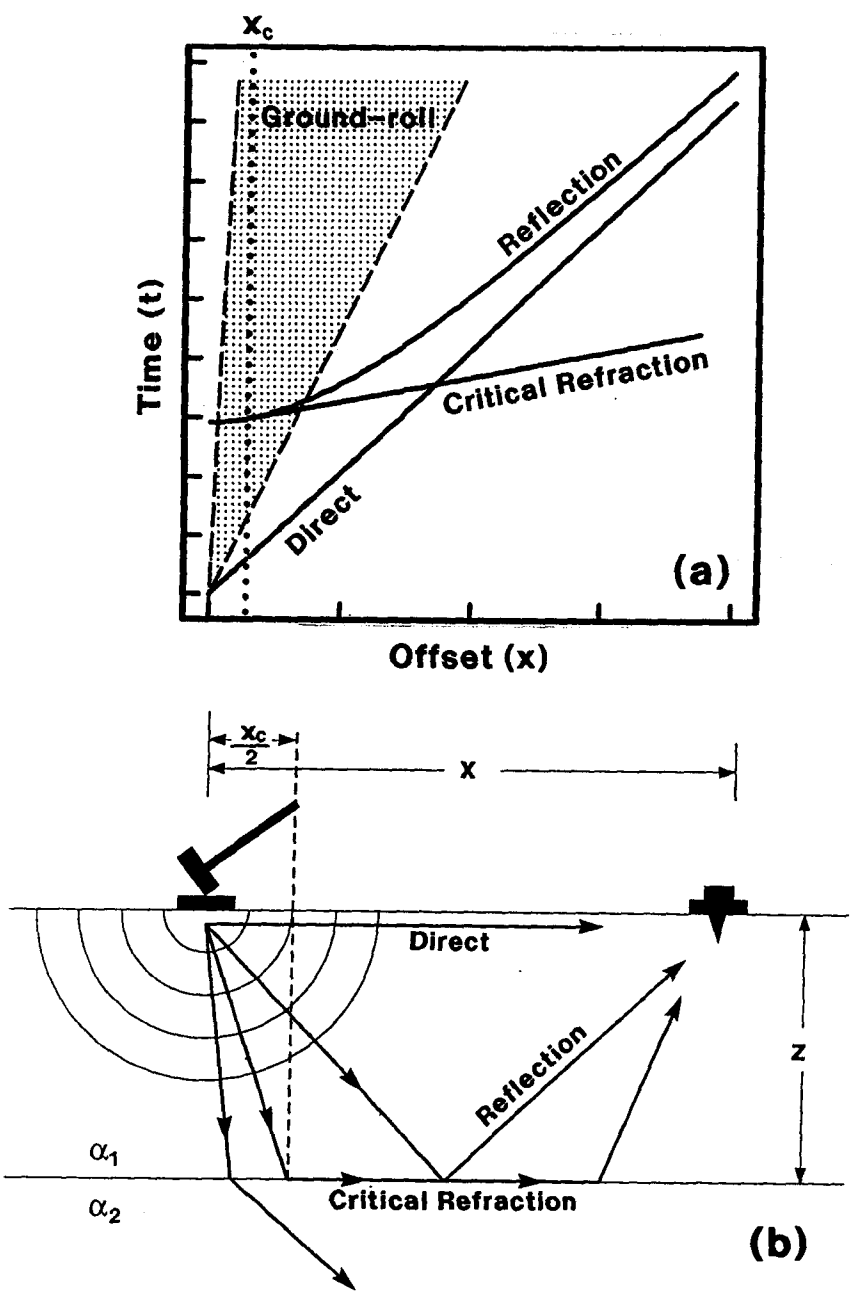

Figure 4.2. Walk-away noise test. (a) Time-distance diagram or common source gather acquired in connection with the simple model subsurface in (b). (b) Characteristic first-order ray-paths within a layer over a half-space for $\alpha_0 < \alpha_1$. Associated event are identified in (a).

3. Critically Refracted Wave:

$$t_3(x) = \frac{x}{\alpha_1} + t_i, \tag{4.3}$$

where

$$t_i = \frac{2z}{\alpha_0 \alpha_1} \left(\alpha_1^2 - \alpha_0^2\right)^{1/2} \tag{4.4}$$

denotes the associated intercept time.

In addition, we define the critical distance

$$x_c = 2z \tan\theta_c = \frac{2z\alpha_0}{(\alpha_1^2 - \alpha_0^2)^{1/2}}, \tag{4.5}$$

where $\theta_c = \sin^{-1}(\alpha_0/\alpha_0)$ represents the critical angle of incidence.

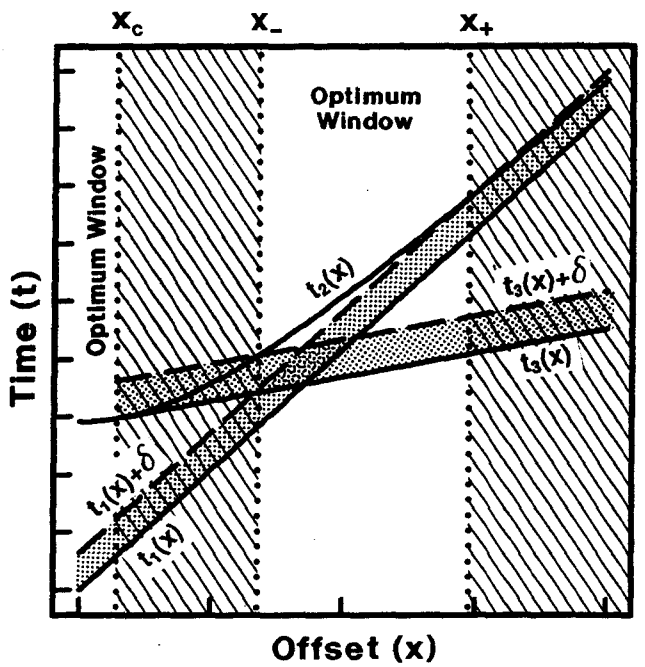

Figure 4.3. Time-distance diagram illustrating the definition of optimum windows as offset ranges over which the reflection is observed as an isolated event. Open regions identify optimum windows while cross-hatched regions indicate interference zones. δ denotes the effective wavelet duration, x_c represents the critical distance and x_- and x_+ represent boundary parameters defined by $t_2(x_-) = t_3(x_-) + \delta$ and $t_2(x_+) = t_1(x_+) + \delta$, respectively.

Note that the critically refracted arrival does not exist for $x < x_c$ and, consequently, in the absence of ground-roll, the reflection is observed as an isolated event at offsets within the critical distance as illustrated in Figure 4.3. This offset range $0 \leq x \leq x_c$ is the optimum

window identified by Hunter et al. (1984). In fact, Hunter et al. extended the window beyond the critical distance, noting that reflection amplitude commonly peaks at the critical distance and, consequently, dominates the so-called interference wavelet in near proximity to the critical distance. In practice, dispersive surface wave or ground-roll travels radially outward from the shot-point at speeds of approximately 0.1-0.6α_0 and, consequently, resides within the optimum window as illustrated in Figure 4.2. Although, this interference poses a potential restriction on utilization of this near-source optimum window, in many cases, this limitation can be overcome by careful selection of instrumentation and real-time pre-emphasis filtering.

As illustrated in Figure 4.3, a second optimum window exists at offsets sufficiently beyond the critical distance to avoid interference between reflected and critically refracted arrivals and within an upper bound associated with the onset of interference between the reflected and direct wave arrivals. Observe that as offset x becomes large compared with target range z, the reflection transit-time $t_2(x)$ approaches that of the direct arrival $t_1(x)$. To quantify the resulting optimum window, we must specify an additional parameter; the effective pulse duration δ. It follows that the lower boundary of the optimum window is the offset for which the difference between reflected and critically refracted transit-times is equal to the effective pulse duration (ie. $t_2(x) - t_3(x) \geq \delta$). From equations (4.3) and (4.4), we obtain

$$x_- = x_c + \frac{\delta\alpha_0\alpha_1^2}{(\alpha_1^2 - \alpha_0^2)}\left\{\frac{\alpha_0}{\alpha_1} + \left[1 + \frac{4z}{\delta\alpha_0\alpha_1}(\alpha_1^2 - \alpha_0^2)^{1/2}\right]^{1/2}\right\}. \tag{4.6}$$

Similarly, the upper bound is that offset for which the transit-time difference between reflected and direct arrivals equals the effective pulse duration (ie. $t_2(x) - t_1(x) \geq \delta$). Equations (4.2) and (4.3) yield

$$x_+ = \frac{2z^2}{\alpha_0\delta} - \frac{\alpha_0\delta}{2}. \tag{4.7}$$

The significance of limiting parameters x_- and x_+ is illustrated in Figure 4.3, where in addition to transit-time-distance relations $t_1(x)$, $t_2(x)$ and $t_3(x)$, we display $t_1(x) + \delta$ and $t_3(x) + \delta$, representing the temporal extent of direct and critically refracted wavelets,

respectively. The optimum window is simply the range of offsets over which the reflection event $t_2(x)$ does not reside within bounded regions $t_3 \leq t \leq t_3 + \delta$ and/or $t_1 \leq t \leq t_1 + \delta$. Note that, in general, effective pulse duration is a transit-time and, consequently, offset dependent parameter due to progressive attenuation and dispersion discussed in the previous chapter. It follows from equations (4.5)-(4.6) and Figure 4.3 that the extent of the actual optimum window will be correspondingly reduced. We shall return to the influence of various model parameters on optimum window characteristics however, first, let us discuss the practical implementation of optimum window data acquisition techniques.

While the optimum window CDP method seeks to deploy an array of detectors substantially within one of the previously defined optimum windows, the optimum offset technique identifies a particularly favorable offset within the window for deployment of a single detector. In either case, having established the optimum source-receiver offset, this configuration is fixed and redeployed at successive intervals along a survey transect to acquire a continuous seismic image of the subsurface.

For present application, we have avoided multichannel recording techniques in favour of a single source-receiver pair in optimum-offset configuration to simplify data acquisition and facilitate intuitive assessment unprocessed profiles. Compared with the optimum offset technique, CDP profiling is conceptually complicated and requires substantial post-acquisition processing, including sorting, velocity analysis, normal-moveout (NMO) correction and subsequent stacking, to yield an interpretable result. Furthermore, despite the great advantage of multiple geophone arrays for spatial filtering of ground-roll in large scale seismic exploration, an exhaustive analysis presented in Appendix B demonstrates that these techniques are of little practical use in small-scale, high-frequency applications including archaeological exploration. In addition, the nature of certain archaeological targets is not well suited for imaging by CDP techniques. In particular, the CDP method was developed in connection with petroleum industry exploration and mapping of semi-continuous geo-structural boundaries and relies entirely on velocity estimates derived from moveout characteristics of associated reflection events. Consequently, while CDP tech-

niques may be advantageous for delineating archaeological stratigraphy, they are not especially well suited for imaging discontinuous archaeological features, including foundations, walls, roads, etc., where the primary signal is scattered rather than reflected energy. In fact in the absence of well defined stratigraphic reflectors, alternative approaches to velocity estimation are critical. To this end, a diffraction-based approach to seismic velocity analysis is developed in Appendix A. In short, the remaining benefit of multi-channel CDP data acquisition, namely, improved signal-to-noise ratio, is in most instances not worth the more cumbersome acquisition logistics and time-consuming post-acquisition data processing. In fact, at the expense of high-frequency content, signal-to-noise ratio can be improved in optimum offset mode by stacking several single-fold shot gathers at each source-receiver location. Such a trade-off may be necessary for detection of deeply buried targets.

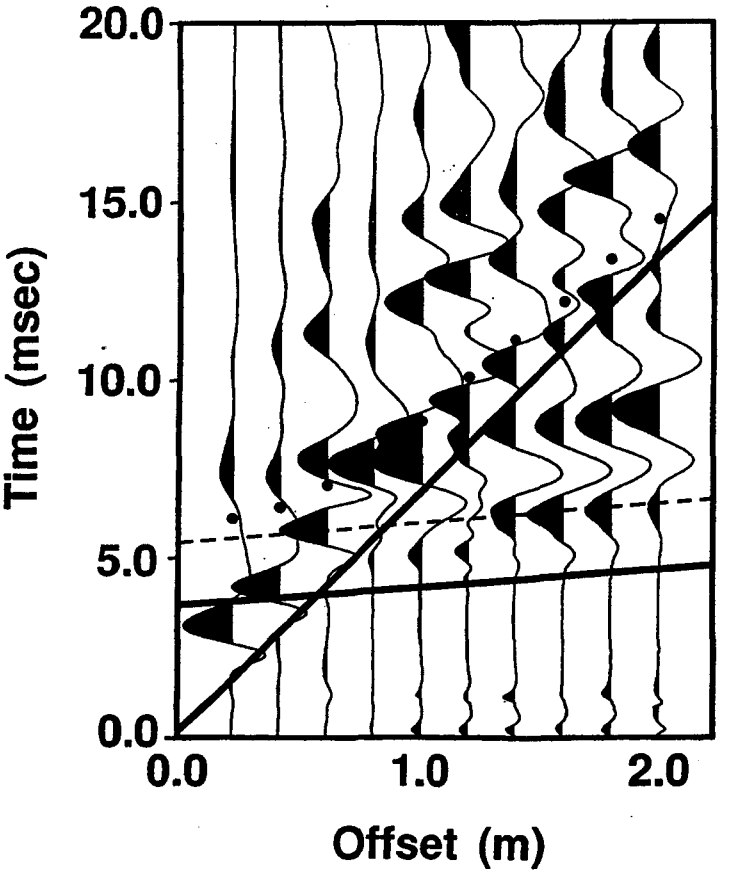

Figure 4.4. Walk-away noise test conducted along the axis of the shallow model block, depicting "best-fit" lines to direct and critically refracted arrivals. Associated velocity estimates α_0=150 m/s and α_1=2000 m/s follow as corresponding reciprocal slopes. Dots indicate predicted reflection transit-times using the foregoing velocities and known target range z=0.5 m.

4.3 Preliminary Model Experiments:

Figure 4.4 displays a walk-away noise test acquired along the axis of the shallow model block with an offset interval of 0.2 m and pre-emphasis filtering at 275 Hz. Offset dependent gains were applied to yield a roughly constant average amplitude. Despite effects due to the block's finite dimensions, these data display the characteristic arrivals illustrated in Figure 4.2. "Best-fit" lines to direct and critically refracted arrivals yield corresponding velocity estimates of approximately α_0=150 m/s and α_1=2000 m/s, respectively, for the sand fill and concrete model. These values are consistent with empirical data tabulated by Molotova and Yassil'ev (1960) and Press (1966)†. Corresponding reflection transit-times computed for a target at z=0.5 m are also indicated. Although there is good agreement between predicted transit times and observed arrivals, identification of the reflection event would have been difficult, at best, without *apriori* knowledge of subsurface structure. In this regard, it must be appreciated that a useful walk-away test was acquired only as a result of *apriori* information. In addition, it is noted that the observed cross-over distance

$$x^* = 2z\left(\frac{\alpha_1 + \alpha_0}{\alpha_1 - \alpha_0}\right)^{1/2} \tag{4.8}$$

and refraction intercept time (equation (4.4)) lead to substantial underestimation of target depth. This disagreement is probably attributable to systematic error in picking the critically refracted phase. Červeny and Ravindra (1971) demonstrate that the critically refracted (head wave) wavelet is phase shifted by -90° relative to the source signature. In view of this relative phase-lead and the existence of a minor precursor to the effective direct arrival onset, the refraction event could be "picked" later as indicated in Figure 4.4, giving an identical velocity but implying a target depth in nearer agreement with the known value.

Figure 4.5 displays optimum window systematics as a function of refractive index α_0/α_1, target range z and wavelet duration δ. In each case, the corresponding model parameter is varied over a plausible range while holding the remaining parameters fixed at

† For discussion of "sub-acoustic" compressional wave velocities in multiphase media see Lester (1947) and Patterson (1956).

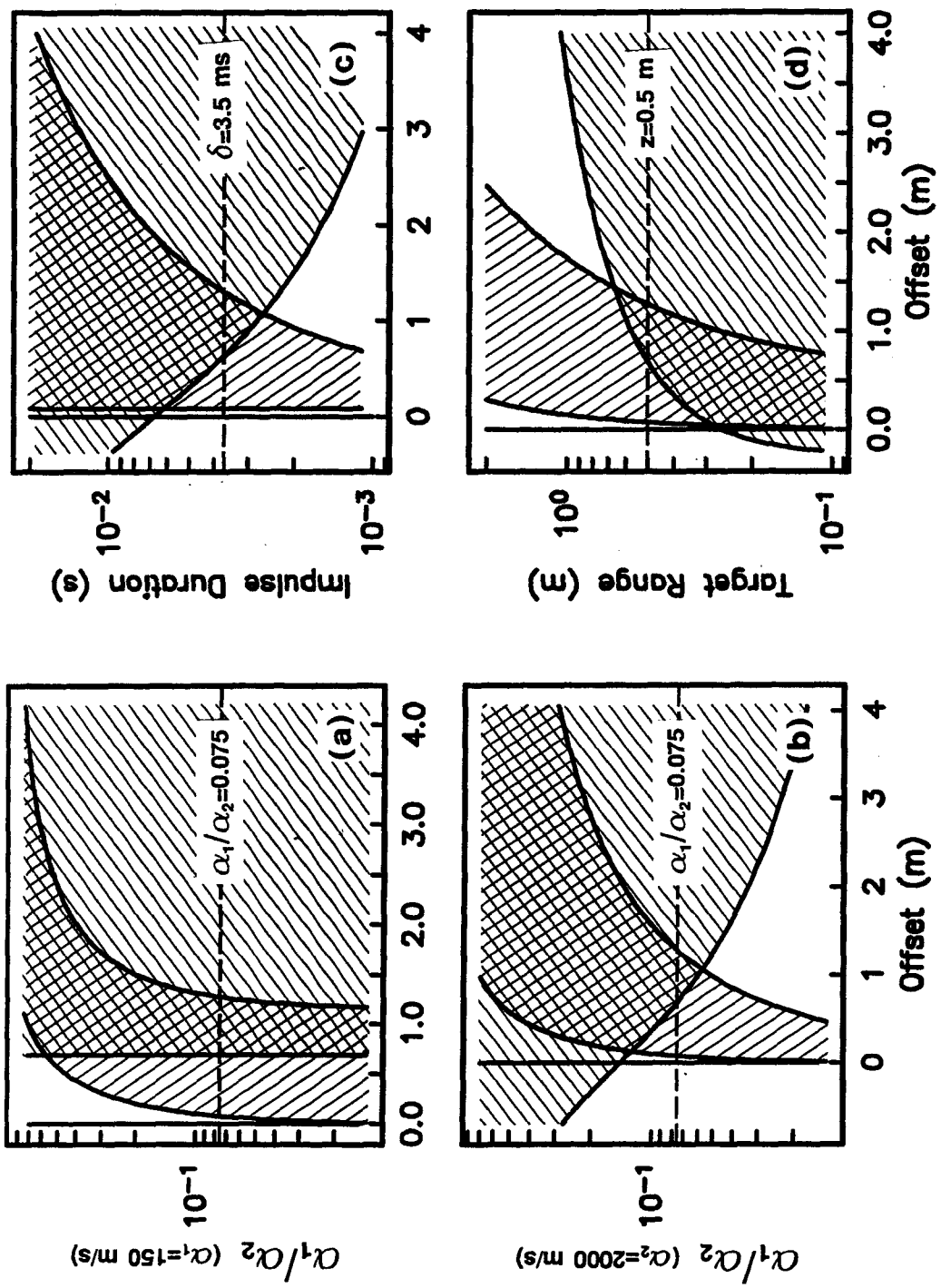

Figure 4.5. Optimum window diagrams illustrating dependent boundary parameters x_c, x_- and x_+ as functions of independent model parameters (a) Refractive index (α_0/α_1) with $\alpha_0 = 150$ m/s, δ=3.5 ms, z=0.5 m; (b) Refractive index (α_0/α_1) with $\alpha_1 = 2000$ m/s, δ=3.5 ms, z=0.5 m; (c) Impulse duration (δ) with $\alpha_0 = 150$ m/s, $\alpha_1 = 2000$ m/s, z=0.5 m; (d) . Target range (z) with $\alpha_0 = 150$ m/s, $\alpha_1 = 2000$ m/s, δ=3.5 ms. Dashed lines indicate reference model values.

reference values α_0=150 m/s, α_1=2000 m/s, z=0.5 m and δ=3.5 ms. It is observed that only a narrow near-source optimum window ($0 \leq x \leq x_c \approx 8$ cm) exists for the reference model. In practice, the minimum source-detector offset was restricted by recorder saturation to 0.2 m and on the basis of the walk-away test in Figure 4.3, an optimum offset of 0.3 m was selected. Since this offset lies beyond the predicted critical distance it follows that the event identified as a reflection from the model is actually an interference wavelet, including critically refracted or head-wave energy as well. Associated error in picking the "reflection" onset and, consequently, depth determinations are certainly well within experimental error stemming from data acquisition. Before turning our attention to resulting optimum offset profiles acquired over the model, let us return presently to the optimum window systematics presented in Figure 4.5. It is observed that useful optimum windows would have existed under a number of plausible conditions, including increased target range, either an increase or decrease in refractive index and, of course, reduced pulse duration. Calculations of this nature will be critical for the planning and design of future field experiments, particularly in cases where targets are localized discontinuous features, preventing acquisition of useful walk-away noise tests. In particular, it should be appreciated that the walk-away test in Figure 4.4 was only possible due to a-priori knowledge of model geometry.

Preliminary optimum offset seismic soundings have been conducted along orthogonal traverses of the shallow model block as denoted A-A' and B-B' in Figure 4.1. Resulting data profiles and corresponding idealized cross-sections are depicted in Figures 4.6 and 4.7. The data are in raw form. The source-receiver configuration is indicated in Figure 4.6a with particular values of optimum offset (x_o) and midpoint interval (Δx) denoted in Figures 4.6a and 4.7a. The continuous event at roughly 2.0 msec on both data sections is the direct arrival from source to receiver. Local variability in the onset of this event is attributed to acquisition error, including uncertainties in source-detector locations and local velocity variations. For example, the obvious "pull-up" around x=1.0 m in Figure 4.7b is attributed to near-surface compaction and consolidation of fill surrounding the

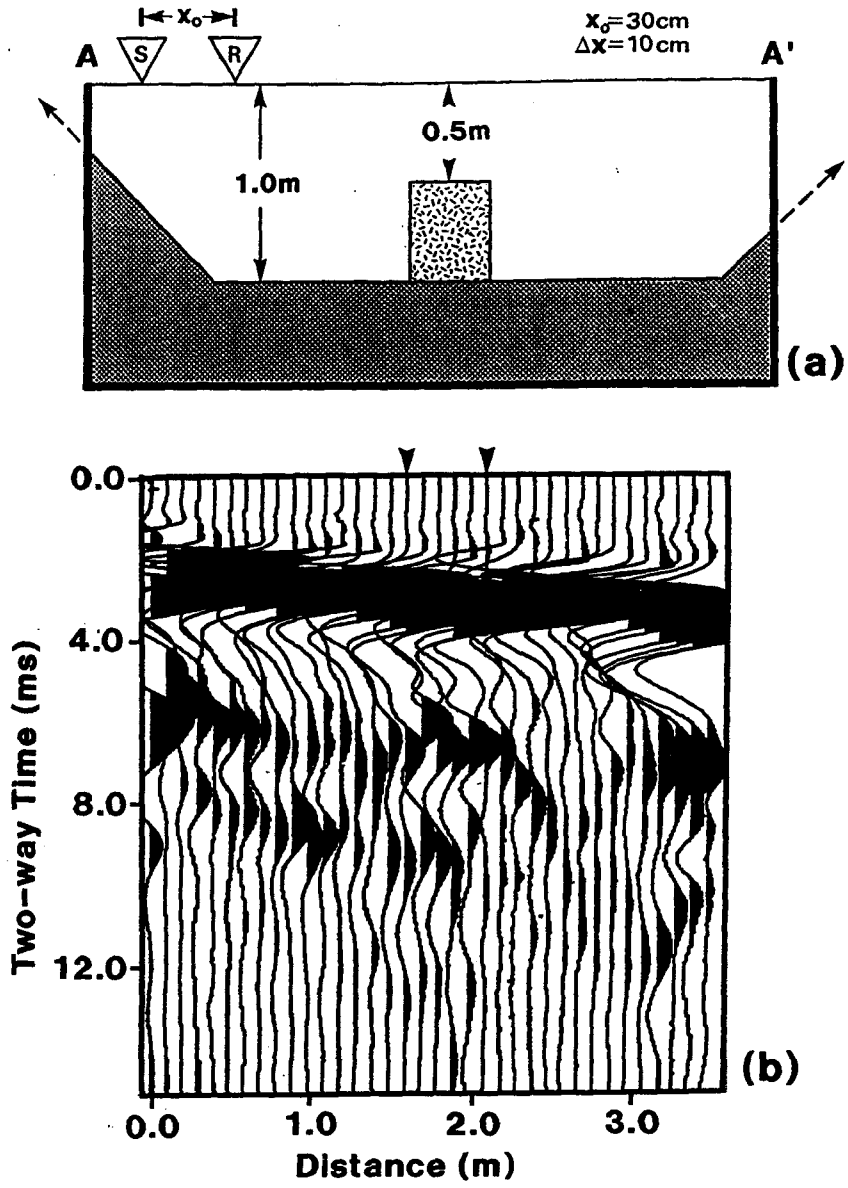

Figure 4.6. (a) Idealized model cross-section along transect A-A' and (b) corresponding optimum offset seismic profile. Arrows indicate approximate locations of model block edges. x_o and Δx denote optimum source-receiver offset and spatial sampling interval, respectively.

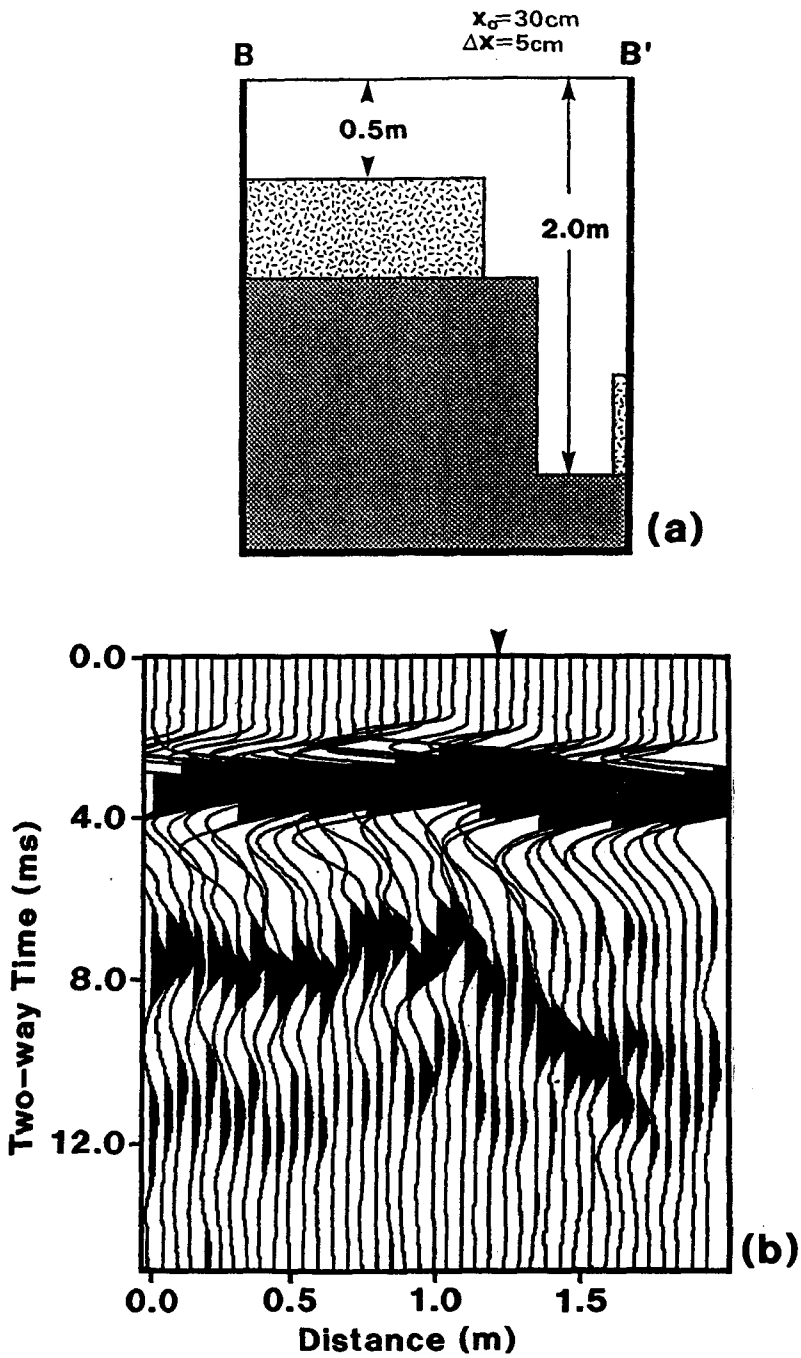

Figure 4.7. (a) Idealized model cross-section along transect B-B' and (b) corresponding optimum offset seismic profile. Arrow indicates approximate location of model block edge. x_o and Δx denote optimum source-receiver offset and spatial sampling interval, respectively.

shot-point used for acquisition of walk-away noise tests described in the previous section. Similarly, the gradual increase in onset time observed with increasing distance in Figure 4.6b, is associated with a corresponding increase in effective fill velocity toward the the center of the model. A simple "first-order" static correction could be accomplished by aligning the direct arrival onset across the data section.

Dipping arrivals at the margins of Figure 4.6b are attributed to reflections from the sloping walls of the void and, in this regard, it is noted that the model void does not slope upward at 45° as indicated in Figure 4.6a but, rather, more gradually and with slight convex curvature as indicated by the photograph in Figure 4.1a. Moreover, the apparent dip of these events is expected to be an less than their true dip due to up-dip migration of corresponding reflection points.

The localized event at approximately 5.5-6.0 msec and extending from roughly 1.4 to 2.3 m is consistent with reflection from the upper surface of the model, suggesting a fill velocity of approximately α_0=175 m/s, only somewhat higher than the estimate obtained from direct arrival times in Figure 4.5. Associated diffraction events are evident at the edges of the model block as indicated by arrows at the top of Figure 4.6b. As discussed in Appendix A, an independent estimate of the fill velocity can be derived from their moveout characteristics. The procedure, illustrated in Figure 4.8, yields an estimate of α_0=215 m/s. While this result is not inconsistent with estimate of α_0 = 150 m/s determined from direct arrivals in Figure 4.4 it also consistent with expected depth-dependent compaction and consolidation of the fill. Using equation 2.79 with z=0.5 m, f_d ~350 Hz and $\alpha_0 \sim$ 200 m/s, we obtain $R_1 = D_1/2 \sim 0.4$ m for the effective Fresnel zone radius and, consequently, according to spatial resolution criteria developed in Chapter 2, the 0.4 m wide model is only marginally resolvable. In particular, it is useful to compare Figure 4.6b with theoretically predicted responses in Figure 2.30. As for the case $\delta x = D_1/2$ in Figure 2.30, the rectangular geometry of the model is suggested but not clearly established by the optimum offset profile in Figure 4.6b. In other words, reflections from the model are not obviously discernible from associated edge diffractions.

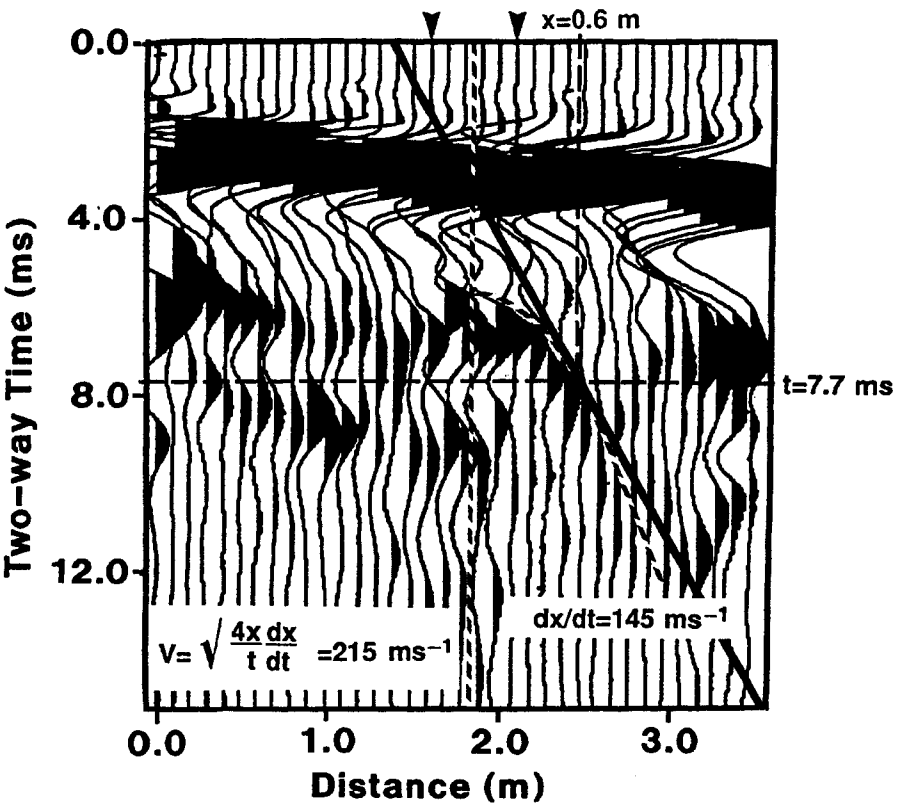

Figure 4.8. Diffraction-based velocity estimation. The velocity estimate follows from the transit time (t=7.7 ms) and local slope (dx/dt=145 m/s) of the diffraction hyperbola at a specified offset (x=0.6 m) from the event's apex.

In contrast, the optimum offset profile acquired along the axis of the model in Figure 4.7b, exhibits a strong continuous (recall that no static corrections have been made) reflection event from the upper surface of the model, arriving at between 5.5 and 6.0 msec and extending from the onset of the traverse to the model's edge at approximately 1.2 m, as illustrated in Figure 4.7a and indicated by the arrow at the top of Figure 4.7b. As in the previous case, this reflection event blends into an evident edge diffraction which coalesces with a second diffraction associated with the step structure in the void floor at approximately 1.5 m. Anomalous amplitudes in the vicinity of 1.5 m and 9.0 ms appear to be the result of constructive interference between these diffraction events and a sub-horizontal event, extending across the profile at approximately 9-10 ms. Although the origin of this

event remains uncertain, its continuity independent of subsurface structure suggests that it may be attributable to a strongly attenuated surface wave or ground-roll arrival.

4.4 Conclusions:

Although foregoing results were acquired under rather ideal conditions, these preliminary soundings demonstrate that with judicious selection of instrumentation and acquisition parameters, the seismic reflection method is capable of resolving power on the scale of archaeological interest.

For sake of comparison, coincident ground-penetrating radar (GPR) profiles were acquired along transects A-A' and B-B', using a Pulse-Ekko IV 100 MHz radar. Acquisition parameters were identical with the exception of a transmitter-receiver antenna separation of 0.4 m compared with an optimum offset of x_o=0.3 m for seismic soundings. In addition, profile B-B' was extended an additional 0.5 m. Resulting GPR profiles are displayed in Figure 4.9. Note that the time scale is in nanoseconds (ns) compared with miliseconds (ms) in Figures 4.4b and 4.7b. Although acquisition errors are less significant, as indicated by the greater continuity of events, resolution of subsurface structure is evidently poorer than that provided by coincident seismic profiles. In fact, despite general opinion that ground-penetrating radar possesses vastly superior resolving power, the foregoing outcome might well have been predicted on the basis of resolution criteria developed in Chapter 2. Assuming a dominant frequency of f_d=100 MHz and a typical velocity of ν_0=0.05 m/ns, we obtain a dominant wavelength of $\lambda_d = \nu_0/f_d \approx 0.5$ m compared with $\lambda_d = \alpha_0/f_d \approx 0.35$ m for seismic soundings with $\alpha_0 = 200$ m/s and $f_d \approx 600$ Hz. For z=0.5 m, associated Fresnel zone diameters are approximately D_1=.75 and D_1=0.6, respectively. Although corresponding resolution limits degrade significantly in both cases with range-dependent attenuation and dispersion, it is evident that seismic soundings in Figures 4.6b and 4.7b possess substantially greater resolution than coincident GPR profiles in Figure 4.9.

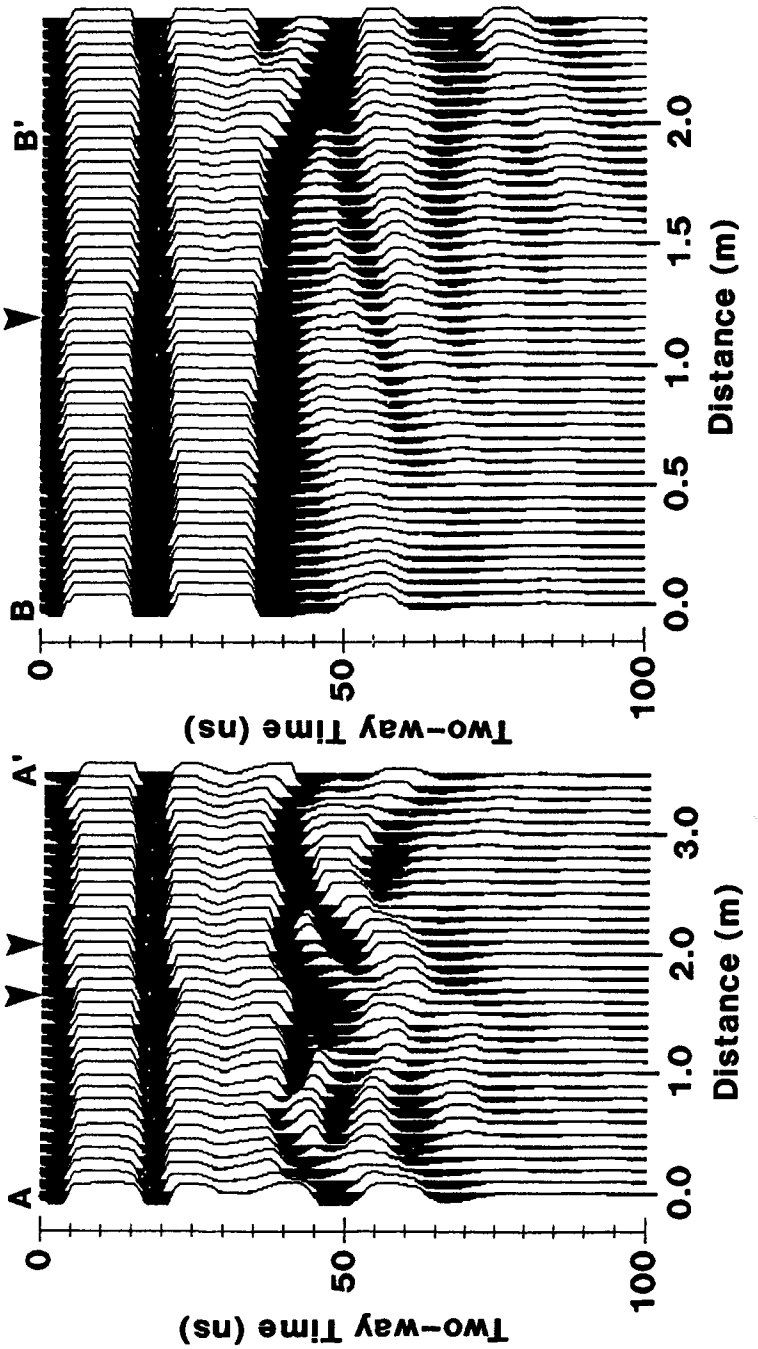

Figure 4.9. Ground-penetrating radar profiles acquired along transects A-A' and B-B' in Figure 4.1b. Compare with idealized cross-sections and corresponding optimum offset seismic profiles in Figures 4.6 and 4.7. Arrows indicate approximate locations of model edges.

Chapter 5

SUMMARY AND DISCUSSION

'Tis a lesson you should heed,
Try again;
If at first you don't succeed,
Try again;
Then your courage should appear,
For if you will persevere
You will conquer, never fear,
Try again.

William Edward Hickson

By the mid 1970s, seismic techniques, particularly the reflection method, had been deemed unsuitable for archaeological prospection due to their insufficient resolving power. Unfortunately, this self-fulfilling prophesy has largely dissuaded subsequent attempts to harness the significant potential of these techniques. This thesis constitutes a re-evaluation of the seismic methods for archaeological application in light of significant technological advances in connection with the adaptation of these techniques for near-surface environmental and groundwater monitoring.

Rather than a purely heuristic approach to the assessing the potential of seismic reflection techniques for archaeological application, the study began with a theoretical analysis of seismic detection and resolution. Detection was defined as the ability to recognize signal in the presence of ambient seismic noise and is a prerequisite for the resolution of subsurface targets. Practical detection limits were derived in Chapter 2 for a certain class of archaeological targets, encompassing discontinuous features of finite dimension. A simple theoretical model predicts that this class of archaeological features is detectable, given only modest dynamic range, for a wide range of plausible material contrasts between the target and host soil. Criteria were also developed for quantifying the resolving power of seismic soundings. That is, the capacity of seismic sounding to distinguish signals arising from separate targets or, more interestingly, the form and dimensions of a given target. These criteria are based on characteristics of the seismic wavelet which is, effectively, the impulse response of the data acquisition system. The connection between wavelet properties and corresponding frequency response was investigated to reveal system characteristics that are

critical for attaining enhanced resolution. Although wavelet phase is an important consideration and high-frequency response is essential, enhanced resolving power is principally achieved by extending system bandwidth.

This finding, together with a commitment to cost-efficient, accessible technology, has guided subsequent design and development of a simple but effective system for detection and resolution of subsurface archaeological remains. A linear systems theory description was given in Chapter 3, demonstrating that net system response is given by the product of subsystem amplitude spectra and the sum of associated phase spectra. Simple theoretical expressions were derived to characterize the response of component subsystems. This analysis has guided procurement and design of complementary instrumentation to yield a balanced frequency spectrum and, consequently, a high-resolution impulse response. In particular, source, detector and in-line pre-emphasis filter components were tailored to compensate for the intrinsically low-pass nature of the subsurface.

To assess the practical performance of the resulting system, preliminary soundings have been acquired along traverses of a full-scale subsurface model, having dimensions representative of common archaeological remains. These experiments were described in Chapter 4, together with a discussion of optimum offset data acquisition techniques to ensure the recording of target reflections with minimum interference from source-generated noise. Compared with the multi-channel CDP method, optimum offset data acquisition is conceptually intuitive and requires little or no post-acquisition data processing to yield an interpretable result. Preliminary optimum-offset profiles presented in Chapter 4 demonstrate, albeit under rather ideal conditions, that the seismic reflection method is, indeed, capable of resolving power on the scale of archaeological interest. In fact, it must be emphasized that these preliminary seismic profiles are raw soundings, and that application of standard enhancement processing techniques, including deconvolution and migration, should yield further extension of the system's resolving power.

At the risk of detracting from the very promising results presented in Chapter 4, it should be stated that a subsequent extension of profile B-B', along the model axis, has

failed to resolve the deeper model structure. In contrast with optimum offset profiles presented in Chapter 4 which were acquired under dry summer conditions, however, these subsequent soundings were acquired during winter under near-saturation conditions. A two-fold decrease in dominant wavelet frequency and corresponding degradation of resolving power testifies to the critical influence of subsurface conditions. Moreover, limited field experiments, in connection with ongoing archaeological excavations in Greece (Appendix M), gave promising but inconclusive results and revealed three potential obstacles to practical implementation of the technique. First, where near-surface soils are hard-packed and/or heterogeneous, source coupling and, consequently, resulting wavelet characteristics vary substantially. Secondly, where archaeological remains are extremely shallow ($< 0.3 - 0.5$ m), there may be no useful optimum window and, in particular, the direct arrival constitutes a major source of interference, masking short-range reflections. Finally, despite high-frequency pre-emphasis filtering, ground-roll can remain a significant source of interference.

Improved acquisition procedures are planned and major system modifications have already been implemented to address these concerns. In particular, while source coupling may be improved, under certain conditions, by detonating the existing source device in prepared, water-filled auger holes, we also plan to investigate the potential of an amplitude modulated, swept-frequency vibratory source. It is anticipated that such a source would be less affected by lateral variations in near-surface soil conditions, resulting in significantly more consistent wavelet characteristics. Moreover, with real-time correlation processing, swept-frequency source techniques could yield significantly enhanced resolution. To provide for enhanced suppression of source-generated noise, including both ground-roll and direct wave arrivals, parallel input circuitry has been incorporated to implement geophone differencing (Knapp, 1986). In short, this technique attenuates horizontally propagating energy by exploiting its simultaneous arrival at two detectors deployed equidistant from the source but at slightly different depths. The output signal is simply the differential output of the two geophones and, since horizontally propagating energy is in-phase at

the two detectors, it is approximately cancelled. The vertical separation between the two detectors is adjusted so that quasi-vertically incident reflection energy is approximately 180° out of phase and, consequently, enhanced by differencing. An alternative approach to attenuating surface waves is polarization filtering, wherein ground-roll energy is identified and subsequently attenuated on the basis of its characteristic particle displacement polarization. The Omni-Phone® polarization filter unit developed by the Terra Linda Group (Gassaway, et al., 1989) comprises a three-component Eddy-Seis detector system coupled with associated A-D conversion and digital electronics for real-time polarization filtering. Further model experiments are planned to assess the practical utility of these methods. As concerns possible exploitation of multiple detector arrays for attenuation of source-generated noise (Rayleigh waves in particular), theoretical analysis presented in Appendix B confirms that these techniques have little practical advantage for small-scale, near-surface applications. Similarly, it is concluded that multichannel data acquisition methods and the associated potential for a minor improvement in signal-to-noise ratio do not justify the significant investment in post-acquisition CDP processing to yield interpretable seismic sections. Moreover, depending on the scale of features investigated, it is not altogether clear that reflection-based velocity analysis, a key step in CDP processing, is practical. Consequently, for such applications, the single-fold optimum offset technique is recommended, together with a combination of CMP and diffraction-based velocity information as described in Appendix A.

Finally, In connection with the traditional role of geophysical prospection in archaeology, that is, pre-excavation detection and mapping of potential archaeological features, it is anticipated that seismic soundings, like ground penetrating radar, will be employed primarily as a secondary technique to provide a cross-sectional view of targets already identified by mapping techniques, including magnetic, resistivity and electromagnetic conductivity measurements. As previously discussed, successful seismic imaging of these targets involves a critical trade-off between the gross dimensions of the archaeological deposit and the degree of contrast between its material properties and those of the surrounding host

matrix. In particular, enhanced reflectivity is associated with significant contrasts in density and, more importantly, seismic velocity. In general, rock structures, including wall and foundation remains, pavement, burial chambers and hearths are better suited for seismic imaging than soil features, including storage pits, simple burials and post molds. Having said this, it is expected that larger-scale soil features, like buried house floors, would be effectively delineated by seismic soundings. In addition, because the dominant wavelength of the seismic pulse depends inversely on the velocity of the host matrix, higher resolution is expected in relatively uncompacted, unconsolidated soils. As a reference to practical application, representative velocity data for a wide range of rocks and unconsolidated sediments are tabulated in Appendix N. These data may used in conjunction with detection and resolution criteria developed in Chapter 2 to assess the capacity of seimic soundings to image specific archaeological features.

Finally, in addition to imaging of localized archaeological features, it is also anticipated that seismic techniques, together with ground penetrating radar, can have a significant role in the delineation of archaeological stratigraphy, from small-scale investigation of midden deposits to large-scale regional paleo-geomorphic surveys.

In conclusion, on the basis of findings presented herein, there can be little question of a promising role for the seismic reflection method in archaeological remote sensing. While there is admittedly much developmental and experimental work remaining, I am confident that this dissertation establishes a solid foundation for future research.

REFERENCES

Aitken, M. J., 1974, *Physics and archaeology*, second edition, Clarendon Press, Oxford.

Aki, K. and Richards, P. G., 1980, *Quantitative seismology: theory and methods*, Freeman and Co., San Francisco.

Al-Chalabi, M., 1973, Series approximation in velocity and traveltime computations: *Geophysical Prospecting*, **21**, 783-795.

Al-Chalabi, M., 1974, An analysis of stacking, rms, average, and interval velocities over a horizontally layered ground: *Geophysical Prospecting*, **22**, 458-475.

Aldridge, D. F., 1993, Elastic wave radiation from a pressurized spherical cavity, internal report, Chevron Petroleum Technology Co.

Aldridge, D. F., 1990, The Berlage wavelet, *Geophysics*, **55**, 1508-1511.

Azimi, Sh. A., Kalinin, A. V., Kalinin, V. V. and Pivovarov, B. L., 1968, Impulse and transient characteristics of media with linear and quadratic absorption laws, *Izvestia Physics of the Solid Earth*, American Geophysical Union, 88-93.

Badri, M. and Mooney, H. A., 1987, Q measurements from compressional waves in unconsolidated media, *Geophysics*, **52**, 772-784.

Berkhout, A. J., 1984, *Seismic resolution: resolving power of acoustical echo techniques*, Handbook of geophysical exploration, Vol. 12, Geophysical Press, Amsterdam.

Born, M. and Wolf, E., 1975, *Principles of optics*, fifth edition, Pergamon Press, New York.

Bracewell, R., 1986, *The Fourier transform and its applications*, second edition, McGraw-Hill Book Co. Inc., New York.

Blake, F. G., 1952, Spherical wave propagation in solid media, *Journal of the Acoustical Society of America*, **24**, 211-215.

Bullen, K. E., 1965, *An introduction to the theory of seismology*, Cambridge University Press, Cambridge.

Butzer, K. W., 1982, *Archaeology as Human Ecology*, Cambridge University Press.

Carson, H. H., 1962, A seismic survey at Harpers Ferry, *Archaeometry*, **5**, 119-22.

Červeny, V., and Ravindra, R., 1971, *Theory of seismic head waves*, University of Toronto Press, Toronto.

Červeny, V., and Soares, J. E. P., 1992, Fresnel volume ray-tracing, *Geophysics*, **57 57**, 902-915.

Claerbout, J. F., 1985, *Imaging the earth's interior*, Blackwell Scientific Publishers, Palo Alto.

Clark, A. J., 1990, *Seeing beneath the soil: prospecting methods in archaeology*, B. T. Batsford Ltd., London.

Cross, G. M., 1992, Array responses for plane and spherical incidence, *Geophysics*, **57**, 1294-1306.

Cross, G. M., and Knoll, M. D., 1991, Diffraction-based velocity estimates from optimum offset seismic data, *Geophysics*, **56**, 2070-2079.

Dalton, D. R. and Yedlin, M. J., 1989, Exact time-domain solutions for acoustic diffraction by a half plane, *Surveys in Geophysics*, **10**, 305-330.

Dalton, D. R. and Yedlin, M. J., 1990, ARMA implementation of diffraction operators with inverse-root singularities, *IEEE Transactions on Geoscience and Remote Sensing*, **38**, 831-837.

Daniels, J. J., 1989, Fundamentals of ground penetrating radar: Proc., Symp. on Application of Geophysics to Engineering and Environmental Problems, Soc. Engr. and Min. Expl. Geophys., 62-142.

Dennison, A. T., 1953, The design of electromagnetic geophones, *Geophysical Prospecting*, bf 1, 3-28.

de Voogd, N. and den Rooijen, H., 1983, Thin-layer response and spectral bandwidth, *Geophysics*, **48**, 12-18.

Dinstel, W. L., 1971, Velocity spectra and diffraction patterns: *Geophysics*, **36**, 415-417.

Dix, C. H., 1955, Seismic velocities from surface measurements: *Geophysics*, **20**, 68-86.

Dobecki, T. L. and Romig, P. R., 1985, Geotechnical and groundwater geophysics, *Geophysics*, **50**, 12, 2621-36.

Dobrin, M. B., 1976, *Introduction to geophysical prospecting*: third edition, McGraw-Hill Inc.

Dobrin, M. B., Simon, R. F. and Lawrence, P. L., 1951, Rayleigh waves from small explosions, *Transactions*, American Geophysical Union, **32**, 822-832.

Dolphin, L. T., Moussa, A. H. and Mokhtar, G., 1977, *Applications of modern sensing techniques to Egyptology*, prepared for National Science Foundation, Office of Inter-

national Programs, Washington, D.C., NSF Grant INT76-00414, published by SRI International, Menlo Park, CA.

Gardner, G. H. F., Gardner, L. W. and Gregory, A. R., 1974, Formation velocity and density-the diagnostic basics for stratigraphic traps, *Geophysics*, **39**, 770-780.

Gassaway, G. S., Berrong, B. H., Angerer, R. H. and Miles, D. R., 1989, Omniphone polarization filtering: an effective way of removing ground-roll without geophone arrays, internal report, Terra Linda Group Inc., San Anselmo, CA.

González-Serrano, A., and Claerbout, J. F., 1984, Wave-equation velocity analysis: *Geophysics*, **49**, 1432-1456.

Gurvich, I. I., 1965, The theory of spherical radiators of seismic waves, Isvestia Physics of the Solid Earth, American Geophysical Union, 684-689.

Hadjidaki, E., 1988, Preliminary report of excavations at the harbour of Phalasarna in West Crete, *American Journal of Archaeology*, **92**, 463-479.

Hamilton, E. L., 1972, Compressional-wave attenuation in marine sediments, *Geophysics*, **37**, 620-646.

Hesse, A., 1969, Detection elastique: Rapport sur l'état d'avancement des recherches, Rapport inédit, R.C.P. 141, Centre de Recherches Geophysiques, C. N. R. S., Garchy.

Hilburn, J. L. and Johnson, D.E., 1980, *Manual of active filter design*, McGraw-Hill Book Co., New York.

Holzman, M., 1963, Chebyshev optimized geophone arrays: *Geophysics*, **28**, 145-155.

Hoover, G. M. and O'Brien, J. T., 1980, The influence of the planted geophone on seismic land data, *Geophysics*, **45**, 1239-1253.

Hosken, J. W. J., 1988, Ricker wavelets in their various guises, *First Break*, **6**, 24-33.

Hubral, P., and Krey, T., 1980, *Interval velocities from seismic reflection time measurements*: Soc. Expl. Geophys. Monograph.

Hubral, P., Schleicher, J., Tygel, M. and Hanitzch, Ch., 1993, Determination of Fresnel zones from traveltime measurements, *Geophysics*, **58**, 703-712.

Hubral, P. and Tygel, M., 1989, Analysis of the Rayleigh pulse, *Geophysics*, **54**, 654-658.

Hunter, J. A., Pullan, S. E., Burns, R. A., Gagne, R. M., and Good, R. L., 1984, Shallow seismic reflection mapping of the overburden-bedrock interface with the engineering seismograph-some simple techniques: *Geophysics*, **49**, 1381-1385.

Hunter, J. A., and Pullan, S. E., 1989, The optimum offset shallow seismic reflection technique: Proc., Symp. on Application of Geophysics to Engineering and Environmental Problems, Soc. Engr. and Min. Expl. Geophys., 143-174.

Ivanova, L. A., Kondratyeva, T. C. and Shcherbo, M. N., 1970, Determination of the absorption of explosion waves in the ground from recordings of stresses and strains, *Izvestia Physics of the Solid Earth*, American Geophysical Union, 81-85.

Jeans, J., 1948, *The mathematical theory of electricity and magnetism*, Cambridge University Press, Cambridge.

Jenkins, F. A. and White, H. E., 1957, *Fundamentals of optics*, third edition, McGraw-Hill Book Co., New York.

Kähler, S. and Meissner, R., 1983, Radiation and receiver pattern of shear and compressional waves as a function of Poisson's ratio, *Geophysical Prospecting*, **31**, 421-435.

Kalinin, A. V., Azimi, Sh. A. and Kalinin, V. V., 1967, Estimate of phase-velocity dispersion in absorbing media, *Izvestia Physics of the Solid Earth*, American Geophysical Union, 249-251.

Kallweit, R. S. and Wood, L. C., 1982, The limits of resolution of zero-phase wavelets, *Geophysics*, **47**, 1035-1046.

Kanemori, T. and Hall, E. M., 1986, A new type of geophone, Eddy-Seis, theoretical study of its response characteristics and method of testing, 56th Annual International Meeting, Society of Exploration Geophysicists, Expanded Abstracts, 451-454.

Kaplan, W., 1981, *Advanced engineering mathematics*, Addison-Wesley, Palo Alto.

Kjartansson, E., 1979, Constant-Q wave propagation and attenuation, *Journal of Geophysical Research*, **84**, 4737-4748.

Knapp, R. W., and Steeples, D. W., 1986, High-resolution common depth point seismic reflection profiling: field acquisition parameter design: *Geophysics*, **51**, 283-294.

Knapp, R. W., 1986, Geophone differencing to attenuate horizontally propagating noise, *Geophysics*, **51**, 1743-1759.

Knapp, R. W., 1990, Vertical resolution of thick beds, thin beds and thin-bed cyclothems, *Geophysics*, **55**, 1183-1190.

Knapp, R. W., 1991, Fresnel zones in light of broadband data, *Geophysics*, **56**, 354-359.

Knopoff, L., 1959, Scattering of compressional waves by spherical obstacles, *Geophysics*, **24**, 30-39.

Koefoed, O., 1981, Aspects of vertical resolution, *Geophysical Prospecting*, **29**, 21-30.

Krohn, C. E., 1984, Geophone ground coupling, *Geophysics*, **49**, 722-731.

Lathi, B. P., 1965, *Signals, systems and communication*, Wiley and sons Inc., New York.

Larner, K., Chambers, R., Yang, M., Lynn, W., and Wai, W., 1983, Coherent noise in marine seismic data: *Geophysics*, **48**, 854-886.

Lepper, C. M., 1981, Guidelines for selecting seismic detectors for high-resolution applications, Report of investigations 8599, U. S. Department of the Interior, Bureau of Mines.

Lester, O. C., 1947, Seismic weathered or aerated surface layer, in *Early Papers of the Society of Exploration Geophysicists*, Soc. Expl. Geophys., Tulsa, 391-394.

Levin, F. K., 1971, Apparent velocity from dipping interface reflections: *Geophysics*, **36**, 510-516.

Lindsey, J. P., 1989, The Fresnel zone and its interpretive significance, *The Leading Edge*, **8**, 33-39.

Linehan, D. S. J., 1956, A seismic problem in St. Peter's Basilica, Vatican City, Rome, Italy, in *Geophysical Case Histories*, Vol. 2, Society of Exploration Geophysicists, 615-22.

Linington, R. E., 1963, The application of geophysics to archaeology, *American Scientist*, **51**, 48-70.

Lipson, S. G., and Lipson, H., 1969, *Optical physics*, Cambridge University Press, Cambridge.

MASCA, 1969, Geophysical surveys: Nemrud Dagh excavations, *MASCA Newsletter*, **5**, 2, Museum Applied Science Center for Archaeology, University of Pensylvania.

MASCA, 1972, Underwater archaeology: sonar surveys in Greece, *MASCA Newsletter*, **8**, 1, Museum Applied Science Center for Archaeology, University of Pennsylvania.

McGehee, M. S., Luyendyk, B. P. and Boegeman, D. E., 1968, Location of an ancient Roman shipwreck by modern acoustic techniques, *A critical look at marine technology*, 4th Annual Conference Marine Technology Society, Washington, D. C., July, 1968.

Mayne, W. H., 1987, On:"High-resolution common-depth-point reflection profiling: field acquisition parameter design" (Discussion): *Geophysics*, **52**, 2011.

Meckel, L. D. and Nath, A. K., 1977, Geologic considerations for stratigraphic modeling and interpretation, Memoir 26, American Association of Petroleum Geologists, Tulsa.

Meissner, R. and Stümpel, H., 1979, Miniseismik in der archäometrie, *Umshau*, **79**, 412-15.

Miller, G. F. and Pursey, H., 1955, On the partition of energy between elastic waves in a semi-infinite solid, *Proceedings of the Royal Society*, **A233**, 55-59.

Miller, G. F. and Pursey, H., 1954, The field and radiation impedance of mechanical radiators on the free surface of a semi-infinite isotropic solid, *Proceedings of the Royal Society*, **A223**, 521-541.

Miller, R. D., Pullen, S. E., Waldner, J. S. and Haeni, F. P., 1986, Field comparison of shallow seismic sources, *Geophysics*, **51**, 2067-2092.

Miller, R. D., Pullen, S. E., Steeples, D. W. and Hunter, J. A., 1992, Field comparison of shallow seismic sources near Chino, California, *Geophysics*, **57**, 693-709.

Mitchell, J. K., 1993, *Fundamentals of soil behavior*, second edition, John Wiley & Sons, New York.

Molotova, L. V., and Vassil'ev, Yu. I., 1960, Velocity ratio of longitudinal and transverse waves in rocks, *Izvestia Physics of the Solid Earth*, American Geophysical Union, 731-743.

Mooney, H. M., 1976, The seismic wave system from a surface impact, *Geophysics*, **41**, 243-265.

Neidell, N. S. and Poggiagliolmi, E., 1977, Stratigraphic modeling and interpretation-geophysical principles and techniques, Memoir 26, American Association of Petroleum Geologists, Tulsa.

Newman, P., and Mahoney, J. T., 1973, Patterns-with a pinch of salt: *Geophysical Prospecting*, **21**, 197-219.

Nowroozi, A. A., 1989, Generalized form of the Dix equation for the calculation of interval velocities and layer thicknesses: *Geophysics*, **54**, 659-661.

Ozawa, K. and Matsuda, M., Computer assisted techniques for detecting underground remains based on acoustic measurement, *Archaeometry*, **21**, 1, 87-100.

Papamarinopoulos, St., Jones, R. E. and Williams, E.H., 1988, Electrical resistance survey of the southern part of the buried ancient town of Stymphalos, *Geoexploration*, **25**, 255-261.

Parr, J. O., and Mayne, W. H., 1955, A new method of pattern shooting: *Geophysics*, **20**, 539-560.

Paterson, N. R., 1956, Seismic wave propagation in porous granular media, *Geophysics*, **3**, 691-714.

Pieuchot, M., 1984, *Seismic Instrumentation*, Handbook of Geophysical Exploration, Geophysical Press, London.

Press, F., 1966, Seismic velocities, in *Handbook of physical Constants*, Geological Society of America, Memoir 97.

Pullan, S. E. and MacAulay, H. A., 1987, An in-hole shotgun source for engineering seismic surveys, *Geophysics*, **52**, 985-996.

Pullan, S. E., Jol, R. M., Gagne, R. M., and Hunter, J. A., 1989, Compilation of high resolution optimum offset shallow seismic reflection profiles from the southern Fraser River delta, British Columbia: Geol. Surv. Can., open file # 1992.

Rapp, G., Gifford, J. A., 1985, *Archaeological Geology*, Yale University Press.

Richards, P. G., 1990, Theoretical seismology, in Desaubies, Y., Tarantola, A. and Zinn-Justin, J., Editors, Oceanographic and geophysical tomography, Elsevier Science Publishers.

Ricker, N., 1953a, The form and laws of propagation of seismic wavelets, *Geophysics*, **18**, 10-40.

Ricker, N., 1953b, Wavelet contraction, wavelet expansion, and the control of seismic resolution, *Geophysics*, **18**, 769-92.

Robinson, E. A. and Trietel, S., 1980, *Geophysical signal analysis*, Prentice-Hall Inc., New Jersey.

Scollar, I., Tabbagh, A., Hesse, A., and Herzog, I., 1990, *Archaeological Prospecting and Remote Sensing*, Cambridge University Press.

Shah, P. M., and Levin, F. K., 1973, Gross properties of time-distance curves: *Geophysics*, **38**, 643-656.

Sharpe, J. A., 1942, The production of elastic waves by explosion pressures. I. Theory and empirical field observations, *Geophysics*, **7**, 144-154.

Sharpe, J. A., 1944, The effect of charge size on reflection records, *Geophysics*, **9**, 131-143.

Sheriff, R.E., 1985, Aspects of seismic resolution, *Seismic stratigraphy II*, Memoir 39, American Association of Petroleum Geologists, Tulsa.

Schoenberger, M., 1974, Resolution comparison of minimum-phase and zero-phase signals, *Geophysics*, **39**, 826-833.

Steeples, D. W., and Miller, R. D., 1988, Seismic reflection methods applied to engineering, environmental, and ground-water problems: Proc., Symp. on Application of

Geophysics to Engineering and Environmental Problems, Soc. Engr. and Min. Expl. Geophys., 1-52.

Strick, E., 1970, A predicted pedestal effect for pulse propagation in constant-Q solids, *Geophysics*, **35**, 387-403.

Taner, M. T., and Koehler, F., 1969, Velocity spectra-digital computer derivation and applications of velocity functions: *Geophysics*, **34**, 859-881.

Telford, W. M., Geldhart, L. P., Sheriff, R. E. and Keys, D. A., 1976, *Applied Geophysics*, Cambridge University Press, New York.

Tite, M. S., 1972, *Methods of physical examination in archaeology*, Seminar Press, London.

Tite, M. S., 1991, Archaeological science - past achievements and future prospects, *Archaeometry*, 33, 139-151.

Trorey, A. W., 1970, A simple theory for seismic diffractions, *Geophysics*, **35**, 762-784.

Trorey, A. W., 1977, Diffraction for arbitrary source-receiver locations, *Geophysics*, **42**, 1177-1182.

Tsai, C. J., 1984, An analysis leading to the reduction of scattered noise on deep marine seismic records: *Geophysics*, **49**, 17-26.

Ulriksen, C. P. F., 1982, Application of impulse radar to civil engineering: Ph. D. Thesis, Lund Univ. of Tech., Published in U. S. A. by Geophysical Survey Systems. Inc.

Weymouth, J. W., 1986, Geophysical methods of archaeological site surveying, *Advances in Archaeological Method and Theory*, 9, 311-395, Academic Press.

Widess, M. B., 1973, How thin is a thin bed?, *Geophysics*, **38**, 6, 1176-80.

Widess, M. B., 1982, Quantifying resolving power of seismic systems, *Geophysics*, **47**, 1160-1173.

Williams, E. H., 1984, Topographical and geophysical investigations at Stymphalos, 1983, *Classical Views*, **28**, 169-196.

Wu, R. and Aki, K., 1985, Scattering characteristics of elastic waves by an elastic heterogeneity, *Geophysics*, **50**, 582-595.

Yilmaz, O., 1987, *Seismic data processing*, Investigations in Geophysics **2**, Society of Exploration Geophysicists, Tulsa.

Ying, C. F. and Truell, R., 1956, Scattering of a plane longitudinal wave by a spherical obstacle in an isotropically elastic solid, *Journal of Applied Physics*, **27**, 1086-1097.

Ziolkowski, A., 1984, *Seismic deconvolution*, International Human Development Co.

UNCITED REFERENCES

Brizzolari, E., Ermolli, F., Orlando, L., Piro, S. and Versino, L., 1992, Integrated geophysical methods in archaeological surveys, *Journal of Applied Geophysics*, **29**, 47-55.

Carabelli, E., 1966, A new tool for archaeological prospecting: the sonic spectroscope for the detection of cavities, *Prospezioni Archaeologicha*, **1**, 25-35.

Chevallier, R., 1966, Prospections Sismiques, in *Études D'Archéologie Aérienne*, Paris, 100-103.

Dalan, R. A., Musser, J. M. and Stein, J. K., 1992, Geophysical exploration of the shell midden, in *Deciphering a Shell Midden*, J. K. Stein, Editor, Academic Press, New York, 43-58.

Goulty, N. R., Gibson, J. P. C., Moore, J. G. and Welfare, H., 1990, Delineation of the vallum at Vindobala, Hadrian's Wall, by a shear-wave seismic refraction survey, *Archaeometry*, **32**, 71-82.

Goulty, N. R. and Hudson, A. L., 1994, Completion of the seismic refraction survey to locate the vallum at Vindobala, Hadrian's Wall, *Archaeometry*, **36**, 327-335.

Krentz, D. H. and Woods, D. V., 1986, An integrated geophysical investigation of the Fort Frontenac archaeological site in Kingston, Ontario, *Canadian Society of Explor. Geophys. Journal*, **22**, 87-97.

Lichtman, G. S., Shiller, G. I. and Pierson, L. J., 1984, Geophysical Evaluation of submerged post-Wisconsin potential archaeological sites, Santa Barbara Channel, California, Expanded Abstracts, 54th Annual International Meeting, Society of Exploration Geophysicists, 189-190.

Sheets, P., 1985, Geophysical exploration for ancient Maya housing at Ceren, El Salvador, *National Geographic Research Reports*, National Geographic Society, Washington, D.C., 645-656.

Stright, M. J., 1986, Evaluation of archaeological site potential on the Gulf of Mexico continental shelf using high-resolution seismic data, *Geophysics*, **51**, 605-622.

Appendix A
DIFFRACTION BASED VELOCITY ESTIMATES FROM OPTIMUM OFFSET SEISMIC DATA

A.1 Introduction:

The Terrain Geophysics Section of the Geological Survey of Canada pioneered and since the early 1980s have popularized the optimum offset technique for high resolution shallow seismic profiling (Hunter et al., 1984; Hunter and Pullan, 1989). The method relies on preliminary expanding offset noise tests to identify a range of source-receiver offsets over which the reflection from a given target interface is received with minimum interference from source generated noise. An optimum offset, selected from within this range, is then used to acquire single fold soundings along profile.

Compared with suitably scaled CDP techniques (Knapp and Steeples, 1986; Steeples and Miller, 1988), optimum offset profiling is conceptually less complicated and has the advantage of requiring little, if any, post acquisition data processing to yield an interpretable result. In part, however, this advantage is sacrificed by the need to collect and analyze supplemental multifold data to determine a velocity function for depth conversion. To reduce the need for these additional data, we propose to make greater use of move-out information supplied by diffraction events to derive supplemental velocity estimates directly from common offset data. In addition, since these estimates require only a pencil and ruler, they represent a convenient source of velocity information in the field.

Diffraction based velocity analysis is familiar to practitioners of ground penetrating radar (GPR) where data are acquired almost entirely in common offset mode. Here we characterize the relationship between a simple method used there and another, more robust technique that leads naturally to a meaningful interval velocity function. Finally, while source and receiver components of GPR systems are often effectively coincident and seldom separated by more than a metre, this is not the case for optimum offset seismic acquisition. Consequently, we examine the effect of non-zero offset on transit time within a constant

velocity medium and evaluate the corresponding influence on apparent velocity.

Previous studies (Dinstel, 1971; Larner et al., 1983; Tsai, 1984) have examined the appearance of scattered energy in a variety of acquisition and display formats, but have focused principally on CMP gathers and the suppression of these events by stacking and velocity filtering. We are concerned, instead, with diffractions in the common offset domain and the velocity implied by transit time moveout as a fixed spread traverses the scatterer.

A.2 Point Diffractions on Common Offset Records:

Consider a point diffractor within a homogeneous, isotropic halfspace as depicted in Figure A.1.

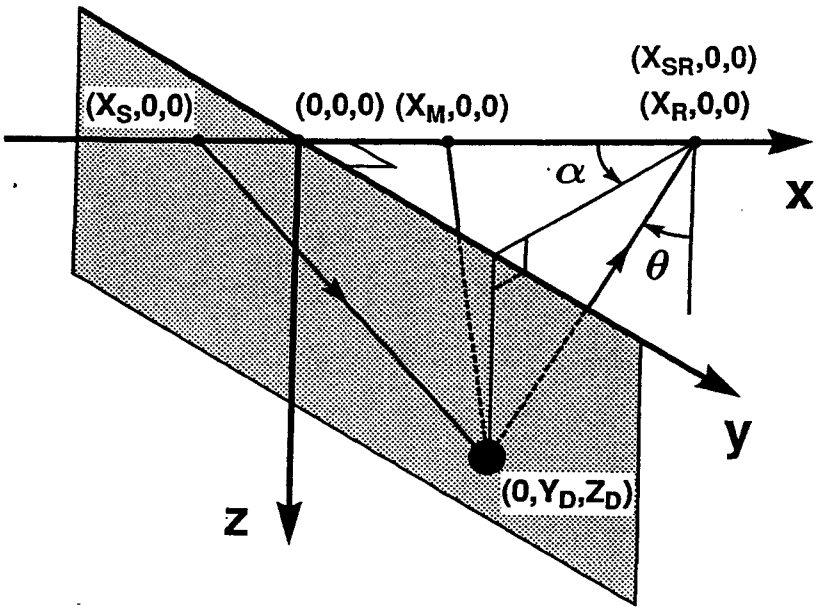

Figure A.1. Point scatterer model and reference coordinate system. X_S, X_M and X_R denote source, midpoint and receiver positions along the x-axis. Y_D and Z_D are, respectively, the y and z coordinates of a point diffractor residing in the yz-plane. X_{SR} denotes the position of a coincident source-receiver pair. θ and α are, respectively, takeoff and azimuthal angles for the ray joining $(X_{SR}, 0, 0)$ and $(0, Y_D, Z_D)$.

A rectangular coordinate system is chosen so that scattered energy detected by an optimum offset survey along the x-axis has minimum arrival time when the spread midpoint is at

the origin. With the spread so positioned, a line segment joining the scatterer and the midpoint is normal to profile and, consequently, minimum length. Note that this implies a scatterer residing in the yz-plane.

For source at $(X_S, 0, 0)$, receiver at $(X_R, 0, 0)$ and point diffractor at $(0, Y_D, Z_D)$, the appropriate transit time expression is

$$t = \frac{1}{V}\left[(X_S{}^2 + r^2)^{1/2} + (X_R{}^2 + r^2)^{1/2}\right], \tag{A.1}$$

where V is a constant velocity and $r = (Y_D{}^2 + Z_D{}^2)^{1/2}$ is the distance from the origin to the scatterer. Expressing source and receiver positions in terms of spread midpoint, X_M, and optimum offset, $\Delta x = X_R - X_S$, as

$$\begin{aligned} X_S &= X_M - \Delta x/2 \\ X_R &= X_M + \Delta x/2 \end{aligned}, \tag{A.2}$$

we obtain the equivalent relation

$$t = \frac{1}{V}\left\{\left[(X_M - \Delta x/2)^2 + r^2\right]^{1/2} + \left[(X_M + \Delta x/2)^2 + r^2\right]^{1/2}\right\}. \tag{A.3}$$

For the time being, we shall consider the case of coincident source-receiver. Setting $\Delta x = 0$ in equation (A.3) and squaring both sides yields for zero offset transit time

$$t^2 = t_0{}^2 + \frac{4X^2}{V^2}, \tag{A.4}$$

where $t_0 = 2r/V$ is the minimum arrival time for scattered energy detected by a coincident source-receiver. Although we have dropped the subscript on X_M to simplify notation, we remind the reader that this variable specifies midpoint position along profile and should not be confused with optimum offset, Δx. Having said this, however, note the obvious similarity between equation (A.4) and the CMP transit time relation for reflection from a dipping planar interface (Levin, 1971). In the latter case transit time is measured as a function of offset about a constant midpoint rather than as a function of midpoint location for a common offset. Both events are hyperbolic.

A.3 Velocity Estimates from Diffractions:

The diffraction pattern resulting for an arbitrary point scatterer is illustrated in Figure A.2a.

As for the case of reflections, a reasonable estimate of the constant velocity, V, can be obtained by exploiting the linearity of equation (A.4) in X^2 vs. t^2 space.

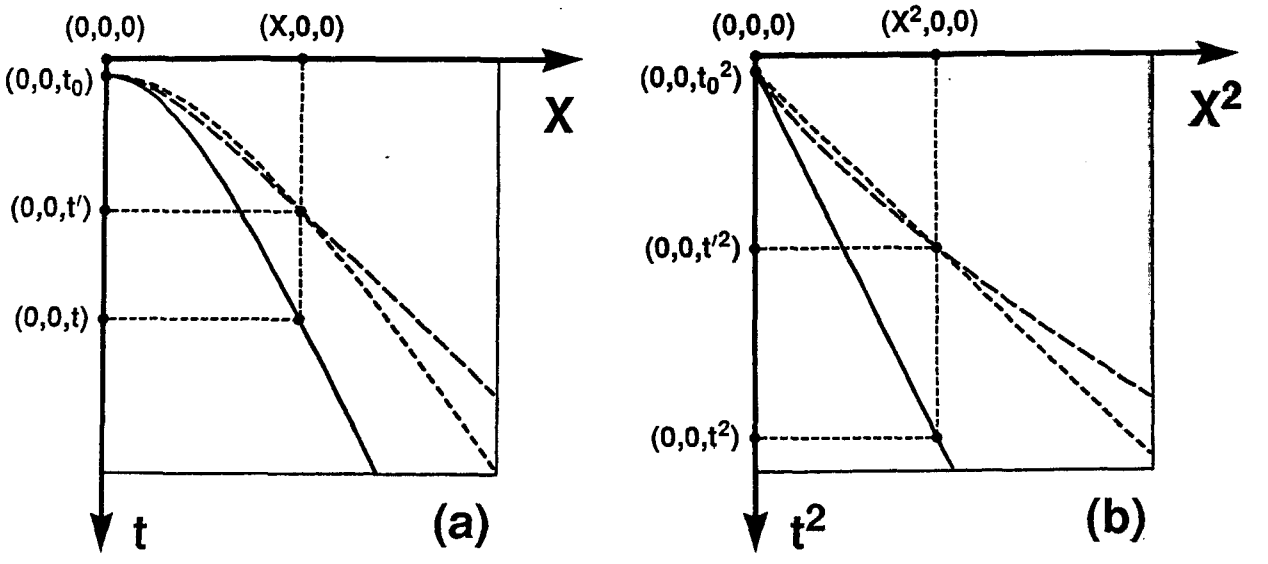

Figure A.2. Model transit time curves. (a) Solid curve relates transit time and midpoint position for both a uniform medium and for straight rays in a stratified medium having an equivalent average velocity. Dashed curve describes true transit time-midpoint relation for a stratified medium. Dotted curve represents transit time-midpoint relation implied by equation (A.5) (b) Selected portion of corresponding curves in coordinates X^2 vs. t^2.

As depicted in Figure A.2b, the diffraction hyperbola maps to a line having intercept t_0^2 and slope $4/V^2$. Rather than determine the arrival time of scattered energy at numerous midpoint locations and perform the required linear regression, practitioners of ground penetrating radar have commonly pursued a more direct approach (Ulriksen, 1987; Daniels, 1989). Having identified the apex of a diffraction event $(0,t_0)$ together with any additional point (X,t) (Figure A.2a), velocity is derived directly from equation (A.4) as

$$V^2 = \frac{4X^2}{(t^2 - t_0^2)}. \tag{A.5}$$

In effect, this amounts to specifying the intercept $(0, t_0^2)$ and a second point (X^2, t^2) on the line described by equation (A.4) and is, ideally, equivalent to the corresponding two-

point slope estimate (Figure A.2b). It follows that, in practice, velocity estimates obtained from equation (A.5) are particularly sensitive to measurement error associated with arrival times.

Implicit differentiation of equation (A.4) with respect to the midpoint variable, X, gives

$$V^2 = \frac{4X}{t}\frac{dX}{dt} = \frac{2X}{tp_x cos\alpha}, \tag{A.6}$$

where $dt/dX = 2p_x cos\alpha$ is the slope of a local tangent to the diffraction event at (X,t). The reader should recognize that p_x is the equivalent Snell parameter with $\alpha = \tan^{-1}(Y_D/X)$ denoting the azimuthal angle as depicted in Figure A.1. As González-Serrano and Claerbout (1984) have demonstrated for the case of reflection events on CMP gathers, equation (A.6) suggests an alternative approach for estimating velocity directly from the constant offset record. In this approach, the interpreter must supply a local slope estimate but need not specify the minimum arrival time, t_0, required by equation (A.5). Although the errors in these measurements are comparable, equation (A.6) is less prone to propagating transit time uncertainties. Also, by incorporating the local slope of the scattering event, equation (A.6), if only by eye, involves a sort of curve fitting to the entire event. Consequently, in addition to yielding velocity directly from the constant offset profile, we expect equation (A.6) to provide a relatively robust estimate.

Now, having set out the basic concepts assuming a uniform medium, let us examine the more interesting situation where velocity is vertically variable. It is in this context that we shall discover the connection between the two direct velocity estimates described above. Consider a point scatterer within a stack of horizontal isovelocity layers having thickness z_k and velocity v_k as depicted in Figure A.3. Let us assume, for the moment, that scattered energy has taken the path of least distance from source to scatterer and back to the coincident receiver. Under this straight ray assumption, transit time is predicted exactly by equation (A.4) upon replacing the uniform velocity, V, by the appropriate

average velocity

$$V_a = \frac{1}{T_0}\sum_{k=1}^{n} v_k \tau_k = \frac{2}{T_0}\sum_{k=1}^{n} z_k, \tag{A.7}$$

where $\tau_k = 2z_k/v_k$ is the two-way vertical transit time within the kth layer and

$$T_0 = \sum_{k=1}^{n} \tau_k = 2\sum_{k=1}^{n} \frac{z_k}{v_k}. \tag{A.8}$$

Here, T_0 is the two-way transit time for an in-plane scatterer located vertically beneath the coincident source-receiver and should be distinguished from t_0, the minimum two-way transit time for an arbitrary scatterer. The two are equivalent only for a diffractor within the plane of survey ($\cos\alpha = 1$) as depicted in Figure A.3.

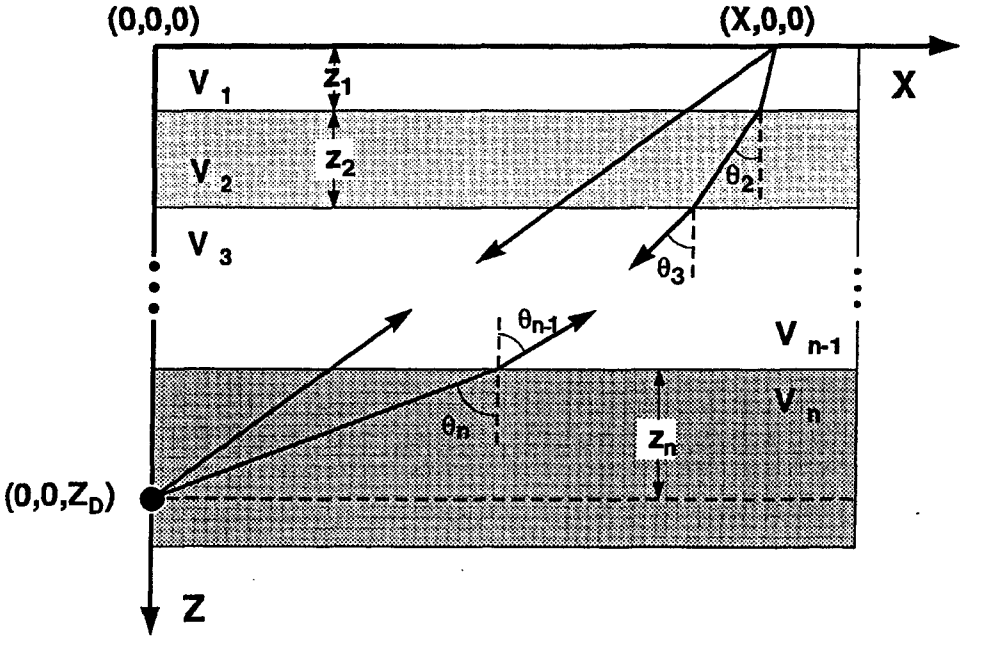

Figure A.3. Stratified earth model depicting both true and straight two-way ray paths joining a coincident source-receiver at (X,0,0) with an in-plane diffractor at $(0, 0, Z_D)$. v_k, z_k and θ_k (k = 1, 2, 3, ..., n) denote velocity, thickness and ray angle respectively for the kth layer.

Now, if v_k and z_k are chosen so that $V_a = V$, the corresponding diffraction event and its mapping in X^2 vs. t^2 are the same as for the case of uniform velocity in Figure A.2. This is not surprising since equation (A.4) was derived under the same straight ray assumption. In short, all that we have said regarding the case of uniform velocity holds for stratified velocity assuming that scattered energy takes the path of least distance. Most importantly, the velocity predicted by equations (A.5) and (A.6) remains constant for all values of X.

In practice, scattered energy reaching the receiver has actually taken the path of least time in accordance with Fermat's principle. Compared with the straight ray case, the path of least time reduces transit through lower velocity layers while increasing the distance traveled at higher velocities as suggested in Figure A.3. Consequently, as the designation indicates, transit time via the least time path is always less than or equal that by the corresponding straight ray path. In particular, least time and least distance paths are equivalent only for an in-plane scatterer located vertically beneath the coincident source-receiver. Otherwise, as X increases, the actual two-way transit time is progressively less than that predicted assuming straight ray geometry. This effect is illustrated in Figure A.2a for an in-plane scatterer. The actual two-way transit time is denoted by t' for comparison with the corresponding least distance arrival time, t, for the same arbitrary midpoint location.

As for the case of reflection from a plane horizontal interface (Dix, 1955), the true diffraction event is nonlinear in X^2 vs. t^2 (Figure A.2b), indicating that equation (A.4) is, strictly speaking, inappropriate for stratified media. Despite this limitation, it follows from Dix's small spread analysis that for X small compared to depth, $Z_D = \sum_{k=1}^{n} z_k$, equation (A.4) yields a sufficiently accurate prediction of transit time when the uniform velocity, V, is replaced by the root-mean-square (rms) velocity

$$V_{rms}^2 = \frac{1}{T_0} \sum_{k=1}^{n} v_k^2 \tau_k. \tag{A.9}$$

It can be demonstrated (Taner and Koehler (1969)) that equation (A.4), with $V = V_{rms}$, is a two term truncation of the Taylor series expansion for $t^2(X)$ about the point X=0. A third term, in X^4, is always negative, excepting the limiting case where $v_1 = v_2 =, ..., = v_n$ or, equivalently, $V_{rms} = V_a = V$. This implies uniform velocity and all higher order terms beyond X^2 are zero.

In light of the foregoing discussion, let us now examine the nature of velocity estimates obtained from equations (A.5) and (A.6) for an in-plane scatterer where the v_k are not all equal. Although the actual event is known to be nonlinear in X^2 vs. t^2, the estimate

obtained by equation (A.5) assumes that it is linear. In other words, the resulting velocity estimate implies the hyperbola through (X, t') depicted in Figure A.2a. Consequently, it is the slope of the corresponding line joining points $(0, t_0^2)$ and (X^2, t'^2) in Figure A.2b that defines the velocity given by equation (A.5). Referring to the same figures, we can characterize the resulting estimate as follows. First, the velocity obtained is clearly dependent upon the variable X and increases as $|X|$. Secondly, it is obvious that this estimate will always exceed the average velocity defined by equation (A.7). Lastly, as we shall discover shortly, the estimate given by equation (A.5) can never exceed the generalized rms velocity, $V_{rms}(p_x)$, that is defined for the case $p_x = 0$ by equation (A.9). Although these observations provide a comparative context, we have yet to describe the meaning of the velocity furnished by equation (A.5). In fact, there is not much physical significance that can be attached to the estimate. The only description we can give is to say that it amounts to a very crude stacking velocity. If we assume that a stacking velocity, V_s, is defined by least squares fitting equation (A.4) to the observed event with $V = V_s$ (Al-Chalabi, 1973), we have

$$V_s^2 = 4\left[m\sum_{i=1}^{m} X_i^4 - \left(\sum_{i=1}^{m} X_i^2\right)^2\right] \Big/ \left[m\sum_{i=1}^{m} t_i^2 X_i^2 - \sum_{i=1}^{m} t_i^2 \sum_{i=1}^{m} X_i^2\right], \qquad \text{(A.10)}$$

where m is the number of (X,t) pairs defining the estimate. Note that given just two points, $(0, t_0)$ and (X, t'), equation (A.10) reduces directly to equation (A.5). Unfortunately, as for the case of uniform velocity, there is little statistical significance associated with a two-point estimate.

Equation (A.6), on the other hand, yields a velocity estimate that is directly related to physical parameters. Returning to Figure A.3, we observe that the midpoint variable, X, can be expressed in terms of discrete layer parameters as

$$X = \sum_{k=1}^{n} x_k = \frac{\cos\alpha}{2} \sum_{k=1}^{n} v_k t_k \sin\theta_k, \qquad \text{(A.11)}$$

where $t_k = \tau_k/\cos\theta_k = \tau_k/(1 - p_x^2 v_k^2)^{1/2}$ is two-way transit time measured along the ray path within the kth layer, $x_k = (v_k t_k/2)\sin\theta_k$ is the horizontal component of the ray path

in the kth layer and θ_k is the angle between the ray and vertical. For the particular case of an in-plane scatterer, $\cos\alpha = 1$. Recalling that Snell's law requires the ray parameter, $p_x = \sin\theta_k / v_k$, to be independent of layering, we can bring this constant outside the summation in equation (A.11) to yield

$$X = \frac{p_x \cos\alpha}{2} \sum_{k=1}^{n} v_k^2 t_k. \tag{A.12}$$

Finally, using equation (A.12) and recognizing that $t = \sum_{k=1}^{n} t_k$, we can rewrite equation (A.6) as

$$V^2 = \sum_{k=1}^{n} v_k^2 t_k \Big/ \sum_{k=1}^{n} t_k = V_{rms}^2(p_x). \tag{A.13}$$

We discover, as a result, that the velocity yielded by equation (A.6) is, the same generalized root-mean-square velocity presented by Shah and Levin (1973). Moreover, as alluded to above, equation (A.13) reduces to Dix's rms velocity defined by equation (A.9) for the case $p_x = 0$. In addition to proving that $V_{rms}^2(p_x)$ never decreases as X increases, Shah and Levin demonstrated that the generalized rms velocity is bounded, as expected, by the smallest and largest v_k in the section. The first of these conclusions follows from equation (A.6) and is tantamount to observing that the local slope of the event in X^2 vs. t^2 is always decreasing (Figure A.2a).

Following the lead of González-Serrano and Claerbout (1984) and Claerbout (1985), we realize that by incorporating the ray parameter, equation (A.6) also leads naturally to interval velocities from two or more in-plane diffractions. In practice, we choose a tangent line having slope $dt/dX = 2p$ and subsequently determine, for each event, the respective point of tangency $(X, t(X))$, where X is measured relative to the respective apex. Now, treating the vertical interval between two in-plane scatterers as an effective unit having interval velocity v_i, it follows from equation (A.12) that

$$X_i - X_{i-1} = \frac{p}{2}\left[\sum_{k=1}^{i} v_k^2 t_k - \sum_{k=1}^{i-1} v_k^2 t_k\right] = \frac{p v_i^2 t_i}{2}. \tag{A.14}$$

Consequently, recognizing that the two-way transit time through the interval, t_i, must account exactly for the difference in total transit time,

$$t(X_i) - t(X_{i-1}) = \sum_{k=1}^{i} t_k - \sum_{k=1}^{i-1} t_k = t_i, \tag{A.15}$$

we find that the interval velocity can be obtained directly as

$$v_i^2(p) = \frac{2}{p} \frac{(X_i - X_{i-1})}{(t(X_i) - t(X_{i-1}))}. \tag{A.16}$$

Alternatively, upon establishing the tangent point for each event, we could have proceeded by evaluating equation (A.6) for the associated rms velocities. Then, with these in hand, the interval velocity follows from a straight forward re-expression of the previous equation

$$v_i^2(p) = \frac{V_{rms,i}^2(p)t(X_i) - V_{rms,i-1}^2(p)t(X_{i-1})}{t(X_i) - t(X_{i-1})}. \tag{A.17}$$

This expression reveals that v_i is, in particular, the rms interval velocity. Equation (A.17) is simply a generalization of the interval velocity due to Dix (1955) in the same sense that equations (A.13) and (A.9) are related (Nowroozi, 1989). The significance of rms interval velocities, compared with other varieties, has been discussed by Al-Chalabi (1974) and Hubral and Krey (1980). In short, although we view the interval as practically homogeneous, it generally includes some degree of velocity heterogeneity. We anticipate that intervals bounded by diffraction events are more likely to possess significant heterogeneity than those established on the basis of major reflection events. In fact, since reflection events are direct manifestations of velocity contrasts, we suggest that accompanying reflection information should aid in assessing the extent of velocity heterogeneity within an interval defined by diffractions. If heterogeneity is insignificant within the interval, its thickness is given by

$$z_i^2 = \frac{v_i(p)^2(t(X_i) - t(X_{i-1}))^2}{4} - (X_i - X_{i-1})^2. \tag{A.18}$$

A.4 Limitation for Out of Plane Diffractions:

To this point, our treatment of a horizontally layered section has focussed on scatterers residing in the plane of survey. We now emphasize that apart from our discussion of

interval velocities, the foregoing analysis holds quite generally for an arbitrary scatterer. The velocity yielded by equation (A.6) is an estimate of the rms velocity described by equation (A.13) independent of the scatterer's location. Unfortunately, the estimate is of little use in the absence of associated depth control. As regards interval velocities, recall that the diffraction pattern for an arbitrary scatterer has local slope $dt/dX = 2p_x\cos\alpha$. Unlike the special case for in-plane diffraction events where $\cos\alpha = 1$, energy radiated from arbitrary scatterers via the same ray parameter cannot, in general, be identified on the basis of a unique local slope. Strictly speaking, even though the factor $\cos\alpha$ has less influence as p_x increases, the graphical method described above is appropriate only for in plane diffractions. Thus, in order to associate diffraction based velocity estimates with a corresponding depth or stratigraphic unit, we must either assume that scatterers reside in plane or determine their true locations. For this reason, an obvious means of deriving the location of a scatterer from its expression on two or more profiles is described below. Although the result is only approximate for stratified media, we shall discover that the error is related to velocity heterogeneity. First we return to the case of uniform velocity.

Consider, once again, a point diffractor within a constant velocity medium as depicted in Figure A.1. Recall that our reference coordinate system was chosen such that the scatterer resides in the yz-plane. We found, on assuming coincident source-receiver, that the observed diffraction pattern is described exactly by equation (A.4). Consequently, the velocity predicted by equations (A.5) and (A.6), is independent of the scatterer's location. Having emphasized this, let us examine the significance of the constant t_0 in equation (A.4).

For a given event, $t_0 = 2r/V$ is the minimum arrival time for scattered energy detected by a coincident source-receiver. Recall that for a point scatterer at $(0, Y_D, Z_D)$, $r = (Y_D{}^2 + Z_D{}^2)^{1/2}$ is the length of a line segment joining the scatterer and the origin. It is important to appreciate that the diffraction event observed for this scatterer is not unique. The very same diffraction pattern would result for any scattering source located at $(0, y, z)$ satisfying $y^2 + z^2 = r^2 = Y_D{}^2 + Z_D{}^2$. That is, for any scatterer residing on a

semicircle of radius r from the origin in the yz-plane. It follows that upon identifying events having a common source on two or more optimum offset profiles, the scattering source may be located identically. Profiles need not be parallel but this aids in identifying common events since their apexes must occur at the same traverse position.

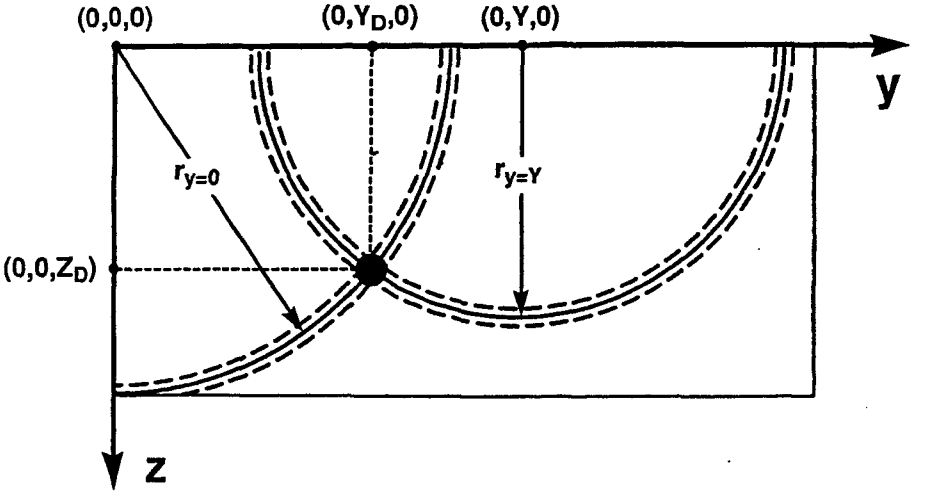

Figure A.4. Location of point scatterer in uniform medium from two optimum offset profiles parallel to the x-axis at y=0 and y=Y. Scatterer's position $(0, Y_D, Z_D)$ is indicated by intersection of circular wavefronts having radii $r_{y=0}$ and $r_{y=Y}$. Dashed curves are a qualitative suggestion of uncertainty.

The strategy is illustrated in Figure A.4 for a profile acquired along the x-axis (y=0) and a second parallel profile at y=Y. Assuming common diffraction events have been identified on both records and velocity estimates subsequently obtained, arcs of radii $r_{y=0} = Vt_{0,0}/2$ and $r_{y=Y} = Vt_{0,Y}/2$ are constructed from respective centers, y=0 and y=Y. The scatterer is located at the intersection of the resulting arcs.

Prior to examining the analogous scenario for a true stratified media, it is again useful to consider the hypothetical case of straight rays in a uniform medium having the effective average velocity. Under this assumption equation (A.4) continues to describe the resulting diffraction pattern if only we replace the constant velocity, V, by the average velocity defined by equation (A.7). Using average velocity estimates from events observed for y=0 and y=Y, we could proceed as described above. Intersection of the resulting arcs would

once again imply the scatterer's location as illustrated in Figure A.5.

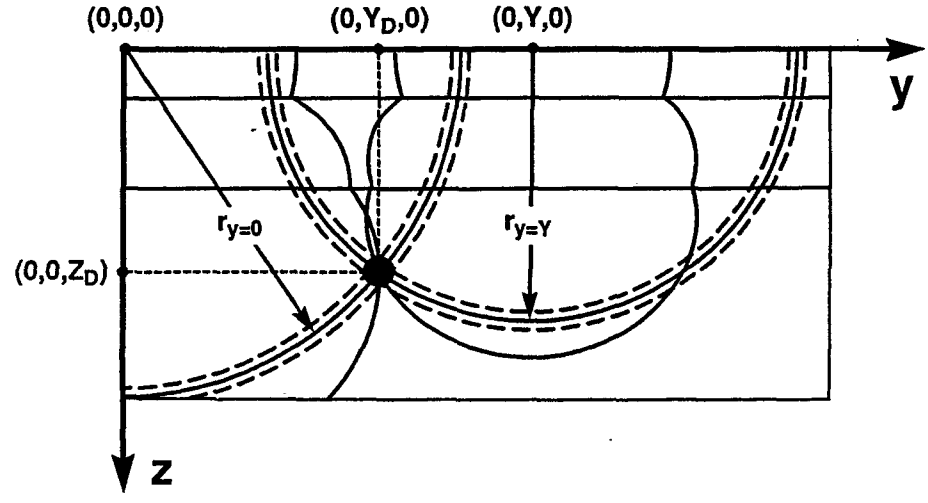

Figure A.5. Location of point scatterer in stratified medium assuming straight rays. Intersection of circular wavefronts based on average velocity estimates coincides with that of "straight ray wavefronts" at the scatterer's location.

We have also depicted what we shall call "straight ray wavefronts" for $t_{0,0}$ and $t_{0,Y}$. These are just the loci of endpoints for straight rays that leave a given source at arbitrary take-off angles and are extended at the appropriate layer velocities for half the corresponding apex time. We observe that the intersection of these so called wavefronts and, consequently, the scatterer's true location coincides with that of the experimentally determined arcs. In other words, If the straight ray assumption were valid, our simple strategy would also properly locate scatterers within stratified media.

We turn now to the actual situation for a horizontally layered section. Recall that the observed diffraction event is really a record of transit time for scattered energy that takes the path of least time to and from the scatterer as a function of X. Here, equation (A.4) approximately describes the actual event on replacing the constant velocity, V, by Dix's rms velocity or what amounts to equation (A.13) evaluated for $p_x = 0$. In practice, however, equation (A.6) yields the generalized rms velocity for some non-zero Snell parameter. Consequently, for the purpose of locating the scatterer's location in the yz-plane, this

estimate should be obtained for X as small as possible since $V_{rms}(p_x)$ increases with X. Practically speaking, however, caution is advised since local slope estimates are obviously subject to greater error as X decreases. Having issued this warning, let us suppose for the time being that we are able to estimate the appropriate rms velocities at X=0 for the pair of diffraction events considered in the foregoing examples. Arcs having the appropriate radii are subsequently constructed as illustrated in Figure A.6.

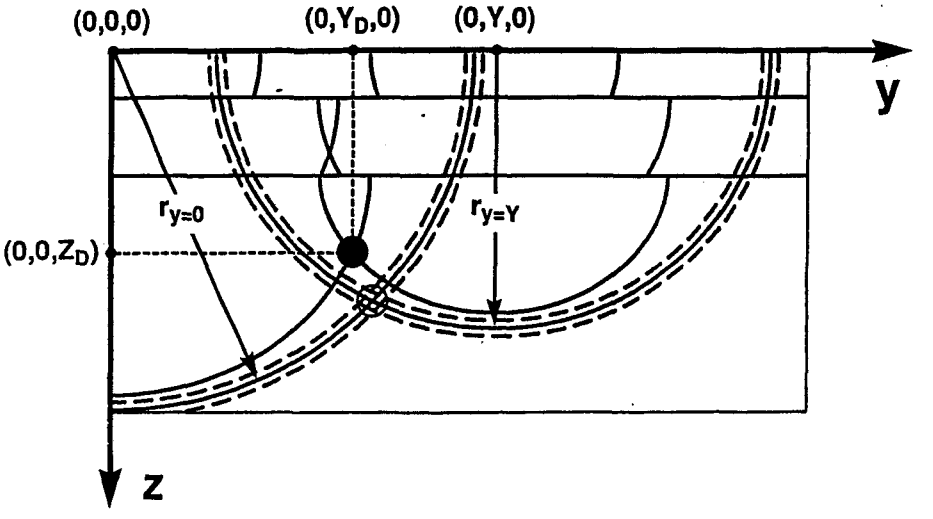

Figure A.6. Approximate location of scatterer in stratified medium respecting Snell's law. Intersection of circular wavefronts based on rms velocity estimates fails to coincide with that of true wavefronts at the scatterer's location.

We have also displayed the true wavefronts for $t_{0,0}$ and $t_{0,Y}$. Like the hypothetical straight ray wavefronts in Figure A.5 intersection of these wavefronts marks the actual location of the scatterer. But, in contrast with the previous examples, intersection of the experimentally derived arcs only approximately locates the scatterer. To provide a sense of scale, the model parameters resulting in Figures A.5 and A.6 are as follows: $Y_D = 60.0\,\text{m}$, $Z_D = 50.0\,\text{m}$, $z_1 = 10.0\,\text{m}$, $v_1 = 750.0\,\text{m/s}$, $z_2 = 20.0\,\text{m}$, $v_2 = 1500.0\,\text{m/s}$, $z_3 = Z_D - (z_1 + z_2) = 20.0\,\text{m}$, $v_3 = 2500.0\,\text{m/s}$. The predicted location is $Y_D = 65.1\,\text{m}$, $Z_D = 62.1\,\text{m}$.

The error is related to the difference between rms and average velocities. A measure

of this difference can be expressed as

$$g(p_x) = \frac{V_{rms}^2(p_x) - V_a^2}{V_a^2} = \frac{\sum_{k=1}^{n} \frac{z_k}{v_k} \sum_{j=1}^{n} \frac{z_j}{v_j} \sum_{i=1}^{n} \frac{z_i}{v_i} \frac{(v_i^2 - v_k v_j)}{(1 - p_x^2 v_i^2)^{1/2}}}{Z_D^2 \sum_{i=1}^{n} \frac{z_i}{v_i} (1 - p_x^2 v_i^2)^{-1/2}}, \qquad \text{(A.19)}$$

where the Snell parameter, p_x, is, in general, different for profiles at y=0 and y=Y. Recalling that rms velocity always exceeds the corresponding average velocity, we recognize that this quantity must be strictly positive. In other words, neglecting other sources of error, the predicted depth for a given scatterer will always exceed the true value. Moreover, the sign of the corresponding error in Y_D depends on the relative magnitude of $r_{y=0}$ and $r_{y=Y}$. In particular, for $r_{y=0} = r_{y=Y}$, the error is zero. Although, in practice, a quantitative assessment of these errors will be difficult at best, there is an important qualitative relationship between the accuracy that can be expected and the velocity structure of the subsurface. For $p_x = 0$, equation (A.19) can be re-expressed as

$$g(0) = \frac{V_{rms}^2(0) - V_a^2}{V_a^2} = \frac{1}{Z_D^2} \sum_{k=1}^{n-1} z_k \sum_{j=k+1}^{n} z_j \frac{(v_k - v_j)^2}{v_k v_j}. \qquad \text{(A.20)}$$

Al-Chalabi (1974) used the term heterogeneity factor to describe this quantity, g(0), since it characterizes the velocity heterogeneity of the subsurface. Where stratification is characterized by sparse but large velocity contrasts, the heterogeneity factor and more generally equation (A.19) will have large values. Consequently, we find that the uncertainty in our method for locating a scatterer is directly related to velocity heterogeneity. In particular, for the model parameters cited above, the heterogeneity factor has a value of g(0)=0.2133. For comparison, the same model with weaker velocity stratification ($v_1 = 750.0\,m/s$, $v_2 = 1000.0\,m/s, v_3 = 1250.0\,m/s$) has a heterogeneity factor of g(0)=0.0360. In this case, the location procedure yields $Y_D = 61.3\,m$, $Z_D = 52.7\,m$. The improvement suggests that in many situations, particularly where diffractions have their origin within unconsolidated overburden, the procedure described here can yield an accurate location and consequently reliable depth control for the associated velocity estimate.

Before proceeding, we return briefly to the assumption that velocity estimates could be obtained, using equation (A.6) at X=0. As cautioned above, this cannot be achieved in practice and, consequently, the scatterers predicted location is subject to additional error. One means of reducing this added error is to obtain two or more velocity estimates for a given event at acceptable values of X and perform an appropriate extrapolation for the corresponding $V_{rms}(p_{x=0})$. We shall return to this issue in following sections.

A.5 Effect of Non – Zero Offset:

The foregoing discussion and analysis of velocities from diffractions has assumed that source and receiver are coincident. Although one might expect that this assumption is warranted in interpreting ground penetrating radar data, that it is also appropriate for shallow seismic data is less evident. Let us now examine the effect of non-zero optimum offset on measured transit time as a function of midpoint position and the resulting influence on velocity estimates yielded by equation (A.6). Referring again to Figure 1, consider a point scatterer within a uniform velocity medium at a distance $r = (Y_D^2 + Z_D^2)^{1/2}$ from the origin. Recall that equation (A.3) describes the two-way transit time at midpoint location $X_M = (X_R + X_S)/2$ as measured by a source-receiver pair located respectively at $(X_S, 0, 0)$ and $(X_R, 0, 0)$ and separated by an optimum offset $\Delta x = X_R - X_S$. As this offset approaches zero, the transit time approaches that given by equation (A.4) and it is from this relation that equations (A.5) and (A.6) derive.

In Figure A.7a, we present a set of characteristic curves that specify the difference between zero offset and non-zero offset transit times, Δt, as a function of X_M/r for $\Delta x/r$ ranging from 0.1 to 50.0. Notice that the transit time difference is normalized by the normal incidence transit time $t_0 = 2r/V$ and that the vertical axis is displayed in logarithmic format. These curves are symmetric about $X_M/r = 0$ and quantify the so called Cheop's pyramid effect described by Claerbout (1985). The effect is especially evident for large values of $\Delta x/r$ where relatively stable plateaus near $X_M/r = 0$ reflect the severely truncated apexes of the corresponding diffraction event for $|X_M/\Delta x| \leq 1/2$. In absolute terms, we

observe that the deviation between zero offset and non-zero offset transit times at $X_M/r = 0$ ranges from approximately 0.1 % of normal incidence time for $\Delta x/r = 0.1$ to nearly fifty times normal incidence time for $\Delta x/r = 50.0$. For $\Delta x/r \leq 5.0$, however, this error decreases rapidly as X_M/r increases.

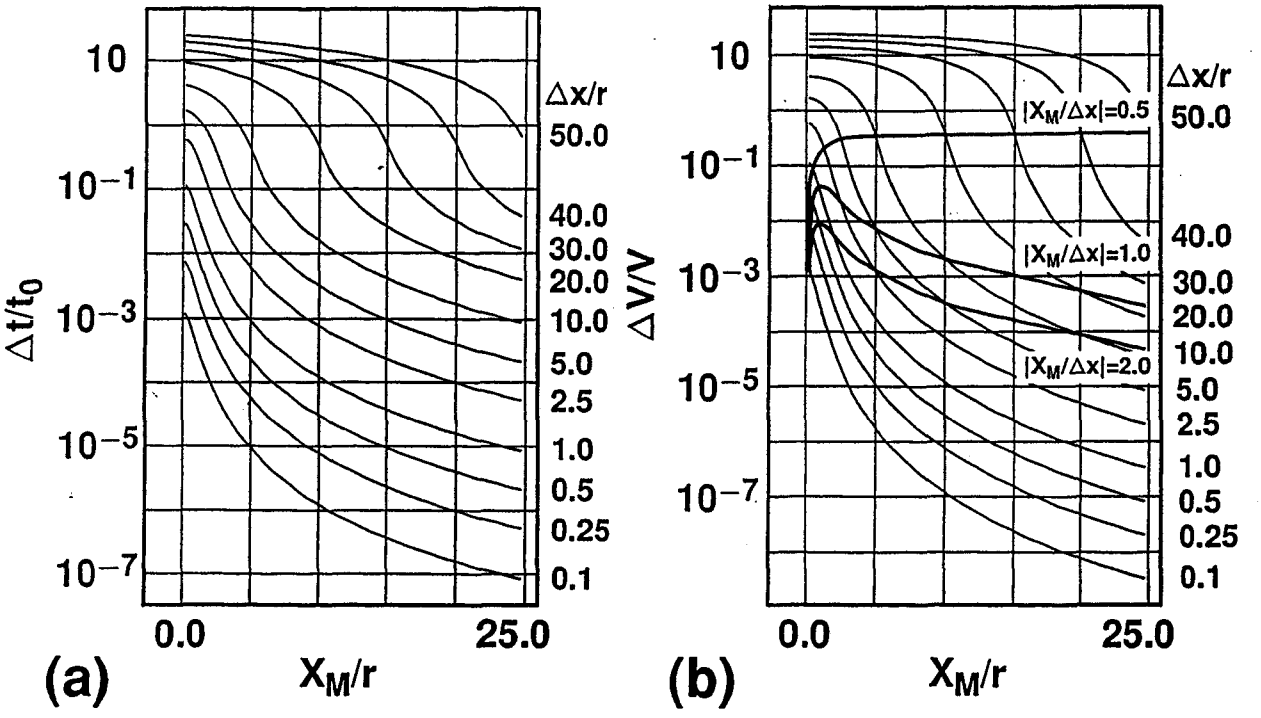

Figure A.7. Effect of non-zero optimum offset for uniform media. (a) Normalized transit time error $\Delta t = (t(\Delta x \neq 0) - t(\Delta x = 0))/t_0(\Delta x = 0)$. (b) Corresponding normalized velocity error $\Delta V = (V_{est.} - V_{true})/V_{true}$ (bold curves display criteria related to expected error limits). Transit time and velocity errors are displayed versus midpoint position scaled by distance from origin to scatterer. Curves are depicted for various ratios of offset to distance.

Of course, these departures from the hyperbolic nature of scattering events also influence velocity estimates predicted by equation (A.6) since this expression involves the local slope of the diffraction pattern. This influence is characterized by the corresponding curves displayed in Figure A.7b. Here the deviation of the predicted velocity from the true value, ΔV, is charted as a function of X_M/r for the same range of $\Delta x/r$. In this case the deviation is normalized by the true velocity. Not surprisingly, the gross character of these curves resembles those for the corresponding transit time disparities but, in general, the relative

error in predicted velocities is somewhat less and decreases more rapidly as $\Delta x/r$ increases. From a practical perspective, these characteristic curves indicate that the error introduced by non-zero optimum offset is not prohibitively large except where $\Delta x/r$ is very large. Otherwise, so long as we apply equation (A.6) at a reasonable distance from the apex of a diffraction event, the resulting error is quite acceptable. As a rule of thumb, estimates should not be made for $|X/\Delta x| < 1/2$ and preferably for $|X/\Delta x| \geq 2$. Respecting this constraint, the error in predicted velocities resulting from non-zero optimum offset never exceeds 1.0 %. An intermediate condition $|X/\Delta x| \geq 1$ also limits error to 1.0 % except over the range $0.25 \leq \Delta x/r \leq 5.0$ where maximum error approaches 5.0 %. Unfortunately, this is precisely the range most frequently encountered in shallow seismology. Curves illustrating these criteria are displayed in Figure A.7b.

Finally, computational analysis indicates that inflation of velocity estimates resulting for non-zero optimum offset increases with velocity heterogeneity. In other words, Figure A.7b should be viewed as characterizing the limiting condition for g(0)=0.0. Let us return, for example, to the situation considered in connection with Figures A.4, A.5 and A.6. If we assume that $v_1 = v_2 = v_3$ and an optimum offset of A..0 m, Figure A.7b predicts that the velocity estimate yielded by equation (A.6) incorporates a maximum error of $\Delta V/V \approx 0.05$ due to offset. In comparison, the velocity model used to generate Figures A.and 6 ($v_1 = 750.0\,\mathrm{m/s}, v_2 = 1500.0\,\mathrm{m/s}, v_3 = 2500.0\,\mathrm{m/s}$) has a heterogeneity factor of g(0)=0.2133 and yields a computed error of $\Delta V_{rms}/V_{rms}(p_{x=0}) \approx 0.085$. In turn, the more weakly stratified model ($v_1 = 750.0\,\mathrm{m/s}, v_2 = 1000.0\,\mathrm{m/s}, v_3 = 1250.0\,\mathrm{m/s}$), having a heterogeneity factor of g(0)=0.0360, results in an intermediate error of $\Delta V_{rms}/V_{rms}(p_{x=0})$ ≈ 0.065. We qualify these findings by stating that for all cases examined, the influence of velocity heterogeneity diminishes rapidly as X_M/r increases. In particular, for the cases cited above, the departure of observed error from that predicted by Figure A.7b becomes practically negligible by $X_M/r = 2.0$. Bearing this in mind, we re-emphasize that the effect of non-zero offset is not the only consideration restricting velocity estimates near X=0. As alluded to earlier, elevated uncertainty in the measurement of local event slope, dt/dX, in

the region about X=0 imposes an additional limitation.

A.6 Concluding Discussion:

In closing, we present a purely demonstrative example to illustrate the mechanics of the method. Figure A.8 is a portion of an optimum offset section (BB-900) acquired by the Geological Survey of Canada on the Fraser River delta, British Columbia (Pullan et al., 1989). The format is the same as for Figure A.2a with the origin located directly over the apex of the analyzed scattering event at approximately 67.5 ms. The optimum offset was 24.0 m and the trace interval is 3.0 m.

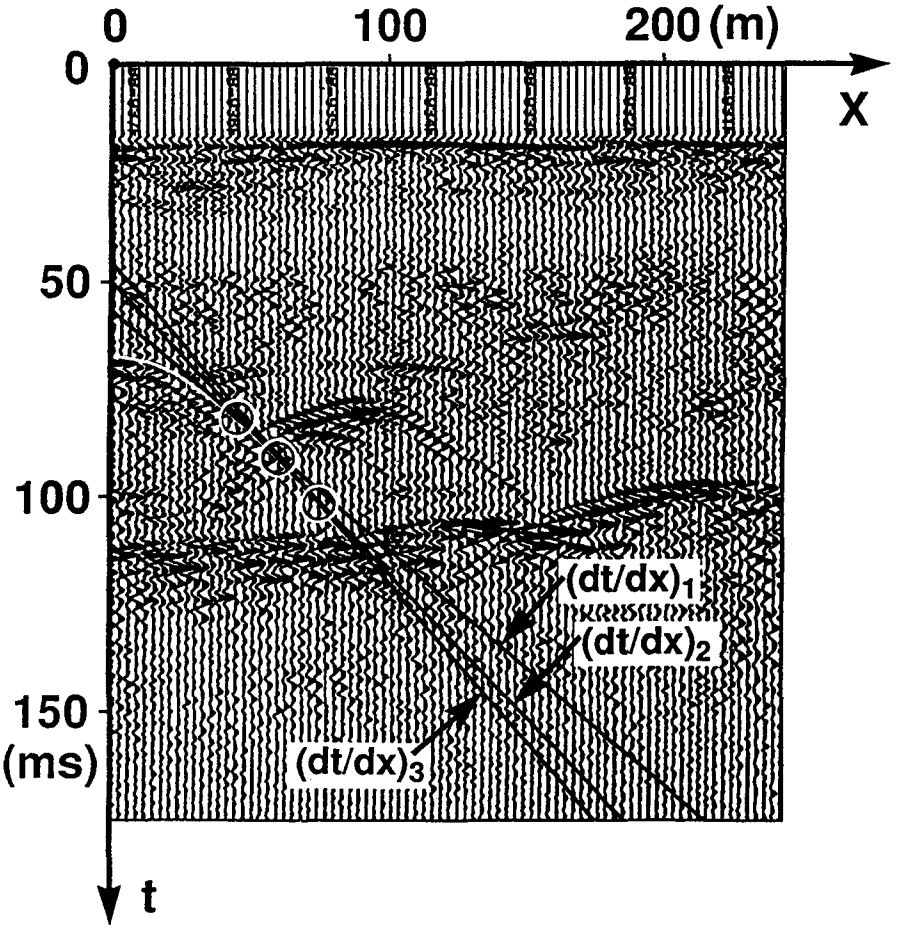

Figure A.8. Portion of optimum offset profile acquired on the Fraser River delta, British Columbia. Tangents to the diffraction pattern at circled points have slopes $(dt/dx)_1$, $(dt/dx)_2$ and $(dt/dx)_3$.

Local tangents to the diffraction pattern are established at distances of $X_1 = 45.0\,\text{m}$,

$X_2 = 60.0\,\text{m}$ and $X_3 = 75.0\,\text{m}$ from the origin. These tangents have measured slopes of $(dt/dx)_1 = 0.595\,\text{ms/m}$, $(dt/dx)_2 = 0.673\,\text{ms/m}$ and $(dt/dx)_3 = 0.733\,\text{ms/m}$. The respective two-way transit times are $t_1 = 81.9\,\text{ms}$, $t_2 = 91.1\,\text{ms}$ and $t_3 = 100.8\,\text{ms}$. Using these values, equation (A.6) yields corresponding rms velocities of approximately $V_1 = 1922\,\text{m/s}$, $V_2 = 1979\,\text{m/s}$ and $V_3 = 2015\,\text{m/s}$. That these estimates increase with distance from the origin is consistent with our analysis of stratified media and, consequently, we view these estimates as generalized rms velocities defined by equation (A.13). Moreover, as we have only marginally violated the restriction $|X/\Delta x| \geq 2$ and there is no seismic evidence for strong velocity heterogeneity, these estimates should be accurate to within about 1 % of the true rms velocities. Of course, the presence of uncertainties in the measured values cited above produces additional error. In the present case we estimate that this additional error is less than 5 % but may approach 10 %, depending on the quality of data. An accompanying depth scale supplied by Pullan et al. and based on a series of borehole velocity surveys, places the apex of the diffraction event at about 53.0 m and implies an average velocity of approximately 1570 m/s to this depth. To furnish a comparison with our findings, we perform a simple extrapolation to project the velocity at X=0 from our estimates at X=45.0, 60.0 and 75.0 metres. Neglecting measurement errors, least squares linear extrapolation yields an estimate of 1786 m/s. Assuming an in-plane scatterer ($p_x = 0$ for $X = 0$), the difference between this estimate and the average velocity determined by Pullan et al. implies a heterogeneity factor of approximately g(0)=0.29. However, since there is no apparent evidence for significant velocity heterogeneity, this value suggests that either the average velocity or the rms velocity is in error.

Numerous sources of error exist. For example, the average velocity structure used by Pullan et al. to generate the accompanying depth scale ignores the existence of lateral velocity variations and this suggests the utility of diffraction based estimates for local velocity control. Inconsistent velocities can also arise from diffractions occurring out of plane but, ordinarily, these events imply a velocity and, thus, a heterogeneity factor that is too low rather than high. In addition, modelling indicates that linear extrapolations yield

results that are almost invariably too high. We have found that the consistency between predicted rms and average velocities can be improved in many cases by a more sophisticated extrapolation. These approaches can also backfire, however, primarily due to the effect of non-zero optimum offset. Finally, it is conceivable that the observed discrepancy arises purely from uncertainties in transit time and local slope measurements.

In addition to illustrating the method we have described for diffraction based velocity estimation, the foregoing example also suggests limitations on the interpretation of velocity estimates derived from a single diffraction. More substantial conclusions and improved confidence can be obtained by analyzing additional scattering events or multiple profiles.

Appendix B

ARRAY RESPONSES FOR PLANE AND SPHERICAL INCIDENCE

B.1. Introduction:

The filtering properties of receiver arrays are well understood and typically characterized assuming plane wave incidence over the length of the array (e.g., Parr and Mayne (1955); Holzman (1963); Dobrin (1976). As the scale of seismic application decreases, however, it is useful to review the basis of this assumption and assess both its theoretical and practical limitations. To this end, the apparent surface wavefield arising for a monochromatic spherical wave is compared with that predicted for plane wave incidence. Corresponding apparent wavenumber distributions facilitate an initial assessment of the plane wave approximation. Subsequently, we examine the influence of systematic deviations between these apparent wavefields on the output of a line array of equispaced, uniformly effective receivers.

Viewed as a spatial filter, the array's response is completely determined by the number of elements, their relative weighting and spatial distribution. The relative attenuation of plane and spherically incident waves depends on the spectral composition of associated apparent waveforms within the aperture of the array. Alternatively, array attenuation properties can be related to time dependent variability of these apparent waveforms and, consequently, it is also useful to characterize the array's time domain response. In addition to the distribution and weighting of individual elements, the time domain impulse response incorporates wavefront geometry and spatial amplitude dependence. As a result, distinct responses arise in connection with plane and spherical incidence. Examination of array filters in both spatial and temporal contexts reveals that the actual attenuation of a spherical wave can deviate appreciably from that predicted assuming plane incidence.

Although the following analysis is illustrated on a scale reflecting archaeological application, the findings are of a general nature and may be appropriately scaled as necessary.

B.2 Apparent Wavefields:

Consider a monochromatic spherical wave of the form

$$\psi_s(x,y,z,t) = \frac{U_0}{4\pi r} H\left[t - \frac{r}{v}\right] \cos\left[2\pi k (r - vt)\right] \tag{B.1}$$

emanating from an image source located at x_s, y_s, z_s within a homogeneous, isotropic halfspace having velocity v. Here, $U_0 = 4\pi u_0^2$ denotes the surface displacement of a point source having initial outward radial displacement u_0, k is the linear wavenumber, $r = [(x-x_s)^2 + (y-y_s)^2 + (z-z_s)^2]^{1/2}$ is the distance from the source to an arbitrary location x, y, z and

$$H[\tau] = \begin{cases} 0, & \tau < 0; \\ 1/2, & \tau = 0; \\ 1, & \tau > 0 \end{cases}$$

is the Heaviside step function. Spatial coordinates are specified in relation to a rectangular coordinate system having its origin at the surface and z increasing with depth as illustrated in Figure B.1.

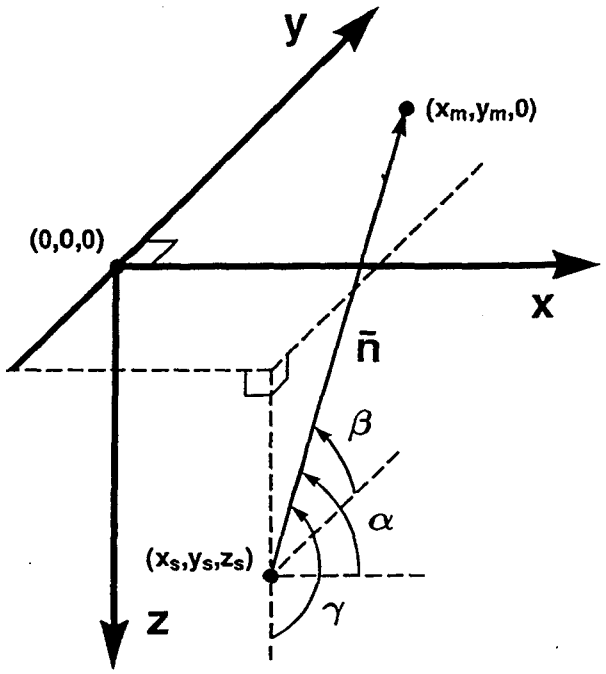

Figure B.1. Rectangular coordinate system for analysis of plane and spherical wavefronts emanating from an image source at x_s, y_s, z_s. Propagation vector n is normal to plane wavefronts incident on the surface at x_m, y_m and has direction angles α, β, γ.

Neglecting free surface interaction and given that sufficient time has elapsed for incident energy to extend over the region of interest, we take $H[t - r/v] = 1$, obtaining

$$\psi_s(x,y) = \frac{U_0}{4\pi r}\cos[\phi_s(x,y)] \tag{B.2}$$

for the instantaneous apparent wavefield detected by omnidirectional sensors on the surface (z=0). The associated phase function is

$$\phi_s(x,y) = 2\pi k(r - vt), \tag{B.3}$$

where $r = [(x - x_s)^2 + (y - y_s)^2 + z_s^2]^{1/2}$. Neglecting the minor influence of spherical divergence, the local apparent wavenumber in the x-direction follows from equation (B.3) as

$$\tilde{k}_{s,x}(x,y) = \frac{1}{2\pi}\frac{\partial\phi_s(x,y)}{\partial x} = \frac{k}{r}(x - x_s). \tag{B.4}$$

A similar expression arises for the local apparent wavenumber in the y-direction

$$\tilde{k}_{s,y}(x,y) = \frac{1}{2\pi}\frac{\partial\phi_s(x,y)}{\partial y} = \frac{k}{r}(y - y_s). \tag{B.5}$$

The associated plane wave system incident at some point x_m, y_m on the surface is given by

$$\psi_p(x,y,z,t) = \frac{U_0}{4\pi r\cos\theta}H\left[t - \frac{r\cos\theta}{v}\right]\cos\{2\pi k[l(x - x_s) + m(y - y_s) + n(z - z_s) - vt]\}, \tag{B.6}$$

where

$$l = \cos\alpha = (\mathbf{n}\cdot\mathbf{u_x})/|\mathbf{n}| = (x_m - x_s)/|\mathbf{n}|$$

$$m = \cos\beta = (\mathbf{n}\cdot\mathbf{u_y})/|\mathbf{n}| = (y_m - y_s)/|\mathbf{n}|$$

$$n = \cos\gamma = (\mathbf{n}\cdot\mathbf{u_z})/|\mathbf{n}| = -z_s/|\mathbf{n}|$$

are direction cosines for the propagation direction vector $\mathbf{n}$ joining the source with the point of incidence as depicted in Figure 1 with $\mathbf{u_x}$, $\mathbf{u_y}$ and $\mathbf{u_z}$ denoting unit vectors in the positive x, y and z directions. Note that as a local approximation to the spherical wave, we take plane wave amplitude and onset to depend on normal distance from the source

$r\cos\theta = (\mathbf{r}\cdot\mathbf{n})/|\mathbf{n}|$, where θ is the angle between the propagation direction vector and a position vector $\mathbf{r}$, locating an arbitrary point x, y, z. This amplitude dependence is a logical modification to the conventional definition of plane waves, providing a reasonable approximation to the effect of spherical divergence in the vicinity of incidence while retaining plane wave geometry. Where it is necessary to differentiate between this form and the conventional constant amplitude plane wave, the former is referred to as a modified plane wave.

Assuming, again, that sufficient time has elapsed to set $H[t - r\cos\theta/v] = 1$, the instantaneous apparent surface wavefield in the vicinity of incidence is

$$\psi_p(x,y) = \frac{U_0}{4\pi r\cos\theta}\cos[\phi_p(x,y)], \tag{B.7}$$

where

$$\phi_p(x,y) = 2\pi k[l(x - x_s) + m(y - y_s) - nz_s - vt] \tag{B.8}$$

is the associated phase function. Ignoring the minor influence of gradual amplitude variation, the corresponding apparent local wavenumber distributions are

$$\tilde{k}_{p,x}(x,y) = \frac{1}{2\pi}\frac{\partial\phi_p(x,y)}{\partial x} = k\cos\alpha \tag{B.9}$$

and

$$\tilde{k}_{p,y}(x,y) = \frac{1}{2\pi}\frac{\partial\phi_p(x,y)}{\partial y} = k\cos\beta. \tag{B.10}$$

As an example, Figure B.2 displays apparent surface wavefields computed using equations (B.2) and (B.7) for spherical and plane waves incident at a point $x_m = 1.7$ m, $y_m = 0.0$ m on the surface. Here, the source is located beneath the origin at $x_s = 0.0$ m, $y_s = 0.0$ m, $z_s = 2.0$ m and the incident wavenumber is k=2.0 m^{-1}, implying a wavelength of 0.5 m. A measure of the difference between apparent wavefields for plane and spherical incidence is obtained by comparing the corresponding apparent wavenumber distributions defined by equations (B.4), (B.5), (B.9) and (B.10). Local apparent wavenumbers arising for the spherically incident wave are depicted in Figure B.3 and exhibit significant departures from the constant values of $\tilde{k}_{p,x} \approx 1.3$ m^{-1} and $\tilde{k}_{p,y} = 0.0$ m^{-1} for plane wave incidence. In the

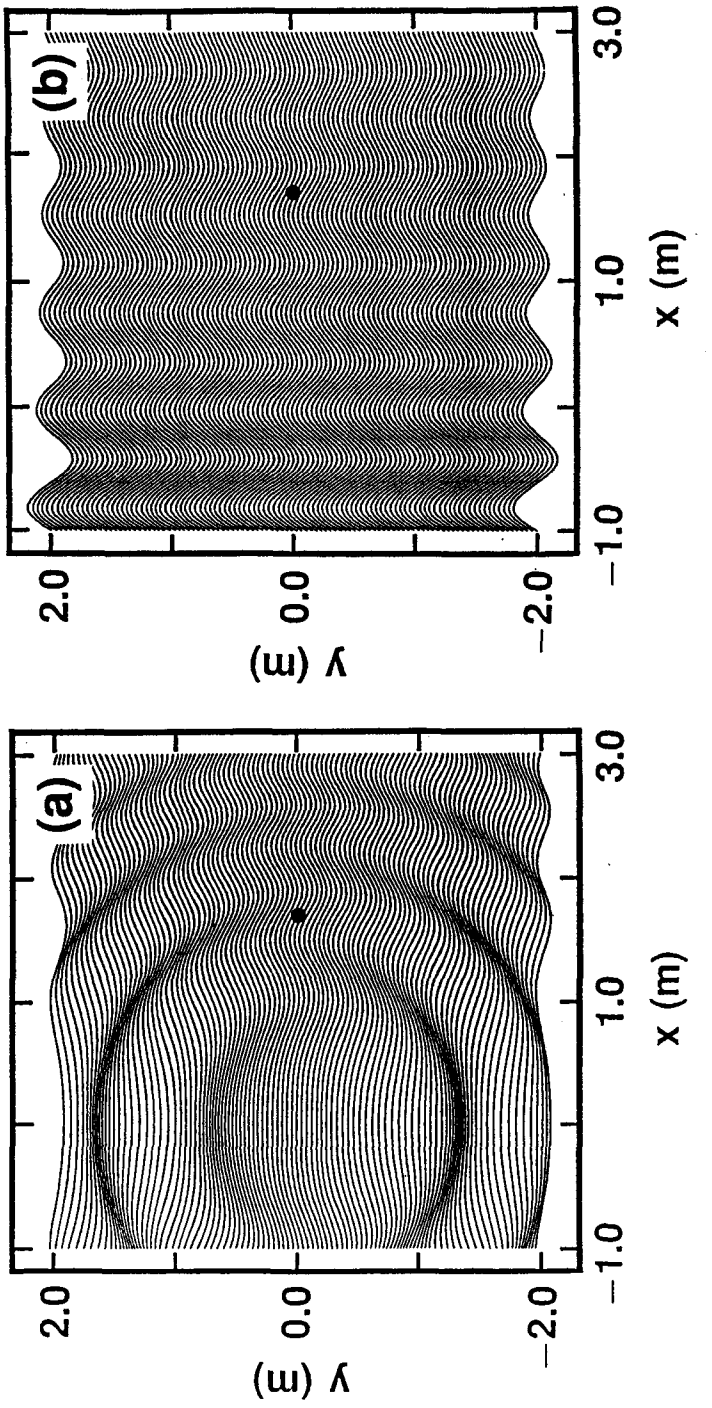

Figure B.2. (a) Apparent surface wavefields arising for a monochromatic spherical wave having its image source at depth $z_s = 2.0\,\mathrm{m}$ beneath the origin. (b) Associated apparent wavefield assuming modified plane incidence at $x_m = 1.7\,\mathrm{m}, y_m = 0.0\,\mathrm{m}$ as indicated by solid circles. Incident waves have $\lambda = 0.5$ m.

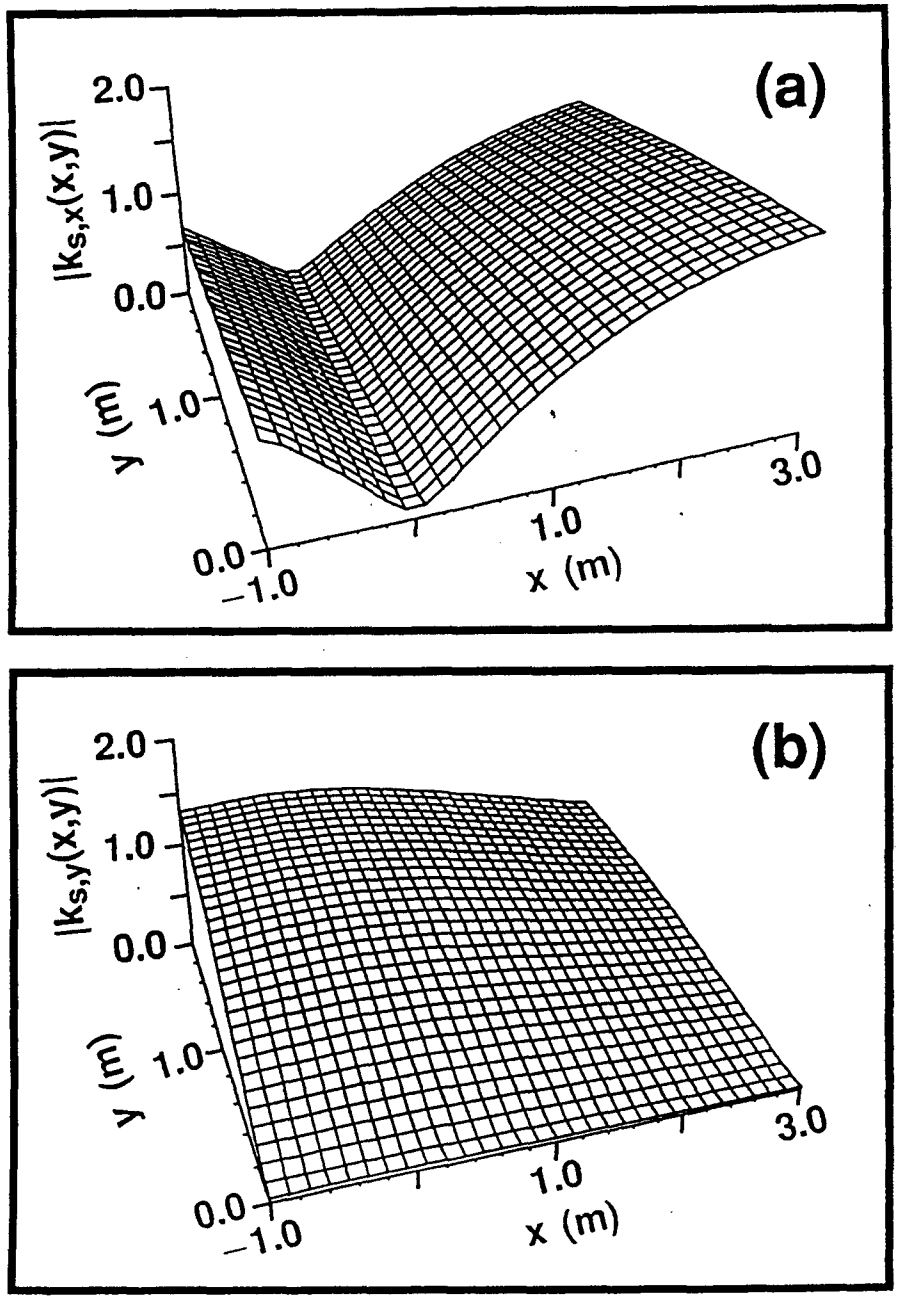

Figure B.3. Local apparent wavenumber distributions in the (a) x-direction and (b) y-direction associated with the apparent surface wavefield in Figure 2a. Corresponding apparent wavenumbers for plane incidence are respectively $\tilde{k}_{p,x} \approx 1.3$ and $\tilde{k}_{p,y} = 0.0\,m^{-1}$. Incident waves have $k = 1/\lambda = 2.0\,m^{-1}$.

following section, a connection is made between the nature of these deviations and the attenuation properties of spatial arrays.

B.3 Spatial Array Filters:

In general, the spatial impulse response of a two dimensional receiver array can be described as

$$a(x,y) = \frac{1}{N}\sum_{j=1}^{N} w_j\,\delta(x - x_j,\, y - y_j), \tag{B.11}$$

where N is the number of elements, x_j, y_j are the coordinates of the jth element, w_j is an associated weighting coefficient and $\delta(x,y)$ is the two dimensional Dirac delta function. The weighting coefficient incorporates factors including the sensitivity, directionality, coupling and electrical connection of the jth receiver. If coordinates x_m, y_m specify the array midpoint, its instantaneous output is $s(x_m, y_m)$, where

$$s(x,y) = a(x,y) ** \psi(x,y). \tag{B.12}$$

Here, $\psi(x,y)$ represents the instantaneous surface wavefield as described by equations (B.2) and (B.7) and ** denotes two dimensional convolution. Alternatively, the filtering process can be described as

$$S(k_x, k_y) = A(k_x, k_y)\,\Psi(k_x, k_y) \tag{B.13}$$

where $A(k_x, k_y)$ is the array's transfer function defined by

$$A(k_x, k_y) = \int_{-\infty}^{+\infty}\int_{-\infty}^{+\infty} a(x,y)\, e^{-i2\pi(k_x x + k_y y)}\, dx\, dy \tag{B.14}$$

and $\Psi(k_x, k_y)$ is the wavenumber domain representation of $\psi(x,y)$ given by its two dimensional Fourier transform with respect to spatial variables x and y. The array output $s(x_m, y_m)$ is obtained from the inverse Fourier transform

$$s(x,y) = \int_{-\infty}^{+\infty}\int_{-\infty}^{+\infty} S(k_x, k_y)\, e^{i2\pi(k_x x + k_y y)}\, dk_x\, dk_y. \tag{B.15}$$

For sake of illustration, further treatment assumes a line array deployed along the x-axis, having an odd number of equispaced elements and unit weighting.

On invoking the foregoing conditions, the array's spatial impulse response can be written as

$$a(x) = \frac{1}{N} \sum_{j=-(N-1)/2}^{(N-1)/2} \delta(x - j\Delta x), \tag{B.16}$$

where Δx is a constant, denoting the distance between adjacent receivers. The associated transfer function is

$$A(k_x) = |A(k_x)|\, e^{i\Theta(k_x)} = \frac{1}{N} \sum_{j=-(N-1)/2}^{(N-1)/2} e^{-i2\pi k_x j\Delta x}, \tag{B.17}$$

where

$$|A(k_x)| = \frac{1}{N}\left|\frac{\sin(N\pi k_x \Delta x)}{\sin(\pi k_x \Delta x)}\right|$$

and

$$\Theta(k_x) = \begin{cases} 0 \pm n2\pi, & \sin(N\pi k_x\Delta x)/\sin(\pi k_x \Delta x) \geq 0; \\ \pi \pm n2\pi, & \sin(N\pi k_x\Delta x)/\sin(\pi k_x \Delta x) < 0 \end{cases}$$

are, respectively, the corresponding amplitude and phase spectra depicted in Figure B.4 for the case N=7.

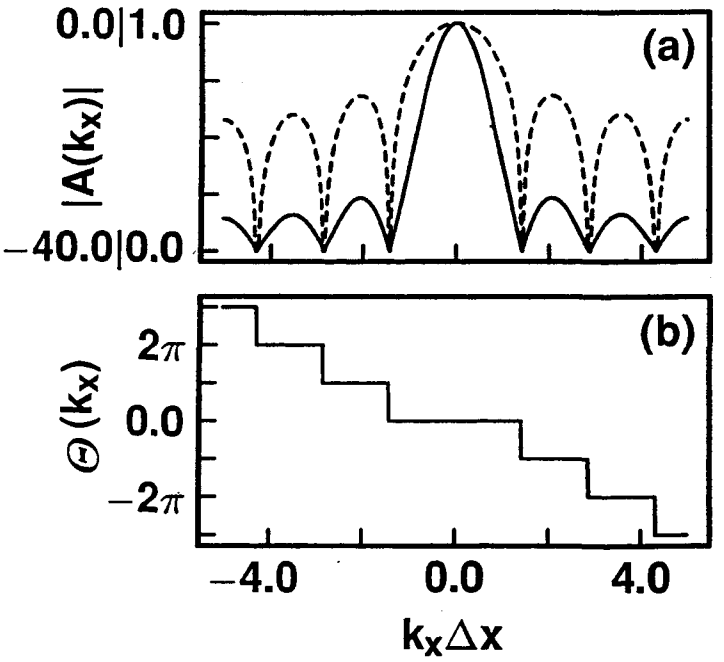

Figure B.4. (a) Amplitude and (b) phase spectra for a linear receiver array having seven equispaced and uniformly effective elements. The ordinate is apparent wavenumber scaled by the detector interval Δx. Dashed spectrum indicates attenuation on a decibel scale truncated at -40.0 dB. The phase angle is measured in radians.

Note that the arbitrary constant $\pm n2\pi$ allows some latitude in displaying an acceptable phase spectrum. In addition to being an odd function, as required, the spectrum in Figure B.4 is physically plausible as we shall find in a later section. It is also important to note that the receiver interval imposes a Nyquist wavenumber of $k_N = 1/(2\Delta x)$ so that $k_N \Delta x = 0.5$. Wavenumbers exceeding k_N are spatially aliased in the process of filtering.

B.4 Attenuation of Apparent Waveforms:

It is evident from the foregoing analysis that the relative attenuation of plane and spherically incident waves depends on the apparent wavenumber compositions of the respective surface wavefields. Consider, for example, apparent waveforms arising along the x-axis in Figure B.2. These waveforms are depicted in Figure B.5 together with a cross-section through the earth model illustrating plane and spherical wavefront systems.

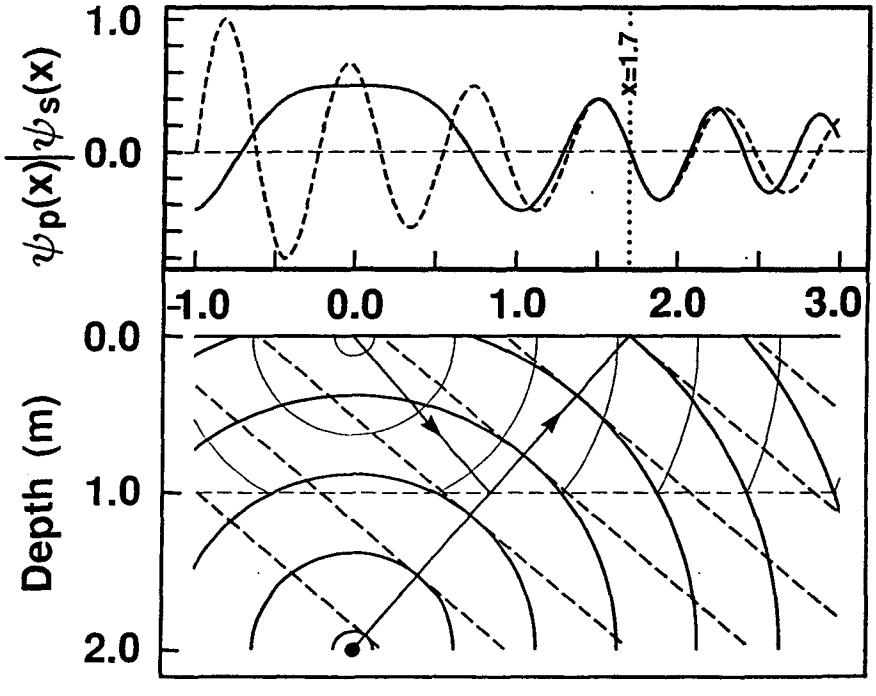

Figure B.5. Apparent waveforms arising along the x-axis in Figures 2a (solid) and 2b (dashed) with crossection through the associated earth model depicting plane (dashed) and spherical (solid) wavefront systems for incidence at x=1.7 m. Reflected wavefronts emanate from an image source at z=2.0 m associated with a point source at the origin and ideal reflection from a plane horizontal interface at z=1.0 m.

It can be seen from this diagram that, despite gradual amplitude variation, modified plane wave incidence yields a spatial waveform having a practically constant apparent wavelength

$$\tilde{\lambda}_{p,x} = \frac{\lambda}{\cos\alpha} \tag{B.18}$$

consistent with equation (B.9), where $\lambda = 1/k$ is the wavelength of the incident wave. In contrast, spherical incidence yields a spatial waveform having variable apparent wavelength

$$\tilde{\lambda}_{s,x}(x) = \lambda\left[1 + \left(\frac{z_s}{x}\right)^2\right]^{1/2} \tag{B.19}$$

as predicted by equation (B.4) for $x_s = 0$. Consequently, a finite length array deployed along the x-axis with midpoint at x_m samples a spatial waveform comprised by a continuous band of apparent wavenumbers rather than the single, unique wavenumber implied by plane incidence. Notice that on setting $x = x_m$, equation (B.19) reduces to equation (B.18) and, thus, there is exact agreement between the corresponding spatial waveforms at the point of incidence as illustrated by Figure B.5. Relative attenuation of plane and spherically incident waves depends on the nature of the departure of $\tilde{\lambda}_{s,x}(x)$ from $\tilde{\lambda}_{p,x} = \tilde{\lambda}_{s,x}(x_m)$ over the aperture of the array. If the departure is insignificant, it is appropriate to assume plane wave incidence and the corresponding attenuation may be read directly from the array's amplitude spectrum for $\tilde{\lambda}_{p,x}$. If, however, local apparent wavenumbers predicted by equation (B.19) differ significantly from $\tilde{\lambda}_{p,x}$, relative attenuation depends on the distribution of $\tilde{\lambda}_{s,x}(x)$ about $\tilde{\lambda}_{p,x}$ as well as the array's response characteristics.

Figure B.5 illustrates that $\tilde{\lambda}_{s,x}(x)$ is less than $\tilde{\lambda}_{p,x}$ for $x > x_m$ and exceeds $\tilde{\lambda}_{p,x}$ for $x < x_m$. It is also evident that the difference $|\tilde{\lambda}_{s,x}(x_m - \epsilon) - \tilde{\lambda}_{p,x}|$ is greater than $|\tilde{\lambda}_{s,x}(x_m + \epsilon) - \tilde{\lambda}_{p,x}|$ where ϵ is a positive constant and $x_m \pm \epsilon \geq 0$. These observations are extended in Figure B.6 by computing the average apparent wavenumber, $\bar{k}_{s,x}(x_m)$, over a range of fixed length windows as a function of the midpoint x_m. The mean value theorem for integrals yields

$$\bar{k}_{s,x}(x_m, y) = \frac{1}{2\delta}\int_{x_m-\delta}^{x_m+\delta} \tilde{k}_{s,x}(x, y)\,dx, \tag{B.20}$$

where $\delta = [(N-1)\Delta x]/2$ is half the aperture length of an equispaced linear array having N elements separated by an interval Δx. Substituting equation (B.4) with $x_s = 0$ and

evaluating, yields the following expression for average apparent wavenumber along the x-axis

$$\bar{k}_{s,x}(x_m) = \frac{k(x_m^2 + z_s^2)^{1/2}}{2\delta}\left[\left(1 + \frac{2x_m\delta + \delta^2}{x_m^2 + z_s^2}\right)^{1/2} - \left(1 - \frac{2x_m\delta - \delta^2}{x_m^2 + z_s^2}\right)^{1/2}\right]. \quad \text{(B.21)}$$

Finally, on expanding the square roots in the previous expression and retaining terms to second order in δ, we obtain the approximate relation

$$\bar{k}_{s,x}(x_m) \approx \tilde{k}_{s,x}(x_m) - \frac{kx_m\delta^2}{2(x_m^2 + z_s^2)^{3/2}}\left[1 - \frac{x_m^2}{x_m^2 + z_s^2}\right]. \quad \text{(B.22)}$$

Although, strictly speaking, this approximation is only valid for $\delta << (x_m^2 + z_s^2)^{1/2}$, it provides useful insight on the relation between local and average apparent wavenumbers. As expected, $\lim_{\delta \to 0} \bar{k}_{s,x}(x_m) = \tilde{k}_{s,x}(x_m)$. More significantly, since the second term in equation (B.22) is positive valued, the magnitude of the average wavenumber impinging on a finite length array is always less than that predicted for plane incidence.

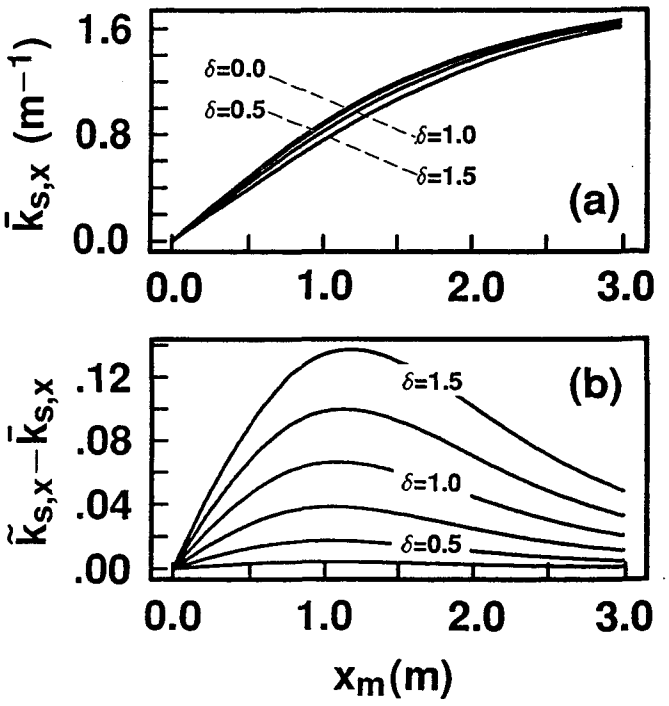

Figure B.6. (a) Comparison between local apparent wavenumber $\tilde{k}_{p,x} = \tilde{k}_{s,x}(x_m)$ at the array midpoint and average apparent wavenumber $\bar{k}_{s,x}(x_m)$ for the solid waveform displayed in Figure 5. Averages are computed for a range of half aperture values δ = 0.0-1.5 m. Note that $\tilde{k}_{p,x} = \tilde{k}_{s,x}(x_m) = \bar{k}_{s,x}(x_m)$ with δ = 0.0 m. (b) Difference between local and average apparent wavenumbers as a function of array midpoint location.

This conclusion is illustrated in Figure B.6 where the average apparent wavenumber computed using equation (B.21) is displayed, together with the local plane-wave value ($\delta = 0$), as functions of x_m for fixed window lengths between 0.5 and 3.0 m. We observe that the difference $\tilde{k}_{s,x}(x_m) - \bar{k}_{s,x}(x_m)$, displayed in Figure B.6, is in all cases positive. The approximate expression (B.22) yields nearly indistinguishable results for $\delta \leq 1.0\,\text{m}$.

Given the nominally low pass nature of receiver arrays, the foregoing conclusion suggests that the actual attenuation of spherical waves is less than that predicted assuming plane incidence. As demonstrated in the previous section and illustrated in Figure B.4, however, the amplitude spectra of spatial filters are generally multi-lobed. Consequently, although the envelope of these lobes decreases monotonically as the wavenumber approaches Nyquist, the attenuation can be high pass in nature over a limited band. Strictly speaking, the array output at an arbitrary midpoint x_m depends on the full wavenumber spectrum comprising the waveform within the array's aperture. But, having issued these qualifications, a useful empirical connection can be made between the average apparent wavenumber given by equation (B.21) and the corresponding attenuation.

In Figure B.7 we display filtered waveforms resulting on application of the spatial filter characterized in Figure B.4 to apparent waveforms arising at the surface for modified plane and spherical waves in Figure B.5. Results are also depicted for a conventional plane wave and array lengths are consistent with those in Figure B.6. For the case $\delta = 0.25\,\text{m}$, the plane wave assumption is evidently adequate as there is no appreciable difference between filtered waveforms. As array length increases, results for modified and conventional plane waves remain approximately concordant but significant deviations arise between these and the filtered waveform for spherical incidence. In particular, in the immediate vicinity of the origin, the attenuation of spherical waves can be severe in comparison with that predicted for plane incidence. Moreover, adjacent to this near source region, a zone develops wherein the attenuation of spherical waves is appreciably less than that predicted for plane incidence. Note that the presence of this region and its extent is directly related to the difference between $\tilde{k}_{s,x}(x_m)$ and $\bar{k}_{s,x}(x_m)$ as charted in Figure B.6. Where the difference

between the average apparent wavenumber and the corresponding value assumed for plane incidence is large, the attenuation predicted assuming plane waves is too high. Beyond this region, $\bar{k}_{s,x}(x_m)$ approaches $\tilde{k}_{s,x}(x_m)$ asymptotically, resulting in increased correlation between the filtered waveforms.

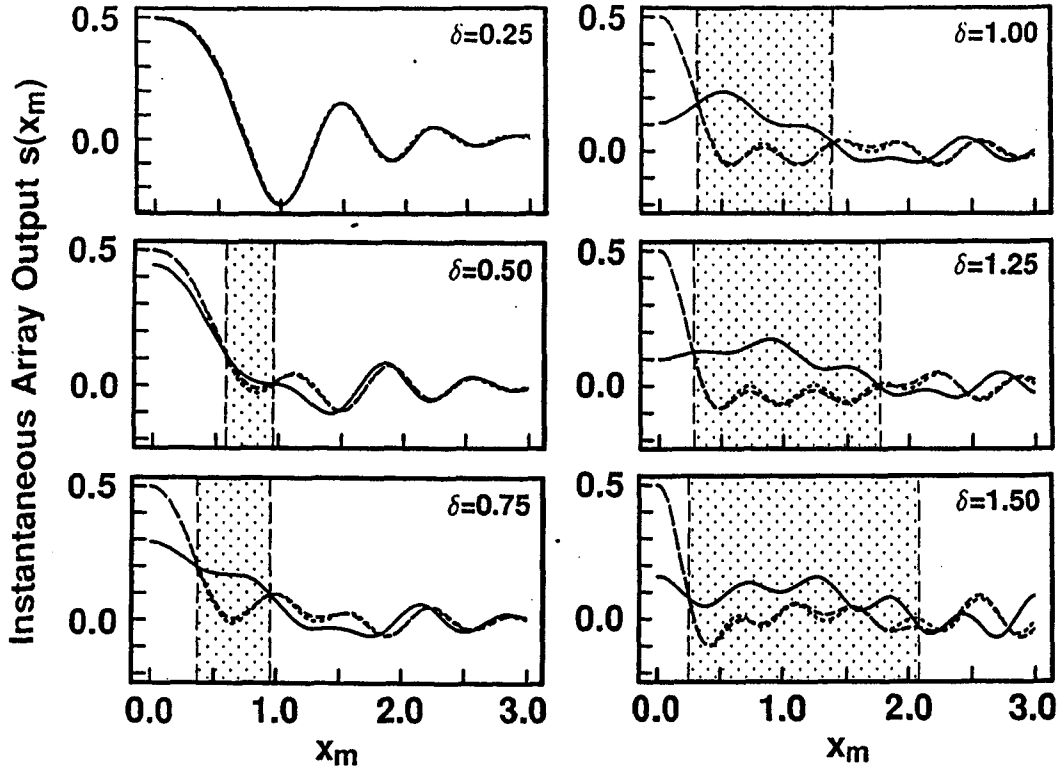

Figure B.7. Filtered apparent waveforms assuming conventional plane (dotted), modified plane (dashed) and spherical (solid) incidence. Unfiltered waveforms are depicted in Figure 5 for an array midpoint located at $x_m = 1.7\,m$. Note that the apparent waveform arising for spherical wave incidence (solid) in Figure 5 remains independent of array midpoint while plane incidence waveform (dashed) varies locally. The filter's amplitude and phase spectra are displayed in Figure 4 and $\delta = 6\Delta x/2$ ranges from 0.0 to 1.5 m. Shading highlights the expanding region associated with attenuation levels consistently overestimated assuming plane incidence.

In addition, although attenuation generally increases as $\tilde{k}_{s,x}(x_m)$ approaches k for large x_m, spatial aliasing becomes dominant for $\Delta x \approx \tilde{\lambda}_{s,x}(x_m)$. While this effect is especially evident for $\delta = 1.5\,m$ in Figure B.7, spatial aliasing occurs for $\delta > 0.75\,m$. In particular, for $\delta = 1.0\,m$, $\Delta x \approx 0.333$ so that the effective Nyquist wavenumber is $k_N = 1.5\,m^{-1}$. Consequently, according to Figure B.6 ($\delta = 0$), plane waves are subject to spatial aliasing for x_m beyond about 2.25 m. Thus, for plane incidence at, say, $x_m = 3.0\,m$, an appar-

ent wavenumber of $\tilde{k}_{s,x}(3.0) \approx 1.66\,m^{-1}$ is aliased as approximately 1.34 m^{-1}. Of course, spherical waves are also subject to spatial aliasing but, as suggested by the positive valued difference between $\bar{k}_{s,x}$ and $\tilde{k}_{s,x}$, the onset of aliasing occurs for x_m greater than that predicted for plane incidence and thereby, in general, has lesser effect at a given x_m. For example, with $\delta = 1.0\,m$, aliasing occurs for spherical waves beyond approximately 2.4 m compared with 2.25 m cited above for plane waves.

In the following section the foregoing conclusions are substantiated by transforming the spatial array response to corresponding time domain representations for plane and spherical incidence.

B.5 Time Domain Array Filters:

The output of an array as a function of time can be written as the convolution

$$s(t) = a(t) * \psi(t), \tag{B.23}$$

where $a(t)$ is the local time domain impulse response of the array and $\psi(t)$ is the time dependent wave function detected at the array midpoint. The equivalent frequency domain operation is

$$S(f) = A(f)\,\Psi(f), \tag{B.24}$$

where

$$A(f) = \int_{-\infty}^{+\infty} a(t)\,e^{-i2\pi f t}\,dt \tag{B.25}$$

is the array's transfer function and $\Psi(f)$ is the frequency domain representation of the wave function $\psi(t)$. The array output is obtained by the inverse Fourier transform

$$s(t) = \int_{-\infty}^{+\infty} S(f)\,e^{i2\pi f t}\,df. \tag{B.26}$$

In particular, the time domain equivalent of equation (B.16) can be written as

$$a(t) = \frac{1}{N} \sum_{j=-(N-1)/2}^{(N-1)/2} \alpha(j)\,\delta(t - t_j), \tag{B.27}$$

where N is the number of receiver elements and $\alpha(j)$ is an amplitude coefficient specifying the amplitude of the incident wave as detected by the jth receiver measured relative to amplitude at the array midpoint x_m. Similarly, t_j is the effective time shift of the jth detector relative to transit time measured at the array midpoint and is associated with the offset $j\Delta x$ from the midpoint in equation (B.16).

Assuming plane incidence, the fixed interval Δx is related to a corresponding fixed time interval Δt_p via a constant apparent horizontal phase velocity $\tilde{v}_{p,x} = f/\tilde{k}_{p,x}$, where $f = kv$ is the frequency of incident waves. Substituting equation (B.9) with $x_s = 0$ yields

$$\tilde{v}_{p,x} = \frac{v\,(x_m{}^2 + z_s{}^2)^{1/2}}{x_m} \tag{B.28}$$

and, thus,

$$\Delta t_p = \frac{x_m \Delta x}{v\,(x_m{}^2 + z_s{}^2)^{1/2}}. \tag{B.29}$$

Consequently, $t_j = j\Delta t_p$ in equation (B.27), yielding a time domain impulse response for plane incidence that has a form resembling the corresponding spatial response except for the relative amplitude coefficient $\alpha(j)$. In fact, for a conventional plane wave, the relative amplitude coefficient is unity for all j. For spherical waves, on the other hand, the apparent velocity along the x-axis $\tilde{v}_{s,x} = f/\tilde{k}_{s,x}$ is not a constant but depends on x as

$$\tilde{v}_{s,x}(x) = \frac{v\,(x^2 + z_s{}^2)^{1/2}}{x}. \tag{B.30}$$

As a result, the time increment associated with the fixed interval Δx depends on j and, thus, the time interval $\Delta t_s(j)$ corresponding to a given offset $j\Delta x$ is given by

$$\begin{aligned} \Delta t_s(j) &= \frac{1}{v}\int_{x_m}^{x_m + j\Delta x} \frac{x}{(x^2 + z_s{}^2)^{1/2}}\,dx \\ &= \frac{1}{v}\left\{\left[(x_m + j\Delta x)^2 + z_s{}^2\right]^{1/2} - \left[x_m{}^2 + z_s{}^2\right]^{1/2}\right\} \end{aligned} \tag{B.31}$$

For spherical incidence, then, $t_j = \Delta t_s(j)$, yielding a time domain impulse response having a fundamentally different form than its spatial analogue.

On incorporating the appropriate relative amplitude coefficients for modified plane and spherical waves,

$$\alpha_p(j) = \frac{x_m^2 + z_s^2}{x_m^2 + x_m j\Delta x + z_s^2} \tag{B.32}$$

and

$$\alpha_s(j) = \left[\frac{x_m^2 + z_s^2}{(x_m + j\Delta x)^2 + z_s^2}\right]^{1/2} \tag{B.33}$$

respectively, the resulting array transfer functions for modified plane and spherical incidence are

$$A_p(f) = \frac{1}{N}\sum_{j=-(N-1)/2}^{(N-1)/2} \alpha_p(j)\, e^{-i2\pi f j\Delta t_p} \tag{B.34}$$

and

$$A_s(f) = \frac{1}{N}\sum_{j=-(N-1)/2}^{(N-1)/2} \alpha_s(j)\, e^{-i2\pi f\, \Delta t_s(j)}. \tag{B.35}$$

The difference between these transfer functions is directly related to the departure of $\tilde{\lambda}_{s,x}$ from $\tilde{\lambda}_{p,x}$ within the aperture of the array and, consequently, to the observed deviation between $\bar{k}_{s,x}(x_m)$ and $\tilde{k}_{s,x}(x_m)$ as discussed in the previous section. Amplitude and phase spectra computed from the foregoing transfer functions for N=7, $\delta = 1.0\,m$ and $x_m = 0.0$, 1.0, 2.0, 3.0, 5.0 and 15.0 m are displayed in Figure B.8. Spectra are also depicted for conventional plane wave incidence as given by equation (B.34) with $\alpha(j) = 1$. It is evident from these spectra that the filtered apparent waveforms depicted in Figure B.7 for $\delta = 1.0\,m$ reflect changes in the array's relative amplitude and phase response for plane and spherical incidence as a function of x_m. Note that for $x_m = 0.0\,m$, plane incidence implies an infinite horizontal phase velocity so that $\Delta t_p = 0.0$. Consequently, the amplitude spectra for plane incidence have unit amplitude over all frequencies, whereas the corresponding spectrum for spherical incidence is less than unity at d.c. and decreases with frequency over the range depicted in Figure B.8. In particular for $k = 2.0\,m^{-1}$ and $v = 300.0\,m/s$, $f = B.0.0\,s^{-1}$ indicating a relative attenuation of approximately 7 dB. Spectra for $x_m = 1.0\,m$ are of special interest as this midpoint value resides within the zone identified in the previous section with attenuation levels that are overestimated under a plane incidence assumption.

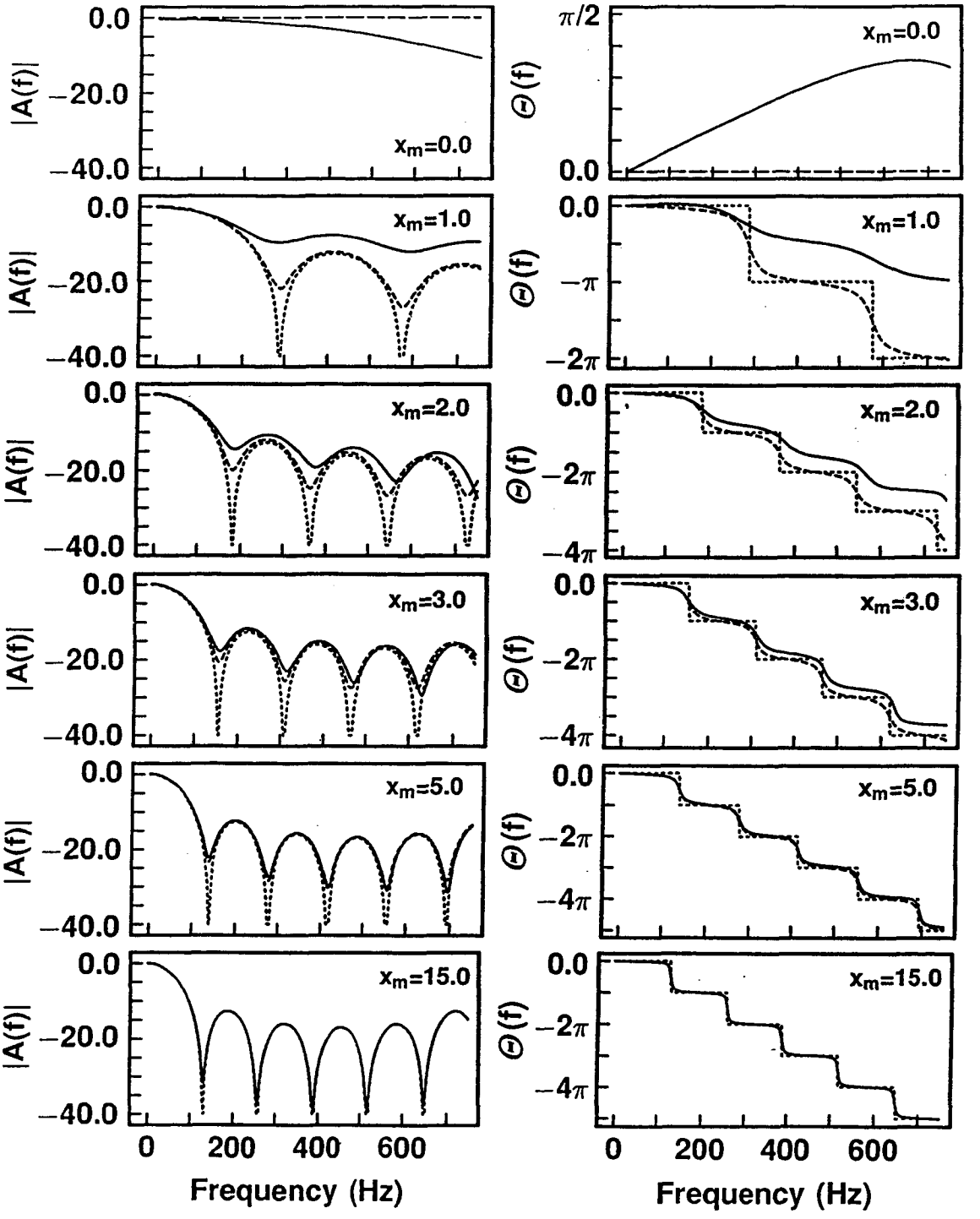

Figure B.8. Amplitude and phase spectra for time domain array responses, assuming conventional plane (dotted), modified plane (dashed) and spherical (solid) incidence. A constant wave speed of 300.0 m/s is assumed, implying an incident wave frequency of 600 Hz. Spectra are computed with $\delta = 1.0$ m for array midpoint location of $x_m = 0.0, 1.0, 2.0, 3.0, 5.0$ and 15.0 m. Amplitude spectra are displayed on a decibel scale arbitrarily truncated at -40.0 dB. Phase angles are measured in radians.

Figure B.8 substantiates this finding and indicates that the spherical wave is attenuated by approximately 12 dB, compared with 24 dB and 26 dB for modified and conventional plane waves respectively. At $x_m = 2.0$ and 3.0 m, the spectra for spherical wave geometry progressively approach those predicted for plane incidence. Moreover, the amplitude spectra continue to corroborate the sense of relative attenuation observed in Figure B.7. Spectra are also displayed for x_m=5.0 m and 15.0 m to illustrate the continued convergence of associated array responses as the distance between the image source and array midpoint becomes large compared with the array's aperture width. It is evident from Figure B.8 that the array's modified plane wave response is intermediate between those for spherical and conventional plane waves. More interestingly, it is apparent that the spherical wave response converges more rapidly toward the modified plane wave response than either of these approach the response for a conventional plane wave. This observation is best illustrated by displaying the corresponding complex transfer functions in polar format as in Figure B.9. By nature, the imaginary part of the transfer function for conventional plane waves is identically zero and, consequently, corresponding phasor diagrams reside on the real axis. Concurrently, the real component takes on the frequency dependent value $\sin(N\pi f\Delta t_p)/N\sin(\pi f\Delta t_p)$. As this quantity changes sign, the corresponding phasor diagram passes through the origin and the associated phase spectrum in Figure B.8 jumps by $-\pi$ radians. In fact, theoretically, these phase discontinuities can take on an arbitrary value $\pi \pm n2\pi$ radians but a constant decrement of π radians is both physically plausible and consistent with phasor diagrams for modified plane and spherical waves. Note that the phase spectra displayed in Figure B.8 for modified plane and spherical waves have been corrected for meaningless wraps of 2π radians introduced computationally as the respective phasor diagrams cross the negative valued real axis. Convergence of the complex array response for spherical incidence to that for modified plane waves reflects the significant influence of relative amplitude variation over the array's aperture. Despite the insight gained by treating the receiver array as a time domain filter, we should not lose sight of the fact that the array is physically deployed in the spatial domain and affects a discrete

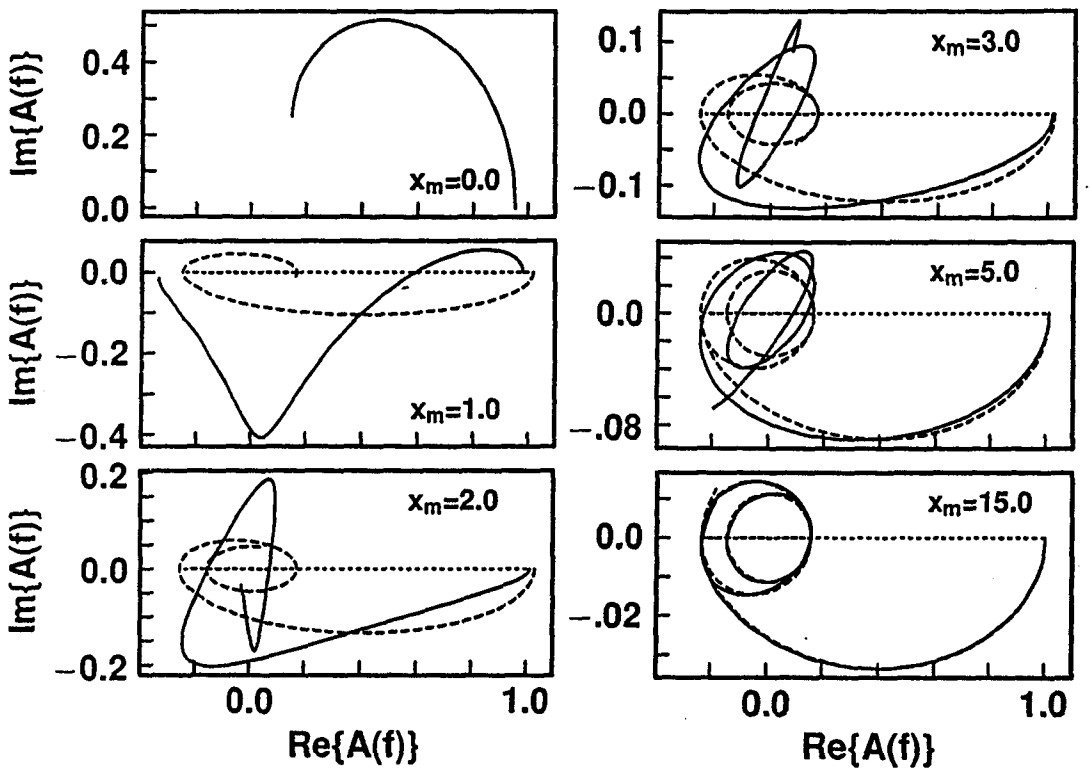

Figure B.9. Polar diagrams characterizing the complex transfer functions associated with the corresponding amplitude and phase spectra in Figure 8 for conventional plane (dotted), modified plane (dashed) and spherical (solid) incidence. Real and imaginary components of a complex transfer function A (f) are denoted by Re {A (f)} and Im {A (f)} respectively.

sampling of the spatial wavefield while responding continuously in time. Consequently, while an appropriate Nyquist wavenumber is associated with the spatial interval separating adjacent elements of the array, the time domain analogue is not a Nyquist frequency in the usual sense. Only, subsequently, on digitizing the array's analog output, does the possibility of temporal aliasing and, thus, a Nyquist frequency arise. Having made this distinction, however, it is useful to consider the time domain analogue of the Nyquist wavenumber associated with the spatial filter. We shall refer to this parameter as the pseudo-Nyquist frequency.

For plane incidence, a pseudo-Nyquist frequency f_N is associated with the Nyquist wavenumber by

$$f_{N,p}(x_m) = k_N \tilde{v}_{p,x}(x_m) = \frac{v k_N}{x_m} (x_m^2 + z_s^2)^{1/2}, \tag{B.36}$$

where $\tilde{v}_{p,x}(x_m)$ is the apparent plane wave velocity relating the constant spatial interval Δx, separating adjacent detectors, with a constant temporal interval Δt_p. Using $k_N = 1.5\,m^{-1}$ from the previous section, effective pseudo-Nyquist frequencies for $\delta = 1.0\,m$ at $x_m = 0.0$, 1.0, 2.0 and 3.0 m are respectively ∞, 1000, 640 and $540\,s^{-1}$. Consequently, aliasing occurs only for the case $x_m = 3.0$ m where the incident wave frequency $f = 600\,s^{-1}$ aliases at approximately $480\,s^{-1}$. More specifically, equation (B.36) confirms that the onset of aliasing occurs at approximately $x_m = 2.25\,m$.

For spherical incidence, the effective time interval between successive array elements is non-constant and, consequently, it is impossible to define a unique pseudo-Nyquist frequency. Instead, in analogy with the average apparent wavenumber considered in the previous section, we introduce an average pseudo-Nyquist frequency

$$\bar{f}_{N,s}(x_m) = k_N \bar{v}_{s,x}(x_m) = \frac{v\tilde{k}_N}{2\delta}\left\{[(x_m+\delta)^2+z_s{}^2]^{1/2} - [(x_m-\delta)^2+z_s{}^2]^{1/2} + z_s \ln\left[\frac{(x_m+\delta)}{(x_m-\delta)}\left(\frac{z_s+[(x_m-\delta)^2+z_s{}^2]^{1/2}}{z_s+[(x_m+\delta)^2+z_s{}^2]^{1/2}}\right)\right]\right\}, \quad \text{(B.37)}$$

where

$$\bar{v}_{s,x}(x_m) = \frac{1}{2\delta}\int_{x_m-\delta}^{x_m+\delta} \tilde{v}_{s,x}(x)\,dx$$

is the average apparent velocity as depicted in Figure B.10.

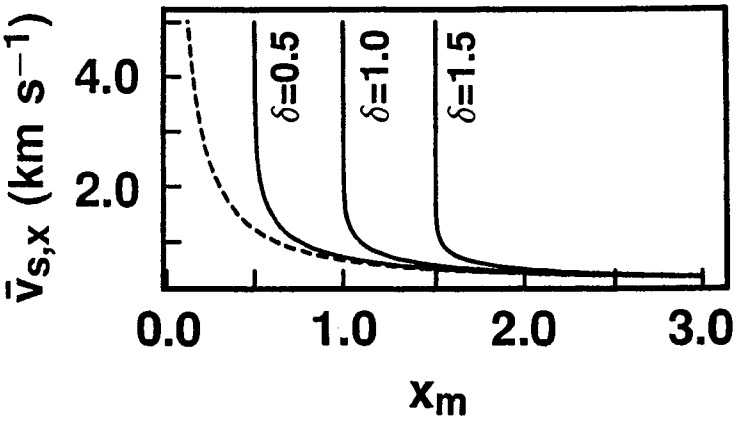

Figure B.10. Average apparent velocity for plane (dashed) and spherical (solid) incidence. Averages are depicted for half apertures of $\delta = 0.5, 1.0$ and 1.5 m. Note that the plane incidence value is equivalent to the average apparent spherical wave velocity for $\delta = 0.0$ m. All curves approach infinity as x_m approaches δ and are arbitrarily truncated at 5.0 km/s for purpose of illustration.

Computational comparison of equations (B.3B. and (B.37) suggests that, in general, the onset of aliasing occurs at a higher frequency than predicted for plane incidence. This is illustrated in Figure B.10, where it is observed that $\overline{v}_{s,x}(x_m)$ always exceeds $\tilde{v}_{p,x}(x_m)$. The average pseudo-Nyquist frequencies associated with these average apparent velocities are obtained by a constant scaling with the appropriate Nyquist wavenumber. Average apparent velocities are displayed to facilitate a consistent comparison over a range of array apertures. Note that for $-\delta \leq x_m \leq \delta$ the argument of the logarithm in equation (B.37) is negative, causing the average pseudo-Nyquist frequency to be undefined. Physically, this result reflects inclusion of x=0, where $\lim_{x\to 0} \overline{v}_{s,x}(x) = \infty$, within the aperture of the array so that the average pseudo-Nyquist frequency over this region must also be infinite.

B.6 Concluding Discussion:

The foregoing analysis identifies theoretical limitations on the plane wave assumption normally invoked on characterizing the attenuation properties of receiver arrays. While the array's spatial response is uniquely defined by the number of elements, their relative weighting and spatial distribution, equivalent time domain representations necessarily incorporate the geometry and spatial amplitude dependence of incident wavefronts. Consequently, as demonstrated above, distinct time domain impulse responses arise in connection with plane and spherical incidence. Moreover, we find that this distinction is manifest spatially as a systematic difference between the spectral compositions of associated waveforms within the array's aperture. Although both perspectives reveal that attenuation predicted assuming plane incidence can deviate appreciably from that experienced by a spherical wave, the practical significance of these deviations is difficult to appraise.

Newman and Mahoney (1973) examined the influence of random implementation errors on the nominal response of uniform, linear tapered and optimally weighted line arrays. Practical uncertainty and error in the effectiveness, position and coupling of individual array elements was modeled by introducing random perturbations of 10 percent standard de-

viation about their nominal spatial distribution and weighting. While resulting deviations from the nominal response were found to be insignificant within the passband, perturbations had an appreciable effect beyond the first notch in the amplitude response, imposing a practical limitation on the rejection capabilities of the array. Newman and Mahoney also acknowledged errors in design assumptions, including the simplifying assumption of plane wave incidence, and suggested that such errors could be treated as equivalent implementation errors. For example, the response of a uniform line array to spherically incident waves can be simulated, while retaining the plane wave assumption, by redistributing individual elements on the appropriate arc of radius in the x-z plane and assigning variable weighting coefficients to account for spherical divergence. Alternatively, by determining the magnitude of required perturbations, we can assess the relative significance of deviations from the plane wave assumption compared with typical implementation errors.

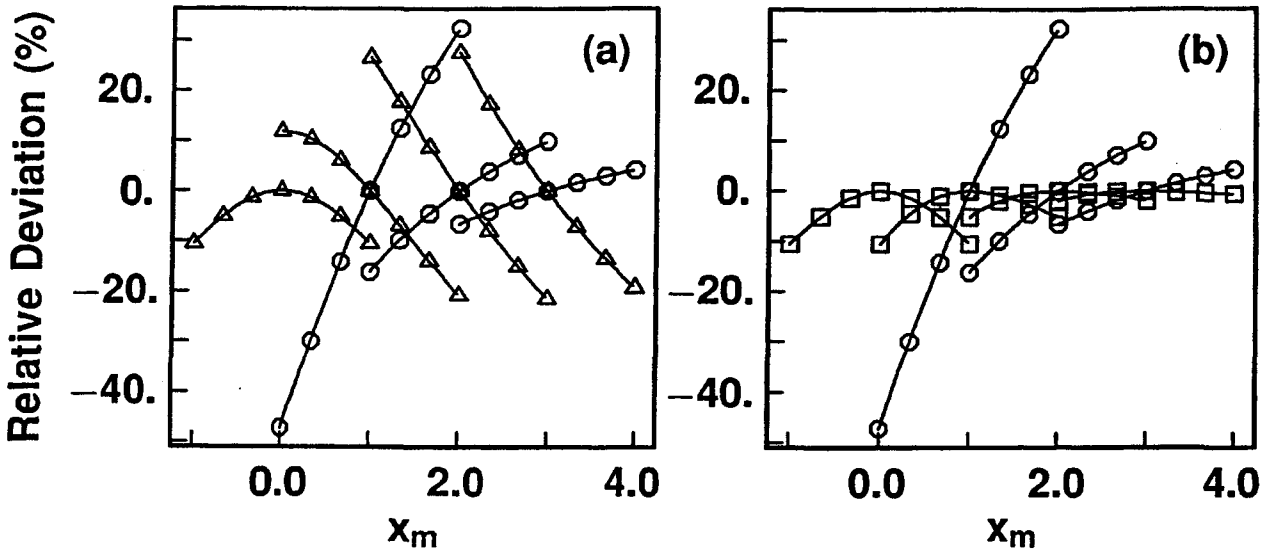

Figure B.11. Relative deviation of amplitude coefficient $\alpha_s(j)$, and effective time lag $\Delta t_s(j)$ from (a) conventional plane wave values: $\Delta = (\alpha_s(j) - 1)$, $\bigcirc = [(\Delta t_s(j)/j\Delta t_p) - 1]$ and (b) modified plane wave values: $\square = [(\alpha_s(j)/\alpha_p(j)) - 1]$, $\bigcirc = [(\Delta t_s(j)/j\Delta t_p) - 1]$. Solid curves connect discrete values for a seven element array deployed with midpoints at 0.0, 1.0 2.0 and 3.0 m. The image source is located x=0.0 m, z=2.0 m.

In Figure B.11a, the relative deviations of amplitude coefficient, $\alpha_s(j)$ and the effective time shift $\Delta t_s(j)$ from the respective values of unity and $j\Delta t_p$ for conventional plane wave

incidence are displayed as a function of element position for array midpoints of 0.0, 1.0, 2.0 and 3.0 m. Two important observations are made. First, the maximum effective errors are significantly larger than the 10 percent perturbations assumed by Newman and Mahoney for typical implementation errors, indicating that for small scale, near source applications implementation errors have a relatively minor influence compared with departures from design assumptions. Secondly, while implementation errors become dominant with increasing distance from the source, it is interesting to note that effective time lag errors diminish rapidly compared with relative amplitude deviations. In other words, although spherical wavefronts may be reasonably approximated as locally plane at a given range from the source, spherical divergence can remain a significant factor. Note that this observation and the comparatively minor deviation between relative amplitude coefficients $\alpha_s(j)$ and $\alpha_p(j)$, illustrated in Figure B.11b, are consistent with the relatively rapid convergence of time domain array responses for spherical and modified plane waves in the previous section. It is emphasized, however, that despite a significant reduction in relative amplitude deviation, relative time lag errors are identical in Figures B.11a and B.11b, reflecting a fundamental limitation of any plane wavefront approximation.

The foregoing observations can be generalized for an arbitrary midpoint offset, image source depth and aperture width in terms of two non-negative, dimensionless parameters $\sigma_\Delta = \delta/x_m$ and $\sigma_z = z_s/x_m$. Defining relative amplitude deviations as

$$\epsilon_{\alpha p} = \alpha_s(j) - 1 \tag{B.38}$$

and

$$\epsilon_{\alpha m} = \frac{\alpha_s(j) - \alpha_p(j)}{\alpha_p(j)} \tag{B.39}$$

for plane and modified plane wave approximations, respectively, the relative time lag deviation by

$$\epsilon_t = \frac{\Delta t_s(j) - j\Delta t_p}{j\Delta t_p} \tag{B.40}$$

and assuming a three element array, so that maximum deviations occur for $j = \pm(N-1)/2$, we obtain the corresponding non-dimensionalized expressions for maximum relative devi-

ation

$$\hat{\epsilon}_{\alpha p} = \left| \left(\frac{1 + {\sigma_z}^2}{1 \pm 2\sigma_\Delta + {\sigma_\Delta}^2 + {\sigma_z}^2} \right)^{1/2} - 1 \right| \tag{B.41}$$

$$\hat{\epsilon}_{\alpha m} = \left| \frac{(1 \pm \sigma_\Delta + {\sigma_z}^2)(1 + {\sigma_z}^2)^{-1/2}}{(1 \pm 2\sigma_\Delta + {\sigma_\Delta}^2 + {\sigma_z}^2)^{1/2}} - 1 \right| \tag{B.42}$$

$$\hat{\epsilon}_t = \left| \frac{1}{\pm\sigma_\Delta} \left[\frac{(1 \pm 2\sigma_\Delta + {\sigma_\Delta}^2 + {\sigma_z}^2)^{1/2}}{(1 + {\sigma_z}^2)^{-1/2}} - (1 + {\sigma_z}^2) \right] - 1 \right|. \tag{B.43}$$

In fact, geometrical analysis indicates that except for $\hat{\epsilon}_{\alpha s}$ when $j < 0$ and $1 < \sigma_\Delta < \left\{ 1 + 2(1 + {\sigma_z}^2)^{1/2} \left[1 - \sigma_z (1 + {\sigma_z}^2)^{-1/2} \right]^{1/2} \right\}$, the foregoing expressions are valid for arbitrary N as illustrated below.

Figures B.12b and B.13b display $\hat{\epsilon}_{\alpha p}$ (Δ) and $\hat{\epsilon}_{\alpha m}$ ($\square$), respectively, for $j = (N-1)/2$ together with the associated relative time lag deviation $\hat{\epsilon}_t$ ($\bigcirc$) as functions of the dimensionless parameters σ_Δ and σ_z. The contour interval is 5 percent. Corresponding distributions for $j = -(N-1)/2$ in Figures B.12a and B.13a are more complicated due to singularities in the relative amplitude coefficients $\alpha_p(j)$ and $\alpha_s(j)$ defined by equations B.32 and B.33 respectively. In particular, for an image source at the surface ($\sigma_z = 0$) and an aperture width equal to twice the midpoint offset ($\sigma_\Delta = 1$), the $j = -(N-1)/2$ detector coincides with the source causing the amplitude coefficient for spherical incidence to be infinite. The same situation arises for the modified plane wave coefficient, however, in this case a similar condition occurs for all σ_z satisfying $\sigma_z = \sqrt{\sigma_\Delta - 1}$. It is evident from equation (B.39) that $\lim_{\alpha_p(j) \to \infty} \epsilon_{\alpha m} = -1$ and, consequently, this condition corresponds to the $\hat{\epsilon}_{\alpha m} = 100\%$ contour in Figure B.13a. Finally, Figure B.14 is a hybrid of Figures B.12a and B.12b, depicting the overall maximum deviation as a function of σ_Δ and σ_z. For the modified plane wave approximation, the relative deviation is always maximum for $j = -(N-1)/2$.

To illustrate the systematics of these generalized error distributions, we return to the specific example illustrated above (Figure B.11). Fixing $z_s = 2.0$ m and $\delta = 1.0$ m, array midpoint offsets of 1.0, 2.0 and 3.0 m have one to one mappings $(\sigma_\Delta, \sigma_z) = (1.0, 2.0)$,

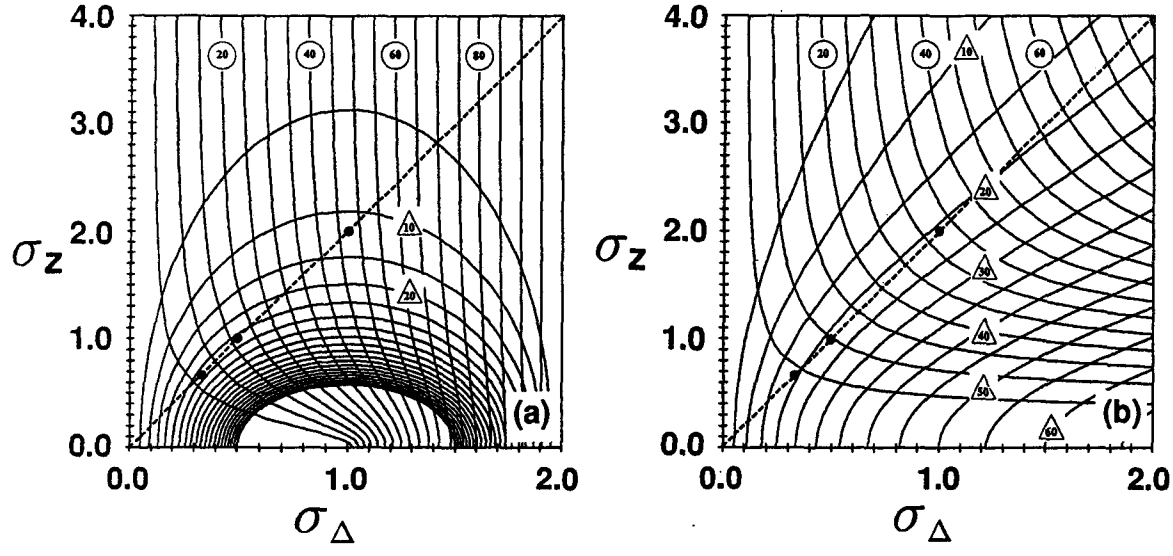

Figure B.12. Maximum relative amplitude (△) and time lag (○) deviations from conventional plane wave values as functions of dimensionless parameters $\sigma_\Delta = \delta/x_m$ and $\sigma_z = z_s/x_m$ for (a) $j = -(N-1)/2$ and (b) $j = (N-1)/2$. Discrete mappings are depicted for $z_s = 2.0$ m, $\delta = 1.0$ m and x_m =1.0, 2.0 and 3.0 m. Compare predicted errors with Figure 11.

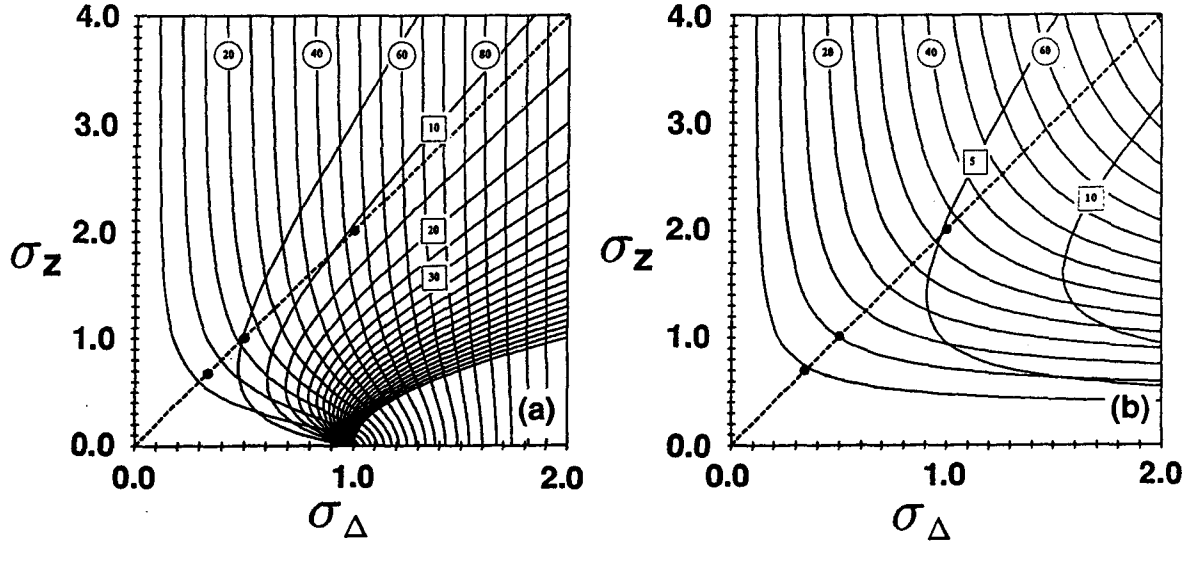

Figure B.13. Maximum relative amplitude (□) and time lag (○) deviations from modified plane wave values as functions of dimensionless parameters $\sigma_\Delta = \delta/x_m$ and $\sigma_z = z_s/x_m$ for (a) $j = -(N-1)/2$ and (b) $j = (N-1)/2$. Discrete mappings are depicted for $z_s = 2.0$ m, $\delta = 1.0$ m and x_m =1.0, 2.0 and 3.0 m. Compare predicted errors with Figure 11.

(0.5, 1.0) and (0.33, 0.B.), respectively. As illustrated in Figures B.12-B.14, these points define a line having slope $z_s/\delta = 2.0$ and passing through the origin. Moreover, as the midpoint offset increases, its mapping approaches the origin and, in general, this trend is accompanied by a reduction in associated relative deviations. In particular, Figure B.14 indicates that the relative time lag error becomes less than 10 % for $\sigma_\Delta = \delta/x_m < 0.4$ or $x_m > 2.5$ m. Concurrently, in agreement with previous observations, the relative amplitude deviation diminishes less rapidly falling to 10 % in this case at approximately $\sigma_\Delta = 0.1$ or $x_m = 10$ m. On the other hand, for an arbitrary value of σ_Δ, increasing σ_z or, in effect, increasing the image source depth generally reduces relative amplitude deviations more rapidly than relative time lag deviations. Indeed, as expected for an image source at infinite depth, the corresponding line on the Figures B.12-B.14 has infinite slope and, consequently resides on the ordinate axis where all relative deviations vanish.

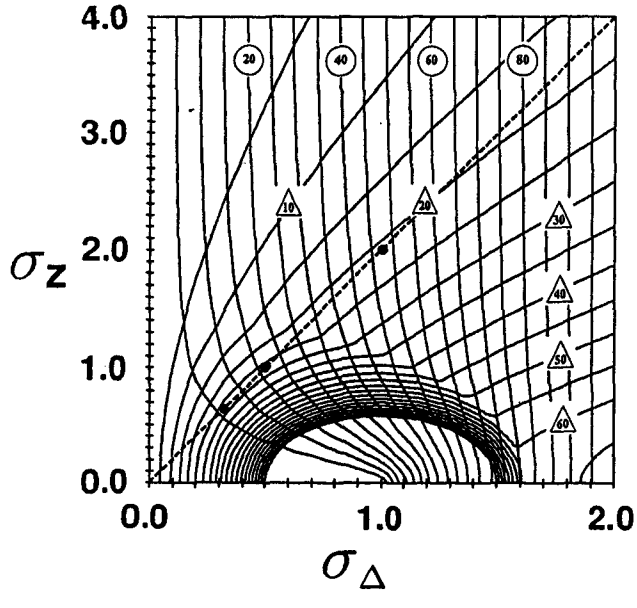

Figure B.14. Composite of Figures B.12a and B.12b, displaying overall maximum deviations from corresponding conventional plane wave values. Note that Figure 13a is the equivalent distribution relative to corresponding modified plane wave values.

In general, the foregoing error analysis reveals that the magnitude of effective implementation errors required to compensate an inappropriate plane wave assumption are primarily controlled by the ratio of reflector depth to aperture width. Moreover, relative

amplitude and time lag deviations diminish at rates governed by the previous parameter as the array's midpoint offset becomes large compared with both reflector depth and aperture width. Finally, as demonstrated by Newman and Mahoney (1973), the response of the uniform array is least influenced by implementation errors and, consequently, departures from design assumptions, including plane incidence. As a result, relative errors arising from a plane wave approximation are significantly magnified in the case of optimally weighted arrays.

In closing, it is noted that this investigation was partly motivated by suspicion that the viability of array filtering for groundroll attenuation in small-scale seismology might have been inappropriately dismissed on the basis of a plane wave assumption. Knapp and Steeples (1986) sought to maximize array length subject to attenuating the highest signal frequency by less than 3 dB. and although not explicitly stated, subsequent analysis assumed plane incidence, concluding that $\delta_{max} = 0.125/\tilde{k}_{max}\,(z_s/2) \sim 0.28/k_{max}$, where the argument $z_s/2$ implies that maximum offset is taken equal to reflector depth. In a related discussion, Mayne (1987) confirmed the foregoing result for a two element array and noted that for an array having a large number of elements, the correct relation is $\delta_{max} \sim 0.48/k_{max}$. From Figure B.4, for example, we note that the corresponding relation for a seven element array is $\delta_{max} \sim 0.44/k_{max}$. Although δ_{max} *can* be theoretically underestimated assuming plane incidence, frequency domain analysis, using equations (B.34) and (B.35) with $f = f_{max}$ and Δt_p evaluated for $x_m = z_s/2$ indicates that the effect is negligible for a wide range of plausible field parameters. Consequently, the present study supports the validity of a plane wave assumption in this context and reinforces the conclusion that array filters are not optimally suited for small scale applications.

Appendix C

RICKER WAVELET EXTREMA: THE RAYLEIGH RESOLUTION CRITERION

The Ricker wavelet is defined by

$$w(t) = (1 - 12f_d^2t^2)\,e^{-6f_d^2t^2}. \qquad (2.31)\,(C.1)$$

Wavelet extrema are, therefore, associated with the roots of the following equation:

$$\begin{aligned}\frac{\partial}{\partial t}w(t) &= -24f_d^2t\,e^{-6f_d^2t^2} - 12f_d^2t\,(1 - 12f_d^2t^2)\,e^{-6f_d^2t^2} \\ &= -12f_d^2t\,[2 + (1 - 12f_d^2t^2)]\,e^{-6f_d^2t^2} \qquad (C.2) \\ &= -12f_d^2t\,(3 - 12f_d^2t^2)\,e^{-6f_d^2t^2} = 0.\end{aligned}$$

Consequently, extrema occur at t=0, $t = \pm\infty$ and

$$(3 - 12f_d^2t^2) = 0 \qquad (C.3)$$

$$t^2 = \frac{1}{4f_d^2}$$

$$t = \pm\frac{1}{2f_d}.$$

With reference to Figure 2.16, it follows that the Ricker wavelet's main lobe occurs at t=0 (for shifted wavelet $w(t - \tau_0)$ at $t = \tau_0$), negative side-lobes at $t = \pm 1/2f_d$ (for shifted wavelet $w(t - \tau_0)$ at $t = \tau_0 \pm 1/2f_d$) and that wavelet amplitude decays asymptotically to zero. Rayleigh's resolution criterion requires that the main lobe of one wavelet coincide with the side-lobe of the other and, consequently, wavelets must be separated by a time interval

$$T_t = \frac{1}{2f_d} = 0.5\,T_d \qquad (C.4)$$

known as the tuning thickness, where $T_d = 1/f_d$ denotes the wavelet's dominant period. It follows that associated reflectors must be separated by half the corresponding range $\alpha_0 T_t = \alpha_0/2f_d$ or $\alpha_0/4f_d = \lambda_d/4.0$; in other words, one quarter of the dominant wavelength at velocity α_0.

Appendix D

RICKER WAVELET INFLECTIONS: THE RICKER RESOLUTION CRITERION

The Ricker wavelet is defined by

$$w(t) = (1 - 12f_d^2 t^2)\, e^{-6f_d^2 t^2}. \qquad (2.31)(D.1)$$

It follows from elementary calculus that the wavelet's inflection points satisfy the associated equation

$$\frac{\partial^2}{\partial t^2} w(t) = 0. \qquad (D.2)$$

Using the result

$$\frac{\partial}{\partial t} w(t) = -12f_d^2 t\,(3 - 12f_d^2 t^2)\, e^{-6f_d^2 t^2} \qquad (C.2)(D.3)$$

from Appendix C, we obtain

$$\begin{aligned}\frac{\partial^2}{\partial t^2} w(t) &= -12f_d^2\,(3 - 12f_d^2 t^2)\, e^{-6f_d^2 t^2} + (-12f_d^2 t)\,\left[-24f_d^2 t - 12f_d^2 t\,(3 - 12f_d^2 t^2)\right]\, e^{-6f_d^2 t^2} \\ &= -36f_d^2\,(48f_d^4 t^4 - 24f_d^2 t^2 + 1)\, e^{-6f_d^2 t^2} = 0.\end{aligned}$$

In addition to inflections at $t = \pm\infty$, associated with the Ricker wavelet's asymptotic amplitude decay, the quartic equation

$$48f_d^4 t^4 - 24f_d^2 t^2 + 1 = 0 \qquad (D.4)$$

yields four additional roots. On substituting $y = \sqrt{48}\, f_d^2 t^2$, the foregoing equation reduces to the quadratic equation

$$y^2 - 2\sqrt{3}\, y + 1 = 0,$$

Having roots

$$\begin{aligned} y &= \frac{2\sqrt{3} \pm \sqrt{(-2\sqrt{3})^2 - 4}}{2} \\ &= \sqrt{3} \pm \sqrt{2} \end{aligned}$$

or $y_1 = 0.318$, $y_2 = 3.146$. Consequently, the Ricker wavelet has inflection points at

$$t = \pm \left[\frac{y_1}{\sqrt{48}\, f_d^2}\right]^{1/2} \approx \pm \frac{0.214}{f_d} \qquad t = \pm \left[\frac{y_2}{\sqrt{48}\, f_d^2}\right]^{1/2} \approx \pm \frac{0.674}{f_d}$$

or, in terms of the wavelet's dominant period $T_d = 1/f_d$, $t \approx \pm 0.214\, T_d$ and $t \approx \pm 0.674\, T_d$. As expected, the lesser roots $t \approx \pm 0.214\, T_d$ lie between the wavelet's center at t=0 and negative side lobes at $t = 0.5\, T_d$ and, therefore, are associated with inflections on the wavelet's main lobe. Consequently, since Ricker's resolution criterion T_R is defined as the temporal separation between main lobe inflection points, we have

$$T_R \approx 0.43\, T_d. \tag{D.5}$$

Finally, it follows that associated reflectors must be separated by half the corresponding range $\alpha_0 T_R$ or $0.43\, \alpha_0 T_d/2 = .215 \lambda_d = \lambda_d/4.65$.

Appendix E
THE SINC WAVELET

A sinc wavelet is effectively the impulse response of an ideal band-pass filter, obtained by subtracting a low-pass filter

$$W_l(f) = \Pi\left(\frac{f}{2f_l}\right) \tag{E.1}$$

with terminal frequency f_l from a second low-pass filter having a higher terminal frequency $f_u > f_l$

$$W_u(f) = \Pi\left(\frac{f}{2f_u}\right) \tag{2.40}(E.2)$$

as illustrated in Figure E.1.

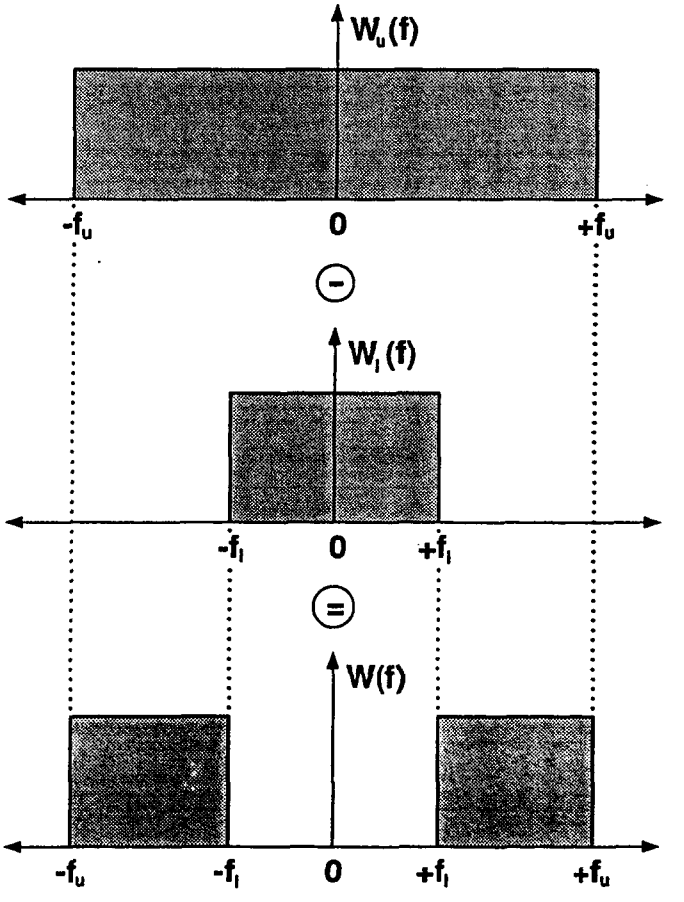

Figure E.1. Subtracting an ideal low-pass spectrum having terminal frequency f_l (b) from a second ideal low-pass filter possessing a higher terminal frequency f_u (a), yields a frequency spectrum that is band-limited between f_l and f_u (c).

Recall that

$$\Pi(\xi) = \begin{cases} 0, & |\xi| > 1/2; \\ 1, & |\xi| \leq 1/2 \end{cases}$$

describes a rectangular function having unit height and base. Consequently, the sinc wavelet is characterized by the Fourier spectrum

$$W(f) = W_u(f) - W_l(f) = \Pi\left(\frac{f}{2f_u}\right) - \Pi\left(\frac{f}{2f_l}\right). \tag{E.3}$$

Using the inverse Fourier transforms

$$w_l(t) = \int_{-\infty}^{+\infty} \Pi\left(\frac{f}{2f_l}\right) e^{i2\pi ft}\, df = \frac{\sin(2\pi f_l t)}{\pi t}, \tag{2.42}(E.4)$$

$$w_u(t) = \int_{-\infty}^{+\infty} \Pi\left(\frac{f}{2f_u}\right) e^{i2\pi ft}\, df = \frac{\sin(2\pi f_u t)}{\pi t} \tag{2.42}(E.5)$$

and taking advantage of the linear properties of the Fourier transform, we observe that the sinc wavelet follows as the difference between associated sinc functions. That is,

$$\begin{aligned} w(t) &= \int_{-\infty}^{+\infty} W(f)\, e^{i2\pi ft}\, df \\ &= w_u(t) - w_l(t) \\ &= \frac{\sin(2\pi f_u t)}{\pi t} - \frac{\sin(2\pi f_l t)}{\pi t} \end{aligned} \tag{2.45}(E.6)$$

Alternatively, equation (E.3) may be written as the convolution

$$W(f) = \Pi\left(\frac{f}{\Delta f}\right) * [\delta(f - f_m) + \delta(f + f_m)], \tag{E.7}$$

where $\delta(\xi)$ is the Dirac delta function, $f_m = (f_l + f_u)/2$ defines the spectrum's midfrequency in terms of upper and lower terminal frequencies f_u and f_l, respectively, and $\Delta f = f_u - f_l$ is the corresponding spectral bandwidth. Using the following tabulated Fourier transforms (Bracewell, 1986),

$$\int_{-\infty}^{+\infty} \Pi\left(\frac{f}{\Delta f}\right) e^{i2\pi ft}\, df = \frac{\sin(\pi \Delta f t)}{\pi t}$$

$$\int_{-\infty}^{+\infty} [\delta(f - f_m) + \delta(f + f_m)]\, e^{i2\pi ft}\, df = 2\cos(2\pi f_m t),$$

together with the convolution theorem of the Fourier transform

$$\int_{-\infty}^{+\infty} X(f) * Y(f)\, e^{i2\pi ft}\, df = x(t)\, y(t),$$

where

$$X(f) = \int_{-\infty}^{+\infty} x(t)\, e^{-i2\pi ft}\, dt$$

$$Y(f) = \int_{-\infty}^{+\infty} y(t)\, e^{-i2\pi ft}\, dt$$

define two arbitrary Fourier transform pairs, we obtain the following, equivalent expression for the sinc wavelet

$$w(t) = 2\,\frac{\sin(\pi\,\Delta f t)}{\pi\, t}\cos(2\pi\, f_m t). \qquad (2.44)(E.8)$$

Appendix F
MINIMUM SECOND MOMENT WAVELET LENGTH

Second moment wavelet length, $L_w(t_0)$, measured relative to reference time t_0 is defined for a real-valued wavelet by

$$L_w{}^2(t_0) = \frac{1}{E_w}\int_{-\infty}^{+\infty} w^2(t)\,(t-t_0)^2\,dt \qquad (2.48)\,(F.1)$$

where

$$E_w = \int_{-\infty}^{+\infty} w^2(t)\,dt \qquad (2.47)\,(F.2)$$

defines total wavelet energy. To determine the particular value of $t_0 = \tilde{t}_0$ for which $L_w{}^2(t_0)$ is minimized, we extremalize equation (A4.1) with respect to $t_0 = \tilde{t}_0$. That is we seek $\tilde{t}_0$ satisfying

$$\frac{\partial}{\partial \tilde{t}_0} L_w{}^2(\tilde{t}_0) = \frac{\partial}{\partial \tilde{t}_0}\left[\frac{1}{E_w}\int_{-\infty}^{+\infty} w^2(t)\,(t-\tilde{t}_0)^2\,dt\right] = 0. \qquad (F.3)$$

Since total wavelet energy given by equation (F.2) is independent of $\tilde{t}_0$, the previous equation reduces to

$$\int_{-\infty}^{+\infty}\frac{\partial}{\partial \tilde{t}_0}\left[w^2(t)\,(t-\tilde{t}_0)^2\right]\,dt = -2\int_{-\infty}^{+\infty} w^2(t)\,(t-\tilde{t}_0)\,dt = 0$$

or

$$\tilde{t}_0\int_{-\infty}^{+\infty} w^2(t)\,dt - \int_{-\infty}^{+\infty} w^2(t)\,t\,dt = 0$$

and, consequently, solving for $\tilde{t}_0$, we obtain

$$\tilde{t}_0 = \int_{-\infty}^{+\infty} w^2(t)\,t\,dt \Big/ \int_{-\infty}^{+\infty} w^2(t)\,dt = \frac{1}{E_w}\int_{-\infty}^{+\infty} w^2(t)\,t\,dt, \qquad (F.4)$$

which we recognize to be the first moment of wavelet energy density about time zero normalized by total wavelet energy.

Appendix G
SECOND MOMENT WAVELET LENGTH AND SPECTRAL CHACTERISTICS

Second moment wavelet length, $L_w(t_0)$, measured relative to reference time t_0 is defined for a real-valued wavelet by

$$L_w{}^2(t_0) = \frac{1}{E_w}\int_{-\infty}^{+\infty} w^2(t)(t-t_0)^2\,dt \qquad (2.48)\,(G.1)$$

where

$$E_w = \int_{-\infty}^{+\infty} w^2(t)\,dt \qquad (2.47)\,(G.2)$$

defines total wavelet energy. The frequency domain equivalent of equation (G.1) is obtained via the power theorem of the Fourier transform (Bracewell, 1986)

$$\int_{-\infty}^{+\infty} x(t)\,y^*(t)\,dt = \int_{-\infty}^{+\infty} X(f)\,Y^*(f)\,df, \qquad (G.3)$$

where

$$X(f) = \int_{-\infty}^{+\infty} x(t)\,e^{-i2\pi ft}\,dt$$

$$Y(f) = \int_{-\infty}^{+\infty} y(t)\,e^{-i2\pi ft}\,dt$$

define two arbitrary Fourier transform pairs and $y^*(t)$ and $Y^*(f)$ denote complex conjugates of $y(t)$ and $Y(f)$, respectively. Thus to facilitate transformation of the numerator in equation (G.1), we set

$$x(t) = y(t) = (t-t_0)\,w(t), \qquad (G.4)$$

yielding

$$\begin{aligned} X(f) = Y(f) &= \int_{-\infty}^{+\infty} (t-t_0)\,w(t)\,e^{-i2\pi ft}\,dt \\ &= \int_{-\infty}^{+\infty} t\,w(t)\,e^{-i2\pi ft}\,dt - t_0\int_{-\infty}^{+\infty} w(t)\,e^{-i2\pi ft}\,dt \end{aligned} \qquad (G.5)$$

Using the derivative theorem of the Fourier transform, the first right-hand term of the previous relation may be written

$$\int_{-\infty}^{+\infty} t\,w(t)\,e^{-i2\pi ft}\,dt = \frac{i}{2\pi}\frac{d}{df}W(f)$$

and, thus, recognizing that the second term is simply t_0 times the Fourier transform of the wavelet $w(t)$, we have

$$X(f) = Y(f) = \frac{i}{2\pi}\frac{d}{df}W(f) - t_0 W(f) \tag{G.6}$$

and

$$X^*(f) = Y^*(f) = -\frac{i}{2\pi}\frac{d}{df}W^*(f) - t_0 W^*(f). \tag{G.7}$$

Consequently, substituting equations (G.4), (G.6) and (G.7) in equation (G.3) yields

$$\begin{aligned} L_w{}^2(t_0) &= \frac{1}{E_w}\int_{-\infty}^{+\infty}(t-t_0)^2 w^2(t)\,dt \\ &= \frac{1}{E_w}\int_{-\infty}^{+\infty}\left\{\frac{1}{4\pi^2}\left|\frac{d}{df}W(f)\right|^2\right. \\ &\left. + \frac{it_0}{2\pi}\left(W(f)\frac{d}{df}W^*(f) - W^*(f)\frac{d}{df}W(f)\right) + t_0{}^2\,|W(f)|^2\right\}df, \end{aligned} \tag{G.8}$$

where

$$|W(f)|^2 = W(f)\,W^*(f),$$

$$\left|\frac{d}{df}W(f)\right|^2 = \frac{d}{df}W(f)\frac{d}{df}W^*(f)$$

and, by Parseval's Theorem,

$$E_w = \int_{-\infty}^{+\infty} w^2(t)\,dt = \int_{-\infty}^{+\infty}|W(f)|^2\,df. \tag{G.9}$$

Finally, on substituting the polar form of the Fourier spectrum

$$W(f) = |W(f)|\,e^{i\Theta(f)}, \tag{G.10}$$

we have

$$\frac{d}{df}W(f) = \left[\frac{d}{df}|W(f)| + i\,|W(f)|\frac{d}{df}\Theta(f)\right]e^{i\Theta(f)}$$

$$\frac{d}{df}W^*(f) = \left[\frac{d}{df}|W(f)| - i\,|W(f)|\frac{d}{df}\Theta(f)\right]e^{-i\Theta(f)}$$

and, consequently, equation (G.8) becomes

$$\begin{aligned} L_w^2(t_0) &= \frac{1}{E_w}\int_{-\infty}^{+\infty}\left\{\frac{1}{4\pi^2}\left[\left(\frac{d}{df}|W(f)|\right)^2+|W(f)|^2\left(\frac{d}{df}\Theta(f)\right)^2\right]\right. \\ &\quad \left.+\frac{it_0}{2\pi}\left(-2i\right)|W(f)|^2\frac{d}{df}\Theta(f)+t_0^2\,|W(f)|^2\right\}df \\ &= \frac{1}{4\pi^2 E_w}\int_{-\infty}^{+\infty}\left\{\left(\frac{d}{df}|W(f)|\right)^2\right. \\ &\quad \left.+|W(f)|^2\left[\left(\frac{d}{df}\Theta(f)\right)^2+4\pi t_0\frac{d}{df}\Theta(f)+4\pi^2 t_0^2\right]\right\}df \end{aligned}, \qquad (G.11)$$

Finally, recognizing that

$$\left(\frac{d}{df}\Theta(f)+2\pi t_0\right)^2=\left(\frac{d}{df}\Theta(f)\right)^2+4\pi t_0\frac{d}{df}\Theta(f)+4\pi^2 t_0^2$$

we obtain the result

$$L_w^2(t_0)=\frac{1}{4\pi^2 E_w}\int_{-\infty}^{+\infty}\left\{\left(\frac{d}{df}|W(f)|\right)^2+|W(f)|^2\left(\frac{d}{df}\Theta(f)+2\pi t_0\right)^2\right\}df. \qquad (G.12)$$

or, with

$$\left(\frac{d}{df}\Theta(f)+2\pi t_0\right)^2=\left[\frac{d}{df}\left(\Theta(f)+2\pi f t_0\right)\right]^2$$

and

$$\frac{d}{df}\left(\ln|W(f)|\right)=\frac{1}{|W(f)|}\frac{d}{df}|W(f)|,$$

the final frequency domain expression

$$L_w^2(t_0)=\frac{1}{4\pi^2 E_w}\int_{-\infty}^{+\infty}|W(f)|^2\left\{\left[\frac{d}{df}\left(\ln|W(f)|\right)\right]^2+\left[\frac{d}{df}\left(\Theta(f)+2\pi f t_0\right)\right]^2\right\}df. \qquad (G.13)$$

Appendix H
WAVELET-ENVELOPE LENGTH EQUIVALENCE

Consider an arbitrary real-valued wavelet $w(t)$. An associated analytic wavelet $\overline{w}(t)$ is defined by

$$\overline{w}(t) = w(t) - i w_{\perp}(t), \tag{H.1}$$

where

$$w_{\perp}(t) = \mathcal{H}\left\{w(t)\right\} = w(t) * \left(\frac{-1}{\pi t}\right) = \int_{-\infty}^{+\infty} W(f)\,[i\ \mathrm{sgn}(f)]\, e^{i2\pi ft}\, df \tag{H.2}$$

defines the quadrature wavelet $w_{\perp}(t)$ given by the Hilbert transform $\mathcal{H}\{w(t)\}$ of the corresponding real-valued wavelet $w(t)$. Note that in the previous expression

$$W(f) = \int_{-\infty}^{+\infty} w(t)\, e^{-i2\pi ft}\, dt$$

denotes the Fourier transform of the real-valued wavelet $w(t)$, * denotes the convolution operation and

$$\mathrm{sgn}(f) = \begin{cases} -1, & f < 0; \\ 0, & f = 0; \\ 1, & f > 0 \end{cases}$$

is the signum function.

The real-valued wavelet envelope follows as the modulus of the analytic wavelet

$$|\overline{w}(t)| = [\overline{w}(t)\ \overline{w}^{*}(t)]^{1/2} = [w^2(t) + w_{\perp}^2(t)]^{1/2}, \tag{H.3}$$

where $\overline{w}^{*}(t)$ denotes the complex conjugate of the analytic wavelet $\overline{w}(t)$. Recalling the definition of second moment wavelet length measured relative to reference time t_0 (2.48) (H.1), we obtain for the wavelet envelope

$$L_{|\overline{w}|}{}^2(t_0) = \frac{1}{E_{|\overline{w}|}} \int_{-\infty}^{+\infty} |\overline{w}(t)|^2 (t - t_0)^2\, dt \tag{H.4}$$

where

$$E_{|\overline{w}|} = \int_{-\infty}^{+\infty} |\overline{w}(t)|^2\, dt \tag{H.5}$$

defines total envelope energy.

Since, in general, the second moment length of a complex-valued wavelet is

$$L_w{}^2(t_0) = \frac{1}{E_w}\int_{-\infty}^{+\infty} |w(t)|^2 (t - t_0)^2 \, dt,$$

with

$$E_w = \int_{-\infty}^{+\infty} |\overline{w}(t)|^2 \, dt,$$

we recognize that equations (H.4) and (H.5) define the length of the analytic wavelet $\overline{w}(t)$ as well as its envelope $|\overline{w}(t)|$.

Substituting equation (H.3) in equation (H.5) yields for total envelope energy

$$\begin{aligned} E_{|\overline{w}|} = \int_{-\infty}^{+\infty} |\overline{w}(t)|^2 \, dt &= \int_{-\infty}^{+\infty} \overline{w}(t)\,\overline{w}^*(t)\, dt \\ &= \int_{-\infty}^{+\infty} \left[w^2(t) + w_\perp^2(t)\right] \, dt \\ &= \int_{-\infty}^{+\infty} w^2(t)\, dt + \int_{-\infty}^{+\infty} w_\perp^2(t)\, dt \\ &= E_w + E_{w_\perp}, \end{aligned} \tag{H.6}$$

where E_w and $E_{w_\perp}$ denote total energies of real and quadrature wavelets, respectively. To examine the relative magnitudes of the two component energies we apply Parseval's theorem, obtaining

$$E_w = \int_{-\infty}^{+\infty} w^2(t)\, dt = \int_{-\infty}^{+\infty} |W(f)|^2 \, df \tag{H.7}$$

$$E_{w_\perp} = \int_{-\infty}^{+\infty} w_\perp^2(t)\, dt = \int_{-\infty}^{+\infty} |W_\perp(f)|^2 \, df. \tag{H.8}$$

Now, from the foregoing definition of the Hilbert Transform (equation (H.2)), it follows that

$$\begin{aligned} W_\perp(f) &= W(f)\,[i\ \mathrm{sgn}(f)] \\ &= |W(f)|\, e^{i\,\Theta(f)}\,[i\ \mathrm{sgn}(f)] \\ &= |W(f)|\left[-\sin\Theta(f) + i\cos\Theta(f)\right]\mathrm{sgn}(f) \end{aligned} \tag{H.9},$$

where $|W(f)|$ and $\Theta(f)$ denote the amplitude and phase spectrum of $w(t)$, respectively. On multiplying both sides of the foregoing expression by the associated complex conjugate, we obtain obtain the squared spectrum

$$|W_\perp(f)|^2 = W_\perp(f)\, W_\perp^*(f) = |W(f)|^2 \,\mathrm{sgn}^2(f)$$

and, consequently,

$$|W_{\perp}(f)| = |W(f)|\,[1 - \delta_0(f)], \tag{H.10}$$

where

$$\delta_0(f) = \begin{cases} 0, & f \neq 0; \\ 1, & f = 0 \end{cases}$$

defines the so-called null function (Bracewell, 1986). In other words, Hilbert transformation annihilates the d.c. spectral component of the original wavelet. Consequently, equations (H.6)-(H.8) yield

$$\begin{aligned} E_{|\overline{w}|} &= E_w + E_{w_{\perp}} \\ &= \begin{cases} 2E_w, & W(0) = 0; \\ 2E_w - |W(0)|^2, & W(0) \neq 0 \end{cases} \end{aligned} \tag{H.11}$$

and, thus, provided that the original waveform possesses no d.c. spectral content (i.e. $W(0) = 0$), the envelope possesses precisely twice the total wavelet energy.

We now consider the second moment of envelope energy density about reference time t_0

$$\begin{aligned} \int_{-\infty}^{+\infty} |\overline{w}(t)|^2 (t - t_0)^2\,dt &= \int_{-\infty}^{+\infty} \overline{w}(t)\,\overline{w}^*(t)\,(t - t_0)^2\,dt \\ &= \int_{-\infty}^{+\infty} \left[w^2(t) + w_{\perp}^2(t)\right]\,(t - t_0)^2\,dt \\ &= \int_{-\infty}^{+\infty} w^2(t)\,(t - t_0)^2\,dt + \int_{-\infty}^{+\infty} w_{\perp}^2(t)\,(t - t_0)^2\,dt \\ &= E_w\,L_w^2(t_0) + \int_{-\infty}^{+\infty} w_{\perp}^2(t)\,(t - t_0)^2\,dt. \end{aligned} \tag{H.12}$$

From the frequency domain representation of second-moment wavelet length, equation (2.59) (see Appendix G), we have

$$\begin{aligned} E_w\,L_w{}^2(t_0) &= \int_{-\infty}^{+\infty} w^2(t)\,(t - t_0)^2\,dt \\ &= \frac{1}{4\pi^2} \int_{-\infty}^{+\infty} |W(f)|^2 \left\{ \left[\frac{d}{df}\Big(\ln|W(f)|\Big)\right]^2 + \left[\frac{d}{df}\Big(\Theta(f) + 2\pi f t_0\Big)\right]^2 \right\} df \end{aligned} \tag{H.13}$$

It follows by inspection that the second moment of wavelet energy density about time t_0 is invariant under application of a frequency-dependent phase-shift that is constant between

zeros in the corresponding amplitude spectrum. Consequently, since Hilbert transformation amounts, in effect, to applying a frequency-independent phase-shift of $\frac{\pi}{2}$ radians, the quadrature wavelet $w_{\perp}(f)$ must have the same second moment of energy density about t_0 as the original wavelet $w_{\perp}(f)$. There is again, however, an exception. Since $i\,\mathrm{sgn}(f) = e^{i\frac{\pi}{2}\mathrm{sgn}(f)} - \delta_0(f)$, the signum function introduces a phase discontinuity at f=0 and, consequently, unless nullified by a corresponding zero in the amplitude spectrum ($|W(0)| = 0$), the second moment of energy density about t_0 becomes infinite for the quadrature wavelet. Thus, we have

$$\int_{-\infty}^{+\infty} w_{\perp}^2(t)(t-t_0)^2\,dt = \begin{cases} E_w L_w{}^2(t_0), & W(0) = 0; \\ \infty, & W(0) \neq 0 \end{cases}. \tag{H.14}$$

Finally, substituting equations (H.11) and (H.14) in equation (H.4) for second-moment envelope length yields

$$L_{|\overline{w}|}(t_0) = \begin{cases} L_w(t_0), & W(0) = 0; \\ \infty, & W(0) \neq 0 \end{cases}. \tag{H.15}$$

Consequently, provided that the original wavelet possesses no d.c. spectral content (i.e. zero-area wavelet), second-moment envelope length is equivalent to wavelet length.

Appendix I

ENVELOPE INVARIANCE UNDER FREQUENCY-INDEPENDENT PHASE-SHIFT

Consider an arbitrary real-valued wavelet $w(t)$. An associated analytic wavelet $\overline{w}(t)$ is defined by

$$\overline{w}(t) = w(t) - i w_{\perp}(t), \tag{I.1}$$

where

$$w_{\perp}(t) = \mathcal{H}\{w(t)\} \tag{I.2}$$

defines the quadrature wavelet $w_{\perp}(t)$ given by the Hilbert transform $\mathcal{H}\{\}$ of the corresponding real-valued wavelet $w(t)$ (see Appendix H). The real-valued wavelet envelope follows as the modulus of the analytic wavelet

$$|\overline{w}(t)| = [\overline{w}(t)\,\overline{w}^{*}(t)]^{1/2} = [w^2(t) + w_{\perp}^2(t)]^{1/2}, \tag{I.3}$$

where $\overline{w}^{*}(t)$ denotes the complex conjugate of the analytic wavelet $\overline{w}(t)$.

Now, applying an frequency-independent phase-shift θ_0 to $w(t)$, yields a wavelet

$$w(t) = \cos\theta_0\, w(t) + \sin\theta_0\, w_{\perp}(t), \tag{I.4}$$

represented as a linear combination of original and quadrature wavelets. The corresponding analytic wavelet follows as

$$\overline{w}(t) = w(t) - i\, w_{\perp}(t), \tag{I.5}$$

where

$$\begin{aligned} w_{\perp}(t) &= \mathcal{H}\{w(t)\} \\ &= \cos\theta_0\, \mathcal{H}\{w(t)\} + \sin\theta_0\, \mathcal{H}\{w_{\perp}(t)\} \\ &= \cos\theta_0\, w_{\perp}(t) - \sin\theta_0\, w(t) \end{aligned} \tag{I.6}$$

since, in general, $\mathcal{H}\{\mathcal{H}\{f(t)\}\} = -f(t)$. Consequently, we have

$$\overline{w}(t) = [\cos\theta_0\, w(t) + \sin\theta_0\, w_{\perp}(t)] - i\,[\cos\theta_0\, w_{\perp}(t) - \sin\theta_0\, w(t)] \tag{I.7}$$

and, therefore,

$$|\overline{w}(t)| = [w^2(t) + w_{\perp}^2(t)]^{1/2} = [w^2(t) + w_{\perp}^2(t)]^{1/2} = |\overline{w}(t)| \tag{I.8}$$

Appendix J
MAXIMUM AMPLITUDE WAVELET

Consider a suite of real-valued wavelets $w_i(t)$ possessing a specified amplitude spectrum $|W(f)|$ and phase spectra $\Theta_i(f)$. Wavelets and their frequency spectra are related by the Fourier transform

$$\begin{aligned} w_i(t) &= \int_{-\infty}^{+\infty} \left[|W(f)|\, e^{i\Theta_i(f)} \right] e^{i2\pi ft}\, df \\ &= \int_{-\infty}^{+\infty} |W(f)| \cos\left[\Theta_i(f) + 2\pi f t\right] df + i \int_{-\infty}^{+\infty} |W(f)| \sin\left[\Theta_i(f) + 2\pi f t\right] df \end{aligned} \quad \text{(J.1)}$$

In particular, since a real-valued wavelet possesses an even amplitude spectrum ($|W(-f)| = |W(f)|$), we have

$$w_i(t) = \int_{-\infty}^{+\infty} |W(f)| \cos\left[\Theta_i(f) + 2\pi f t\right] df. \quad \text{(J.2)}$$

Consequently, it follows that no wavelet possessing the specified amplitude spectrum $|W(f)|$ can have amplitude exceeding

$$w_{max} = \int_{-\infty}^{+\infty} |W(f)|\, df. \quad \text{(J.3)}$$

Moreover, it is evident that this maximum amplitude occurs only for a wavelet or wavelets possessing a linear phase spectrum

$$\Theta_{max}(f) = n\pi - 2\pi f \tau, \quad \text{(J.4)}$$

where n denotes an arbitrary integer value. Finally, however, since a constant phase shift of $n\pi$ rad affects only the polarity of the wavelet, we are left with the odd phase spectrum

$$\Theta_{max}(f) = -2\pi f \tau \quad \text{(J.5)}$$

associated with a zero-phase wavelet, time shifted by t time units. Thus, maximum amplitude is ultimately associated with the zero-phase wavelet having phase spectrum $\Theta(f) = 0$ and, consequently, having maximum amplitude w_{max} given by equation (J.3) at t=0 (from equation (J.5).

Appendix K
THE MINIMUM-LENGTH CAUSAL WAVELET

Second moment wavelet length, measured relative to the onset of a causal source disturbance $t_0 = 0$ is defined for a real-valued wavelet by

$$L_w{}^2(0) = \frac{1}{E_w}\int_{-\infty}^{+\infty} w^2(t)\, t^2\, dt \qquad (2.48)(K.1)$$

where

$$E_w = \int_{-\infty}^{+\infty} w^2(t)\, dt \qquad (2.47)(K.2)$$

defines total wavelet energy. Following the development of Berkhout (1984), we rewrite the foregoing expression in discrete form as

$$L_w^2[0] = \frac{1}{E_w}\sum_{n=0}^{\infty}[n\,\Delta t]^2\, w^2[n\,\Delta t], \qquad (K.3)$$

where

$$E_w = \sum_{n=0}^{\infty} w^2[n\,\Delta t]. \qquad (K.4)$$

Let us now expand equation (K.3) explicitly as

$$L_w^2[0] = \frac{1}{E_w}\left\{\Delta t^2\, w^2[\Delta t] + [2\Delta t]^2\, w^2[2\Delta t] + [3\Delta t]^2\, w^2[3\Delta t] + \ldots\right\} \qquad (K.5)$$

or, equivalently, as

$$L_w^2[0] = \frac{1}{E_w}\left\{\Delta t^2\sum_{n=1}^{\infty} w^2[n\,\Delta t] + (2^2-1)\,\Delta t^2\sum_{n=2}^{\infty} w^2[n\,\Delta t] + (3^2-2^2)\,\Delta t^2\sum_{n=3}^{\infty} w^2[n\,\Delta t] + \ldots\right\}, \qquad (K.6)$$

where, for example,

$$\Delta t^2\sum_{n=1}^{\infty} w^2[n\,\Delta t] + (2^2-1)\,\Delta t^2\sum_{n=2}^{\infty} w^2[n\,\Delta t] = \Delta t^2\sum_{n=1}^{\infty} w^2[n\,\Delta t] - \Delta t^2\sum_{n=2}^{\infty} w^2[n\,\Delta t] + 2^2\Delta t^2\sum_{n=2}^{\infty} w^2[n\,\Delta t]$$

$$= \Delta t^2\, w^2[\Delta t] + 2^2\Delta t^2\sum_{n=2}^{\infty} w^2[n\,\Delta t]$$

and we recognize that the first term on the right-side of the foregoing result $\Delta t^2\, w^2[\Delta t]$ is equivalent to the first term of the series in equation (K.5).

Consequently, writing the series in equation (K.6) as

$$\sum_{m=1}^{\infty}\left[m^2-(m-1)^2\right]\Delta t^2\sum_{n=m}^{\infty}w^2\left[n\,\Delta t\right]=\left\{\Delta t^2\sum_{n=1}^{\infty}w^2\left[n\,\Delta t\right]+\left(2^2-1\right)\Delta t^2\sum_{n=2}^{\infty}w^2\left[n\,\Delta t\right]\right.$$
$$\left.+\left(3^2-2^2\right)\Delta t^2\sum_{n=3}^{\infty}w^2\left[n\,\Delta t\right]+\ldots\right\},$$

we obtain for second-moment wavelet length, the discrete form

$$L_w^2\left[0\right]=\frac{1}{E_w}\left(\sum_{m=1}^{\infty}\left[m^2-(m-1)^2\right]\Delta t^2\sum_{n=m}^{\infty}w^2\left[n\,\Delta t\right]\right)$$

or, on substituting equation (A9.4) for total wavelet energy,

$$L_w^2\left[0\right]=\sum_{m=1}^{\infty}\left[m^2-(m-1)^2\right]\Delta t^2\left(\sum_{n=m}^{\infty}w^2\left[n\,\Delta t\right]\Big/\sum_{n=0}^{\infty}w^2\left[n\,\Delta t\right]\right). \qquad \text{(K.7)}$$

Finally, we consider a suite of wavelets possessing a specified amplitude spectrum and, consequently, the same total energy E_w. We define the minimum-phase or minimum-delay wavelet $\tilde{w}(t)$ as the member of the wavelet suite possessing maximum partial energy at any time $m\Delta t$ $(m \geq 0)$

$$\sum_{n=0}^{m}\tilde{w}^2\left[n\,\Delta t\right]>\sum_{n=0}^{m}w_i^2\left[n\,\Delta t\right], \qquad \text{(K.8)}$$

where the subscript i indicates that the respective inequality holds for each member of the wavelet suite $w_i(t)$. It follows that the minimum-phase wavelet must also possess minimum tail energy

$$\sum_{n=m}^{\infty}\tilde{w}^2\left[n\,\Delta t\right]<\sum_{n=m}^{\infty}w_i^2\left[n\,\Delta t\right] \qquad \text{(K.9)}$$

and, consequently from equation (K.7), that the minimum-phase wavelet is characterized by minimum second-moment length

$$L_{\tilde{w}}\left[0\right]<L_{w_i}\left[0\right]. \qquad \text{(K.10)}$$

Appendix L
SECOND-MOMENT LENGTH OF THE RICKER WAVELET

The second-moment length of an arbitrary wavelet $w(t)$ is defined by

$$L_w{}^2(t_0) = \frac{1}{E_w}\int_{-\infty}^{+\infty} w^2(t)(t-t_0)^2\,dt, \qquad (2.48)\,(L.1)$$

where

$$E_w = \int_{-\infty}^{+\infty} w^2(t)\,dt \qquad (2.47)\,(L.2)$$

represents total wavelet energy. Re-expressing equation (2.31) for the Ricker wavelet as

$$w(t) = (1-2bt^2)\,e^{-bt^2}, \qquad (L.3)$$

where $a = 12f_d^2$ and $b = 6f_d^2$, the corresponding second-moment length about the origin follows as

$$\begin{aligned} L_w^2(0) &= \frac{1}{E_w}\int_{-\infty}^{+\infty} t^2\left(1-2at^2+a^2t^4\right)e^{-2bt^2}\,dt \\ &= \frac{1}{E_w}\left[\int_{-\infty}^{+\infty} t^2 e^{-2bt^2}\,dt - 2a\int_{-\infty}^{+\infty} t^4 e^{-2bt^2}\,dt + a^2\int_{-\infty}^{+\infty} t^6 e^{-2bt^2}\,dt\right], \end{aligned} \qquad (L.4)$$

where

$$E_w = \int_{-\infty}^{+\infty} e^{-2bt^2}\,dt - 2a\int_{-\infty}^{+\infty} t^2 e^{-2bt^2}\,dt + a^2\int_{-\infty}^{+\infty} t^4 e^{-2bt^2}\,dt. \qquad (L.5)$$

Now, recalling the normal error integral

$$\int_{-\infty}^{+\infty} e^{-cx^2}\,dx = \left(\frac{\pi}{c}\right)^{1/2}, \qquad (L.6)$$

for an arbitrary positive valued constant c, the constituent integrals in equations (L.4) and (L.5) are evaluated as follows. Consider, for example, the integral

$$\int_{-\infty}^{+\infty} t^2 e^{-2bt^2}\,dt = \int_{-\infty}^{+\infty} t^2 e^{-ct^2}\,dt, \qquad (L.7)$$

where $c = 2b$. Integration by parts yields

$$u = t \qquad dv = t\,e^{-ct^2}\,dt$$

$$du = dt \qquad v = -\frac{1}{2c}e^{-ct^2}$$

$$\int_{-\infty}^{+\infty} t^2 e^{-ct^2}\,dt = -\frac{t}{2c} e^{-ct^2}\Big|_{-\infty}^{+\infty} + \frac{1}{2c}\int_{-\infty}^{+\infty} e^{-ct^2}\,dt$$

and, consequently, using equation (L.6) and $c = 2b$ we obtain

$$\int_{-\infty}^{+\infty} t^2 e^{-ct^2}\,dt = \frac{1}{2c}\left(\frac{\pi}{c}\right)^{1/2} = \frac{1}{4b}\left(\frac{\pi}{2b}\right)^{1/2}. \tag{L.8}$$

Similarly, for

$$\int_{-\infty}^{+\infty} t^4 e^{-2bt^2}\,dt = \int_{-\infty}^{+\infty} t^4 e^{-ct^2}\,dt, \tag{L.9}$$

we have

$$u = t^3 \qquad dv = t\,e^{-ct^2}\,dt$$

$$du = 3t^2\,dt \qquad v = -\frac{1}{2c} e^{-ct^2}$$

$$\int_{-\infty}^{+\infty} t^4 e^{-ct^2}\,dt = -\frac{t^3}{2c} e^{-ct^2}\Big|_{-\infty}^{+\infty} + \frac{3}{2c}\int_{-\infty}^{+\infty} t^2 e^{-ct^2}\,dt$$

and, consequently, substitution of (L.8) yields

$$\int_{-\infty}^{+\infty} t^4 e^{-ct^2}\,dt = \frac{3}{4c^2}\left(\frac{\pi}{c}\right)^{1/2} = \frac{3}{16b^2}\left(\frac{\pi}{2b}\right)^{1/2}. \tag{L.10}$$

In similar fashion, we obtain

$$\int_{-\infty}^{+\infty} t^6 e^{-ct^2}\,dt = \frac{15}{8c^3}\left(\frac{\pi}{c}\right)^{1/2} = \frac{15}{64b^3}\left(\frac{\pi}{2b}\right)^{1/2}. \tag{L.11}$$

Finally, on substituting (L.6), (L.8), (L.10) and (L.11) in equations (L.4) and (L.5), we obtain

$$L_w^2(0) = \frac{1}{E_w}\left(\frac{\pi}{2b}\right)^{1/2}\left(\frac{1}{4b} - \frac{6a}{16b^2} + \frac{15a^2}{64b^3}\right), \tag{L.12}$$

where

$$E_w = \left(\frac{\pi}{2b}\right)^{1/2}\left(1 - \frac{2a}{4b} + \frac{3a^2}{16b^2}\right). \tag{L.13}$$

Noting that $a = 2b = 12f_d^2$, the preceeding result reduces to

$$L_w^2(0) = \frac{7}{12}\left(\frac{1}{b}\right) \approx \frac{0.972}{f_d^2} \tag{L.14}$$

or, equivalently,

$$L_w(0) \approx \frac{0.31}{f_d} = 0.31\,T_d, \tag{L.15}$$

where $T_d = 1/f_d$ represents the dominant period of the wavelet.

Appendix M
FIELD EXPERIMENTS IN GREECE

Tentative approval was obtained in 1989 for an extensive programme of field experiments in connection with excavations sponsored by the Canadian Archaeological Institute at Athens (CAIA). Although necessary permits were finally denied with equipment already in Greece, we gained access for limited testing at two ancient sites under the supervision of Prof. St. Papamarinopoulos of the University of Patras.

At Stymphalia, in Arcadia, an extensive electrical resistivity survey has revealed much of the plan of ancient Stymphalos, a city of the fourth century B.C. buried in lacustrine sediments associated with seasonal flooding of Lake Stymphalos (Papamarinopoulos, et al., 1988; Williams, 1984). Seismic soundings were acquired in connection with well defined resistivity anomalies to investigate the practical influence of data acquisition parameters, including optimum offset, charge size, pre-emphasis filter frequency, stack-fold, etc.. Although results provided valuable insight on the selection of field parameters, soundings gave no conclusive indication of the nature of subsurface remains giving rise to associated resistivity features. In particular, where archaeological remains were known to be extremely shallow (<30 cm), direct wave arrivals constituted a restrictive source of interference, masking diffracted-reflected arrivals from archaeological targets.

A second site, Phalasarna, on the northwest coast of Crete was a prosperous maritime port by the fourth century B.C.. Archaeologists believe that later, during the first century B.C., the Romans destroyed the town and blocked the harbour's entrance as a policing measure (Hadjidaki, 1988). Owing to recent tectonic uplift of western Crete, the ancient harbour is presently several metres above sea level and inundated by 2-5 metres of sediment. Soil conditions at Phalasarna are significantly different than those encountered at Stymphalos, offering a useful perspective on the importance of ground conditions. Compared with sediments at Stymphalos, those at Phalasarna are poorly sorted and strongly consolidated. Consequently, while source-subsurface coupling was immaterial at Stym-

phalos, it was a principal concern at Phalasarna. In particular, variations in coupling efficiency gave rise to substantial variability in wavelet characteristics, rendering identification of coherent events difficult at best. Despite these complications, optimum offset seismic soundings were successful in confirming the continuity of a harbour wall, exposed by limited excavations. In addition, a small-scale seismic refraction survey within the harbour area provided controls on harbour geometry in good agreement with test trench stratigraphies reported by Hadjidaki (1988).

In summary, although restricted access prevented adequate field trials of the seismic reflection method, limited experiments yielded promising results and revealed potential obstacles to practical field implementation of the method. The author has recently been awarded a NSF-NATO Post-Doctoral Fellowship to conduct an exhaustive programme of field trials in connection with ongoing archaeological investigations at Stymphalos and Phalasarna in 1996.

Appendix N
SEISMIC VELOCITY DATA

Material	Velocity in km/sec V_P	V_S	Remarks*
Alluvium	.5 –2.0	..	*f*; near surface
	3.0 –3.5	..	*f*; depth 2000 meters
Clay	1.1 –2.5	..	*f*
Diluvium	.7 –1.8	..	*f*
Embankments and fill	.4	..	*f*
Loam	.8 –1.8	..	*f*
Loess	.3 – .6	..	..
Sand			
loose	.2 –2.0	..	*f*
loose	1.0	.4	*f*; above water table
loose	1.8	.5	*f*; below water table
calcareous	.8	..	*f*
wet	.75–1.5	..	*f*
Weathered layer	.3 – .9	..	*f*
Glacial			
till	.43–1.04	..	*f*; unsaturated
till	1.73	..	*f*; saturated
sand and gravel	.38– .50	..	*f*; unsaturated
sand and gravel	1.67	..	*f*; saturated
River, Bay	1.1 –1.8	..	..
Suboceanic	over 1.6	over .6	*f* and *l*; see Figure 2
Shallow water fine-grained; off San Diego, Calif.	1.46–1.68	..	in situ ultrasonic measurement sea water

* *f* = field determination; *l* = laboratory determination

Figure N.1. Compressional seismic wave velocities in unconsolidated sediments (After Press, 1966).

	v_p (km s^{-1})
Unconsolidated materials	
Sand (dry)	0.2–1.0
Sand (water saturated)	1.5–2.0
Clay	1.0–2.5
Glacial till (water saturated)	1.5–2.5
Permafrost	3.5–4.0
Sedimentary rocks	
Sandstones	2.0–6.0
Tertiary sandstone	2.0–2.5
Pennant sandstone (Carboniferous)	4.0–4.5
Cambrian quartzite	5.5–6.0
Limestones	2.0–6.0
Cretaceous chalk	2.0–2.5
Jurassic oolites and bioclastic limestones	3.0–4.0
Carboniferous limestone	5.0–5.5
Dolomites	2.5–6.5
Salt	4.5–5.0
Anhydrite	4.5–6.5
Gypsum	2.0–3.5
Igneous/Metamorphic rocks	
Granite	5.5–6.0
Gabbro	6.5–7.0
Ultramafic rocks	7.5–8.5
Serpentinite	5.5–6.5
Pore fluids	
Air	0.3
Water	1.4–1.5
Ice	3.4
Petroleum	1.3–1.4
Other materials	
Steel	6.1
Iron	5.8
Aluminium	6.6
Concrete	3.6

Figure N.2. Compressional seismic wave velocities in rocks (After Keary and Brooks, 1991).